Persistent Current Joints Between NbTi Superconducting Wires

Greg Brittles

St Anne's College

University of Oxford

A thesis submitted for the degree of

Doctor of Philosophy

Hilary Term 2016

Abstract

Persistent Current Joints Between NbTi Superconducting Wires

Greg Brittles
St Anne's College

A thesis submitted for the degree of Doctor of Philosophy in
The University of Oxford
Hilary Term 2016

Persistent current joints are critical components of superconducting magnets, and improvements in their properties are key to the production of next generation devices. Despite having been made routinely for more than half a century, the science underpinning the performance of joints between NbTi wires remains poorly understood. At this critical juncture, where new jointing methods are being sought for NbTi, it is essential that we develop a sound understanding of the factors influencing joint quality. The aim of this thesis was to identify the characteristic microstructural and superconducting properties of joints produced by the three standard jointing methods for NbTi: soldering, spot welding and cold pressing.

There were three main components to this work. The first was to obtain a complete characterisation of $J_c(B,T)$ and $B_{c2}(T)$ for the raw materials from which the joints were made, which was done by standard magnetic methods. Where relevant, the results have been interpreted in terms of the basic pinning mechanisms and microstructures in the materials tested. The implications for joint performance are discussed.

Secondly, a novel magnetic method was developed to measure the superconducting performance of joints over an unprecedented range of operational conditions. The method involves winding a very small NbTi coil, closing the coil with the joint of interest, and testing the sample in a conventional SQUID magnetometer. The current carrying ability of joints can be measured simply from magnetic hysteresis loops, which enabled the performance of a range of joints to be analysed in fine detail and with

considerable convenience. Furthermore, owing to the extremely low coil inductance and highly sensitive SQUID magnetometer employed, current decay curves corresponding to voltages as low as 10^{-14} V could be obtained in very short measurement times of just 20 minutes. Unfortunately, unexpectedly large drift in the background magnetic field was found to dominate in most measurements, but nevertheless the measurements provided an extremely rapid method of proving that the joints are truly superconducting. Suggestions are made as to how the technique could be improved to permit precise measurements of joint $I_c(B,T)$ and V-I curves in the persistent mode regime, which would enable much needed fundamental studies into superconductivity in joints.

Finally, the joint testing technique was employed to measure the superconducting performance of soldered, spot welded and cold pressed NbTi joints. The results were analysed along with the raw material superconducting properties and microstructures in the joints, which were obtained by scanning electron microscopy (SEM). This allowed the performance-limiting factors in each joint to be established. As a result of this study, a new soldering/cold pressing method is proposed which may permit direct metal-to-metal bonding between NbTi materials without the need for Pb or harmful chemicals.

Acknowledgements

During my time at Oxford I have benefited from the support, advice and friendship of an enormous group of people, to whom I am extremely grateful.

To my D.Phil supervisors, Chris Grovenor and Susie Speller. For your dedication, unfathomable scientific knowledge, support, encouragement to pursue "Friday afternoon" experiments, and last, but, not least, for removing all those unnecessary commas from my thesis.

To my industrial collaborators. Paul Noonan, Andrew Varney and Heather Rugg of Agilent Technologies, for funding, materials and advice. Tom Bradshaw, Cyril Lockett, Simon Canfer, Victoria Bayliss and John Vandore of the Science and Technologies Facilities Council, as well as Stephen Milward and Alexey Dobrynin of Diamond Light source, for technical assistance, provision of samples and use of equipment in this project. Ziad Melhem of Oxford Instruments, for providing me with a summer internship that got me into this field in the first place.

Collaborators at the Clarendon Laboratory. Dharmalingam Prabhakaran (Prabhak), Andrew Boothroyd, Amir Haghighirad, Tony Hickman, Rob Storey and Yuwei Ge, for helpful advice and use of test facilities.

Various members of the superconductivity community for countless useful discussions at various points in the project. Damian Hampshire and Mark Raine of Durham University. John Durrell, Mark Ainslie and Archie Campbell of Cambridge University. M'Hamed Lakrimi of Siemens Magnet Technology.

All of the staff at Oxford materials, who are too numerous to mention individually but have made my time in the department a pleasure. Also to the Worshipful Company of Founders, St Anne's College and the Institute of Physics for various grants that have allowed me to travel to conferences in Karlsruhe (Germany), Charlotte (NC, USA) and Lyon (France) to learn and share my work.

To my fellow officemates, for providing a much-needed distraction from my studies. Juliana Mohd Janurudin, Hugh Taylor, Katie Moore, Haibo Jiang, Jiale Wang,

Tayebeh Mousavi, Hanis Ayuni, Canan Aksoy (thanks for the microscope help), Tim Davies, Josef Hazi and Will Darby.

Finally, to my family. Mum (Bev), Dad (Paul), Joanna, Kylie and Campbell, for your support and appreciation for the pictures in my publications. In your honour the tagline for this thesis is "Something to do with magnets???", which I gather is what you think I've been doing all this time. To the Bowers (Andy, Angie and Hannah) for all of the Sussex weekends spent writing. And last (but by no means least) to Katie Bower, for your encouragement, positivity, willingness to break the "no science at the dinner table" rule on occasion, and for reminding me that when all this is through, "you still won't be a *proper* Doctor".

Statement of Originality

The work reported in this thesis was carried out by the author in the Department of Materials, University of Oxford, between October 2012 and March 2016, under the supervision of Prof. C.R.M. Grovenor and Prof. S.C. Speller.

No part of this thesis has been previously submitted for a degree at this or any other university. The work of other authors has been freely drawn upon and is duly acknowledged in the text. A list of references has been given at the end of the thesis.

Some of the work described in this thesis has been published in the following journals and presented at conferences listed below:

Publications

G. D. Brittles, P. Noonan, S. A. Keys, C. R. M. Grovenor, and S. Speller, "Rapid characterisation of persistent current joints by squid magnetometry," Supercond. Sci. Technol., vol. 27, no. 12, p. 122002, 2014.

G. D. Brittles, T. Mousavi, C. R. M. Grovenor, C. Aksoy, and S. C. Speller, "Persistent current joints between technological superconductors," Supercond. Sci. Technol., vol. 28, no. 9, p. 093001, 2015.

G. D. Brittles, C. Aksoy, C. Grovenor, T. Bradshaw, S. Milward, and S. Speller, "Microstructural properties and magnetic testing of spot welded joints between Nb-Ti filaments," IEEE Trans. Appl. Supercond., (in press).

Key Conference Presentations

Oxford Materials Symposium, Oxford, UK, Mar 2014, winner of Hetherington Prize for best oral presentation - "Persistent current joints in high field superconducting magnets".

Applied Superconductivity Conference, Charlotte (NC), USA, Aug 2014, oral presentation - "Persistent current joints between technological superconductors".

Joint UK-Japan Workshop on Physics and Applications of Superconductivity, Kings College, Cambridge, UK, April 2015, oral presentation - "Inductive resistance testing of superconducting joints by SQUID magnetometry".

European Conference on Applied Superconductivity, Lyon, France, Sep 2015, poster - "Microstructural and superconducting properties of persistent mode joints between NbTi conductors"

This thesis is approximately 40,000 words in length.

Contents

Chapter 1

Introduction

1.1 Background - Joints in Superconducting Magnets

The manufacture of electromagnets from technological superconducting wires is by far the largest engineering application of superconducting materials. Superconducting magnets are commonly used in applications that employ high magnetic fields for sustained periods of time. Commercial applications include nuclear magnetic resonance (NMR) instruments, magnetic resonance imaging (MRI) scanners, laboratory scale research magnets and superconducting magnetic energy storage systems (SMES). Very large scale applications also exist, such as the Large Hadron Collider (LHC) [1], the upcoming International Thermonuclear Experimental Reactor (ITER) [2] and ultra-high field facilities such as those at the National High Magnetic Field Laboratory (NHMFL) in Tallahassee, Florida.

In these applications, superconducting materials are unmatched in their ability to generate strong, uniform and highly stable magnetic fields, enabling high sensitivity measurements and fine control of particle beams. These advantageous properties arise from the ability to confine supercurrents to high inductance (L) coils with exceedingly low operational resistances (R). Under these conditions, the current shows an almost negligible attenuation, sustaining the magnetic field produced to better than 1 ppb/hr in some cases; a decay timescale ($\tau = \mathrm{L/R}$) of tens of thousands of years [3]. This so called persistent mode (PM) transforms driven electromagnets into quasi-permanent magnets.

Joints between superconducting wires are integral components of these PM magnets since their terminals must be short-circuited in order to confine the supercurrent to the circuit. A superconducting shunt known as a persistent current switch (PCS) is employed to isolate the magnet from the power supply once charged [4]. Further joints are required to connect together the multiple coils from which such magnets are constructed. Magnets must be built in this modular fashion predominantly because of limited single wire lengths [6].

The resistance of each joint made adds to the DC losses in the superconducting coils, so determining the total resistance and hence field stability of the magnet. A typical 9.4 T, 400 MHz NMR magnet with a self-inductance of 40 H has ~10 joints carrying an operating current of 100 A, each of which must have a resistance of less than $5 \times 10^{-12}\,\Omega$ in order to minimise field drift to <10 ppb/hr. Joints with operational resistances of $10^{-13} - 10^{-14}\,\Omega$ are routinely manufactured for commercial NbTi MRI magnets. The production of these so called persistent current joints (herein referred to simply as joints) requires a truly superconducting current path to be established between the parent conductors.

1.1.1 Motivation for Joint Development

The development of reliable jointing techniques is of critical importance to the future of applied superconductivity. Next generation commercial magnets employing high temperature superconducting (HTS) materials are presently under development, with candidate conductors including rare-earth barium copper oxide coated conductors (REBCO CCs), magnesium diboride (MgB_2) wires and tapes, and bismuth strontium calcium copper oxide (BiSCCO) multifilamentary wires and tapes (for which both the Bi-2212 and Bi-2223 compounds are contenders). These are all fragile and chemically sensitive ceramic materials for which jointing techniques often require high pressures, high temperatures and oxygen-controlled atmospheres. Commercially viable jointing methods for these materials are still being sought, without which the deployment of these conductors in commercial magnets may be severely compromised.

Whilst these materials may be the magnet conductors of the future, it appears that the low temperature superconducting (LTS) materials of today will continue to play an important role for the foreseeable future. For NbTi wires, the present workhorse

conductor for fields of up to ∼10 T, joints are made routinely by magnet manufacturers by a well established soldering technique. Nevertheless, NbTi joint development remains an active field of research for several reasons.

Firstly, measures must be taken to mitigate the inferior superconducting performance of the solders compared to wires, requiring them to be located in low field regions of the magnet (typically <1 T) or specially shielded. These measures complicate and constrain the design of these devices, and improved jointing techniques may simplify magnet manufacturing processes.

There are also business incentives for the elimination of Pb in superconducting solders, since the present exemption of superconducting technologies from European Union restrictions on the use of Pb will expire on 30^{th} June 2021 [5, 6]. There is thus a need to develop replacement Pb-free solders, or adopt an alternative Pb-free jointing method. Any change to the well established production line is of concern to magnet manufacturers, since the cost of a single joint failure can easily be the entire profit margin on the magnet. With this in mind it is imperative that new jointing methods for NbTi are developed in a scientific manner, such that they may be implemented with near-perfect reproducibility on the production line.

1.2 Aims and Overview of This Thesis

Research into NbTi joints has been led predominantly by magnet manufacturers, and as-such the literature is understandably focussed more on the engineering performance of the joints rather than on pure materials science or physics. A full review of the available literature on NbTi joints is presented in Chapter 2.

In order to develop new jointing methods in an effective, scientific manner, the starting point must be a sound understanding of the factors determining joint quality. The level of knowledge in this regard (at least in the academic community) is extremely poor. The aim of this thesis is to establish the characteristic microstructural and superconducting properties of NbTi joints made by the three major techniques presented in the literature; soldering, spot welding and cold pressing. It is hoped that the results of this investigation will provide a strong foundation from which to progress with joint development.

The starting point of this project was to measure comprehensively the superconducting properties of each individual component material used to make the joints. This

was done by standard magnetometry techniques which are explained in Chapter 3, and the results are presented in Chapter 4. Secondly, having identified the importance of measuring joint performance over a wide range of operating conditions in order to permit fundamental studies, a novel magnetic joint characterisation technique was devised to achieve this. Chapter 5 discusses the development of this technique. Finally, the measurement technique was put to work to measure the superconducting performance of a range of NbTi joints, which were subsequently dissected and analysed under the microscope. Chapter 6 presents these results and discusses the factors determining their performance.

This discussion will begin with an introduction to the basic physical principles underpinning the performance of technological superconducting wires.

1.3 Basic Theory of Superconductivity

This section describes the fundamental electromagnetic properties of the superconducting state, and explains their physical origin using the results of well established theories.

1.3.1 Zero Resistance

Superconductors exhibit zero resistance below a certain *critical temperature* (T_c). The Bardeen-Cooper-Schrieffer (BCS) theory of 1957 [7] is the accepted quantum mechanical description of this phenomenon. The theory proposes that superconductivity arises from an attractive potential between electron pairs, which causes them to condense into a composite boson known as the Cooper pair. All Cooper pairs in the system have the same momentum (a *macroscopic quantum state*), for which there is an energy gap ($2\Delta \approx 3.5\ \mathrm{k}_B T_c$) to the nearest empty state. Pair-breaking (resistance) can only occur if an amount of energy greater than this gap is supplied to the Cooper pairs.

The maximum Cooper pair current density is the depairing current density, J_d, at which the kinetic energy of the pair exceeds the gap energy. Magnetic fields and thermal processes also contribute to pair breaking, giving rise to critical fields (discussed in Section 1.3.2) and the critical temperature, T_c.

The electron pairing mechanism of the BCS theory was a phonon mediated interaction of electrons with the crystal lattice. This is the accepted explanation for "conventional" LTS materials, but cannot explain the pairing mechanism in "unconventional" HTS materials, for which the search goes on [8].

1.3.2 Diamagnetism

Superconductors are also diamagnetic – generating currents to either partially or completely shield their interior from an applied field. Simple equations were first derived in the phenomenological electrodynamic theory of F. and H. London in 1935 [9] which describe the exponential attenuation of a magnetic field inside a superconductor by screening currents. However, since the magnetisation curve of a superconductor is completely reversible with both field *and* temperature, this indicates that the transition from the normal (non-superconducting) state to the superconducting state is a thermodynamic phase change. Owing to this fact, a more general thermodynamic theory of superconductivity was produced by Ginzburg and Landau (GL) in 1950 [10].

This theory derives two important length scales associated with superconductivity. The first is the GL penetration depth, λ, which is the characteristic length over which magnetic fields are attenuated inside the superconductor. The second is the GL coherence length, ξ, which is the characteristic length over which the superconducting order parameter, ψ (which is related to the number density of superconducting charge carriers), changes at a superconducting/normal interface. The ratio of these lengths is the GL parameter, $\kappa = \lambda/\xi$, which is a material-dependent quantity.

In 1957, Abrikosov [11] showed that there are two solutions to the GL equations, leading to type-I and type-II superconductivity with distinct magnetic characteristics, as sketched in Figure 1.1.

1.3.2.1 Type-I Superconductivity

Materials with $\kappa<1/\sqrt{2}$ are known as type-I superconductors, and are typically elements. As is shown in Figure 1.1a, these exhibit perfect diamagnetism up to a critical field B_c, completely expelling magnetic fields from their interior (the Meissner effect) [12]. B_c is too small for magnet applications, so these materials are of little technological use.

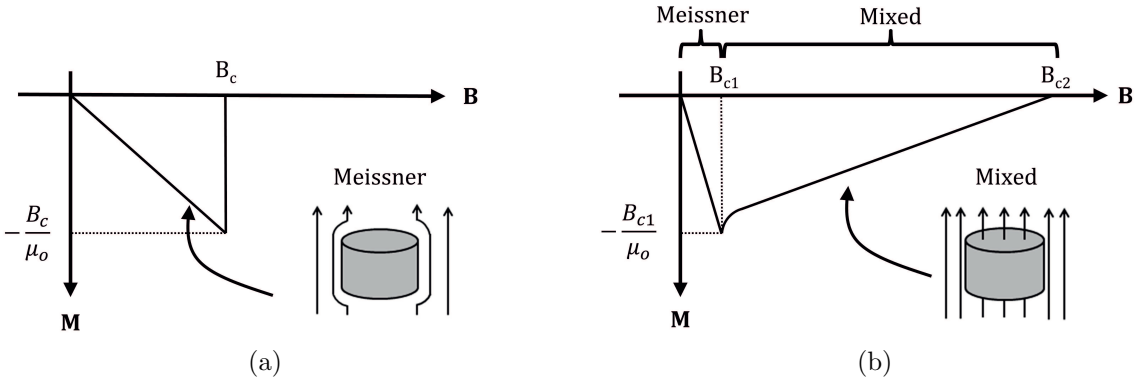

Figure 1.1: Sketch of the reversible magnetisation curves of (a) type-I and (b) type-II superconductors.

1.3.2.2 Type-II Superconductivity

Materials with $\kappa > 1/\sqrt{2}$ are known as type-II superconductors, which are typically alloys and compounds. As shown in Figure 1.1b, these also exhibit the Meissner effect up to a lower critical field (B_{c1}), but at higher fields they permit the penetration of quantised *flux lines* into the material. Each of these contains an amount of flux $\Phi_o = h/2e$, where h is Planck's constant and e is the elementary charge. Each flux line is shielded by an induced supercurrent vortex which flows on a radial scale λ, attenuating the field over the same length scale. The order parameter falls from the equilibrium external value to zero in the centre of the vortex over a radial scale ξ. Each vortex therefore has a normal core of radius ξ, whilst the material between the vortices remains superconducting, and so the material is said to be in the mixed (or vortex) state.

Under equilibrium conditions in homogeneous, isotropic materials, the flux vortices form an hexagonal Abrikosov lattice with nearest neighbour spacing $d = \sqrt{2\Phi_o/\sqrt{3}B}$. The density of flux vortices increases with field, until at the upper critical field (B_{c2}) the normal cores overlap and superconductivity is lost altogether. B_{c2} is given by:

$$B_{c2} = \frac{\Phi_o}{2\pi\xi^2}. \tag{1.1}$$

This can be very large indeed, typically tens of Teslas in state-of-the-art materials, and thus all technological superconductors are type-II.

1.4 Critical Currents in Inhomogeneous Superconductors

1.4.1 Flux Flow

The use of superconductors in magnet applications requires a transport current to be passed through the material in the background field produced by the magnet. When a current density $\boldsymbol{J}$ is passed through the superconductor, a Lorentz force per unit volume ($\boldsymbol{F} = \boldsymbol{J} \times \boldsymbol{B}$) acts on the flux lattice. As sketched in Figure 1.2, this causes the flux lines (with their normal cores) to move through the superconductor at a velocity $\boldsymbol{v}$, producing an electric field $\boldsymbol{E} = \boldsymbol{v} \times \boldsymbol{B}$ which opposes $\boldsymbol{J}$. This is known as *flux flow resistance* and produces a linear V-I curve [13].

1.4.2 Flux Pinning

In order to pass a current without resistance, the flux lines must be secured against the Lorentz force (pinned). Real materials are inevitably inhomogeneous to some extent, containing defects that locally perturb the superconducting order parameter or penetration depth, as will be discussed further in Section 1.4.3. In these regions the free energy of the vortex is reduced, creating potential wells to which they are attracted. By deforming the flux lattice, the flux lines can take up these positions and are held with a net pinning force per unit volume, F_p. Transport currents can therefore be passed with densities as high as the critical current density, J_c, at which the Lorentz force per unit volume matches the average pinning force per unit volume in the sample [14]:

$$F_p = |\boldsymbol{J_c} \times \boldsymbol{B}|. \tag{1.2}$$

Any further increase in current density induces flux flow, producing a measurable voltage which allows J_c to be measured. Pinning forces can therefore be calculated from $J_c(B)$ values obtained from V-I curves.

Flux pinning also drastically alters the magnetic response of inhomogeneous type-II superconductors to changes in field. There is a force balance between external magnetic pressure which acts to redistribute the flux lines, and flux pinning in the sample which acts to hold them in place, establishing a so-called *critical state* [15]. This adds an irreversible component (hysteresis) to the magnetisation curve which is typically orders of magnitude larger than the reversible type-II magnetisation curve.

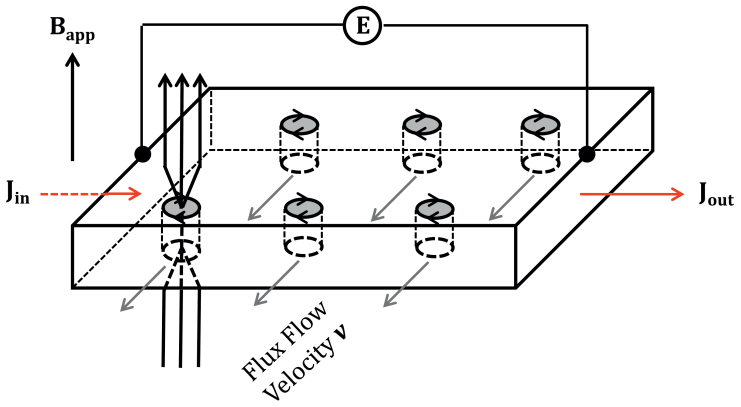

Figure 1.2: Sketch demonstrating flux flow in type-II superconductors.

$J_c(B)$ can also be calculated from the irreversible magnetisation curve using critical state models. This is the approach taken in this thesis and is discussed in full in Section 3.1.

1.4.3 Pinning Mechanisms

The production of technological wires with high J_c values relies on engineering an array of flux-pinning defects in the microstructure of the superconductor. According to Dew Hughes [16], the effectiveness of an ensemble of pinning centres is determined by four main factors.

The first is the superconducting nature of the pinning sites, since pinning occurs due to differences in the superconducting properties of the matrix and the defect. The most common are defects producing small differences in κ ($\Delta\kappa$ *pinning*), for example due to composition variations. The strongest pinning is caused by non-superconducting defects, for example normal particles (*normal pinning*).

The second factor is the size and spacing of the pinning defects compared to both ξ and λ, which determines the mechanism by which the vortices interact with the pinning sites. *Core pinning* is the interaction of vortex cores with defects that produce variations in the superconducting order parameter over length scales of $\sim\xi$. *Magnetic pinning* is the interaction of the vortex screening currents with magnetization currents flowing in the superconductor due to local variations in B. These defects must be of size $\sim\lambda$, since this is the length scale over which B may vary in a superconductor.

The third is the size of each dimension of the pinning defects compared with the flux lattice spacing (d) and the orientation of the field lines. These determine both the interaction length over which an individual flux line is pinned and the number of flux lines pinned by each defect. *Point* defects have all their dimensions smaller than d, and interact with a single vortex over a short length. *Line* defects have one dimension larger than d, and can interact with one well aligned flux line over a long interaction length, or multiple misaligned flux lines over a short interaction length. Similarly, *surface* defects have two dimensions larger than d, and *volume* defects have all three dimensions larger than d. The anisotropy of pinning defects in many materials leads to anisotropic pinning and thus a dependence of J_c on the angle of the applied field on the sample (the *field-angle*).

The final factor is the rigidity of the flux lattice, which must undergo elastic distortion for individual flux lines to move towards low energy positions at the pinning sites. The energy cost associated with this prevents full occupation of all pinning sites and reduces the overall pinning strength.

The pinning force per unit volume is given by:

$$F_p = \eta L f_p = -\eta L \Delta W / x, \tag{1.3}$$

where η is an efficiency factor associated with rigidity of the flux lattice, L is the length of flux line per unit volume pinned by interaction with the pinning site, and f_p is the pinning force per unit length of the pinned flux line, which is equal to ΔW, the work done in depinning the flux line, divided by x, the effective range of the pinning interaction.

Dew-Hughes [16] calculated expressions for $F_p(b{=}B/B_{c2})$ for various physically reasonable combinations of normal/$\Delta\kappa$ pinning, core/magnetic interactions, and point/line/surface/volume defects, by inserting the relevant energy terms and length scales for each into Equation 1.3. The expressions derived were of the Fietz-Webb [17] form:

$$F_p \propto B_{c2}^n(T) f n(b), \tag{1.4}$$

each having a characteristic pinning function ($fn(b)$). Some of Dew-Hughes' pinning functions have been employed to understand the pinning mechanisms operating in the joint materials discussed in Chapter 4 of this thesis.

1.4.4 Flux Creep

The flux pinning potential wells have a finite depth, and so at any non-zero temperature there is a finite probability that a flux line will "hop" out of a potential well and become depinned – a process known as *flux creep* [18]. This produces an exponential V-I characteristic at low electric fields, before the onset of flux flow.

1.4.5 Flux Jumps

In the critical state, the superconductor is susceptible to thermally activated events known as *flux jumps*, in which there is either a partial or complete collapse of the pinned flux in the sample and a sudden fall in magnetisation [19]. Such an event typically begins with a small temperature rise somewhere in the sample, the source of which might be friction caused by sample movement, or flux annihilation near B_{c1}, for example. The temperature rise causes a local reduction in J_c (i.e. pinning force), leading to the depinning of flux lines in the area and thus further heat generation. From here either the hotspot will grow with time, resulting in a runaway cascade of further depinning events (a *flux avalanche*), or it will shrink over time, allowing the temperature to re-stabilise. The severity of the incident is determined by a multitude of thermal and electronic factors that will not be discussed here, but a review of the field has been written by Mints and Rakhmanov [20].

1.5 Technological Superconducting Wires

In order to use superconductors in commercial electromagnets, high quality superconducting wires must be made in kilometre lengths, wound into coils, cooled to cryogenic temperatures and charged to very high currents. In order to withstand these thermomechanical stresses and for the magnet to perform stably, all technological superconducting wires are mechanically robust metal/superconductor composites. A number of further considerations apply for these wires which will be summarised in this section. A full review can be found in the book by M. Wilson [21].

1.5.1 Thermal Stability

During operation, magnet wires experience forces which can lead to wire movement and thus heat generation and flux jumps. If insufficiently cooled, the normal zone may propagate and induce a thermal runaway process known as a *quench*, in which the entire stored energy of the magnet is dissipated as heat, potentially destroying the magnet.

To achieve adequate thermal stability, the superconductor is subdivided into fine filaments and embedded in a high conductivity matrix (usually oxygen-free high conductivity (OFHC) copper). This reduces the heat generated by a flux jump event, provides a low resistance shunt for current flow in the event of a hotspot being generated, and increases the cooling power to each filament to aid recovery [22]. In most NbTi/Cu wires the NbTi filaments are drawn to a diameter of $\lesssim 50\,\mu$m to ensure they operate stably at 4.2 K and in fields greater than 1 T. Some typical NbTi/Cu multifilamentary wire cross sections are provided in Figure 1.3.

However, under normal circumstances the matrix is not a current-carrying component and reduces the average current density in the wire. The engineering critical current density, $J_e = I_c/A$, where A is the total cross sectional area of the wire, is often used as the performance metric for technological conductors.

1.5.2 De-coupling the Filaments

When the current in a magnet is ramped, the background field on the magnet wires changes. As a result, screening current loops (magnetisation currents) are induced inside the wires, which pollute the field quality in the magnet bore and are responsible for ac-losses. Intrafilament screening currents flow up and down single filaments and are essentially persistent. These are reduced in magnitude by reducing filament diameter. Interfilament screening currents on the other hand flow in large loops along the filaments and across the low resistivity matrix and are not remedied by this (as shown in Figure 1.4a). It is standard practice to twist the filaments inside the wire, (as shown in Figure 1.4b), in order to reduce the length scale of the current loops and thus the resultant magnetisation.

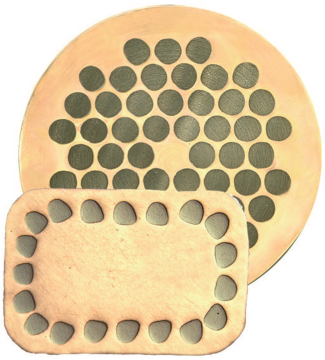

Figure 1.3: Optical cross sections of commercial multifilamentary NbTi/Cu wires produced by Oxford Instruments Superconducting Technology (OST). The wires contain numerous NbTi filaments embedded in a Cu matrix. Image courtesy of OST © 2015.

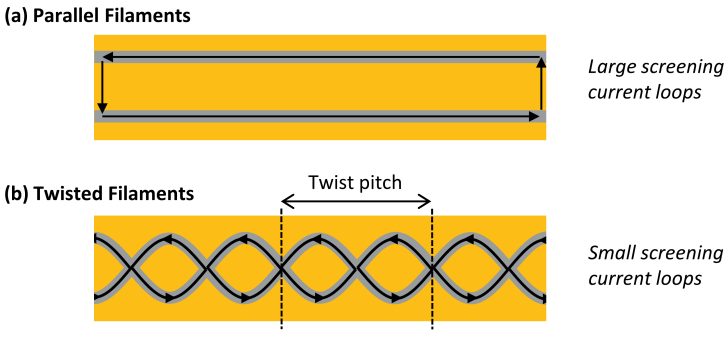

Figure 1.4: Sketches showing interfilament screening currents flowing between two superconducting filaments in a Cu matrix. By twisting the filaments, the length scale of the current loops is decreased, and thus also the magnetisation.

1.5.3 Critical Current Distributions

Despite highly controlled manufacturing processes, filament non-uniformities are inevitable when producing kilometre-length superconducting wires. Non-uniformities can be classified into *intrinsic* or *extrinsic* categories [23]. Intrinsic non-uniformities relate to variations in chemistry and microstructure that affect local J_c values. Extrinsic non-uniformities relate to variations in cross sectional area (for example *filament sausaging* in NbTi wires), which affect filament I_c values.

These inhomogeneities lead to a Gaussian-like distribution of filament critical current values over the length of the conductor. The overall V-I characteristics of this object are a sum of contributions from every infinitesimal current-carrying length of filament in the conductor. This is one cause of non-linearity in the measured V-I curve [24]. Furthermore, since the filaments are connected by a low resistivity matrix, current sharing amongst the filaments can also occur at relatively high electric fields, producing an additional Ohmic voltage [25]. A power-law V-I characteristic is commonly seen for technological conductors:

$$V \sim I^n, \tag{1.5}$$

for which the n-value reflects the degree of critical current homogeneity over the tested length of the wire. Very homogeneous wires have high n-values and thus exhibit sharp superconducting-normal transitions.

It is possible to establish whether the critical current of a wire is intrinsically or extrinsically limited by plotting the n-value as a function of B, obtained by measuring V-I curves in various background fields. As sketched in Figure 1.5, the plot has a uniform negative slope in the intrinsically limited case, whilst there is a plateau at low fields in the extrinsically limited case [23].

1.6 NbTi/Cu Wires

NbTi/Cu wires are the workhorse present-generation magnet wires and the subject of the present study into joints. Multifilamentary wires are made in kilometre lengths by a well established thermomechanical process that will now be briefly described. A comprehensive review of this field has been written by P. Lee [26].

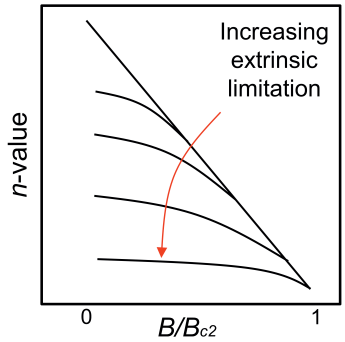

Figure 1.5: A sketch showing the dependence of the n-value on B for superconducting wires with increasing degrees of extrinsic critical current limitation.

1.6.1 NbTi Alloy Preparation

The process begins with the production of an initial Nb-Ti alloy billet. Most commercial NbTi alloys are made to a composition of 46–48 wt.% Ti, for which maximal T_c and $B_{c2}(4.2\,\mathrm{K})$ values of 9.2 K and 11.5 T are obtained (as shown in Figure 1.6a), and the subsequent pinning properties are highest. A billet is produced by consumable electrode vacuum arc melting and electron beam or plasma arc melting. As can be seen from the phase diagram in Figure 1.6b, due to the wide composition gap between the liquidus and solidus, melting often results in compositional inhomogeneity, and the billet must be remelted several times to obtain an homogeneous alloy.

1.6.2 Wire Drawing

The NbTi starting billet is cleaned, loaded into an OFHC Cu can, evacuated and sealed. In some cases a thin Nb foil is wrapped around the NbTi as a diffusion barrier to prevent the formation of Cu-Ti intermetallics during later heat treatments. The billet is then extruded into a rod. To produce a multifilamentary wire, the rod is then sliced into short lengths, restacked inside another Cu can, sealed and extruded once more. The rod is then subjected to a series of cold-drawing and heat treatments to create an optimised pinning nanostructure (discussed in Section 1.6.3) whilst reducing the wire's diameter. The wire is then twisted to decouple the filaments before drawing to the final diameter. Finally, the wire is annealed at low temperature to increase the conductivity of the Cu matrix, then insulated.

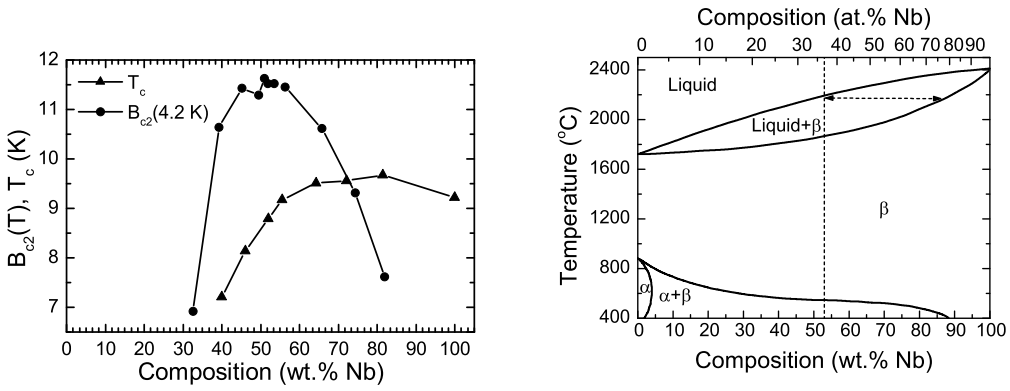

(a) (b)

Figure 1.6: (a) The upper critical field and critical temperature of single-phase NbTi of various compositions. (b) The Nb-Ti phase diagram. The wide composition gap between the liquidus and solidus is indicated by the arrow. The dotted line indicates the standard 53 wt.% Nb alloy composition. Both figures were drawn with data from [26].

1.6.3 Flux Pinning

The thermomechanical processes performed in the manufacturing process create dense, ribbon-like sheets of α-Ti precipitates, whose $\sim$1–4 nm thickness and $\sim$4–10 nm separation are well matched to ξ and the flux lattice spacing respectively at $\sim$5 T and 4.2 K (as shown in Figure 1.7a). α-Ti is in the normal state under these conditions and provides effective flux pinning. The drawing process leads to anisotropy in the pinning nanostructure and thus J_c [27], which is discussed further in Section 4.1.5.

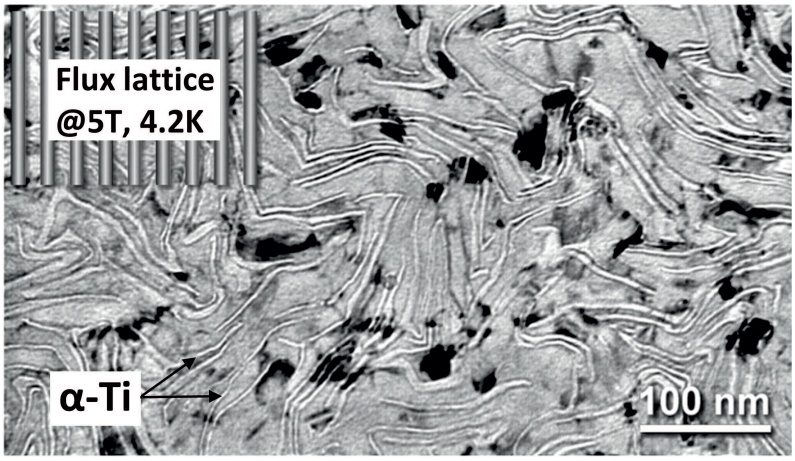

Figure 1.7: A transmission electron micrograph of the nanostructure of Nb- 47wt.%-Ti filaments, showing α-Ti (white) ribbons in a Nb-Ti matrix. The thickness and spacing of the α-Ti is approximately equal to the fluxoid size and spacing at 5 T, as shown [26]. Image © Wiley 2001.

Chapter 2

Literature Review

This chapter presents a review of the literature surrounding persistent current joints, with a particular focus on jointing methods for NbTi wires. I have recently co-authored a review article on persistent current joints between technological superconductors in *Superconductor Science and Technology* (*SuST*) [28], which draws heavily on the text presented here. The sections in the review article on MgB_2 and BiSCCO joints were written by S. Speller, and that on technological solders was written by T. Mousavi, neither of which feature in this chapter.

The chapter begins with some comments on the general structure of persistent current joints. The V-I characteristics of joints, including their measurement techniques, are then discussed. Finally a review is made of present methods for joining NbTi filaments.

2.1 The General Structure of Persistent Current Joints

The production of joints between all technological wires invariably involves two main processes; the chemical or mechanical removal of the metallic matrix to expose the superconductor, followed by an appropriate thermomechanical process to produce a supercurrent path between the parent conductors. A variety of joint structures and manufacturing procedures exist to accommodate the widely varying physical properties of different technological wires, including their filamentary structures, mechanical properties and chemical compositions. This section provides some basic general

descriptions of joint structure and highlights how the physical makeup of joints is expected to influence their performance.

2.1.1 Joint Architecture

The overall architecture of a joint can be described by its internal structure and the relative orientation of the wires, as sketched in Figure 2.1. There are three basic structures (butt joints, lap joints and indirect joints) and the wires can be oriented in either the termination or continuation arrangement (sometimes referred to as "praying hands" and "shaking hands" joints respectively).

The choice of joint architecture is governed by the filamentary structure of the wire, the method by which the joint will be made and the requirements of the application. For NbTi wires, since the copper matrix can be dissolved and the filaments exposed over long lengths, lap joints and indirect joints are most commonly used. The termination orientation is usually employed in commercial magnets since the wires can be non-inductively bound together, minimising the field they produce and making them more handleable.

The influence of joint geometry on their V-I properties has not been investigated in detail in the literature. In the simplest case, one might reasonably assume that the total critical current of a joint ($I_{c,\mathrm{joint}}$) is equal to the sum of critical currents in each current path through the joint ($\Sigma_i I_{c,i}$). Each $I_{c,i}$ value might be considered the minimum value of the following integral along each current path:

$$I_{c,i} = \int_{A_i} J_{c,\mathrm{joint}}.dA_i, \tag{2.1}$$

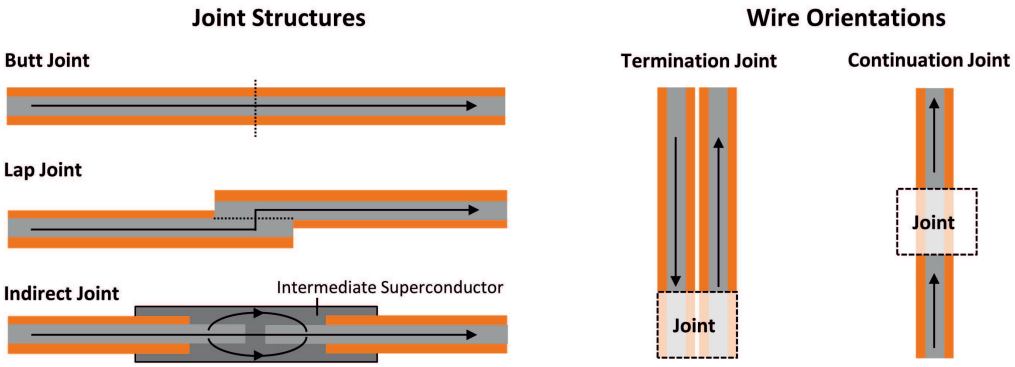

Figure 2.1: Some common basic joint structures and wire orientations.

where $J_{c,\text{joint}}$ is the critical current density everywhere in the joint and dA_i is an infinitesimal area through which the current flows in a particular path.

Under these assumptions we can make two simple but useful comments on the expected influence of geometry on joint critical current. As sketched in Figure 2.2(a), providing the jointing process does *not* damage the filaments, it ought to be possible to produce joints with any critical current value up to a maximum value of $I_{c,\text{wire}}$ by simply expanding the total current transfer area (A), i.e. the joint length (l) and width (w). Kim et al [29] demonstrated an increasing $I_{c,\text{joint}}$ with A by polishing an increasing number of steps into a multifilamentary BiSCCO lap joint. However, as sketched in Figure 2.2(b), if the filaments *are* damaged in forming the joint, then the maximum current able to enter the joint is less than $I_{c,\text{wire}}$, and this presumably cannot be remedied by increasing the joint dimensions.

This simple picture does however neglect the effects of current sharing and settling processes (discussed further in Section 2.2.2.3), which likely influence the V-I properties in a complicated manner and are expected to depend heavily upon the architecture of the joint. Relationships between basic geometrical factors such as joint length on transient behaviour, joint critical current and resistance are yet to be established.

In addition to the current transfer area, the directionality of current flow with respect to the microstructures in the joint materials may also be important if there is significant anisotropy of the superconducting properties within the joint. The angle between the current and any local magnetic field will also influence the forces on the flux line lattice, inducing further anisotropy in joint performance.

2.1.2 Inhomogeneity

The application of chemical and thermal processes to the filaments during jointing perturbs their carefully tailored chemistry and microstructure, whilst the application of pressure often changes their cross sectional area. Furthermore, in most cases an intermediate superconductor is synthesised between the filaments by a crude method such as soldering, for which there can be only limited control over uniformity of superconducting properties. Industry standard NbTi joints are a prime example. These consist of a mass of partially contacted filaments, connected with PbBi solder which is left to solidify around the filaments in a metal cup. Such joints are inevitably

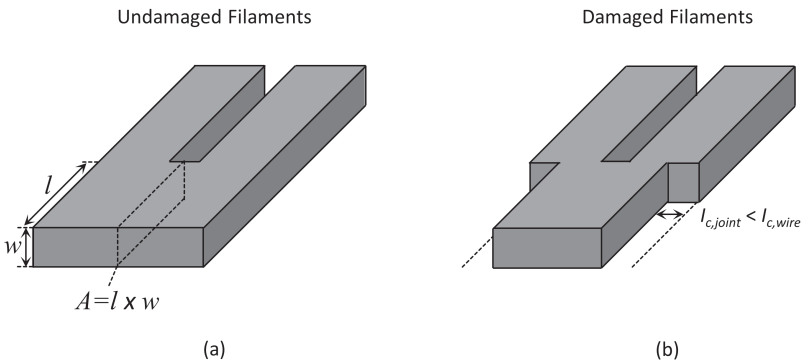

Figure 2.2: Sketches illustrating joint current capacity and geometry, described in the main text. (a) A joint between two filaments in which the jointing process does not damage the filaments. (b) A joint in which the filaments are damaged in the joint region.

highly inhomogeneous, and it is likely that this is a major factor underpinning their V-I characteristics, as is discussed further in Section 2.2.

2.1.3 Thermomechanical Factors

Numerous thermomechanical factors also play a role in determining joint performance. Removal of the stabilising matrix from the filaments and the formation of a large volume of superconducting material in the joint increases the risk of flux jumping. Thermal conductivity, thermal expansion coefficients and mechanical properties of joint materials at low temperatures must therefore be considered, as these can influence quench processes in magnets and the lifetime of joints under thermal cycling in service [30, 31].

A large mismatch between the thermal expansion coefficients of the filaments and an intermediate filler material will induce strain during cooling which may lead to joint failure by detachment or the formation of cracks if there is insufficient ductility of all materials [30]. Lorentz forces will also act on the current-carrying filaments, placing the joints under additional strain that may harm joint performance. Such considerations are of particular importance to strain sensitive and brittle conductors such as Nb_3Sn [32].

2.1.4 Summary

Joint architecture and material composition are largely decided based on the physical requirements of the wires to be joined and the intended application. In most cases indirect joints are made, employing an intermediate superconducting filler to connect the exposed filaments from each wire. The result is a superconducting composite with non-trivial geometry and highly inhomogeneous superconducting and physical properties. These characteristics influence the structural integrity, thermal stability and superconducting performance of the joint as a whole. They also make fundamental studies on real joints somewhat difficult to perform.

2.2 The V-I Characteristics of Persistent Current Joints

For fundamental physics and engineering studies on technological superconductors, the voltage-current (V-I) characteristics and their field and temperature dependencies are of paramount importance, as these hold vital information on performance-limiting features of the specimen. As composite type-II superconductors, joints are subject to all of the same resistive mechanisms as for technological conductors

Fundamental studies on the V-I characteristics of joints are extremely scarce in the literature by comparison with studies on technological conductors. The basic mechanism behind the resistances measured in joints is almost never discussed. This is likely due in part to the commercial, engineering focus of joint development; an endeavour led predominantly by magnet manufacturers.

This section summarises the available literature on the V-I characteristics of joints, as measured by both the four-probe technique and inductive resistance testing (IRT). The phenomenon of settling of currents in closed superconducting circuits is discussed, including its implications on the acquisition of joint V-I data by the IRT technique.

2.2.1 Four-Probe V-I Measurements on Joints

The most commonly applied V-I measurement technique for technological superconducting wires is the four probe method (discussed fully in [33]), a procedure also used

for joint characterisation. In brief, the measurement process is as follows; the sample is cooled to the desired temperature in the desired background field, a slowly increasing current is passed through the sample, and the voltage generated is monitored across two potential taps of separation l_v. At currents near I_c, the voltage rises above the background noise level and the V-I behaviour of the sample becomes measurable. The current is rapidly reduced to zero to avoid damage to the sample.

From these data a certain critical criterion is used to extract a value for I_c. For technological wires, a critical electric field criterion (E_c) of typically 10 or 100 μV/m is most commonly employed, allowing the trivial dependence of the measured voltage on the test length ($V = El_v$) to be eliminated. Although this convention is often used in $I_{c,\text{joint}}$ measurements [34], the conversion is not strictly justified since joints are lumped objects with non-trivial geometry. $I_{c,\text{joint}}$ is better defined by a threshold value of voltage or resistance. It should also be noted that due to sensitivity limitations of the four-probe technique, the criterion employed will naturally yield I_c values larger than those relevant for PM operation.

In some cases the quench current of the joint is reported [35], and some researchers also report the critical current ratio ($\text{CCR} = I_{c,\text{joint}}/I_{c,\text{wire}}$) in order to compare the performance of a joint with that of the wires [29].

A typical four-probe V-I measurement (made on a Nb_3Sn - NbTi joint) is shown in Figure 2.3. This plot demonstrates that at zero external field the joint is truly superconducting, having an immeasurably low resistance up to some critical current at which the voltage begins to rise linearly with current. Similar linear high voltage trends have been found by other researchers for various multifilamentary joints [36,37]. The application of an external magnetic field suppresses $I_{c,\text{joint}}$, as expected for any type-II superconductor, with increasing non-linearity at higher fields.

Detailed analysis of the structure of V-I curves in this voltage range has not been made in the literature. The linear trend seen in 0 T could be interpreted as a flux flow transition, however, as has been suggested by Wen et al [36], it is perhaps more likely that the linear trend is due to current sharing between filaments through copper pathways in the joint. The increasing non-linearity in the curves at high background fields may be due to inhomogeneous superconducting material in the joint, leading to a broadening of the transition. Fundamental studies are required to ascertain the loss mechanisms at play in this voltage regime.

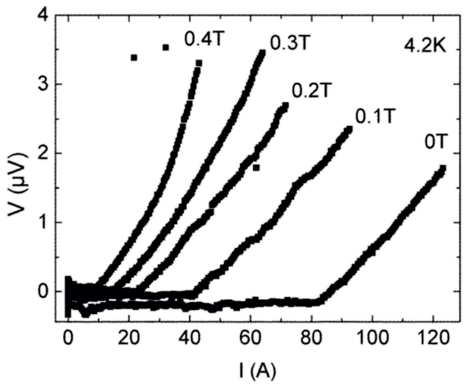

(a)

Figure 2.3: V-I curves of a soldered Nb_3Al/NbTi joint measured by the four probe method, reproduced from [38] © 2006 IEEE.

Whilst an understanding of the V-I characteristics at high voltages will add to an overall understanding of the behaviour of these joints (including quench characteristics), these V-I trends are not generally applicable at the low voltages of the PM regime ($\lesssim 10^{-10}$ V). The practical voltage measurement floor for the four-probe technique is typically $\sim 10^{-9}$ V, and so it cannot generally be employed to directly measure the V-I characteristics of wires and joints under PM conditions [39, 40]. An alternative technique, inductive resistance testing (IRT), is instead employed to measure V-I characteristics at much lower voltages.

2.2.2 Inductive Resistance Testing of Joints

The IRT method, otherwise known as the current decay or field decay method, measures the V-I characteristics of an inductive superconducting circuit from the temporal-decay of circulating currents. This technique has been used to analyse loss mechanisms in technological wires [39, 40] and is the standard tool for characterising joints, capable of measuring resistance values at the femto-ohm level [36, 41–46].

2.2.2.1 Conventional Setup

A diagram of a conventional IRT measurement rig is provided in Figure 2.4. The rig is typically cooled in a bath of liquid cryogen at a single temperature (T), however cryocoolers [46] and (in this thesis) gas-temperature controlled cryostats [45] have been used to vary the test temperature. The sample under investigation is a small test coil, closed by the joint of interest. The test coil incorporates a loop, of inductance

L, into which currents can be magnetically induced. In some cases a power supply and persistent current switch are instead used to charge the test coil [47]. A PM superconducting magnet is used to apply a modest background field to the joint. The field is aligned perpendicular to the loop of the test coil, in order to minimise inductive coupling of the two. The current (I) flowing in the loop at any time (t) is measured with a calibrated local field sensor. This is usually a cryogenic Hall probe, and is sometimes shielded from external fields with a superconducting shield [48]. A heater is mounted on the test loop to drive the circuit normal when required.

2.2.2.2 Measurement Procedure

The typical procedure for measuring a decay curve is as follows. The system is cooled to the measurement temperature (T) and a background field (B_{app}) is applied to the joint. The induction coil is charged up to the required value whilst a region of the test loop is held above T_c by a local heater. The heater is switched off, allowing the test loop to cool down. The current in the test loop is approximately zero. The current in the induction loop is then ramped down to zero, inducing the desired current I_o in the test loop. The current begins to decay due to resistive voltages in the circuit, and an $I(t)$ curve is measured. The resistive voltage is equal to the inductive voltage, which is calculated from the current decay rate (dI/dt) using:

$$V = -LdI/dt \tag{2.2}$$

A V-I plot is obtained from the time derivative of the $I(t)$ curve.

A typical IRT data set, measured for a multifilamentary Nb_3Sn joint, is shown in Figure 2.5. Similar V-I behaviour acquired by the IRT method has been presented by both Wen et al [36] and Cheng et al [43] for various multifilamentary NbTi joints.

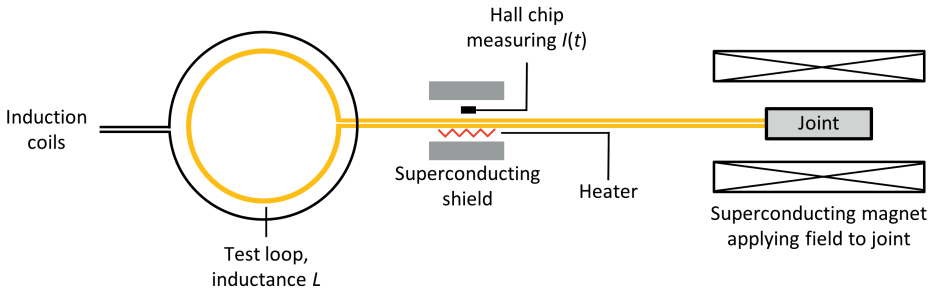

Figure 2.4: A schemtic illustration of a conventional IRT rig.

The measurements are dominated by the "settling" phenomenon, as will now be discussed.

2.2.2.3 "Settling"

The currents induced in the test loop are inhomogeneously distributed in the wire, filling up from the outside to the inside of the wire's cross section (as evidenced by changes in inductance with current [49]). The initial measured V-I characteristics are dominated by a transient *settling* phenomenon in which the current falls rapidly as it is redistributed over the entire superconducting cross section [48].

Inhomogeneous current induction has also been demonstrated within joints in transport measurements by Mizumaki and Yamamoto [50]. A Hall probe array was attached along the length of a diffusion bonded multifilamentary NbTi joint, made in the termination orientation. It was found that as a transport current through the joint was increased, the current penetrated further along the length of the joint.

Settling times are shortest when the maximum possible current is induced, since the entire superconducting cross section is flux penetrated. Decays taken at starting currents below $I_{c,\mathrm{wire}}$ are often dominated by settling over most of the V-I range, restricting the range over which the intrinsic V-I properties of the specimen can be measured. This is problematic for joint testing, since in order to test them it is required that $I_{c,\mathrm{joint}} < I_{c,\mathrm{wire}}$, and thus any test current will naturally be below $I_{c,\mathrm{wire}}$ and settling effects will be considerable. It is thought that the entire V-I curve shown in Figure 2.5d is due to settling rather than any intrinsic resistance in the joint [48]. There appear to be no measurements presented in the literature which convincingly demonstrate the intrinsic V-I properties of joints without the influence of settling effects in the wires. Such measurements may improve our understanding of performance-limiting factors in joints.

2.2.2.4 Sensitivity

The advantage of the IRT method over the four probe method is that V-I measurements can be made at very low voltages (below the picovolt level), which are then relevant to PM operation. Unlike the four probe method, the resistance sensitivity of the IRT method increases as the measurement time (Δt) is extended, since any

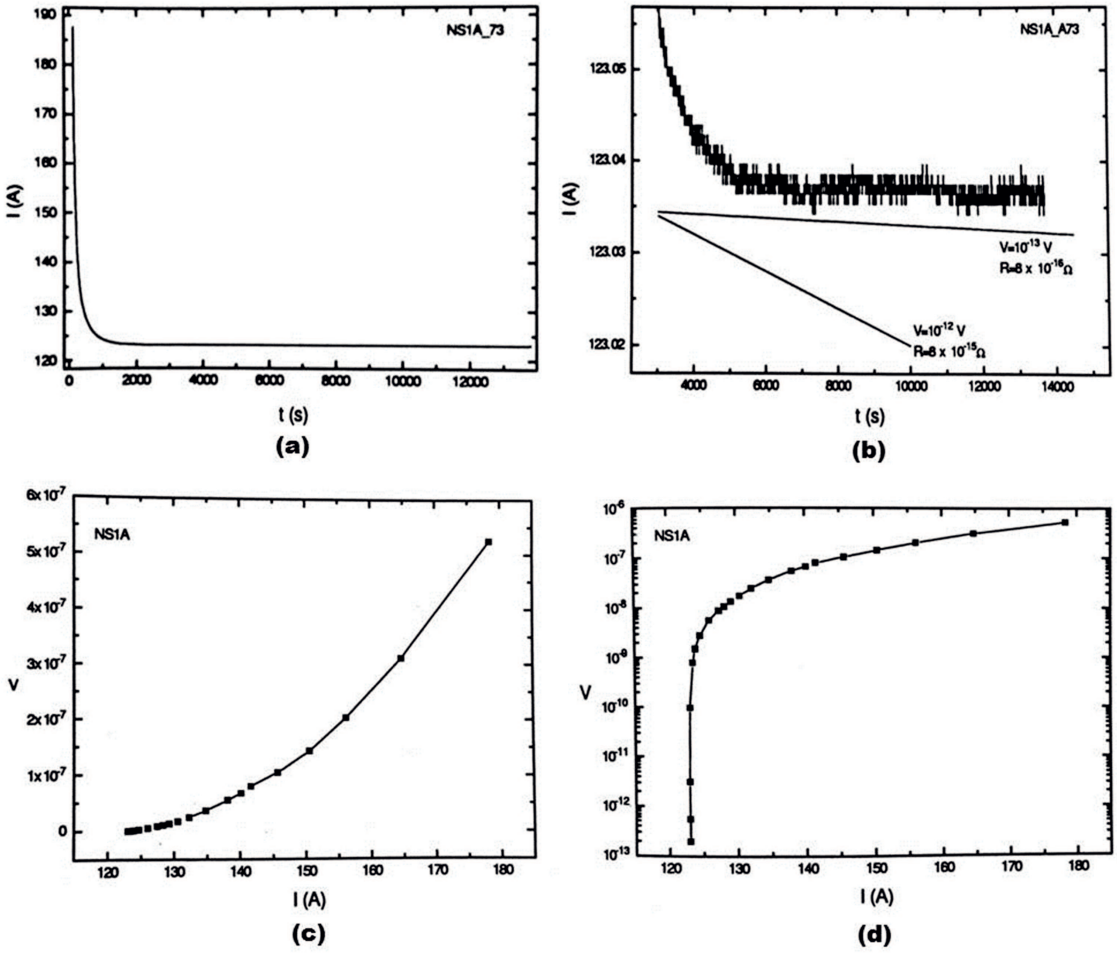

Figure 2.5: IRT data for a Nb_3Sn joint at 4.2 K in self field, reproduced with permission from the D.Phil thesis of D. Ryan [48]. (a) The $I(t)$ decay curve following induction of the maximum possible current in the test loop (187 A). (b) A magnified plot of the low electric field region of the decay curve, showing the hypothetical decays corresponding to voltages of 10^{-12} V and 10^{-13} V. (c) and (d) show voltage versus current on linear and semi-logarithmic scales respectively, calculated using Equation 2.2.

arbitrarily small resistance would eventually lead to a measurable fall in current. Resistance sensitivity is limited by; (i) the test coil inductance (L), which determines both the decay rate for a given voltage and the degree of coupling to noise-inducing external fields and so should be minimised, and (ii) current sensitivity (i.e. the noise level in the $I(t)$ curve, $|\delta I/I|$), which depends on the sensitivity of the field sensor ($|\delta B/B|$), measurement electronics and ambient conditions. The minimum measurable resistance is given by:

$$R_{min} = \frac{V_{min}}{I} = L\frac{|\delta I/I|}{\Delta t}. \tag{2.3}$$

In cases in which a decay cannot be distinguished from the noise during the elapsed measurement time (such as after 5000s in Figure 2.5b), Equation 2.3 is used to place an upper limit on the immeasurably small joint resistance.

Basic Hall probe IRT rigs typically have current noise levels of $|\delta I/I| \sim 1\text{–}10 \times 10^{-4}$, and coil inductance values $L \gtrsim 0.1$ μH, which can reach the $10^{-14}\,\Omega$ level over timescales of several hours [3, 42, 43, 47]. Park et al [34] recently extended a single decay measurement over a period of one year to confirm their joint resistance was below $10^{-18}\,\Omega$. Measurement times can be reduced significantly by using more sensitive field sensors such as fluxgate magnetometers, SQUID magnetometers (used in this thesis) [45], or by taking care to shield the Hall probe and use low noise electronics (as used by D. Ryan to produce the data in Figure 2.5). Reducing coil inductance would have the same effect.

2.2.2.5 Summary

The V-I characteristics of joints hold vital information on their performance limiting features and the basic source of their resistance. Both the four probe technique and the IRT method have been employed to measure joint V-I properties.

The four probe technique lacks the sensitivity to directly access the V-I behaviour of joints in the persistent mode regime, and at measurable voltages commonly yields linear V-I behaviour that does not extrapolate to the PM regime.

IRT measurements are instead taken in order to characterise joints at the necessary sensitivity level. The transient settling of currents induced in superconducting circuits makes interpretation of these data difficult. Most researchers simply use the

IRT method to confirm an acceptably low joint resistance for an engineering application.

In the absence of V-I measurements relating to intrinsic resistive processes in joints, discussions on the basic mechanisms at play in the PM regime are limited. Further fundamental studies are required in this regard.

2.3 Jointing Methods for NbTi

Superconducting magnets have been wound from NbTi/Cu wires for the past half century, and so industrial jointing techniques for these materials are rather mature and widely employed. There have been many publications and patents demonstrating joints for NbTi in normal operation in liquid helium (LHe) at 4.2 K. This section summarises the available literature on these joints.

2.3.1 Oxidation

A core problem for joining Nb-based materials is surface oxidation as a result of exposure to oxidising agents (nitric acid, water, solvents and air) during removal of the Cu matrix [44]. Whilst the oxidation states of Nb-Ti alloys have not been widely investigated, Nb itself has a very high oxygen affinity, and under these oxidising conditions rapidly forms a thin NbO layer, followed by slow growth of a dense and highly stable layer of insulating Nb_2O_5 [51]. These oxides inhibit metal-to-metal bonding and so are problematic for jointing. Elimination of oxides requires heating to $\sim$2000 K under ultra-high vacuum conditions, or dissolution in hazardous hydrofluoric acid (HF) solutions [51, 52], which are unattractive for industrial joint manufacture.

The oxidation problem is dealt with differently in each of the three major jointing techniques discussed in this section. Discussion begins with the industry standard technique (soldering with PbBi alloys) before progressing to cold pressing and spot welding. It should also be said that solid state diffusion bonding has been investigated in a few cases [50, 53], but since this technique requires extended heat treatments in protective atmospheres at moderate temperatures (450^{o}C) it is industrially undesirable and omitted from discussion.

2.3.2 Soldered Joints

The availability of PbBi (discussed in Section 2.3.2.1), a superconducting solder with relatively high J_c and B_{c2} values, allows for the production of superconducting NbTi/solder interfaces. Providing the joints are installed in low magnetic field regions (typically $< 1\,\mathrm{T}$ [54]), they are easily able to meet the required performance specification.

Due to the oxidation problem discussed, poor wetting reportedly prevents soldering to bare NbTi filaments, and common fluxes are unable to remedy this [55]. In light of this issue, the most commonly used method in the literature is Thornton's matrix replacement technique [35,38,43,47,53] – an open air process in which the Cu matrix is dissolved whilst minimising exposure of the filaments to oxygen.

The two wires to be joined are firstly submerged in a bath of molten Sn at a temperature typically in the region of 350^oC, dissolving the Cu matrix and coating each filament with a thin metal layer. Higher temperatures can be employed to speed up the dissolution, however, as can be seen from the NbTi phase diagram in Figure 1.6b, at temperatures above 400^oC (if not lower), the carefully tailored α-Ti pinning nanostructure in the filaments may be degraded. The Sn-coated filaments of both wires are then transferred in open air to a bath of molten superconducting solder (typically a PbBi alloy) at a similar temperature, dissolving the Sn and coating the un-oxidised filaments with the solder. The solder-coated filaments from both wires are finally submerged in a metal cup filled with the same superconducting solder. This cup is typically about $15\,\mathrm{cm}^3$ in volume. Some spare wire (with the Cu matrix intact) is often coiled into the solder cup in case the joint needs to be remade. The large solder mass helps to secure the wires against movement [56], and is also expected to provide a degree of magnetic shielding to the filaments.

This method appears to be extremely effective, and PbBi/NbTi joints capable of carrying 1000 A at 4.2 K and 1 T have been demonstrated [47], with resistances in the range $10^{-13} - 10^{-14}\,\Omega$. Joint performance is expected to be heavily influenced by the superconducting properties of the solder, and so a discussion of superconductivity in PbBi is valuable at this stage.

2.3.2.1 PbBi Superconducting Solder

PbBi was the object of pioneering studies into type-II superconductivity and flux pinning in the 1960s and '70s, led by Campbell, Evetts and Dew-Hughes [14, 19, 57–59]. It was useful as a research material for type-II superconductivity because extremely reversible (low pinning) samples of pure PbBi-ϵ phase could be produced with relative ease, whose B_{c2} value could be changed simply by composition. Simple heat treatments could be applied to produce highly homogeneous arrays of Bi precipitates, permitting detailed studies into flux pinning.

The binary Pb-Bi phase diagram is provided in Figure 2.6a. The system has two superconducting phases, ϵ and α, as well as almost pure Bi, which is non-superconducting at 4.2 K. The system is type-II superconducting with $T_c \sim 8.3$ K for samples of overall compositions from ∼1.1 wt.% Bi to the eutectic composition of 55.5 wt.% Bi [59]. The B_{c2} values for the α and β phases are dependent upon Bi content, as plotted over their full composition ranges in Figure 2.6b.

The ϵ phase has the highest B_{c2} values of the two, ranging from 0.86 T at the Pb-rich limit of 23 wt.% Bi to as high as 1.77 T at the Bi-rich limit of ∼40 wt.% Bi. However, high Bi contents cannot be sustained at room temperature. As can be seen from the phase diagram, the solubility of Bi in the ϵ phase decreases markedly with reducing temperature. At room temperature, solid state diffusion is rapid in these alloys [14], causing Bi to precipitate out of the ϵ phase, eventually reaching an equilibrium value of ∼33.5 wt.% with an associated B_{c2} value of 1.33 T [59]. Therefore, any solder samples containing more than ∼33.5 wt.% Bi would expect to have a two-phase ϵ/Bi microstructure.

Similarly, the degree of flux pinning in PbBi is also highly dependent upon thermal history. In single-phase ϵ samples the bulk pinning force is immeasurably small and magnetisation curves are completely reversible except for a small amount of surface pinning [14]. On the other hand, eutectic specimens containing dense arrays of micron-sized Bi precipitates can have very high J_c values of $10^7 - 10^8$ Am^{-2} at 4.2 K [58]. Flux pinning occurs by the magnetic interaction of flux vortices with the surface of these large, normal state, Bi particles. This was convincing demonstrated by Coote et al [60], who showed that the following Dew-Hughes function for magnetic/volume/normal pinning provided an excellent fit to the eutectic pinning curves:

$$fn \sim b^{1/2}(1-b). \tag{2.4}$$

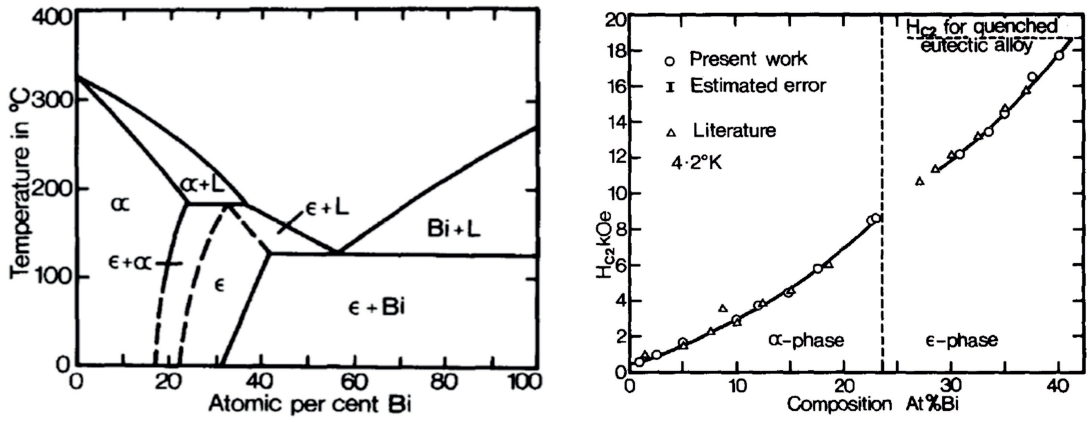

(a) (b)

Figure 2.6: (a) Pb-Bi binary phase diagram. (b) Upper critical field at 4.2 K versus Bi content for the α and ϵ phases. Both figures are reproduced with permission from [59].

Campbell also showed that J_c in PbBi alloys is directly proportional to the ϵ/Bi phase boundary area per unit volume [14]. By the same room temperature diffusion processes, the Bi particles tend to undergo spheroidisation and Ostwald ripening (the growth of large particles by consumption of nearby small particles), and so the volume pinning force and thus J_c also falls as the sample thermally ages. It is expected that thermal history will therefore influence the superconducting properties of the solder contained in joints, and thus also their performance.

2.3.2.2 PbBi/NbTi Joints

There have been no studies reporting joint $I_c(B)$ curves, which might demonstrate the precise relationship between joint performance and solder superconducting properties. However, several authors have reported individual critical current measurements for NbTi joints made with PbBi solder [35, 47, 53, 61], from which some comments can be made. It should be noted however that the final solder composition of any joint made by this method will inevitably contain minor amounts of Cu and Sn as a result of the joint manufacturing procedure, which may influence their performance.

Thornton [35] found that joints made with more Bi-rich solders (in the range of 30–55.5 wt.% Bi) had higher critical currents. This is understandable since J_c values in PbBi increase with the density of ϵ/Bi interphase boundaries as discussed. Swenson and Marciewicz [53] also report that their PbBi eutectic joints ceased to superconduct somewhere between 1.5 and 1.75 T, which is reasonable for the B_{c2} values seen in

PbBi solder, although may suggest a supersaturated Bi content in the PbBi-ϵ phase. Whilst these findings suggest that joint properties may be simply limited by the bulk solder properties, both these studies also found that joints made with ternary PbBiSn solder exhibited relatively poor performance, suggesting that filament/solder interactions may be important in this case.

The NbTi/solder interfacial chemistry that results from this soldering method is essentially unknown, as is its importance in determining joint performance. Determining such relationships will be important for identifying the figures of merit in a solder, as we seek a replacement for PbBi.

2.3.3 Cold-Pressed Joints

As a mechanically soft alloy, NbTi filaments can also be joined by simply pressing the filaments together at room temperature. Since this technique involves no intermediate materials, if direct metal-to-metal bonds can be achieved then joints with in-field performance similar to NbTi material itself might be expected. One might also expect such a simple process to be fairly easy to reproduce, as has been claimed by some researchers [44].

A common basic process is employed to make these joints [3,36,41,47,62–64]. Firstly, the Cu matrix is dissolved in nitric acid. The filaments are often (but not always) then cleansed in HF:H_2O or HF:H_2O:HNO_3 solutions, which reportedly removes any oxides and organic films that might inhibit bonding [63]. The filaments from the two NbTi wires are then rinsed, dried, twisted or braided together and uniaxially pressed inside a metal tube (crimped). Cu [63], Nb [64] and CuNb [44] crimps have all been used. Process details are discussed in the original patent by Nuding [63].

Joint quality for this process is expected to be determined chiefly by (i) the filamentary arrangement in the joint, (ii) the pressure with which filaments are held together in the crimp and degree of deformation undergone in pressing, (iii) the mechanical and superconducting properties of the crimp, and (iv) the chemistry at the filament-filament and filament-crimp interfaces.

Liu et al [3, 44] have recently produced joints between multifilamentary wires with R$<10^{-13}\,\Omega$ for currents as high as 468 A (1 T, 4.2 K). Wen et al (1992) also demonstrated joints capable of carrying appreciable currents in fields as high as 6 T (although

their resistance was not measured). It certainly appears that joint performance akin to that of bulk NbTi material is achievable.

Liu et al [44] found that in their joints (which were made between HF-cleansed 35 μm NbTi filaments in a CuNb crimp), pressure and joint I_c were actually uncorrelated in the range of 4–20 MPa. The influence on resistance could not be determined due to insufficient resistance measurement sensitivity. Scanning electron micrographs of the joints showed that increased pressures caused more filament deformation but had little effect on filament bonding. One of their images is reproduced here in Figure 2.7, which shows the filament bundle after pressing at 20 MPa. Although the interfacial chemistry was not discussed by the authors, there are distinct boundaries between the filaments which suggest that the filaments are not metallurgically bonded. This suggests that the HF treatment is not wholly effective in producing a clean NbTi surface to be joined, which is understandable since some amount of oxide will inevitably regrow while the filaments are in open air between the cleansing and pressing steps. This calls into question the exact role of the hazardous HF cleansing stage, which is arguably the largest drawback of this technique.

A variation on this method has recently been patented by Blumenthal and Lakrimi [65]. In their magnetic welding method, the bare filaments are smashed together by two workpieces which are accelerated into contact at speeds of more than 100 ms^{-1}. It is claimed that this dynamic pressing method blows away the oxides on impact to permit metal-to-metal bonding without the need for prior HF cleansing. The superconducting performance and microstructure of the joints are not reported.

2.3.4 Spot Welded Joints

Spot welding (or resistive welding), a technique commonly employed to join sheet metal, has also been used to join NbTi filaments [62, 64, 66–68].

Spot welding involves pinching the workpieces to be joined between two electrodes, locally piercing the surface oxides, then passing a high current, short duration pulse through the two. Resistive heating at interfaces is sufficient to locally melt the material, dissolving oxide barriers and bonding the work pieces [69]. This technique is therefore of interest for joining NbTi, since it overcomes the need for dissolving oxides in hazardous HF.

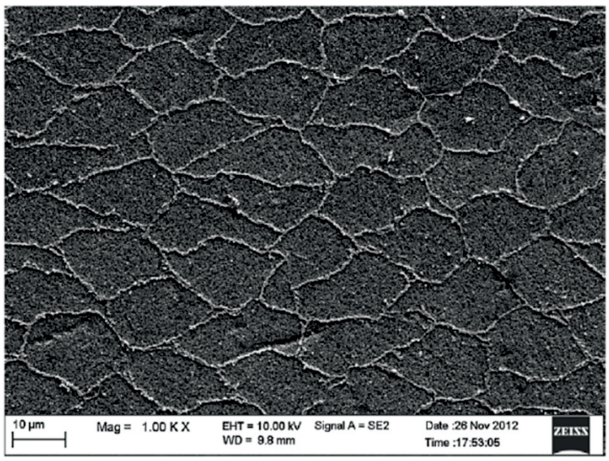

Figure 2.7: Secondary electron (SE) image of NbTi filaments pressed at 20 MPa. The individual filaments are clearly visible and thus not completely metallurgically bonded. Image reproduced with permission from [44].

The original patent for spot welded joints made directly between Nb-Zr monofilaments was filed by Karvonen in 1970 [67]. He reports that joints made directly between the monofilaments have poor performance ($\sim$10 % of wire I_c at 4.2 K and 3 T [67]). Although the cause is not discussed, this might be due to heat damage to the material in the joint region, reducing B_{c2} and/or J_c. He reports that the performance improves to more than 80 % (even in fields of up to 6 T) by laying the filaments side by side on a suitably thick NbTi foil and spot welding each filament to the foil at multiple locations along the length of the filaments (as sketched in Figure 2.8). Exactly why this helps to improve performance is not clear. One would assume that if the filaments are heavily heat damaged (such as sketched earlier in Figure 2.2b), then expansion of the current transfer area by making multiple joints in series, and providing an additional current path through the foil, would have little benefit. Perhaps the foil actually acts as a heat sink, helping to reduce the amount of heat damage done to the filaments in the first place.

This technique has since been extended to join multifilamentary NbTi wires, for which the filaments from each wire are individually twisted or braided before being spot welded to the foil [64]. Copper sheets can also be soldered to the joint for thermomechanical stabilisation. Joints with resistances less than $10^{-13}\,\Omega$ have been demonstrated with critical currents similar to the undamaged wire [66].

It seems as though, in principle, good joints can be made by this technique, without the use of HF cleansing [64]. However, the chief concern surrounding this technique is the potential for heat damage to the carefully tailored flux pinning nanostructure of

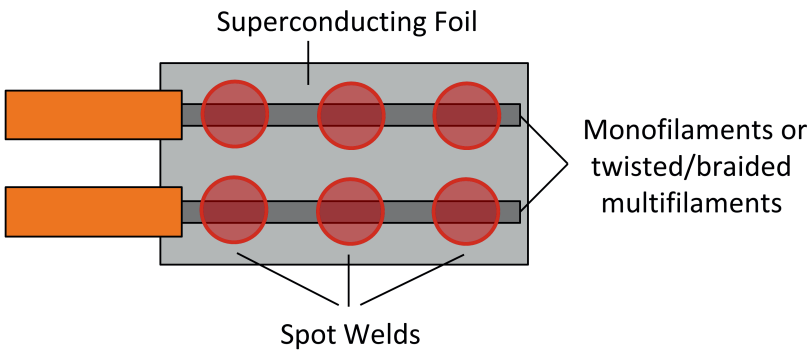

Figure 2.8: Schematic of a typical spot welded joint architecture, with monofilaments or twisted/braided multi-filaments spot welded at several locations to a Nb/NbTi superconducting foil.

the NbTi filaments, which may make quality control on the production line difficult (a concern that has been raised by others [65]). Without any microstructural analysis of spot welded joints presented in the literature, no further comments can be made.

Chapter 3

Magnetic Measurements on Superconductors

Magnetic measurements are indispensable in fundamental studies on superconductors, offering a convenient and contactless means of acquiring critical parameters and performance metrics. Commercial magnetometers are now standard pieces of laboratory equipment used widely to characterise technological superconducting wires, tapes and bulks. This chapter outlines the core physics and practical methods employed to analyse magnetic measurements underlying this work.

The chapter begins with an introduction to magnetometry on superconductors, followed by a description of Bean's model, which is an extremely useful tool for understanding the magnetic behaviour of inhomogeneous (flux-pinning) superconductors. The method employed in this work for extracting $J_c(B,T)$ values from magnetic hysteresis loops is then discussed, including the application of self-field corrections to eliminate sample shape effects. Measurement protocols for the acquisition of $B_{c2}(T)$ values are also outlined. Finally, the magnetic properties measurement system (MPMS) used throughout this work is described in detail.

A program was written in Python to perform all of these analyses throughout this work, and the code is now the standard tool used by the research group. This has been used to characterise a wide range of Pb-free superconducting solders, now accepted for publication in *SuST* [70].

3.1 Magnetometry on Superconductors

The basic aim of magnetic measurements is to obtain the magnetisation ($\boldsymbol{M}$) of a material as a function of magnetic field ($\boldsymbol{B}$), temperature (T) and time (t). From this, fundamental material properties can be obtained. The magnetisation is most commonly acquired from measurements of the magnetic moment ($\boldsymbol{m}$), which is the integrated magnetisation over the sample volume (V):

$$\boldsymbol{m} = \iiint_V \boldsymbol{M} dV. \tag{3.1}$$

Such measurements are performed routinely by commercial magnetometers, which measure a component of $\boldsymbol{m}$ by moving the sample through a set of voltage pickup coils. The magnetometer used in this project is described in Section 3.5.

As has been discussed, inhomogeneous type-II superconductors exhibit both a reversible and irreversible magnetisation ($\boldsymbol{M}_{rev}$ and $\boldsymbol{M}_{irr}$). $\boldsymbol{M}_{rev}$ is associated with individual vortices and their equilibrium arrangement, and so is intrinsic to the superconducting state of the material (in much the same way as the magnetisation of ferromagnets can be related to their atomic moments).

On the other hand $\boldsymbol{M}_{irr}$ is associated with eddy currents of density $\boldsymbol{J}$ flowing macroscopically throughout the sample. These are induced by changes in applied field, which due to flux pinning establishes field gradients in the sample in accordance with Maxwell's equations:

$$\nabla \times \boldsymbol{B} = \mu_o \boldsymbol{J} + \mu_o \epsilon_o \frac{\partial \boldsymbol{E}}{\partial t}, \tag{3.2}$$

$$\nabla \times \boldsymbol{E} = -\frac{\partial \boldsymbol{B}}{\partial t}. \tag{3.3}$$

This irreversible component is dominant in technological materials, which exhibit strong flux pinning. $\boldsymbol{M}_{irr}$ is influenced by sample shape and is not itself intrinsic to the material, whilst $\boldsymbol{J}$ can in principle be related to elementary pinning forces and the material's electric field characteristics ($\boldsymbol{E}(\boldsymbol{J},\boldsymbol{B},\mathrm{T})$). The irreversible component of the magnetic moment ($\boldsymbol{m}_{irr}$) is therefore more usefully expressed as the integral of contributions from all current loops (of radius $\boldsymbol{r}$) flowing within the sample:

$$\boldsymbol{m}_{irr} = \frac{1}{2} \iiint_V (\boldsymbol{r} \times \mathbf{J}) dV. \tag{3.4}$$

The ultimate aim of magnetic measurements on technological superconductors is to extract $\boldsymbol{J}(\boldsymbol{B},T,t)$ from measurements of $\boldsymbol{m}_{irr}(\boldsymbol{B},\mathrm{T},\mathrm{t})$. However, due to the interrelation of $\boldsymbol{E}$, $\boldsymbol{B}$ and $\boldsymbol{J}$, this is an iterative problem which cannot be solved analytically. Simplified "critical state models" are therefore commonly used to analyse and interpret the magnetic behaviour of flux-pinning superconductors. The most basic and widely used of these is Bean's model [15,71], which has been employed throughout this thesis and so will now be described.

3.2 Bean's Critical State Model

3.2.1 Assumptions

Bean makes three assumptions in order to simplify the problem. The first is the "critical state" assumption, which is that $J{=}0$ for $E{=}0$, $J{=}J_c$ for $E{>}0$ and $J{=}{-}J_c$ for $E{<}0$. It follows that persistent currents are induced at a density J_c in any magnetic flux penetrated regions of the sample. Such a scenario strictly requires an infinite n-value, but is physically reasonable for technological superconductors, which ordinarily have $n{\gtrsim}20$ [72].

The second is the "constant J_c" assumption – that J_c is sensitive only to external magnetic fields, and is otherwise constant everywhere in the sample. This assumption is valid providing the self field is small compared to the field range over which J_c varies considerably, for which B_{c2} might be considered a reasonable benchmark. Self field corrections discussed later allow for a first order correction for the errors introduced by this assumption. The Meissner effect is also usually ignored, which occurs at a field typically much smaller than B_{c2} for technological materials.

Bean's final assumption is of "semi-infinite" sample geometry – that flux penetrates the sample in directions perpendicular to its edges, and thus induced currents flow parallel to the sample edges. This simplifies the internal flux profile in samples with a non-circular cross section.

Whilst critical state models employing more realistic J-B relationships (e.g. the Kim model [73, 74]) and power-law J-E relations [75] have also been developed to improve measurement precision, the requirement for iterative analysis algorithms is often unattractive. Due to its simplicity, Bean's model remains the most widely employed critical state model.

Bean's model will now be applied to a simple sample geometry employed in this thesis, demonstrating how J_c may be extracted from hysteresis measurements.

3.2.2 Magnetic Hysteresis

The sample geometry most commonly employed in this study and which will now be considered is a solid cylinder of diameter $2R$ and length $2c$. Employing standard (r,z,θ) cylindrical polar co-ordinates, the sample is oriented with its cylinder axis parallel to an external applied field, $\boldsymbol{B}_{app} = (0,B_{app},0)$, as sketched in Figure 3.1.

The field $\boldsymbol{B}$=$(0,B_z,0)$ inside the sample can now be calculated. Under Bean's assumptions, Equation 3.2 simplifies to:

$$\frac{dB_z}{dr} = -\mu_o J_c(B_{app}), \tag{3.5}$$

indicating that flux penetrates the sample with a linear gradient determined by J_c at the experimentally selected external field value B_{app}. Strictly one ought to allow for anisotropy of J_c, and in this case since currents are induced in the azimuthal $(\hat{\theta})$ direction, the relevant component would be J_c^{θ}. However for brevity J_c will be assumed isotropic at this stage.

Azimuthal currents are induced to flow in flux-penetrated regions of the sample, with a direction dependent upon the sign of the local field gradient. The direction and magnitude of currents flowing in the sample therefore both change with the ramping direction and magnitude of the applied field, producing *hysteretic* magnetic behaviour as will now be exemplified.

A real hysteresis loop measured for a PbBi cylinder at 4.2 K is shown in Figure 3.2, along with sketched magnetic flux profiles and current distributions at key points around the loop. The loop begins from a zero-field-cooled (ZFC) initial state followed by ramping the external field over a full five quadrants, i.e. from 0 to $+B_{max}$, $+B_{max}$ to 0, 0 to $-B_{max}$, $-B_{max}$ to 0 and finally 0 to $+B_{max}$. These sections of the full loop will be referred to as quadrants 0 to 4 respectively throughout this thesis.

Upon increasing the applied field from zero, flux begins to penetrate the sample and induce shielding currents in a thin shell at the sample's edge, as shown at point (a). A negative (diamagnetic) moment is measured. At the penetration field $(B_{app}$=$B_p)$,

$$B_p = \mu_o R J_c(B_p), \tag{3.6}$$

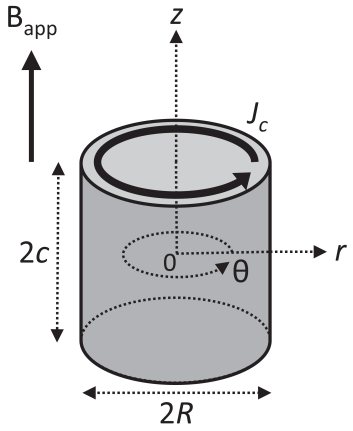

Figure 3.1: Sketch of a cylindrical superconductor in an axial applied field – the experimental geometry most commonly employed in magnetic measurements made throughout this thesis.

flux first reaches the centre of the sample and a local maximum in the absolute moment is measured at point (b). As field is increased further, the flux gradient and hence moment decreases in direct proportion to $J_c(B_{app})$, as shown at point (c). At point (d), $B = B_{c2}$ and J_c falls to zero, as does the moment. Upon ramping down the field once more, currents are now induced in the opposite sense as magnetic flux is now trapped in the sample, yielding a positive moment as shown at point (e). An overall peak moment is found at point (f), where the average value of J_c within the sample is highest. This occurs at an applied field value of $-B_{peak}$ rather than zero, due to the finite positive self-field trapped by the sample, as will be discussed further in Section 3.3. The remaining quadrants of the loop are then acquired by sweeping to negative fields and back through to positive fields.

3.2.3 Measurement of J_c

In the fully penetrated state, the irreversible moment m_{irr} can be related to J_c by integration of Equation 3.4 over the cylinder volume:

$$m_{irr}(B_{app}) = \frac{1}{2}\int_{-c}^{c} dz \int_{0}^{R} J_c(B_{app}) 2\pi r^2 dr = \frac{RV}{3} J_c(B_{app}). \tag{3.7}$$

This allows $J_c(B_{app})$ to be measured from $m_{irr}(B_{app})$ in any quadrant. However, the experimentally measured moment (m) inevitably contains reversible background components which must be subtracted. Since these are common to the curves taken in both increasing and decreasing fields (m^+ and m^- respectively), it is good practice to

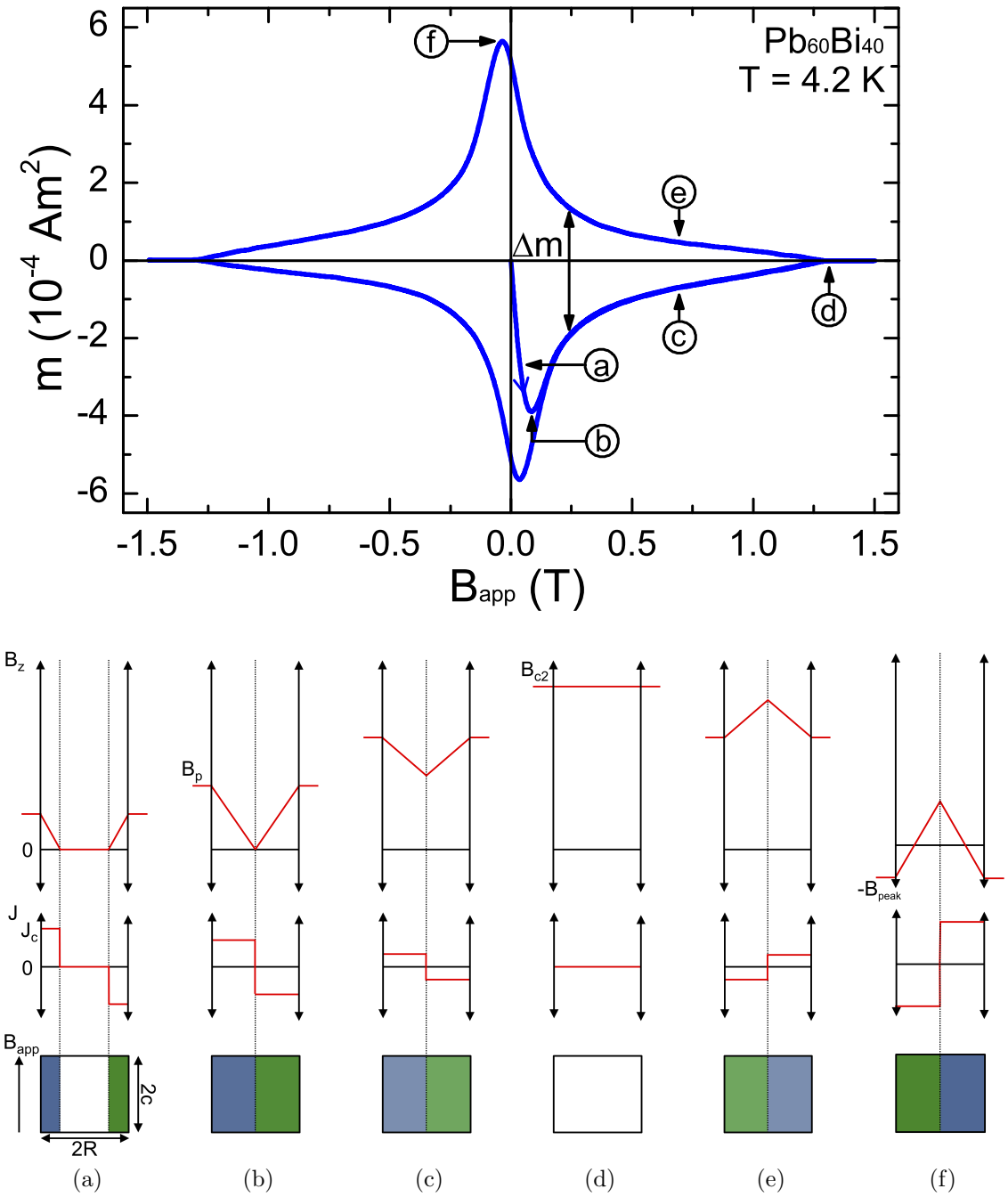

Figure 3.2: ZFC magnetic hysteresis loop measured for a PbBi cylinder at 4.2 K in an axial magnetic field. The hysteresis width Δm at one field is shown, and magnetic field and current profiles at key locations indicated in the hysteresis loop are sketched in subfigures (a–f). Top and middle: Internal B and J_c profiles across the diameter of the sample. Bottom: Vertical cross section through the centre of the sample showing current carrying regions (green for currents flowing into the page, blue for currents flowing out of the page). Further description is provided in the main text.

discount reversible components by employing the hysteresis width ($\Delta m{=}m^+ - m^-$), as indicated in Figure 3.2:

$$J_c(B_{app}) = \frac{3}{2RV}\Delta m(B_{app}). \tag{3.8}$$

3.3 Self-Field Corrections

Whilst Bean's "constant J_c" assumption is necessary to simplify the calculation of internal fields, in reality J_c will vary inside the sample with the local field $\boldsymbol{B}(r,z)$. A first order correction can be made for this assumption by adjusting the value of B ascribed to J_c from the external field value B_{app} to a relevant average of $\boldsymbol{B}(r,z)$ over the entire sample. This partially mitigates sample shape effects by accounting for the field produced by the sample itself – the "self-field". In general, the field in the sample can be expressed as:

$$\mathbf{B}(r,z) = \mathbf{B}_{app} + \mathbf{B}_{self}(r,z) + \mu_o \mathbf{M}_{rev}(r,z). \tag{3.9}$$

$\mathbf{M}_{rev}(r,z)$ would ordinarily be corrected for by a standard demagnetising factor $\boldsymbol{N}$ [76], however this is usually negligible for technological superconductors. $\boldsymbol{B}_{self}(r,z)$ is the self-field produced by macroscopic currents flowing throughout the sample, which is usually a significant contribution in the samples tested in this project.

In this work, a procedure outlined by Wiesinger et al [77] was followed to make the self-field corrections. A one-off calculation of the self-field profile is first made for the sample shape under consideration, from which a number of correction parameters and functions are extracted. Incorporating the self field into Equation 3.9, $m(B_{app})$ is transformed to $m(B)$, allowing $J_c(B)$ to be extracted using the method described in Section 3.2.3. The most common sample geometry employed in this work was a cylinder with $R/c = 0.8$, which will be used as an example in the following.

3.3.0.1 The Self-Field Profile, $b_{self}(r,z)$

In accordance with Bean's model in the fully penetrated state, the self field profile is calculated assuming an average azimuthal J_c flows throughout the cylinder. This current density generates an associated self-field $\boldsymbol{B}_{self}(J_c,r,z)$ which has both axial and radial components $B_{self,z}$ and $B_{self,r}$. At any point (r,z) in the sample, $\boldsymbol{B}_{self}$ is calculated by integrating over the field contributions from infinitesimal current loops,

which are calculated with standard complete elliptical integral equations [78] and need not be discussed in detail. A Python code was written to allow $\boldsymbol{B}_{self}(J_c,r,z)$ to be calculated for any R/c sample geometry. An array of 50 x 50 (r,z) data points could typically be calculated in a few hours.

The J_c value employed to calculate the self field is an arbitrary scaling factor. A flat volume-average of $B_{self,z}$ serves as a useful normalisation value, from which an axial "demagnetising factor" D is defined:

$$\frac{1}{V}\int_0^R\int_{-c}^{c} B_{\mathrm{self},z}(J_c,r,z)2\pi r dz dr = \frac{\mu_o(1-D)m_{irr}}{V}. \tag{3.10}$$

D is analogous but not identical to the standard demagnetising factor N used for *homogeneously* magnetised samples such as ferromagnets [76], since in this case the magnetisation is *inhomogeneous*. Substituting in the Bean expression m_{irr}=$(1/3)RVJ_c$ from Equation 3.7, D can be calculated and has a value of 0.291 (3 s.f.) for the present geometry.

A normalised, J_c-independent self field profile ($\boldsymbol{b}_{\mathrm{self}}(r,z)$) is then obtained simply from:

$$\boldsymbol{b}_{\mathrm{self}}(r,z) = \boldsymbol{B}_{\mathrm{self}}(J_c,r,z)\frac{V}{\mu_o(1-D)m_{irr}}. \tag{3.11}$$

The axial and radial components $b_{\mathrm{self},z}(r,z)$ and $b_{\mathrm{self},r}(r,z)$ are plotted in Figures 3.3a and 3.3b.

Two key values are noted for later use. The first is the maximum axial self field ($b^{max}_{self,z}$), which is found in the centre of the sample:

$$b^{max}_{self,z} = b_{\mathrm{self},z}(0,0) = 3.88\,(3\text{ s.f.}). \tag{3.12}$$

The second is the minimum axial self field ($b^{min}_{self,z}$), which is negative and found at the edge of the sample:

$$b^{min}_{self,z} = b_{\mathrm{self},z}(R,0) = -0.234\,(3\text{ s.f.}). \tag{3.13}$$

The accuracy of the self field calculation was verified by computing D, $b^{max}_{self,z}$, and $b^{min}_{self,z}$ for a wide range of sample geometries for which values are also reported by Wiesinger [77], all of which were in perfect agreement.

Employing normalised units and neglecting the reversible magnetisation, Equation 3.9 can be re-expressed as:

$$\mathbf{b}(r,z) = \mathbf{b}_{app} + \mathbf{b}_{self}(r,z), \tag{3.14}$$

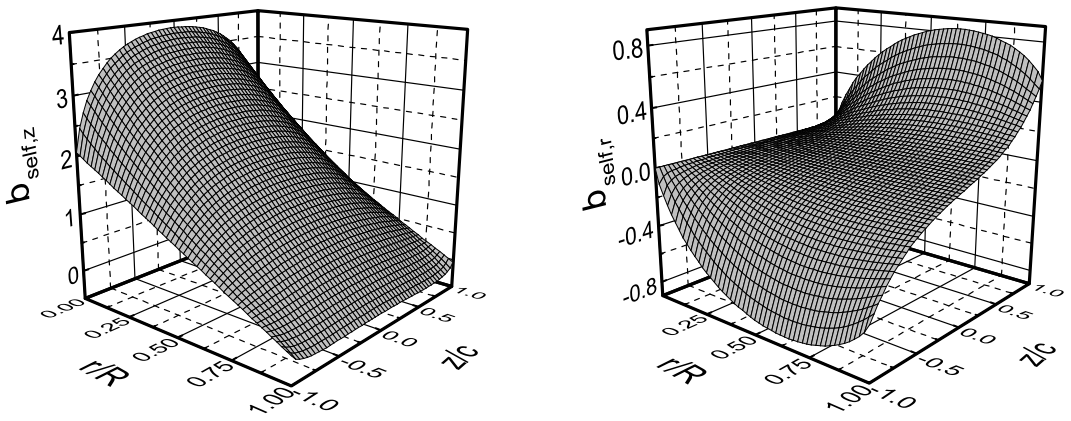

(a) (b)

Figure 3.3: (a) Axial and (b) radial self fields calculated for the sample geometry $R/c = 0.8$. Values are normalised to the volume-averaged axial self field in the sample.

allowing the total field $\boldsymbol{b}(r,z)$ to be calculated anywhere in the sample for any normalised applied field $\boldsymbol{b}_{app}$. Ignoring any anisotropy of J_c, which is not considered in this model, only the magnitude of $\boldsymbol{b}(r,z)$ is of importance, and is given by:

$$b(r,z) = [(b_{app} + b_{\mathrm{self},z}(r,z))^2 + b^2_{\mathrm{self},r}(r,z)]^{\frac{1}{2}} \tag{3.15}$$

Finally, a relevant average of $b(r,z)$ over the sample volume (b_{av}) must be taken. Since b_{av} will eventually be assigned to a J_c value measured from a magnetic moment, which is itself an average of $J_c(r,z)$ weighted by current loop area, the same weighting must therefore be applied in averaging $b(r,z)$:

$$b_{av} = \frac{\int_0^R \int_{-c}^{c} b(r,z) r^2 \pi dz dr}{\int_0^R \int_{-c}^{c} r^2 \pi dz dr} = \frac{3}{RV} \int_0^R \int_{-c}^{c} b(r,z) r^2 \pi dz dr. \tag{3.16}$$

b_{av} is a function of b_{app} that needs to be calculated only once for a given sample geometry. Similarly, it is also convenient to calculate the field-correction function (C_B):

$$C_B = b_{av} - |b_{app}|, \tag{3.17}$$

which quantifies the field correction needed to transform b_{app} to b_{av}. This can be evaluated over a wide range of b_{app} values, and then used simply as a reference table when applying self field corrections to real hysteresis loops. Both functions $C_B(b_{app})$ and $b_{av}(b_{app})$ are plotted in Figures 3.4a and 3.4b respectively.

Figure 3.4a demonstrates the non-linear corrections that must be made when the applied field is swept through zero, and is of a similar magnitude to the self-field, i.e. in the range $-b_{self,z}^{min} \lesssim b_{app} \lesssim -b_{self,z}^{max}$. A further important parameter from Figure 3.4b (which was not mentioned by Wiesinger), is the applied field at which b_{av} is a minimum. For this sample geometry this occurs at a value $b_{app}^{peak} = -0.551$, which is so-named since this is the applied field at which the peak moment is expected.

Shown in Figure 3.4c is the same PbBi hysteresis loop as before, this time plotted along with m_{irr}-B_{app} lines corresponding to these key self field parameters. The first two lines are those associated with $b_{self,z}^{max}$ and $b_{self,z}^{min}$, which are given by:

$$\text{for } b_{app} = b_{self,z}^{max}: \quad m_{irr} = \frac{V}{\mu_o(1-D)} \left(\frac{1}{-b_{self,z}^{max}} \right) B_{app}, \tag{3.18}$$

$$\text{for } b_{app} = b_{self,z}^{min}: \quad m_{irr} = \frac{V}{\mu_o(1-D)} \left(\frac{1}{-b_{self,z}^{min}} \right) B_{app}. \tag{3.19}$$

Data points lying between these two curves are most heavily influenced by self field effects, for which the applied corrections are non-linear. The $b_{self,z}^{max}$ line also predicts the line of first penetration from the initial ZFC state. In the plot this line can be seen to pass through the intersection of the initial curve (quadrant 0) and the fully penetrated curve (quadrant 4), in line with expectation.

The final line drawn is that associated with b_{app}^{peak}:

$$\text{for } b_{app} = b_{app}^{peak}: \quad m_{irr} = \frac{V}{\mu_o(1-D)} \left(\frac{1}{b_{app}^{\text{peak}}} \right) B_{app}, \tag{3.20}$$

which is indeed seen to pass through the hysteresis peak in Figure 3.4c. As expected, this shows the peak to be associated with a minimum in the average field in the sample, which is well quantified by the self field calculation.

Hysteresis loops measured for the same PbBi sample at various temperatures are also plotted in Figure 3.4d. The key features in each loop are again captured by the same self field lines. The same behaviour is also seen in various samples tested throughout this thesis. This provides a convincing demonstration that the asymmetry in the loops is a sample shape effect which is well quantified by the self field analysis.

The congruence of the calculated self field parameters to both literature values and real features of measured data demonstrates that self-field effects are well understood and that these corrections can be applied with confidence.

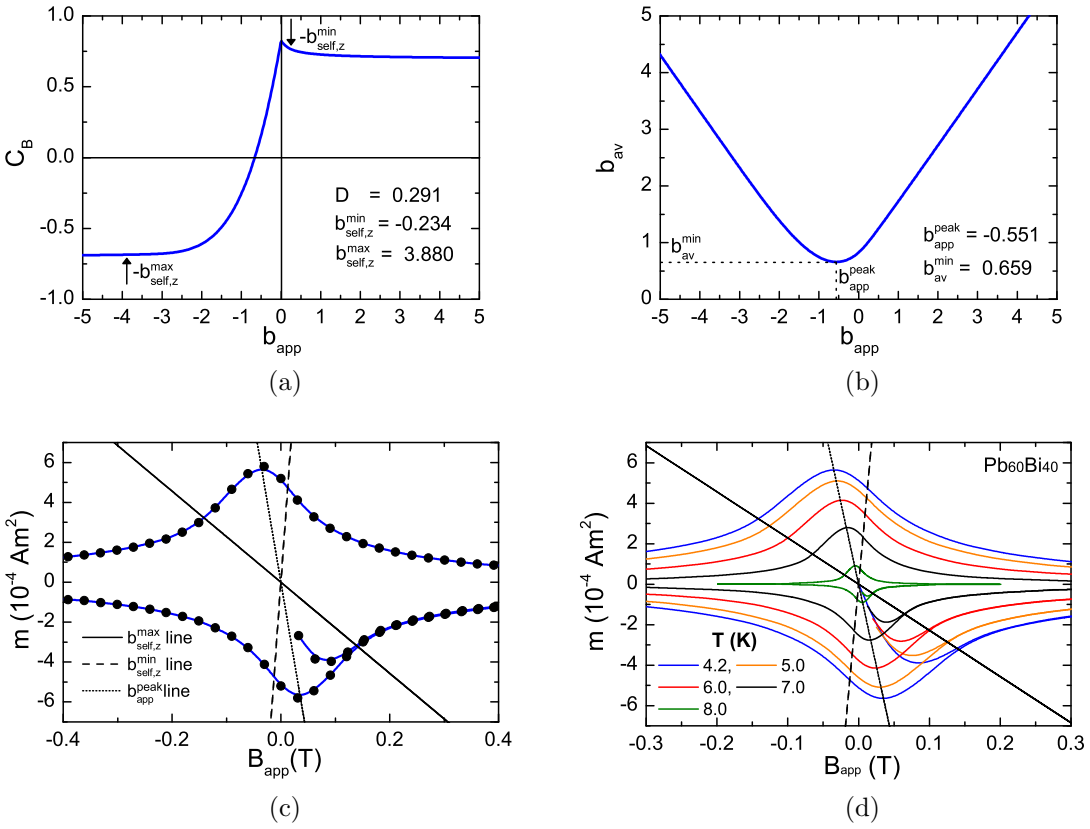

Figure 3.4: (a) The field correction function versus normalised applied field, with key self field values indicated. (b) The normalised average field in the cylinder versus normalised applied field, which exhibits a minimum as indicated at a normalised applied field value b_{app}^{peak}. (c) A PbBi hysteresis loop (4.2 K), with key self field lines also plotted as discussed in the text. (d) Further loops measured for this sample at various temperatures along with the same self field lines. The lines pass through the same features of the loop at each temperature, showing them to be determined by sample shape.

3.3.0.2 Applying the Self-Field Corrections

Finally, the hysteresis data $m_{irr}(B_{app})$ can be transformed to $m_{irr}(B)$ by applying the following self-field correction:

$$B = |B_{app}| + C_B \frac{\mu_o(1-D)}{V}|m_{irr}|. \tag{3.21}$$

Figure 3.5a shows an example of such a transformation to the 4.2 K PbBi hysteresis data (quadrants 1 and 4). At fields beyond ∼0.3 T the correction is imperceptibly small. At lower fields, quadrant 1 is shifted towards higher fields whilst quadrant 4 is shifted towards lower fields. This reflects the opposing self field direction in both cases. At still lower fields however, the applied field falls below the self-field and a few points on both curves are shifted towards higher fields, reflecting the dominance of self field in this regime.

$J_c(B)$ was then extracted from the self field corrected hysteresis width $\Delta m(B)$, as plotted in Figure 3.5b (alongside the uncorrected $J_c(B_{app})$). It is evident from the plot that applying the corrections eliminates the anomalous low field plateau in J_c values, producing a smooth and monotonically decreasing $J_c(B)$ curve.

3.4 Upper Critical Field Measurement

$B_{c2}(T)$ defines the phase boundary between the superconducting and normal states, outlining the ultimate operational envelope of a given material, and so is of paramount importance. A wide range of techniques exist for the measurement of B_{c2} and the reader is directed to the article by Fickett [79] for more information. In magnetic measurements, B_{c2} is the field at which the magnetisation falls to the background level. For LTS materials, in DC magnetic measurements this is often indistinguishable from the field at which the hysteresis loop closes (which is strictly the irreversibility field, B_{irr} [80]). The fine distinction between the two is somewhat unimportant from a technological standpoint. In this work, DC magnetisation measurements were employed to acquire $B_{c2}(T)$ from both hysteresis loops (m-B) and temperature sweeps (m-T), as demonstrated in Figure 3.6.

A standard technique was followed for the measurement from m-B data [14]. The reversible magnetisation $M_{rev}(B)$ was first calculated from the sum of quadrants 1 and 4 of the self-field corrected hysteresis loop, and B_{c2} was subsequently measured by

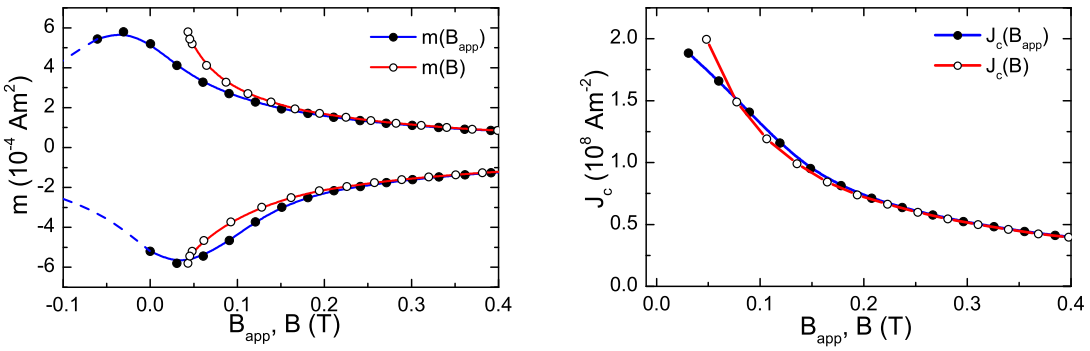

(a) (b)

Figure 3.5: (a) PbBi hysteresis data with and without self field correction. (b) $J_c(B)$ calculated from the self field corrected hysteresis width $\Delta m(B)$, along with $J_c(B_{app})$ calculated from the uncorrected hysteresis width $\Delta m(B_{app})$.

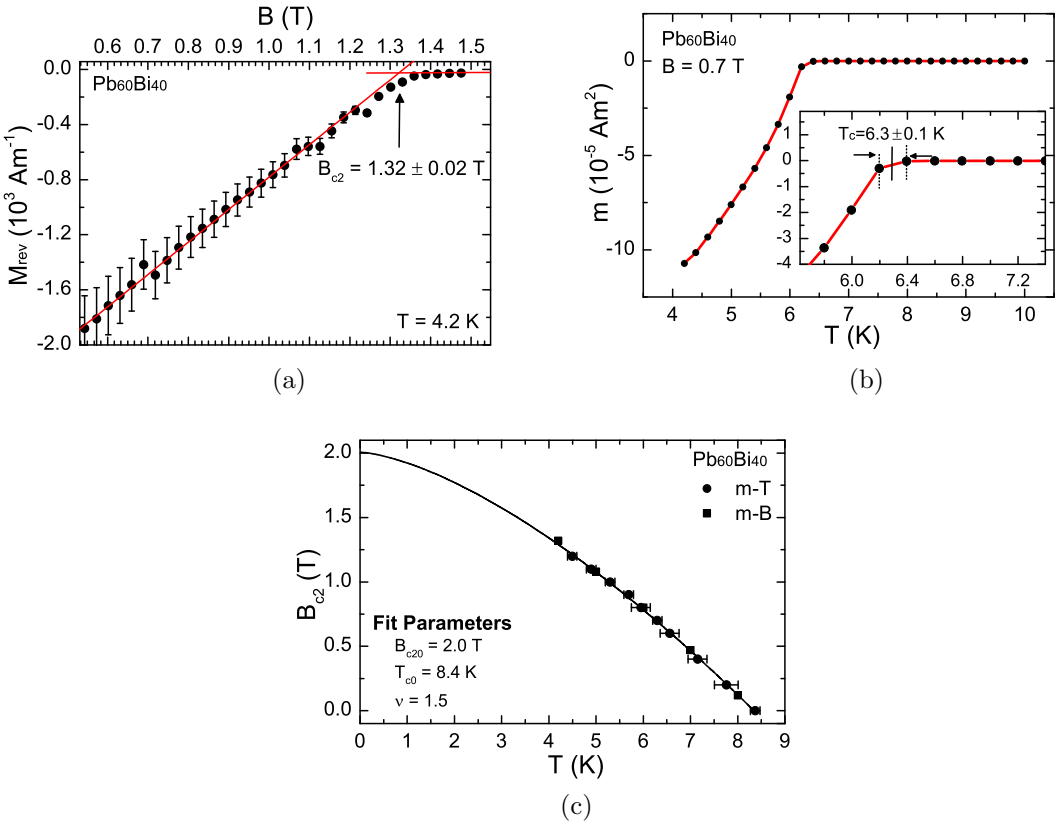

(a) (b)

(c)

Figure 3.6: Measurements taken on a PbBi sample demonstrating acquisition of $B_{c2}(T)$ from m-B and m-T data. (a) B_{c2} obtained by extrapolating the linear reversible magnetisation to the background level. (b) Measurement of T_c from the transition onset of an m-T curve. (c) Resultant $B_{c2}(T)$ values acquired from both methods. A fit is made to Equation 3.22 with the parameters indicated.

extrapolating the linear trend in $M_{rev}(B)$ to the background level. This is exemplified in Figure 3.6a. In some cases the background noise level was too high for this approach and a less precise measurement was taken from the field at which the hysteresis loop closed.

However, the vast majority of $B_{c2}(T)$ measurements were taken from m-T sweeps, since these could be acquired in much shorter times than hysteresis loops due to the low T_c of the samples tested. The following measurement protocol was employed to generate the m-T data. The sample is first cooled to 4.2 K in zero-field before sweeping the magnetic field to the first desired value. This places the sample in a state of either partial or complete flux penetration. The sample is then warmed through T_c while measuring the moment, usually in steps of 0.2 K. There is a typical overshoot of $\sim$25 % of the step size for each temperature change (i.e. $\sim$0.05 K). T_c is taken to be the value at which the moment drops to the background level (the superconducting transition onset), as exemplified for PbBi in Figure 3.6b.

The sample is then cooled once more before sweeping the field to the next value and again measuring m-T on warming. This process is repeated in background fields of up to $\sim B_{c2}(4.2\,\mathrm{K})$, in order to obtain $T_c(B)$ over the full measurable range (which is identical to $B_{c2}(T)$). It is not necessary to reduce the field to zero between measurement of each m-T curve, since the measured transition temperature depends only on B, and is not influenced by recent changes in B. This minimises the amount of field sweeping associated with these measurements and thus the helium boil-off in the magnet.

It is important to note that the $m(T)$ curves obtained reflect changes in both $J_c(T)$ and the flux distribution in the sample as it is warmed. Transition width is often taken as an indicator of sample homogeneity, however this only applies when flux pinning is negligible, i.e. for very low fields or very clean samples. This is not the case here.

The $B_{c2}(T)$ data acquired from both m-B and m-T measurements are plotted together in Figure 3.6c. The equivalence of both measures in this case is evident. For one InSnBi sample tested in this thesis the surface critical field B_{c3} was found to cause a disagreement between these two measures, which is discussed fully in Section 4.4.3.1.

$B_{c2}(T)$ is commonly parametrised with the following expression:

$$B_{c2}(T) = B_{c20}(1 - t^{\nu}) \tag{3.22}$$

where $t{=}T/T_{c0}$ (the reduced temperature), $B_{c20}{=}B_{c2}(T{=}0\,\mathrm{K})$, $T_{c0}{=}T_c(B{=}0\,\mathrm{T})$ and ν is a material dependant constant commonly found to be $\sim$1.5 – 2.0 in "dirty" technological materials [81–83]. The theoretical basis of this temperature dependence was addressed in the Werthamer, Helfand and Hohenberg (WHH) theory [84].

3.5 Magnetic Properties Measurement System

Magnetic measurements have been made throughout this project with a commercial magnetometer known as the Magnetic Properties Measurement System (MPMS XL-7) from Quantum Design Inc. The system is owned by the Claredon Laboratory, and I am very grateful for the assistance of D. Prabhakaran in use of the device throughout the project. The system is able to provide highly sensitive measurements of $m(B,T,t)$ over a wide range of conditions, allowing for comprehensive characterisation of both bulk superconducting samples and joints.

The system has four main hardware control systems; a magnetic field control system; a temperature control system; a superconducting quantum interference device (SQUID) magnetometry system and a sample handling system. Each of these is controllable by automated user-defined sequences. In this section the functionality of each of these systems will be described. A photograph of the MPMS in-situ at the Clarendon Lab is provided in Figure 3.7.

3.5.1 Magnetic Field Control

The MPMS incorporates a 7-T NbTi superconducting magnet, which produces a stable and highly uniform magnetic field over the sample space – a necessity for high sensitivity SQUID magnetometry. The field variation (δB/B) is quoted to be $\lesssim$0.01% over the 4 cm space over which the sample is moved during measurements. In persistent mode (PM), the steady state relaxation rate of the field (δB/Bδt) is quoted to be $\sim$ 1 ppm/hr. Field relaxation and uniformity over an extended length are of high importance when undertaking joint characterisation, and so these were explicitly measured and are discussed later in Section 5.7.

The current in the magnet is controlled by a Kepco power supply, and field strength is controllable to a precision of typically $\sim$0.2 mT (except near zero field, where the remanent field can be $\sim$1 mT). The field can be swept in any of three modes. The first

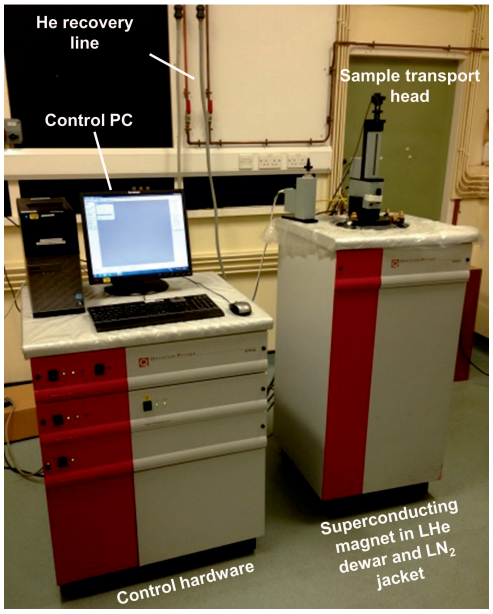

Figure 3.7: Photograph of the MPMS XL-7, with major components labelled.

is *hysteresis mode*, in which the magnet remains driven by the power supply at all times, allowing for semi-continuous field sweeping which is useful for hysteresis measurements. The second is *no-overshoot* mode, in which the current is ramped asymptotically toward the target value (avoiding overshooting), before being placed into PM. The final is *oscillate* mode, in which the current undergoes oscillations of decreasing amplitude about the target value before being placed into PM. These oscillations reduce field errors and minimise field relaxation following large field changes.

3.5.2 Temperature Control

Temperature in the sample space is moderated by static He gas. The gas is extracted from liquid He (LHe) boil-off in the magnet dewar, and warmed by copper heaters at the bottom of the sample space to between 4.2 and 300 K. Temperatures of 1.9 K can also be reached by pumping on a small pot of LHe, but this often led to program instabilities when warming through 4.2 K and so was generally avoided. Temperature is monitored by Cernox sensors in the heating region, which are calibrated to give the desired temperature in the sample location to within $\sim 0.5\%$.

3.5.3 SQUID Magnetometry System

The MPMS employs an entirely superconducting DC SQUID magnetometry system capable of measuring magnetic moment over a wide sensitivity range from 10^{-11} to $10^{-2}\,\mathrm{Am}^2$. A schematic of the measurement system (adapted from the user manual with permission from Quantum Design) is supplied in Figure 3.8, and the basic measurement process is as follows.

The sample is physically moved in a series of steps through a superconducting pickup coil, inducing a persistent current in the coil which is proportional to the change in flux caused by each movement. The 3 cm long pickup coil is wound in a second-order gradiometer configuration, having two clockwise central turns and two anti-clockwise outer turns. If the coil is perfectly "balanced" (i.e. each turn has identical size), the coil is sensitive only to local changes in flux produced by the sample and insensitive to the uniform background field. This permits measurement of very small magnetic moments in very large background fields. In a typical "scan", the sample is moved through the gradiometer over a $2-4$ cm length in either 24 or 32 steps (in approximately 10 seconds). Several scans are commonly taken to give a measurement and standard deviation.

The pickup loop is inductively coupled to a thin-film SQUID device via an intermediate flux transformer, producing a highly linear voltage in response to the current in the loop. The field on the loop is maintained at a suitably low level by a superconducting shield. Before each measurement, and whenever the magnetic field is changed, the pickup loop and transformer are quenched to eliminate any remanent persistent currents.

At each point in the scan, the voltage signal is filtered, amplified and averaged many thousands of times to give a precise voltage reading. For appropriately small samples producing a magnetic dipole field, the voltage scan has a characteristic "ideal dipole" form to which a calibrated functional form may be fitted. An example of such a scan is provided in Figure 3.8. Voltage offsets and drifts are corrected for, and the longitudinal magnetic moment (i.e. the component of the total moment along the direction of motion) is acquired from the voltage scan. This is performed automatically by the MPMS by in-built regression routines, and the resultant moment is recorded in a data file.

As standard practice, all system variables, raw voltage scans, and fit diagnostic data are recorded, which is often useful when scrutinizing anomalous data points.

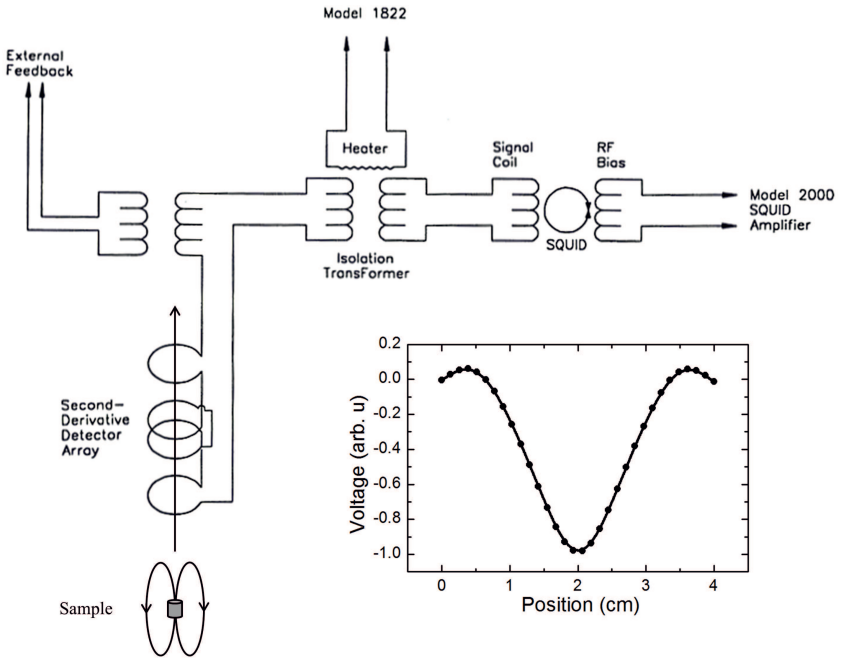

Figure 3.8: Schematic of the SQUID measurement electronics in the MPMS, along with a typical voltage scan from which the magnetic moment is measured (reproduced and adjusted with permission from Quantum Design Inc.).

3.5.4 Sample Handling System

The sample is contained in the temperature controlled bore of the superconducting magnet, which has a diameter of ∼9 mm. Although the useable sample space is 5 mm in diameter, samples are ideally sized at ∼2–3 mm in diameter and no more than 5 mm in length so as to avoid calibration errors in moment measurements.

Samples are typically loaded into non-magnetic plastic straws of 5 mm diameter and 200 mm length, and held in place with adhesives such as Kapton tape, or simply by pressure from small sections of folded straw. It is good practice to make several pin-holes above and below the sample to ensure He gas can flow freely around the sample. Sample mounting methods vary between samples and will be discussed on an individual basis, however the objective is to hold the sample securely in place (minimising movement-induced noise) in the desired field orientation, without introducing an excessive magnetic background signal. Uniform support structures which are longer than the pickup coil length theoretically produce no signal.

The straw is mounted onto a probe and inserted into the magnet bore. The probe attaches to a stepper motor which allows the sample to be centred and moved through

the gradiometer coil. It is important to note that the straw can deflect significantly from the axial direction, which adds to the overall uncertainty in sample alignment. At maximum deflection the bottom of the straw will make contact with the walls of the sample space (a 2 mm deflection), giving a maximum angular deflection of $\sim 6^o$. This is important to note both in terms of the field-angle on the sample (particularly important for anisotropic samples), and also in terms of the measured (axial) component of the total moment acquired by the magnetometer.

3.5.5 SQUID-VSM

Although the vast majority of work was performed with the MPMS XL-7, for a brief period near the end of the project I was also granted access to the latest version of the MPMS – the SQUID VSM (vibrating sample magnetometer), courtesy of Stephen Milward and Alexey Dobrynin at Diamond Light Source (DLS).

In addition to DC extraction moment measurements, this system is also able to function in VSM mode, in which the sample is vibrated with an amplitude of a few mm inside the gradiometer. As well as improving measurement sensitivity this greatly reduces the measurement time from $\sim$10 s to $\sim$1 s. The magnetic field and temperature control systems were also much quicker, permitting field sweep rates of up to 500 Oe/s and temperature sweep rates of up to 20 K/min. The maximum field was similarly 7 T.

Chapter 4

Superconducting and Microstructural Properties of Joint Materials

The superconducting properties of the current carrying component materials of joints are expected to play a major role in determining overall joint performance. In order to execute a scientific study into NbTi joints, measurement of the superconducting and microstructural characteristics of the raw materials comprising the joints is an essential body of work.

This chapter discusses the magnetic measurements and resultant $J_c(B,T)$ and $B_{c2}(T)$ values for each jointing material employed, and their importance in the context of jointing. The NbTi wire that will be joined is first discussed, followed by various low melting point superconducting alloys (both leaded and one new Pb-free alloy) used to produce soldered joints, and finally the commercial bulk Nb used as a crimp material in cold-pressed joints.

4.1 Niobium Titanium Wire

When measuring the superconducting properties of joints, it is important to note that the wire also provides a resistive contribution to the circuit and sets the maximum attainable joint $I_c(B,T)$. It is therefore essential to fully characterise the superconducting properties of the wire to be joined before analysing the joints themselves. The pertinent measurements to be made in this respect are $B_{c2}(T)$, $I_c(B,T)$ and the n-value, which together determine the V-I characteristics of the wire.

The most direct method of making such measurements is the four-probe transport technique. However, owing to the high currents involved and cryogenics required for continuous temperature control, these are not trivial measurements to implement and require specialist equipment and expertise. Unfortunately at the time of this work there were changes under way in the Clarendon Laboratory (where such measurements have been made routinely for many decades), which meant that this work could not be readily carried out. It was therefore decided that a purely magnetic method would be employed to characterise the particular NbTi wire used for jointing throughout this thesis.

The wire's $I_c(B,T)$ and $B_{c2}(T)$ values were measured at fields of up to 7 T and temperatures from 4.2 to 10.0 K using the MPMS-XL SQUID magnetometer described in Section 3.5. Since the n-values could not readily be attained magnetically, available literature data on a similar wire was used to estimate the V-I characteristics and thus the contribution to joint resistance from the wire itself. This section gives details of the measurements made and the subsequent analysis performed.

4.1.1 Sample Preparation

The conductor used in this project was Supercon Inc T48BG monofilamentary NbTi/Cu wire donated by Agilent Technologies. The wire is composed of a nominally 200 μm diameter Nb-45 wt.%Ti filament surrounded by a 100 μm thick Cu matrix and a 15 μm thick layer of Formvar insulation. This gives an overall wire diameter of 0.43 mm and bare Cu:non-Cu ratio of 3:1. An optical cross section of the wire is shown in Figure 4.1a. Monofilamentary wire is employed for a number of reasons discussed later in Chapter 5, but for the most part this is to simplify the analysis of joint properties.

In order to carry out measurements in the MPMS, an 86.5 mm length of wire was wound into an open coil a hollow G10 (glass reinforced plastic) former and secured with cyanoacrylate adhesive and Kapton tape as shown in Figure 4.1b. The coil had a single-layer of ~6 turns and a diameter of 4.5 mm between wire cores. The sample was mounted in a straw as shown, with the applied field perpendicular to the wire axis in order to measure $I_c(B_\perp)$. Measurements made with the field held parallel to the wire axis ($B_\parallel$) are also of importance for joints, and these are discussed separately in Section 4.1.5.

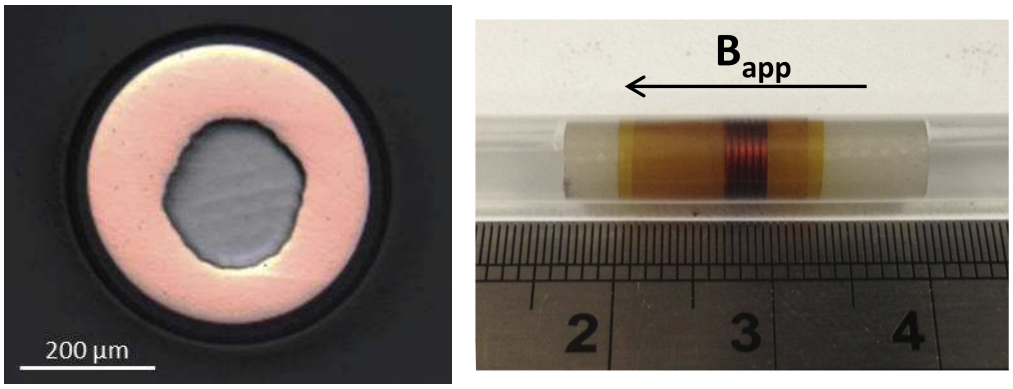

(a) (b)

Figure 4.1: (a) Optical cross section of wire employed in this study, containing a single NbTi filament clad in Cu and insulated with Formvar. (b) Photograph of the sample coil mounted in a standard 5 mm straw, which is subsequently loaded into the MPMS with the coil axis parallel to the applied field as shown.

4.1.2 $B_{c2}(T)$

The $B_{c2}(T)$ of the wire was measured according to the m-T procedure outlined in Section 3.4. DC moment was measured as a function of temperature in 0.1 K steps between 5.0 and 10.0 K, in background fields up to 7.0 T, in 1 T intervals. These data are plotted in Figure 4.2a. $T_c(B)$ values were extracted from the onset temperatures in each curve to a precision of ± 0.05 K, and these values are plotted as $B_{c2}(T)$ in Figure 4.2b.

The standard WHH expression for $B_{c2}(T)$ was fitted to the data. Due to the 7.0 T field limitation however, the portion of the $B_{c2}(T)$ curve acquired here is too limited to obtain a physical fit for the parameters ν and B_{c20} to these data. However, it is generally accepted that $\nu = 1.7$ provides a universal fit for NbTi over a wide composition range (as shown by Lubell [81]), therefore this figure was fixed. Optimised values for T_{c0} and B_{c20} were then found to be 9.0 K and 14.1 T respectively, which are consistent with literature values [85]. For completeness it should be emphasised that Lubell found a slightly larger B_{c20} value was required for fits to data above 10 T, however this is inconsequential for the present work on joints which occurs at fields well below 7.0 T.

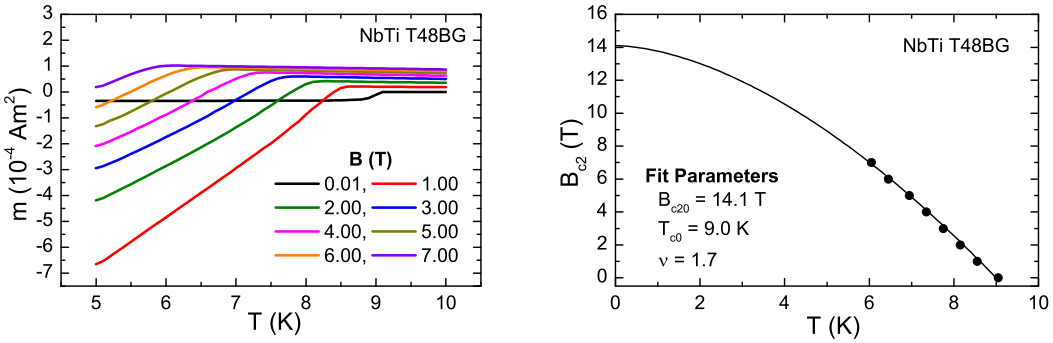

Figure 4.2: (a) Magnetic moment versus temperature, measured on warming in applied fields of up to 7 T. (b) $B_{c2}(T)$ values extracted from the onset T_c value for each curve in (a). A fit is made to the data with Equation 3.22, as described in detail in the main text.

4.1.3 $I_c(B,T)$

Magnetic hysteresis loops were measured on the coil at temperatures of 4.2, 5.0, 6.0, 7.0 and 8.0 K. Since only the hysteresis width in positive fields is required to obtain a complete I_c data set, the initial magnetisation curve (quadrant 0) was not measured and data was taken only in fields above -1.5 T, maximising data density. The raw hysteresis loops are shown in Figure 4.3a.

Flux jumps occurred commonly at low fields and temperatures. This was expected given the 200 μm filament diameter of this wire, which is well above the thermal stability limit of $\sim$50 μm for NbTi at 4.2 K, as was discussed in Section 1.5.1. The affected data were removed from the set before calculating $I_c(B_{app},T)$ by scaling the hysteresis width $\Delta m(B_{app},T)$ to a limited number of generic I_c values reported by the wire manufacturer. These were 110 A at 3 T and 80 A at 5 T at a temperature of 4.2 K. A further value of 50 A at 7 T is slightly beyond the accessible range of the measurements (due to incomplete flux reversal in the filaments).

Although these I_c values could not be confirmed directly by in-house measurements, they can be compared to theoretical values calculated from a relevant critical state model for this experimental geometry. Wilson [21] derived the relation between filament magnetisation and J_c for a circular wire in a transverse field by considering a Bean-like penetration of the field in elliptical segments towards the centre of the filament. For a fully penetrated filament of radius r_f and length l_f, the following

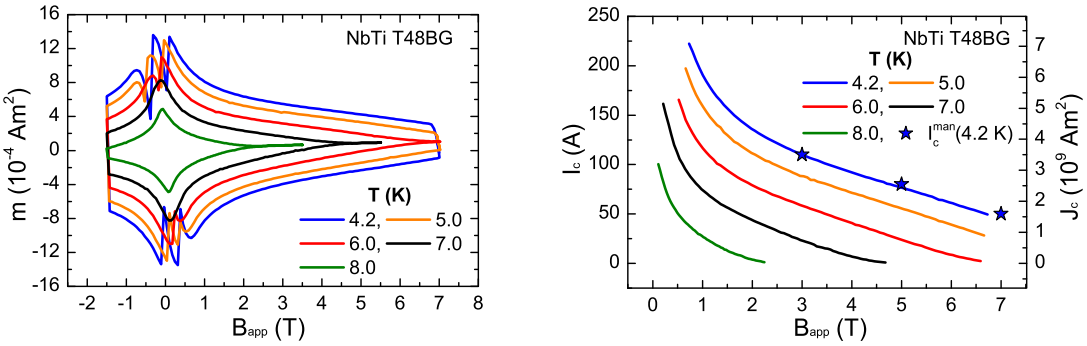

(a) (b)

Figure 4.3: (a) Magnetic hysteresis loops measured at $4.2 \leq \mathrm{T} \leq 8.0\,\mathrm{K}$ in applied fields cycled from $-1.5 \rightarrow 7.0 \rightarrow -1.5\,\mathrm{T}$. (b) $I_c(B_{app}, T)$ obtained by scaling the hysteresis width to the manufacturer's $I_c(3.0\,\mathrm{T}, 4.2\,\mathrm{K})$ value. Additional manufacturer I_c values are shown as stars in the figure and are consistent with the scaled measurements from the hysteresis width.

relationship is obtained:

$$\Delta m_{Wil} = \frac{8}{3} r_f^3 l_f J_c. \tag{4.1}$$

Microscopic analysis of the wire's cross section suggested an average r_f of $104 \pm 3\,\mu\mathrm{m}$. Accordingly the wire I_c values calculated from the hysteresis width at 3 T and 5 T using Wilson's model are $123 \pm 4\,\mathrm{A}$ and $86 \pm 3\,\mathrm{A}$, which are in reasonable agreement with the manufacturer values. This suggests that the tested length meets specification and increases the confidence in employing manufacturer values. The resultant scaled $I_c(B_{app}, T)$ data are provided in Figure 4.3b. Overall, including a slight extrapolation to the 7 T manufacturer value, the scaled data and manufacturer values agree to within $\sim$4%, which is taken to be a representative error on the scaled I_c values.

Finally, it should be highlighted that self field corrections have *not* been applied in this case. This is because fundamental studies are not of interest here, and rather the goal of these measurements is to predict the wire's operational performance, which is arguably more conveniently parametrised in terms of B_{app} than B. A counter-argument to this statement is that strictly the self-fields in magnetisation measurements and transport measurements will differ slightly. However, such corrections are insignificant compared with the uncertainty in the measurement of current when characterising joints (discussed later in Section 5.5), and so will not be discussed further here.

4.1.4 *V-I* Characteristics

In order to estimate the contribution of wire resistance to joint resistance measurements, the *V-I* characteristics of the wire must be acquired. It was shown by D. Ryan [48] that in fields below 9.0 T at 4.2 K, the *V-I* characteristics of monofilamentary NbTi follow the standard empirical power law (Equation 1.5) over an extraordinarily large electric field range – from 10^{-11} to 10^{-4} Vm^{-1}.

Discussed in this section is a procedure designed to estimate $n(B_{app}, T)$ for the wire used in this investigation, using literature n-values measured for a similar wire by Ryan. A relationship is first established between n and I_c for his data. Secondly, some reasonable and conservative assumptions are made to extrapolate this $n(I_c)$ relationship to a wider range of fields and temperatures. Finally, this relationship is applied with the $I_c(B_{app}, T)$ values of the wire studied here to obtain $n(B_{app}, T)$ for this material. The wire's *V-I* characteristics are then finally estimated.

4.1.4.1 $n(B,T)$

Figure 4.4a shows the n-value and I_c data digitally extracted from the D.Phil. thesis of D. Ryan [48]. Ryan's measurements were made on a wire from the same manufacturer and nominally identical to that used in this study, differing only by having half the thickness of Cu. He measured the n-values at 4.2 K and fields between 6.0 and 10.5 T. All subsequent analysis was performed specifically as part of the current investigation.

The data in Figure 4.4a were re-plotted as n versus I_c in Figure 4.4b, for which a linear correlation was found:

$$n = \alpha I_c + 1 \tag{4.2}$$

with $\alpha = 1.32 \pm 0.03\ \mathrm{A}^{-1}$. To enable a first order estimate of the n-values of the present wire from available I_c data, the relationship found for Ryan's wire is assumed to hold for the present wire. Implicit in this assumption is that the Gaussian-like distributions of critical currents in the two wires are identical. Although not directly verifiable, this assumption is thought to be reasonable given their physical similarities. Their respective critical currents differ by less than 6 %. Caution must be shown however not to over-stretch the range of temperatures and fields over which this relationship is assumed to hold.

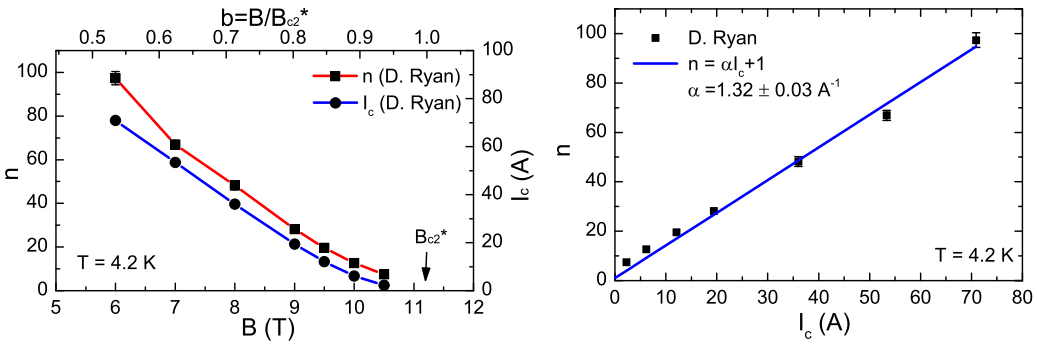

(a) (b)

Figure 4.4: (a) $n(B, 4.2\,\mathrm{K})$ and $I_c(B, 4.2\,\mathrm{K})$ for a similar monofilamentary NbTi wire to that used in this study (data was digitally extracted from the D.Phil. thesis of D. Ryan). B_{c2} is taken to be 11.2 T by extrapolating the n-value to unity (Ohmic). (b) The same data is re-plotted as n versus I_c, to which a linear fit is made.

Several authors have found that similar simple $n(I_c)$ relationships hold over temperature and field ranges of at least 4.2 K to 7.5 K and 4.0 T to 10.0 T respectively (measurement limited) [86, 87]. It appears reasonable to assume that Equation 4.2 holds over the temperature range of interest in this study, $4.2 \leq \mathrm{T} \leq 8.0\,\mathrm{K}$. However, since Ryan's data set is limited to reduced fields b=B/B_{c2}>0.5, assuming a field validity range requires more caution.

As was discussed in Section 1.5.3, $n(b)$ depends upon the degree of intrinsic (chemical and microstructural) or extrinsic (filament deformation) limitation of I_c [23]. Where intrinsic limitations are dominant, the n-value continues to increase down to low fields. However, technological wires are usually extrinsically limited to some extent, leading to saturation of the n-value at low fields. Although no such saturation is evident in Ryan's data, in the interest of making a conservative estimation of $\mathrm{n}(b < 0.5)$, a saturated value equal to $n(b$=0.5) has been assumed.

In summary, for the wire used in this study $n(B_{app}, T)$ is calculated with the following simple expressions, which have also been plotted in Figure 4.5a:

$$\text{for } b > 0.5 \quad n(B_{app}, T) = \alpha I_c(B_{app}, T) + 1, \tag{4.3}$$

$$\text{for } b \leq 0.5 \quad n(B_{app}, T) = \alpha I_c(b = 0.5, T) + 1, \tag{4.4}$$

The uncertainty in the estimated n-values themselves is $\sim$5 %, deriving from errors in both the fit constant α and measured I_c values.

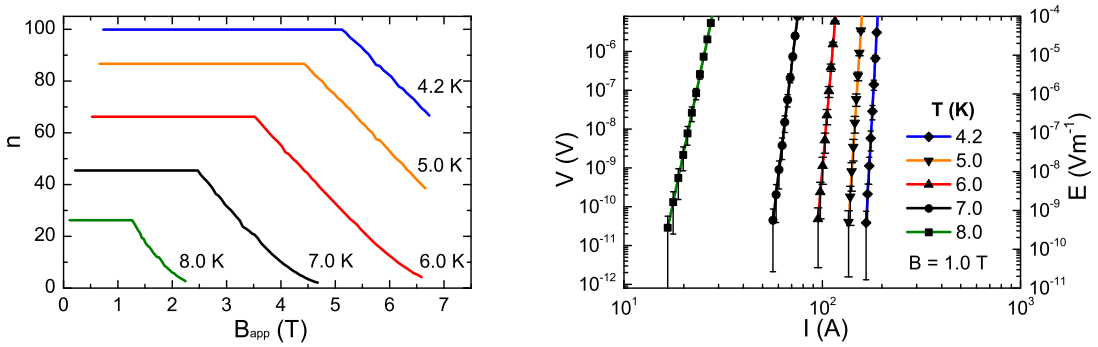

(a) (b)

Figure 4.5: n-value of NbTi-T48BG versus applied magnetic field and temperature, calculated from Equations 4.3 and 4.4 and wire $I_c(B,T)$ data. Error on the plotted values is ∼5 %. (b) V-I characteristics of an 8 cm length of the wire at 1.0 T at each temperature calculated with the empirical power law in Equation 1.5. The data are plotted over the E-field range from 10^{-11}–10^{-4} Vm^{-1}, for which the power law has been experimentally verified by Ryan.

With the $n(B,T)$ and $I_c(B,T)$ data established, the V-I characteristics of the wire can finally be calculated from the power law in Equation 1.5. Remembering that the I_c values derive from manufacturer transport measurements, a conservative critical electric field (E_c) of 1 $\mu\mathrm{Vcm}^{-1}$ has been used. Calculated values at an applied field of 1.0 T at each temperature are plotted in Figure 4.5b. Voltages were scaled to a wire length of 8 cm, which is the total length used in jointed coils discussed in the rest of the thesis.

4.1.5 Anisotropy of $I_c(B,T)$

The thermomechanical process by which NbTi wires are made produces elongated defects which exhibit anisotropic flux pinning and J_c, as has been studied by several authors [27, 88–90]. Anisotropy of J_c is of interest for the study of NbTi joints, since in these the current must have a radial component in order to flow into and out of the filaments. The critical current density along each of the symmetry axes in the filaments ($J_{c,r/z/\theta}$) is dependent upon the applied field direction, which is ordinarily held either transverse ($B_\perp$) or longitudinally ($B_\parallel$) to the filament axis during measurements.

A comprehensive set of such measurements were made by Martinelli and Turck [88] on monofilamentary wires similar to those used in this study. The configurations

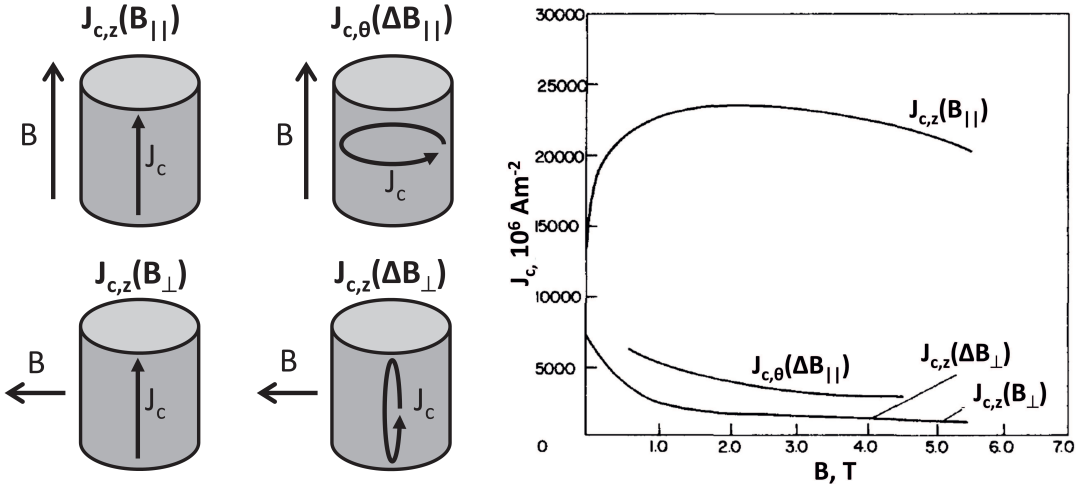

Figure 4.6: (a) Schematic of a NbTi filament in an applied field, indicating the various J_c components and field orientations that can be measured. (b) $J_c(B)$ in each of these configurations, measured by Martinelli and Turck and reproduced with permission from [88].

employed are sketched in Figure 4.6a and the results obtained are plotted in Figure 4.6b. $J_{c,z}(B_\parallel)$ and $J_{c,z}(B_\perp)$ values were both acquired by transport measurements. Magnetic measurements (denoted by ΔB) were used to acquire $J_{c,\theta}(\Delta B_\parallel)$ and to provide a second measure of $J_{c,z}(\Delta B_\perp)$ (which was found to be identical).

$J_{c,z}$ is enhanced by a factor of $\sim 10-15$ when the field is aligned parallel to z rather than perpendicular to it. This increase has been explained in terms of both the "force-free" effect (in which the alignment of current and field reduces the Lorentz force to almost zero), and an increased pinned length of the flux lines along the elongated defects [91].

The joints measured in this thesis are tested with the joined filaments held in the $B_\parallel$ configuration, and so the current density component $J_{c,r}(B_\parallel)$ will contribute to current flow into and out of the filaments. Whilst $J_{c,r}$ cannot easily be measured by standard magnetic or transport measurements, it is expected to be similar in magnitude to $J_{c,\theta}$ due to the likeness of the microstructures along these two directions. It can be seen from Figure 4.6b that $J_{c,\theta}(\Delta B_\parallel)$ is ~2–3 times larger than $J_{c,z}(B_\perp)$, which is the ordinary limitation on wire performance in coils. Therefore, if at all, the anisotropy of J_c in the wire will only serve to enhance rather than degrade joint performance.

4.1.6 Magnetic Measurements in Near-Longitudinal Fields

The high values of $J_{c,z}(B_{\|})$ produce an unusual magnetic response in the wire when the applied field makes a shallow angle to the wire axis. Such effects were observed in magnetic hysteresis loops measured in this project on wires mounted almost longitudinally in the MPMS, as will now be described.

A set of wires were aligned vertically in the MPMS by embedding them in a G10 block as shown in Figure 4.7a. A G10 rod was first turned to $\phi 5$ mm to fit snuggly in the sample straw. A set of nine fine holes were drilled axially in the rod, and a single NbTi wire was glued into each with a thin layer of epoxy resin. A cylinder of length 2.79 mm was sliced from the rod on a diamond saw, cleaned in acetone and mounted in the sample straw for testing in the MPMS. Irrespective of how well aligned the sample is inside the straw, the applied field will inevitably subtend a small angle to the wire axis due to slight deflection of the straw in the sample chamber. As discussed previously in Section 3.5.4, this deflection is estimated to be $\lesssim 6^{o}$.

Magnetic hysteresis loops were measured at the standard temperatures from 4.2 to 8.0 K. The sample was cooled in zero-field and the field was swept over all five quadrants to $\pm B_{max}$, however measuring only in fields above -1.5 T in order to maximise the data density. These measurements are presented in Figure 4.7b.

The loops exhibit a number of unusual characteristics. Firstly, the initial magnetisation curves (quadrant 0) are larger in magnitude than quadrant 4 in each loop. Secondly, the loops are highly asymmetric about both m=0 and $B_{app,||}$=0. Finally, there are broad hysteresis peaks in each quadrant rather than at B_{app}=0.

Martinelli and Turck explain how this behaviour results from the small transverse field component on the wire, which induces large axial currents (of density close to $J_{c,z}(B_{\|})$), shielding the interior of the sample from becoming fully penetrated by the longitudinal field. In their study, the axial currents were directly observed from measurements of the sample's transverse moment with perpendicular pickup coils.

As will be discussed fully in Section 5.4.7, similar asymmetries and anomalous peaks are present in magnetic measurements made on some of the joints investigated in this study, and so it is possible that incomplete flux penetration might also explain these effects.

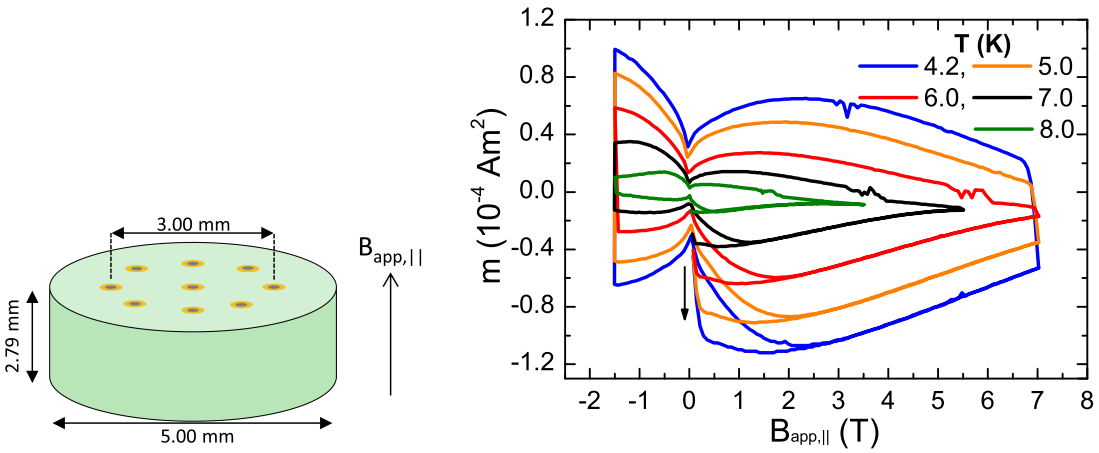

Figure 4.7: (a) Sketch of the sample made for magnetic measurements on NbTi in longitudinal fields, in which nine short lengths of NbTi wire are embedded upright in a G10 block. (b) ZFC magnetic hysteresis loops measured in longitudinal fields. $B_{app,||}$ was swept fully to $\pm B_{max}$ although moments were measured only in fields above -1.5 T. The arrow indicates the initial magnetisation curves.

4.2 PbBi-Based Solders

PbBi alloys are used commonly as superconducting solders, having the highest known $B_{c2}(T)$ values amongst the low melting point superconductors [59].

A preliminary survey of $J_c(B,4.2\text{K})$ and microstructure was first carried out on three key PbBi-based jointing solders used in the literature. The first sample was $Pb_{60}Bi_{40}$ (all quantities in wt.%), which is close to the solubility limit of Bi in the superconducting ϵ phase (at 126 ^{o}C) [59]. The second was the eutectic $Pb_{44.5}Bi_{55.5}$ composition, which is known to form a dense array of finescale Bi precipitates which act as effective flux pinning sites – a popular solder choice in jointing [60]. The final alloy was $Pb_{34.5}Bi_{55.5}Sn_{10}$, which is the eutectic composition with a 10 wt.% substitution of Sn for Pb. This composition was of interest since both Swenson and Merkiewicz [53] and Thornton [35] found that PbBiSn solders tended to perform far worse than PbBi in NbTi joints. It was therefore of interest to test the influence of Sn additions on the microstructure and superconducting properties of the solder.

4.2.1 Sample Preparation

The raw Pb, Bi and Sn components with 4N, 4N and 3N respective purities were acquired from Advent Research Materials (UK). Appropriate quantities of each were weighed out to a total mass of 20 g per sample, and the components were sealed under argon into ϕ10 mm fused silica tubes. The tubes were held in a box furnace at 300 ^{o}C for three hours to allow the components to melt and mix completely with minimal oxidation (preserving the composition). The tubes were air cooled and smashed once cool to retrieve the solder ingots.

Given the dependence of thermal history on microstructure and thus superconducting properties for these solders, it was of interest to investigate the influence of cooling rate on solder performance. Each ingot was split into two pieces, and each half was melted separately in an alumina crucible on a hot plate (at 300 ^{o}C in air). One sample was then hot plate cooled (HPC) at $\sim$35 ^{o}C/min (solidifying after $\sim$5 mins), and the other was air cooled (AC) at $\sim$17.5 ^{o}C/s (solidifying after $\sim$10 s). Although the cooling profiles used in commercially manufactured joints are kept secret by magnet manufacturers, these two HPC/AC conditions were thought to be reasonable upper and lower limits to the typical processes, which certainly don't involve quenching in LN_2.

Pellets of ϕ5 mm and $\sim$2.5 mm thickness were then punched out of each ingot with a mechanical press, and mounted for SEM and MPMS measurements. This work was carried out at an early stage of the project, and it was later realised that this geometry was far from ideal for magnetic measurements due to self-field effects. The ideal geometry is a long, narrow cylinder such that end effects are negligible and the internal fields are similar to external applied field value. Sample preparation techniques were improved upon in subsequent work to produce narrower cylinders.

4.2.2 Microstructure

The solders were first investigated in the SEM within a week of manufacture, and the microstructures seen for the air-cooled and hot plate-cooled samples were indistinguishable. This is broadly consistent with the superconducting measurements, (presented in Section 4.2.3) which show that the range of cooling rates employed had only a minor effect on J_c values. It should be highlighted that due to fast room temperature diffusion in these alloys [19, 57] the microstructures of the differently cooled

samples will have equilibrated further by the time that microscopy was carried out compared to their condition at the time of superconducting measurements. However, on the whole it seems that cooling rate is not a major factor in joint making. The microstructure of the hot plate-cooled samples are presented here.

EDX phase maps showing the phases present in the three solders are shown in Figure 4.8. Figures 4.8a and 4.8b were obtained at an accelerating voltage of 10 kV on the Merlin-SEM, whilst Figure 4.8c was taken at 20 kV on the 5510-SEM (with differences in resolution apparent). The results of chemical analysis on each sample are also summarised in Figure 4.8d.

Wide area EDX scans at low magnification confirmed that the actual compositions matched the nominal values to within a few percent in each sample. Each sample contains a matrix of superconducting PbBi ϵ-phase (33 ± 1 wt.% Bi on average), in addition to particles of essentially pure Bi (<2 wt.% Pb), as expected from the phase diagrams provided in Figure 4.9 [59].

The Bi particles vary in size from the micron scale (large) to several hundred nanometres and below (small). The PbBi-eutectic and PbBiSn samples appear to contain a majority of large Bi particles, whilst the $Pb_{60}Bi_{40}$ sample has a greater fraction of smaller particles, with a small number of large particles. The spread in particle size in each sample can be understood by the solidification processes expected from the phase diagram.

In the $Pb_{60}Bi_{40}$ sample (Figure 4.8a), small Bi particles are precipitated out of the ϵ phase as the sample cools below the eutectic temperature (126 ^{o}C), due to the decreasing solubility of Bi in the ϵ phase with reducing temperature. Larger particles grow by consuming nearby smaller particles through solid state diffusion (Ostwald ripening), which is fast in these alloys [19, 57]. Evidence for Ostwald ripening in the $Pb_{60}Bi_{40}$ sample is provided in Figure 4.10, in which larger Bi particles are surrounded by zones with fewer small Bi particles. The diffusion distances are seemingly too large for all Bi particles to be consumed with the cooling rates applied, and so many remain in the final microstructure.

In the PbBi-eutectic and PbBiSn samples an initially fine array of ϵ/Bi lamellae are expected to form by eutectic solidification. This microstructure subsequently coarsens as the sample continues to cool (again by solid state diffusion), and the Bi particles become rounder as they grow. This is particularly evident for the PbBi eutectic microstructure in Figure 4.8b. There will be further precipitation of small

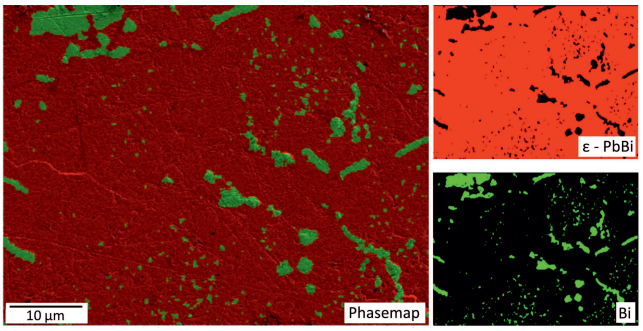

(a)

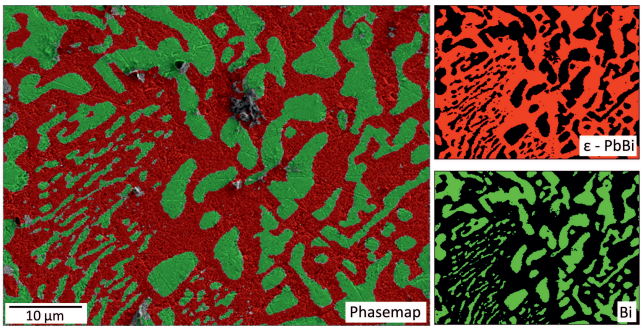

(b)

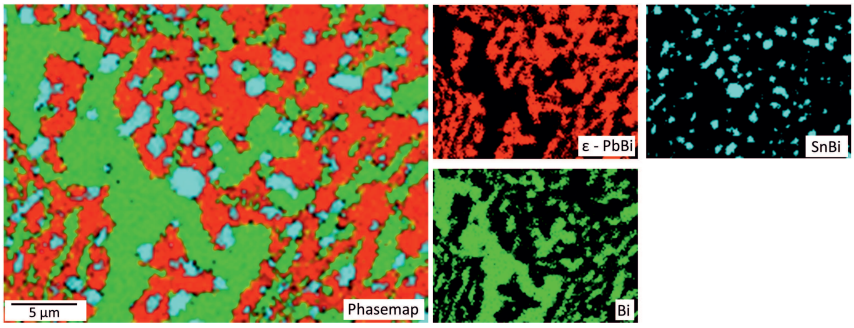

(c)

Sample	Measured Composition (wt.%)	Phase	Phase Composition (wt.%)	Phase fraction (vol. %)
$Pb_{60}Bi_{40}$	59/41	ε – PbBi	66/34	80
		Bi	~100	20
$Pb_{44.5}Bi_{55.5}$	42/58	ε – PbBi	67/33	64
		Bi	~100	36
$Pb_{34.5}Bi_{55.5}Sn_{10}$	34/54/12	ε – PbBi	67/33	41
		Bi	~100	38
		SnBi	93/7	21

(d)

Figure 4.8: EDX phase maps showing the microstructures of the HPC PbBi-based solders produced – (a) $Pb_{60}Bi_{40}$, (b) $Pb_{44.5}Bi_{55.5}$ and (c) $Pb_{34.5}Bi_{55.5}Sn_{10}$. (a) and (b) were taken on the Zeiss Merlin-SEM at 10 kV, whilst (c) was acquired with the 5510-SEM at 20 kV. (d) The chemical makeup of each sample.

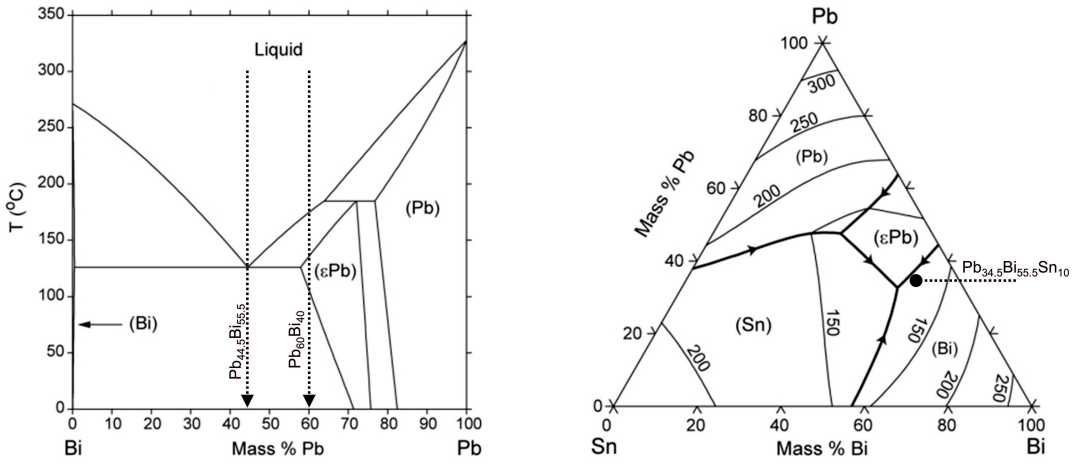

(a) (b)

Figure 4.9: (a) Calculated Pb-Bi phase diagram and (b) calculated liquidus projection with isotherms of the Pb-Bi-Sn phase diagram. The solders produced here have been identified by dotted lines. Data from [92].

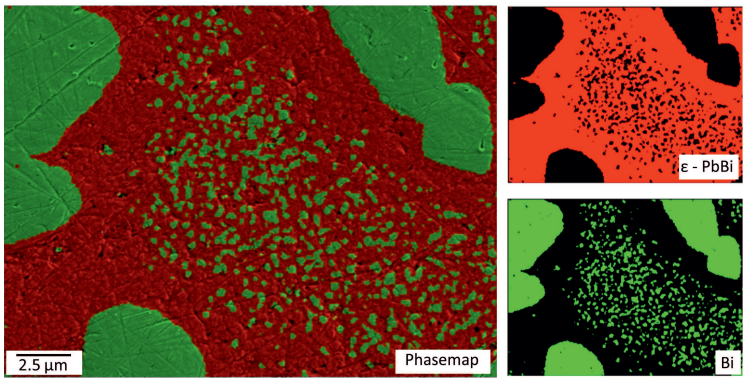

(a)

Figure 4.10: EDX phase maps on the hot plate-cooled $Pb_{60}Bi_{40}$ sample, showing regions with fewer Bi particles surrounding the larger Bi precipitates, evidencing Ostwald ripening.

Bi particles from the ϵ phase as occurs in the $Pb_{60}Bi_{40}$ sample. The absence of many small Bi particles in the final microstructure suggests that in these alloys they coarsen more readily. This is likely due to the large number of nearby eutectic Bi particles, to which the required diffusion distances are shorter.

The PbBiSn sample contains additional micron-scale SnBi precipitates of spherical shape and with typical Sn content $\sim 93 \pm 2$ wt.%.

4.2.3 Superconducting Properties

For magnetic measurement in the MPMS, the samples were mounted axially in straws and held in place with cotton wool. In these preliminary tests there was time only to acquire a single 4.2 K hysteresis loop for each sample. Measurements were made within a few days of casting. The PbBiSn samples were tested on day 2, the PbBi-eutectic samples on day 3, and the $Pb_{60}Bi_{40}$ samples on day 4. The raw hysteresis loops are provided in Figure 4.11a. Self field corrections were made for this sample geometry and $J_c(B)$ was calculated. The results are shown in Figure 4.11b. Due to flux jumping in the PbBiSn sample, the field range over which J_c could be calculated was severely restricted. Finally, plots of the pinning force versus reduced field ($b{=}B/B_{c2}$) are provided for the hot plate-cooled samples in Figure 4.11c. Identical forms are found for the air-cooled samples.

Firstly, regardless of cooling rate and composition, all samples are found to have very similar B_{c2} values ($\sim$1.35 – 1.40 T at 4.2 K). Noise near B_{c2} limits the measurement precision to $\sim$0.05 T, which is improved upon in later samples. As was discussed in Section 2.3.2.1, Evetts and Wade [59] showed that the B_{c2} of the epsilon phase at 4.2 K increases with Bi content from a value of 1.34 T at the room temperature equilibrium composition ($Pb_{66.5}Bi_{33.5}$), to 1.77 T at the maximum Bi solubility ($\sim Pb_{60}Bi_{40}$). The B_{c2} values measured for the samples produced here are therefore in good agreement with the expected room temperature values. This suggests that the superconducting ϵ phase matrix in each of the samples was almost completely equilibrated at the time of measurement, in agreement with microstructural analysis of the solders. This confirms that diffusion in these alloys is rapid, that the ϵ phase rapidly reaches thermal equilibrium for the cooling rates appropriate for jointing, and so joints made with these solders are expected to superconduct in fields of up to 1.3–1.4 T (neglecting any shielding effects or solder-filament interactions).

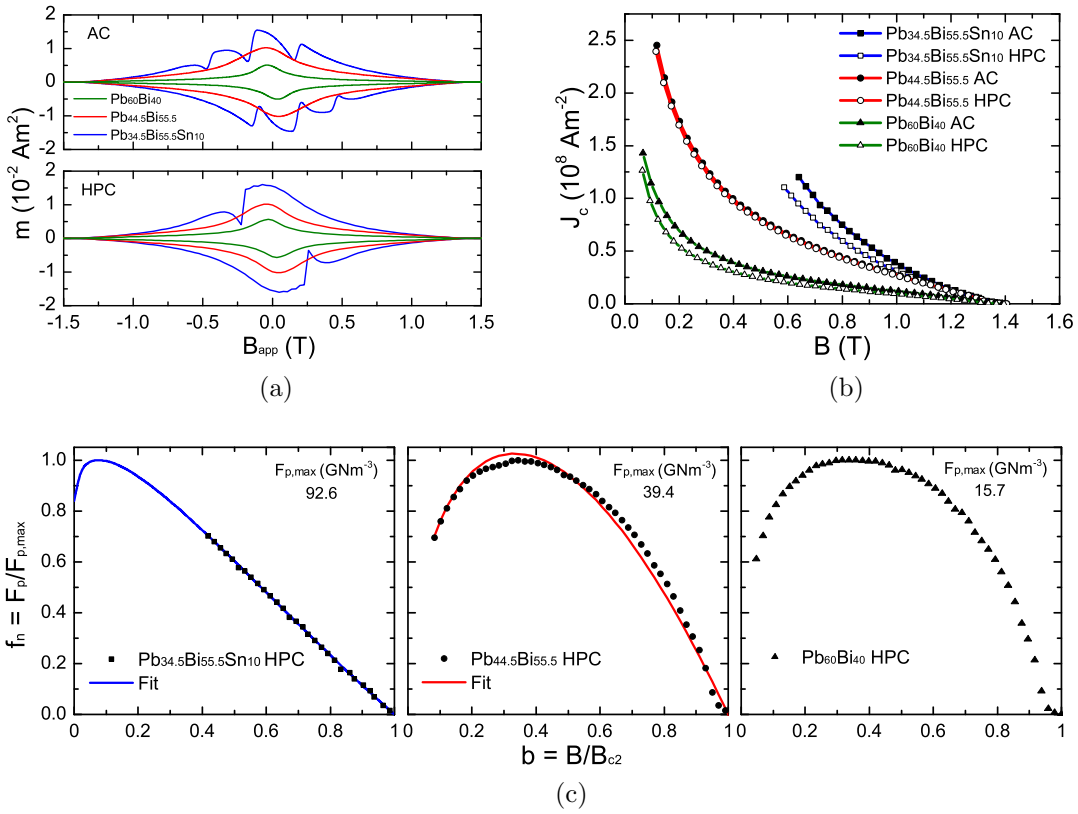

Figure 4.11: (a) Magnetic hysteresis loops measured for both air cooled (AC) and hot plate cooled (HPC) Pb-based solders at 4.2 K. Flux jumping is evident for the PbBiSn sample. (b) Critical current density versus magnetic field (self field corrected) extracted from (a). (c) Normalised pinning force versus reduced field for the HPC samples at 4.2 K. The fitted curves are discussed in the main text.

Secondly, it can be seen from Figure 4.11b that cooling rate also has a small effect on J_c, and in each case the hot plate-cooled samples have slightly lower J_c values than the air-cooled samples. This is understandable since annealing tends to cause growth of the Bi particles, reducing the density of ϵ/Bi interphase boundaries and thus diminishing flux pinning [60]. PbBiSn shows the largest difference in J_c between the air-cooled and hot plate-cooled samples of $\sim$20 %. However, this can be partially attributed to these samples being the first tested. The others underwent one or two more days of annealing at room temperature before being tested, over which time the microstructural influence on J_c is expected to have further reduced. Overall, unless joints are quenched from the melt (which has not been considered here), it is not expected that moderate differences in cooling rate will have a large influence on joint critical current.

Solder composition has the strongest permanent influence on J_c, and broadly speaking increases with the amount of normal material in each sample. Pinning mechanisms in each sample have been evaluated by fitting the Dew-Hughes expressions presented in [16] to the pinning plots shown in Figure 4.11c. As also found by Coote et al [60], pinning in the two-phase PbBi eutectic specimen is well fitted by the expression for magnetic pinning of vortices at the surface of large normal particles (in this case presumably the Bi particles):

$$F_p = A_0 b^{1/2}(1-b) \tag{4.5}$$

with $A_0 = 1.05 \times 10^8\,\mathrm{Nm}^{-3}$. This expression exhibits a peak at a reduced field $b = 0.33$, in excellent agreement with the measured peak at $b = 0.32 \pm 0.02$. Although temperature was not varied here, Coote et al [60] showed this fit to apply to their eutectic specimen at all measured temperatures from 4.5 to 8.1 K.

Although there is no peak in the pinning plot for PbBiSn (due to the restricted measurement range caused by flux jumping), the available data are well reproduced by a sum of Equation 4.5 and the following expression for core volume normal pinning:

$$F_p = A_1(1-b)^2. \tag{4.6}$$

with relative strengths $(A_0) = 1.03 \times 10^8\,\mathrm{Nm}^{-3}$ and $(A_1) = 0.78 \times 10^8\,\mathrm{Nm}^{-3}$. This suggests that almost all of the enhancement in pinning compared with the PbBi eutectic is provided by the core volume normal mechanism. Chemical analysis of the two specimens (shown previously in Figure 4.8d) also suggests that both samples contain an almost equal fraction of Bi particles (36 – 38 vol.%), whilst the PbBiSn sample

contains an additional 20 vol.% of SnBi precipitates. It is therefore suggested that the additional core volume normal pinning contribution is provided by the SnBi precipitates seen in the EDX maps.

Pinning in the $Pb_{60}Bi_{40}$ sample is not well fitted by this expression, or indeed any physically reasonable sum of Dew-Hughes expressions. This is investigated in greater depth in Section 4.3.

Overall, given that PbBiSn had the highest J_c of the three samples, the poor performance of PbBiSn joints seen by several authors [35,53] is not thought to be associated with inferior bulk superconducting properties (assuming the same microstructures are found in their joints as in this solder). However, since ∼60% of the solder volume is non-superconducting, it is possible that solidification of non-superconducting Bi and Sn(Bi) phases could be preferentially nucleated at the filament surfaces, electrically isolating the filaments from the superconducting ϵ phase (as suggested but not investigated by Swenson and Merkiewicz [53]). This raises an important factor for the development of new Pb-free solders – that interactions of the solder with the filaments must be considered.

A final remark should also be made on flux jumping and the consequences for the thermal stability of joints. The PbBiSn sample exhibited significant flux jump events, and although the PbBi samples measured here were stable, flux jumping is common in highly irreversible PbBi alloys [57]. Whilst the differing thermal properties and pinning mechanisms will cause the intrinsic stabilities of the solders to differ, the flux jumping of the PbBiSn solder seen here may well be a simple consequence of its higher J_c values. This is evident from a reduction in flux jump events seen for the air cooled sample, which had a slightly lower J_c than the hot plate cooled sample.

Joints are commonly embedded in a pot of solder several cm^3 in size, all of which may become magnetised if the joints are unshielded. Flux jumps in these large bulks should therefore be considered as a potential source of thermal instability.

4.3 Commercial $Pb_{60}Bi_{40}$

The soldered joints investigated in this study were made with a commercial $Pb_{60}Bi_{40}$ solder of 3N purity obtained from 5N Plus (UK) LTD. In order to analyse the performance of these joints, it was necessary to obtain a complete set of solder $J_c(B,T)$ and $B_{c2}(T)$ measurements over a wide temperature range. In this section a set of detailed

magnetic measurements are presented on a sample of ideal geometry for which a confident analysis could be made.

4.3.1 Sample Preparation

A number of pellets were first melted in an alumina crucible on a hot plate at 300°C. The clean metal underlying the surface layer of dross was cast into a ϕ10 mm Cu mould, and subsequently extruded using a Hounsfield tensometer into a smooth ϕ2 mm rod. A 2.5 mm long cylinder was cut from the rod with a diamond saw to obtain a cylinder of well defined geometry with the ideal size for the MPMS. The cylinder's precise dimensions were measured to be 2.00 x 2.51 mm with vernier callipers, for which the self-field parameters were then calculated as was discussed in Section 3.3.

The sample was mounted into an MPMS straw as shown in Figure 4.12. A 4 cm length of straw was folded carefully along its length, and the cylinder was laid lengthways in the groove and secured with a 4 cm length of Kapton tape. The folded straw with sample attached was then inserted into a standard straw, holding the sample axially in the applied field. A standard 4 cm scan length was employed, and so the supporting structures were almost undetected. This became the standard mounting method employed by the group for solder samples.

The sample was tested after 0, 30 and 90 days at room temperature following extrusion, to ensure that temporary changes to the pinning properties imparted by the casting and extrusion processes had disappeared.

4.3.2 Superconducting Properties

4.3.2.1 $B_{c2}(T)$

$B_{c2}(T)$ was measured primarily by the m-T technique, measuring the superconducting onset temperature in various applied fields. A typical m-T data set is provided in Figure 4.13a. Measurements were also taken from the reversible magnetisation calculated from m-B hysteresis loops (which are presented later in Figure 4.14a). $B_{c2}(T)$ values measured by both the m-T and m-B methods are plotted in Figure 4.13c, falling on the same curve.

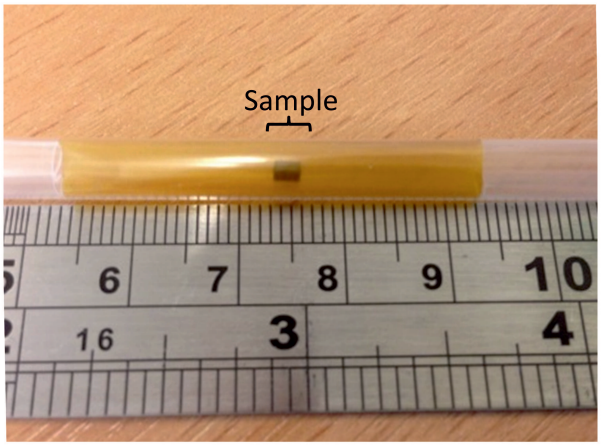

Figure 4.12: Photograph of the solder sample mounted in a straw for MPMS measurement

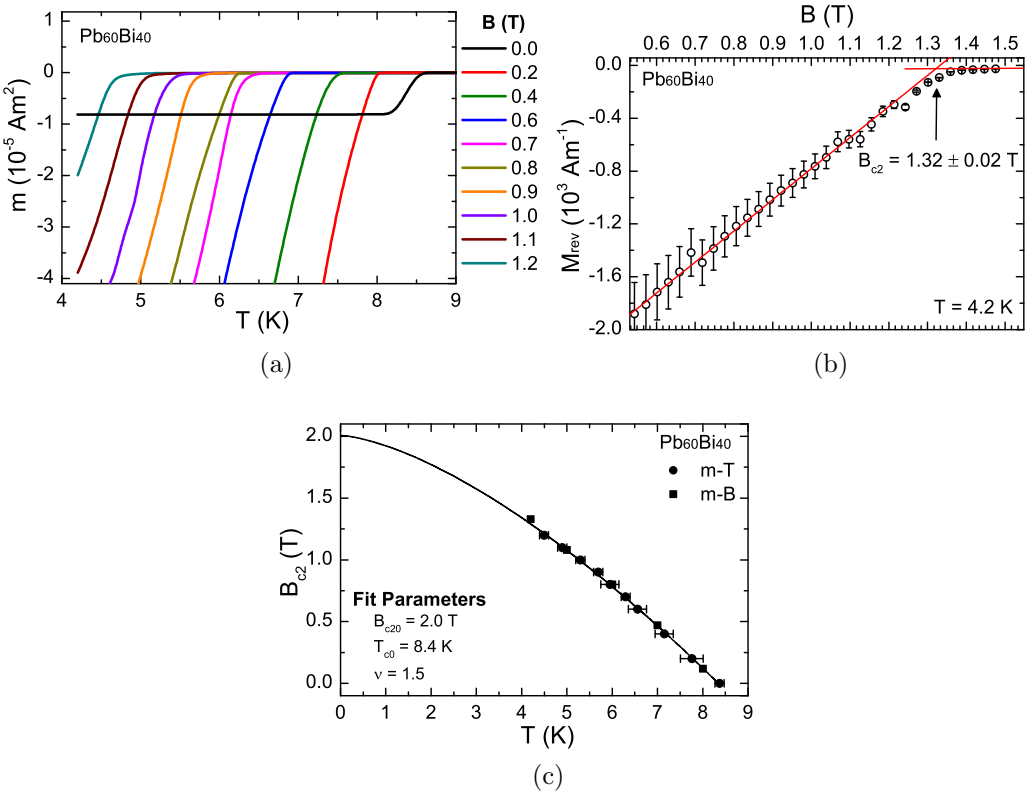

Figure 4.13: Upper critical field measurement for the commercial $Pb_{60}Bi_{40}$ sample (30 days aged). (a) Magnetic moment versus temperature (m-T) in background fields of up to 1.2 T. (b) Reversible magnetisation measured from the mid-point of quadrants 1 and 4 of a 4.2 K hysteresis loop (m-B), indicating precise B_{c2} measurement. (c) Upper critical field as a function of temperature, extracted from both m-T and m-B measurements.

$B_{c2}(T)$ is well fitted by the WHH expression with parameters $B_{c20} = 2.0\,\mathrm{T}$, $T_{c0} = 8.4\,\mathrm{K}$ and $\nu = 1.5$. Pb-Bi alloys can be regarded as dirty for Bi concentrations in excess of $\sim$6 wt.% (for which $\kappa > 2$) [59], and so this value of ν is understandable for this 40 % Bi alloy. As expected, $B_{c2}(T)$ remains constant over time, having a value of $1.32 \pm 0.02\,\mathrm{T}$ at 4.2 K in excellent agreement with Evetts and Wade's value of 1.33 T. This shows that the chemical composition of the superconducting ϵ phase is equilibrated. The pinning properties were however found to change over long timescales.

4.3.2.2 $J_c(B,T)$

Detailed five-quadrant magnetic hysteresis loops were measured at temperatures between 4.2 and 8.0 K after annealing at room temperature for 0, 30 and 90 days following extrusion. Self field corrections were performed and $J_c(B,T)$ values were extracted with a typical error of a few percent, dominated by uncertainty in the measured moment. As will be shown in the discussion to follow, flux pinning in the sample falls over time and the measurements made after 90 days appear to be representative of an equilibrated microstructure. The hysteresis and J_c data measured after 90 days of annealing are provided in Figures 4.14a and 4.14b respectively. These are expected to be representative of the solder properties in real joints (assuming identical microstructures are found), and so these measurements have been employed in the analysis of joints later in the thesis.

In order to better understand the relationships between microstructure and flux pinning in this alloy, pinning plots have been produced for this sample at various stages in the annealing process and at multiple temperatures, as will now be discussed.

4.3.2.3 Flux Pinning

Figure 4.15a demonstrates the annealing characteristics of the extruded sample, showing hysteresis loops and associated pinning plots measured at 4.2 K after 0, 30 and 90 days of annealing at room temperature. For reference, pinning data from the hot plate-cooled $Pb_{60}Bi_{40}$ sample discussed previously in Section 4.2.3 is also plotted. The pinning forces were normalised to the peak values in each curve, and these values have been plotted as a function of ageing time in the inset.

It can be seen from Figure 4.15b that the casting and extrusion process (used to produce a sample of ideal geometry) had the effect of temporarily increasing the

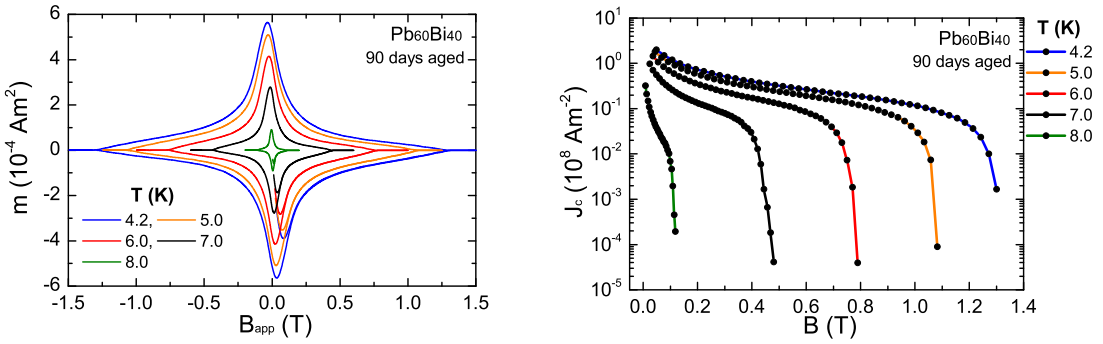

(a) (b)

Figure 4.14: (a) Magnetic moment versus applied field at various temperatures for the $Pb_{60}Bi_{40}$ sample after 90 days of ageing at room temperature. (b) Critical current density as a function of magnetic field (self-field corrected).

degree of pinning in the sample by a factor of ∼3 over the hot plate-cooled value. Over the subsequent 90 days spent annealing at room temperature, the pinning strength gradually returned to exactly the hot plate-cooled value, which appears to be an equilibrium level.

The normalised pinning curves ($fn(b)$) for each ageing time and for the hot plate-cooled sample form a universal curve, indicating that the fundamental pinning mechanism(s) are unchanged by the extrusion and subsequent annealing processes. Similar annealing behaviour was seen by Campbell et al [14,58] for a eutectic PbBi specimen, and the reduction in pinning was caused by growth and spheroidization of the Bi precipitates (seen in SEM micrographs), both of which reduce the density of ϵ/Bi interphase boundaries. The reduction of pinning with time at room temperature for my sample is expected to have been caused by similar annealing of the Bi microstructure, although no attempts were made to monitor this process under the microscope. Campbell also states that cold work at room temperature has little influence on the Bi particles, and changes J_c by less than 10 %. It is therefore likely that the enhanced J_c in the cast and extruded sample investigated here was caused by the rapid solidification upon casting into the Cu mould (producing a finescale array of Bi particles) rather than by the extrusion.

These annealing characteristics are strong evidence that the Bi precipitates are the dominant source of flux pinning in this sample, and since they occupy more than 20 vol.% of the specimen, this seems a reasonable assumption. However, it is therefore surprising that the pinning curves for the $Pb_{60}Bi_{40}$ sample tested here bear little resemblance to the pinning function in Equation 4.5 which provides such a good

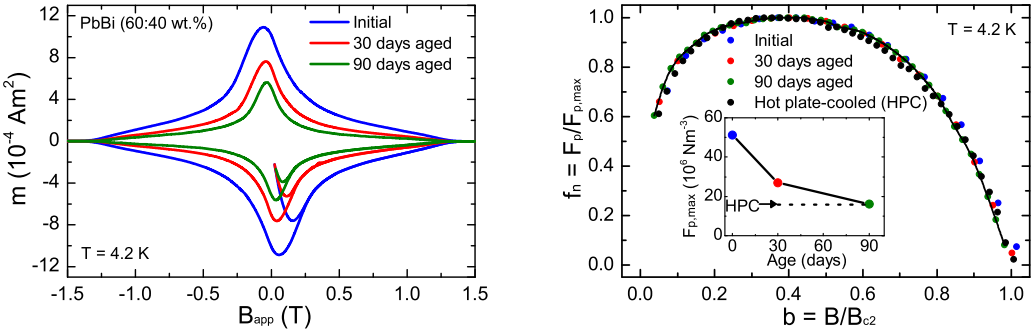

(a) (b)

Figure 4.15: (a) 4.2 K magnetic hysteresis measurements taken for the $Pb_{60}Bi_{40}$ sample after room temperature ageing for 0, 30 and 90 days after extrusion. (b) Shows the normalised pinning force as a function of reduced field for each of these curves, in addition to that measured for the previously discussed hot plate-cooled $Pb_{60}Bi_{40}$ sample. The line is a guide to the eye. The peak pinning force ($F_{p,max}$) versus sample age is also provided in the inset, which slowly falls back to the hot plate-cooled (equilibrium) value.

description for the eutectic alloy. The 4.2 K curves in Figure 4.15b exhibit a broad peak centred around $b = 0.40$ which can only be reproduced to some extent if there is a dominant contribution from point $\Delta\kappa$ pinning:

$$F_p(b) = A_3 b^2(1-b). \tag{4.7}$$

However, this is thought to be physically unreasonable given the relative weakness of $\Delta\kappa$ pinning over normal pinning, and that diffusion in these materials is so rapid that structural defects and chemical inhomogeneities are rapidly eliminated. Calculations by Campbell suggest that structural defects such as dislocations provide a negligible pinning contribution in PbBi alloys [14]. Why then cannot the pinning plots be reproduced by functions associated with normal particles?

To investigate this further, the temperature dependence of pinning in the sample is considered, and plots are provided in Figure 4.16. These data relate to measurements made after 90 days of ageing, however identical forms were found at all stages of the annealing process. The data points for which self field corrections were most significant are indicated by the hatched areas and should therefore be most heavily scrutinised. It is clear that as temperature is increased, the form of $f(b)$ changes. The curve evolves from a rounded shape to being much broader and flatter, and there is a gradual shift of the main peak towards lower reduced fields, reaching $b \approx 0.1$ at 8.0 K.

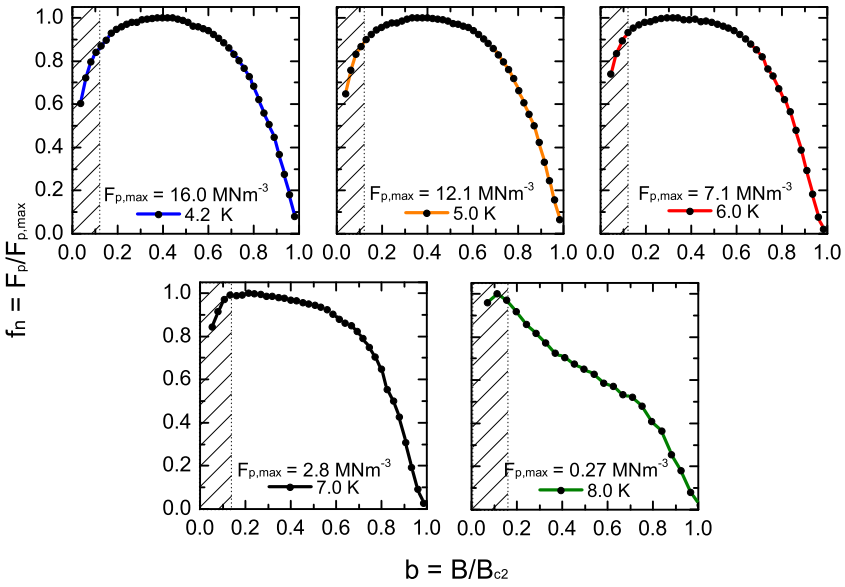

Figure 4.16: The normalised pinning force (fn) in the 90 days aged PbBi sample as a function of the reduced magnetic field at temperatures from 4.2 to 8.0 K. There is an evolution of the pinning function with temperature. Data points within the hatched areas were subjected to the largest self field corrections and should be treated with caution.

At this point its validity becomes questionable due to the importance of self-field effects. At 8 K, the plot is highly asymmetric.

Without a convincing fit to these curves, only qualitative comments can be made regarding the potential causes of this behaviour. One possibility is that multiple mechanisms are at play in this alloy. This is known to cause peak broadening, and the inability to describe the data by a direct summation of basic pinning functions may be due to rigidity of the flux lattice, which can prevent all pinning centres being employed [16]. The temperature dependence however is not easily explained without a $\Delta\kappa$ mechanism.

Another possibility is the influence of particle size on elementary pinning interactions, as is discussed in full by Campbell [58]. For normal particles of size comparable to the flux lattice spacing ($\lesssim 1\,\mu m$ at 1 T), there is a loss in effective pinning force due to flux lattice rigidity, which prevents flux lines being pinned independently on both sides of a single particle. At larger particle sizes, vortex energy variation in the neighbourhood of the particles is less abrupt, and again there is a reduced pinning efficiency as a result. It is evident from the SEM micrographs in Figure 4.8a that in the $Pb_{60}Bi_{40}$ sample there is a wide range of particle sizes from $\sim$10 μm to less than

100 nm. It is plausible that complex interactions of the flux lattice with particles in different size ranges may be distorting the field dependence of the overall pinning force. Since different field ranges are sampled at different temperatures, this could give a temperature dependence to $fn(b)$. This could be investigated in further work by annealing the samples at temperatures just below their melting point, which would homogenise the Bi particles and allow any differences in the pinning properties to be ascertained.

4.4 InSnBi

Alongside the work on joints, other members of the research group (led by T. Mousavi) were investigating Pb-free superconducting solders for magnet applications [70], to which this work made a minor contribution. Searching predominantly within the In-Sn and In-Sn-Bi systems, the alloy showing the highest $J_c(B,T)$ was $In_{50}Sn_{35}Bi_{15}$ (weight %). It was of interest to produce and test a joint with this InSnBi solder, which was carried out and the results are presented later in Section 6.1.5. In order to analyse the results it was necessary to characterise the superconducting properties of the solder under the same test conditions as the joint. A bulk solder sample was therefore extracted directly from the solder bath in which the joint was produced, leaving no ambiguity regarding any differences in composition of the jointing solder compared with the sample tested by T. Mousavi. Full microstructural analysis was also carried out on the solder sample. In this section, the microstructural and superconducting properties of this bulk InSnBi sample are presented.

4.4.1 Sample Preparation

The solder used to produce the joint was made from raw components of In (4N), Sn (3N) and Bi (4N) from Advent Research Materials (UK). The components were weighed out in appropriate proportions to a total mass of 20 g, melted down in a small alumina crucible in air and held at 350 ^{o}C for 30 mins. At this point the joint was produced in the solder bath by the solder matrix replacement method. In brief, two Sn-coated NbTi filaments were submerged in the molten solder for 10 mins (coating the pair in solder), before removing them from the bath and allowing the solder coating to solidify, forming a rudimentary joint.

An MPMS sample was then made from the remains of the solder bath. The extruder was unavailable at the time of this experiment, and so a 2 mm diameter Cu mould was manufactured to allow samples of a suitable size for magnetic measurement to be produced. Casting the solder into the mould yielded a very smooth and uniform ingot from which a ϕ2.13 x 2.65 mm cylinder was sliced. An identical sample was sliced for microscopy. Magnetic measurements took place 2 days after casting, and microscopy was performed around a week after casting, over which time the sample was stored at room temperature.

4.4.2 Microstructure

The ternary In-Sn-Bi phase diagram is shown in Figure 4.17a, with the measured composition of the sample tested here indicated. A transverse cross section of the sample was inspected in the Zeiss Merlin SEM, at an accelerating voltage of 10 kV. The results of chemical analysis on the sample are tabulated in Figure 4.17b. EDX phase maps at both low magnification (representative of the entire sample) and high magnification are provided in Figures 4.17c and 4.17d respectively.

The overall composition was confirmed to be accurate to within 1 %, and thus negligibly altered by the jointing process that was carried out in the solder bath before casting. The sample has a three-phase microstructure consisting of a majority β phase of composition $In_{67}Sn_{23}Bi_{10}$ (pink/purple in the phase map), in addition to γ phase of composition $In_{35}Sn_{51}Bi_{14}$ (blue in the phase map) and $In_2Bi(Sn)$ of composition $In_{53}Bi_{41}(Sn_6)$ (orange in the phase map). The final microstructure is consistent with the solidification process expected from the phase diagram. The first liquid solidifies at $\sim$95 ^{o}C to form $\beta + \gamma +$ Liquid. This produces the β/γ stripes seen in Figure 4.17c. As the sample cools further, this solidification continues and the composition of the remaining liquid follows the liquidus line towards the ternary eutectic point E1. Here the remaining liquid at the β/γ interface undergoes ternary eutectic solidification to form $\beta + \gamma + In_2Bi$ in close proximity, as shown in Figure 4.17d.

The microstructure in these low melting point alloys ages very rapidly at room temperature (stabilising typically within a week at room temperature [70]). Microscopy was performed approximately a week after sample preparation, and the microstructures found are very coarse compared to those found in an air cooled sample investigated by T. Mousavi. The images presented here are therefore thought to represent a mature stage in the thermal ageing process.

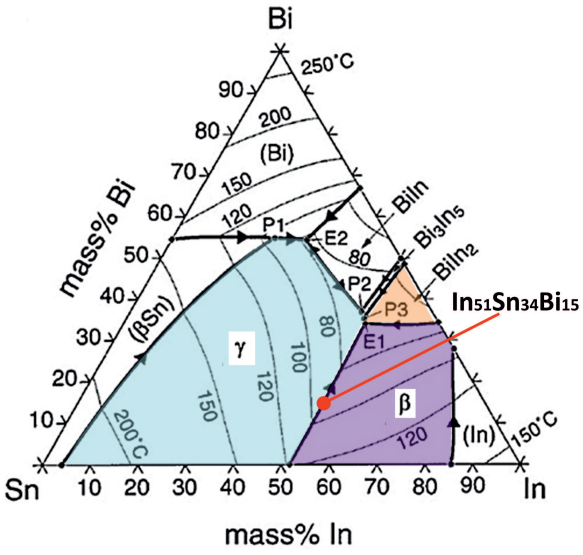

(a)

Sample	Measured Composition (wt.%)	Phase	Map	Phase Composition (wt.%)	Phase fraction (vol. %)
$In_{50}Sn_{35}Bi_{15}$	51/34/15	β - InSnBi		67/23/10	51
		γ - InSnBi		35/51/14	28
		In_2Bi(Sn)		53/41(6)	21

(b)

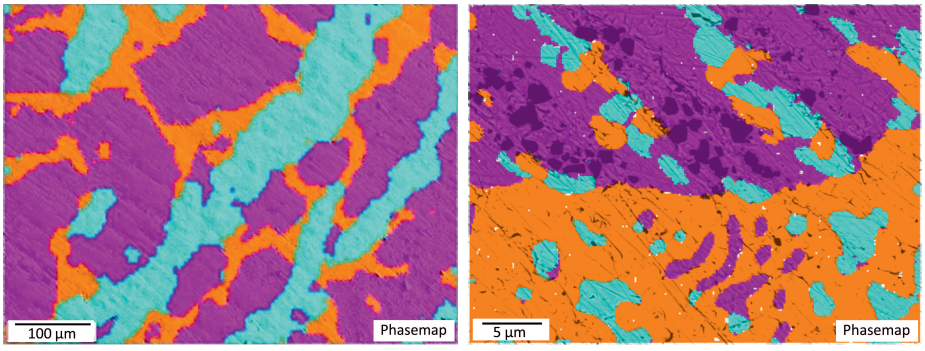

(c) (d)

Figure 4.17: (a) Calculated liquidus projections and isotherms of the ternary In-Sn-Bi phase diagram, reproduced with permission from [93]. The measured composition of the InSnBi sample under investigation is indicated. (b) Overall composition and phase chemistry of the sample, obtained by EDX analysis. (c) Low magnification EDX phase map typical of the entire sample. (d) High magnification EDX phase map at a typical β/γ interface. The black marks are pores filled with polishing media.

Finally it should be commented that the β phase was found to be porous. These pores became filled with polishing media during sample preparation and appear as black marks in Figure 4.17d. The cause was not investigated however has been discovered in many In-based solders studied by the group.

4.4.3 Superconducting Properties

The binary Sn-In [70,94–96], Bi-In [94] and Bi-Sn [95] systems have all been reported on in the literature, and it is known that the β, γ and $BiIn_2$ phases are all superconductors. The superconducting properties of each depends upon their precise phase chemistry, including the solute content of any ternary additions. Superconducting parameters are not available for the precise ternary phase compositions found in the sample tested here, however some representative figures can be quoted. $BiIn_2$ has a T_c value of 5.6 K [94]. In the Sn-In binary system, the γ phase was found to have T_c values ranging from $\sim$3.6 – 5.1 K for In contents ranging from $\sim$16 – 31 wt.%, whilst the β phase was found to have T_c values ranging from $\sim$5.9 – 6.7 K for Sn contents ranging from $\sim$24 – 35 wt.% [70]. The solder composition under investigation here was selected so as to produce a majority β phase, since this had the best superconducting properties. The air cooled solder sample tested by T. Mousavi had an overall T_c value of 6.9 K and a B_{c2} value of 0.18 T at 4.2 K, and these are expected to represent the properties of the majority β phase which has a composition similar to that of the present sample.

4.4.3.1 $B_{c2}(T)$

$B_{c2}(T)$ was measured by the standard m-T and m-B methods. However, due to features of the hysteresis loops that were not found for any other samples tested in this thesis, the various measurements were inconsistent and require some discussion.

Plotted in Figure 4.18a are portions of hysteresis loops measured at 4.2, 5.0 and 6.0 K, focussing on the transition to the normal state. The full hysteresis loops are presented later in Figure 4.19a, and the peak hysteresis width is around two orders of magnitude larger than the scale shown here. On close inspection of the superconducting to normal transition, it is clear that the hysteresis width drops abruptly to almost zero at a considerably lower field than that at which the moment drops to the background level. These fields are labelled B_{c2} and B_{c3} respectively in the figure, for reasons that will now be made clear.

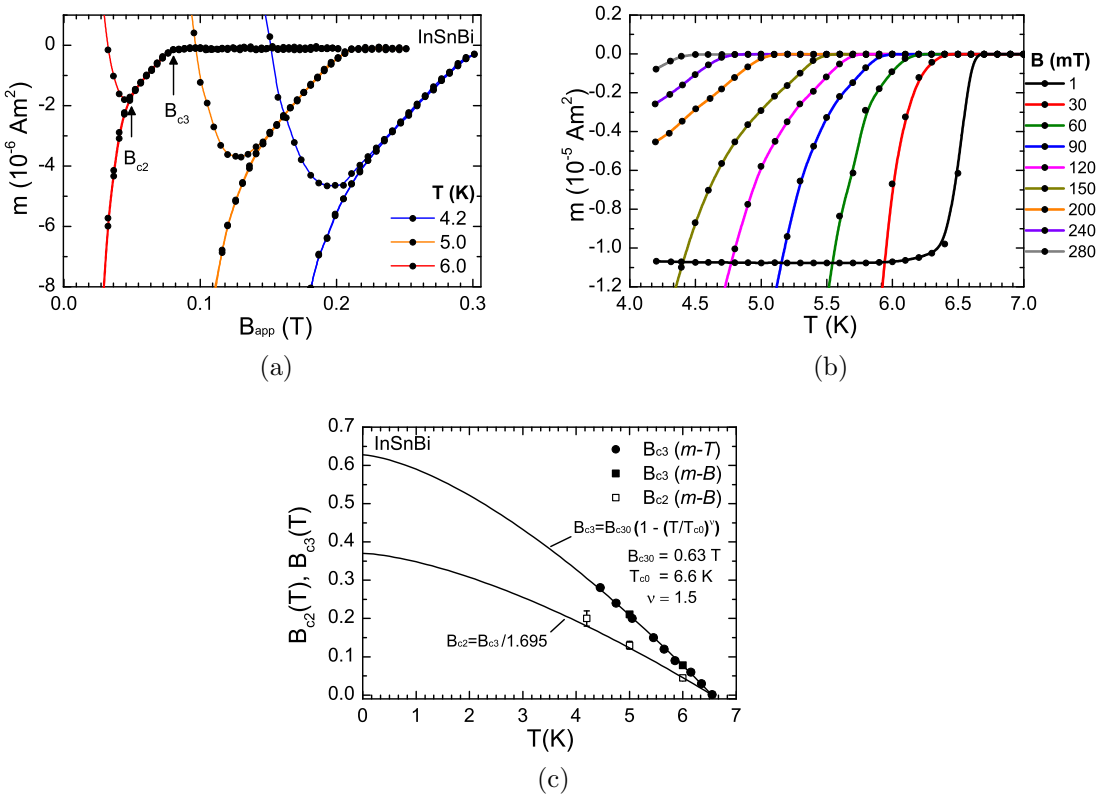

Figure 4.18: (a) Magnetic hysteresis loops (m-B) for InSnBi at various temperatures, showing seemingly reversible behaviour at fields between the values labelled B_{c2} and B_{c3}, as discussed in the text. (b) Magnetic moment versus temperature curves measured in various applied background fields. For this sample, the onset temperatures correspond to B_{c3} rather than B_{c2}. (c) $B_{c3}(T)$ and $B_{c2}(T)$ values extracted from m-B and m-T measurements. Fits to the data are explained in the main text.

A few possible explanations were considered. The first was the onset of thermal depinning of flux lines at an irreversibility field B_{irr}. This is commonly seen in HTS materials, and although also found in LTS materials, B_{irr} and B_{c2} are ordinarily indistinguishable. It is unlikely that this mechanism could produce a field gap as large as that found here. Furthermore, it is also possible that the hysteresis width is not truly zero in the seemingly reversible portion, but merely below the resolution of the magnetometer. Such behaviour has been found previously by Campbell et al [14] in measurements made on highly reversible PbBi samples, however subsequent transport measurements showed that there was in fact a finite critical current over the entire field range.

The second explanation considered was that the field at which the hysteresis loop closes represents B_{c2} of the majority phase, beyond which one of the other two phases continues to superconduct. The fields at which the hysteresis loop closes are indeed consistent with the B_{c2} values expected for the β phase, however since the γ and $BiIn_2$ phases are expected to have inferior superconducting properties they cannot explain the remanent superconductivity well beyond B_{c2} of the β phase.

The most plausible explanation is that there exists a significant surface current which persists up to a surface critical field (B_{c3}). It was shown by James and de-Gennes [97] that for fields applied parallel to the surface of a type-II superconductor, superconductivity can persist beyond the bulk B_{c2} up to a value of:

$$B_{c3} = 1.695 B_{c2}. \tag{4.8}$$

Measuring the ratio B_{c3}/B_{c2} from the hysteresis loops in Figure 4.18a yields values of 1.6 ± 0.1 and 1.7 ± 0.1 at 5.0 K and 6.0 K respectively. These are in good agreement with the 1.695 theoretical figure, supporting the theory of surface currents persisting up to B_{c3}. It is thought that this effect was significant in the InSnBi sample due to the mirror-like surface of the cast ingot, whilst other samples such as PbBi and Nb were extruded or machined to size, producing a microscopically roughened surface.

Provided in Figure 4.18b are m-T curves measured at various background fields. The onset transition temperatures are plotted in Figure 4.18c alongside B_{c2} and B_{c3} measurements from the hysteresis loops. It is clear for this sample that the m-T method provides a measure of B_{c3} rather than B_{c2}, highlighting the importance of employing multiple methods to ensure that results are consistent and thus reliable.

The important figure for joints is B_{c2}, since surface currents cannot contribute to current transfer between joined filaments. However, measurement accuracy of B_{c2}

is relatively poor due to the background signal provided by the surface currents, and furthermore only three values are available. On the other hand, $B_{c3}(T)$ could be measured with considerable accuracy, and is well fitted by the WHH expression with parameters $B_{c30} = 0.63\,\mathrm{T}$, $T_{c0} = 6.6\,\mathrm{K}$ and $\nu = 1.5$. $B_{c2}(T)$ was therefore fitted by dividing the fit for $B_{c3}(T)$ by 1.695, which modifies only the fit prefactor to $B_{c20} = 0.37\,\mathrm{T}$. The fitted curve passes through the measured values within one error bar, and yields a value of 0.18 T at 4.2 K, in agreement with the value measured by T. Mousavi.

4.4.3.2 $J_c(B,T)$

Shown in Figure 4.19a are hysteresis loops measured for the InSnBi solder at 4.2, 5.0 and 6.0 K. Also plotted is the b_{app}^{peak} line from self field analysis, showing that the asymmetry of the loops is associated with the sample's shape, which is accounted for in the analysis.

The self field corrected $J_c(B,T)$ data are presented in Figure 4.19b. The values measured here are in agreement with measurements by T. Mousavi to within ∼50 %. Exact agreement would not be expected due to slight variation in actual composition, differing casting methods used and the time between casting and measurement (i.e. thermal histories). Thermal ageing characteristics were not investigated for this air-cooled solder due to time constraints, and these values may fall with time as the microstructure grows at room temperature. These values should be taken as indicative, but their field and temperature dependence are not expected to change.

At the lowest fields in the plot, the J_c values measured here are comparable to those of $Pb_{60}Bi_{40}$, which is certainly promising. However, the field dependence is significantly worse due to the much lower B_{c2} value for InSnBi (∼0.18 T at 4.2 K) than PbBi alloys (∼1.3 T at 4.2 K). As a benchmark performance requirement, J_c(1.0 T, 4.2 K) of $Pb_{60}Bi_{40}$ is also indicated in the plot. It is clear that for InSnBi joints to exhibit a similar performance to the industry standard PbBi joints, they would have to be shielded to a much higher degree, maintaining the field below ∼0.1 T. However, even if it were possible to completely shield any external field on the joint, the self field of the current passing through the joint may itself be a limiting factor. For a conductor carrying a current I, which is shared equally between N filaments of diameter d_f, the self field at the surface of each filament is given by:

$$B_{\mathrm{self}} = \frac{\mu_o I}{\pi d_f N}. \tag{4.9}$$

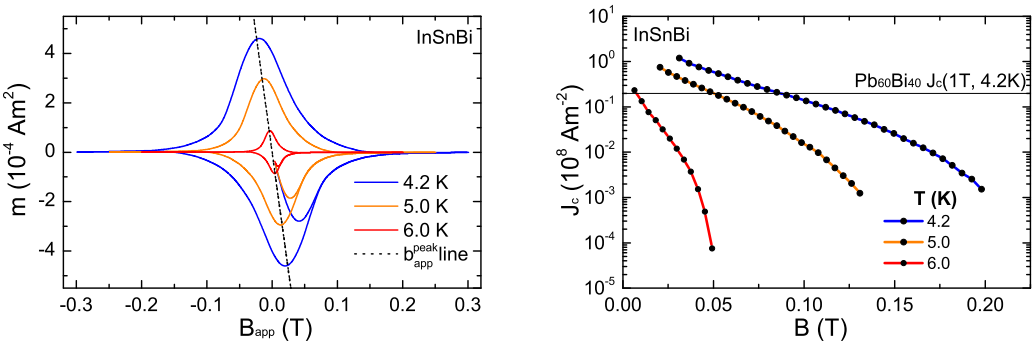

(a) (b)

Figure 4.19: (a) Magnetic hysteresis loops measured for the InSnBi solder at various temperatures. (b) Critical current density versus magnetic field, with self field corrections applied. The $J_c(1.0\,\mathrm{T}, 4.2\,\mathrm{K})$ value of $Pb_{60}Bi_{40}$ is indicated as a technological benchmark.

The maximum supercurrent (I_{max}) that could pass through the joint is therefore the value at which this self field equals the value of B_{c2} for the solder at the surface of the filaments ($B_{c2,\mathrm{solder}}$):

$$I_{max} = \pi d_f N \frac{B_{c2,\mathrm{solder}}}{\mu_o}. \tag{4.10}$$

We note that this limit is independent of joint length and cannot be improved by simply expanding the joint dimensions. At 4.2 K an InSnBi joint between the 200 μm NbTi monofilaments used in this thesis would be limited to just 90 A in self field. The suitability of this solder in magnet applications would therefore depend upon the filament dimensions of the wire to be joined, but is likely to be too low. This emphasises the need for solders with sufficiently high B_{c2} values, which is aside from the need for high J_c.

4.4.3.3 $F_p(B,T)$

Finally, pinning forces were extracted from the J_c data in Figure 4.19b. Since they did not exhibit any common peaks, each curve was normalised to the value of the pinning force at a reduced field value of $b = 0.5$. These data are presented in Figure 4.20a. The field range over which self field effects are appreciable is indicated by the hatched region.

The pinning curves at each temperature largely conform to a universal curve that is well fitted by the Dew-Hughes expression for core volume normal pinning ($fn \sim (1-b)^2$). The expression provides an excellent fit to the data at 4.2 K and

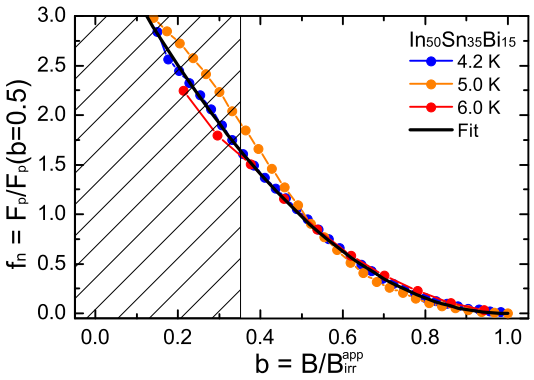

Figure 4.20: Normalised pinning force as a function of reduced magnetic field at each temperature, with normalisation values quoted.

6.0 K, however there is a small degree of deviation in the 5.0 K curve. This occurs over the entire field range and is not associated with any self field effects. Introduction of additional Dew-Hughes functions did not improve the fit and therefore does not suggest a root-cause for this additional pinning component.

The spread in superconducting properties of the constituent phases may be the cause of the this complex behaviour. It is possible that the γ phase is normal in almost all of the measurements, providing the majority of normal pinning measured. The deviation in the 5.0 K curve might be explained by a superconducting-normal transition in the $BiIn_2$ phase (with $T_c = 5.6$ K) at an intermediate field on this curve. Without measuring the superconducting properties of each phase individually, little more can be said.

4.5 Niobium

Nb is a candidate crimping material in cold-pressed NbTi joints due to its chemical compatibility with NbTi and moderate superconducting performance at 4.2 K. In this project bulk, annealed Nb of 3N purity from Goodfellow (UK) was used to produce numerous cold-pressed joints between NbTi filaments.

Superconductivity in Nb has, of course, been widely studied, and factors such as chemical purity and thermomechanical history are known to influence its superconducting properties [98]. A fundamental investigation of links between chemical, microstructural and superconducting properties are certainly beyond the scope of this

investigation. Nevertheless, in order to understand the role of Nb as a current carrying material in joints, the superconducting performance of the same material used to make these joints must be characterised.

A sample was therefore put through the standard set of m-B and m-T measurements from which $J_c(B,T)$ and $B_{c2}(T)$ were acquired. These results are now presented.

4.5.1 Sample Preparation

The Nb was supplied in the form of a ϕ5 mm rod, and so a solid cylinder was turned on a lathe to the standard size employed for MPMS measurements. The measured dimensions of the sample were 1.94 mm in diameter by 2.54 mm in length. The cylinder was cleaned in acetone and mounted axially in a plastic straw in the same fashion as for the solders.

4.5.2 Superconducting Properties

The superconducting properties of this sample were measured using the SQUID-VSM rather than the MPMS used for the other bulk samples. The measurement sequences employed were largely unchanged, but the ability to rapidly change field, sweep the temperature and measure the moment allowed the measurements to be carried out with far greater precision.

4.5.2.1 $B_{c2}(T)$

Presented in Figure 4.21a are m-T curves measured at various fields. Temperature was swept continuously at a typical rate of 1 Kmin^{-1} whilst measuring the moment once per second, generating very densely populated m-T curves. $B_{c2}(T)$ values were extracted from the onset temperatures and plotted in Figure 4.21b. Additional points measured from the field values at which hysteresis loops closed (m-B), measured at temperatures from 4.3 K to 8.0 K, are also plotted. The two measures differ only very slightly, likely due to minor criterion differences.

The standard empirical expression for B_{c2} was fitted to the curve as indicated. A linear trend is observed over the measured range ($T/T_c \gtrsim 0.5$), which is a standard result of Ginzburg-Landau theory and commonly seen in clean Nb samples [69, 99].

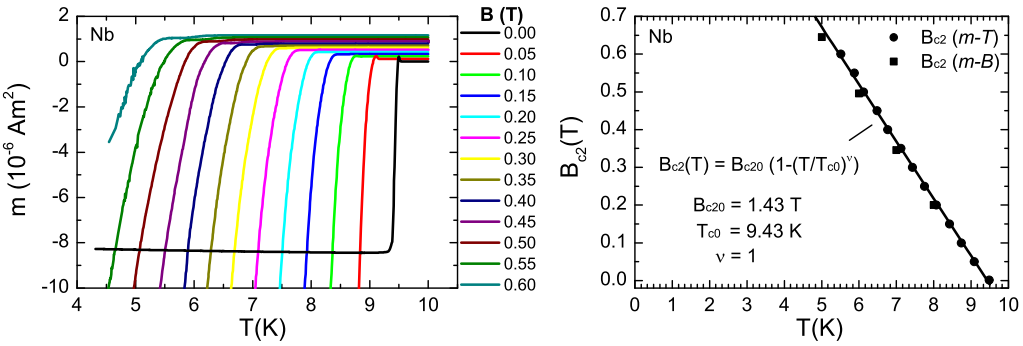

Figure 4.21: (a) Magnetic moment versus temperature (m-T) curves measured at various fields. (b) Upper critical field as a function of temperature measured from the transition onsets in the m-T curves and hysteresis loops (m-B) presented later in Figure 4.22a. A linear trend is observed.

4.5.2.2 $J_c(B,T)$

Presented in Figure 4.22a are magnetic hysteresis loops measured at various temperatures from 4.3 to 8.0 K (the system was unstable at 4.2 K due to a cooling malfunction).

Flux jumping occurred frequently at lower temperatures, which is unsurprising given the sample's reasonably high J_c and mm-scale dimensions. These are not merely a disturbance to the measurement of J_c but also highlight the potential in-field thermal instability of joints made with Nb crimps of several mm^3 in size. Due to the prevalence of flux jumps, the field range over which J_c could be calculated by use of the hysteresis width (Δm) was extremely limited. Quadrant 1 alone was therefore used to extend the field range, neglecting the reversible background, which is small in any case. The measurements were confirmed to be consistent with those taken from the full width at fields where both measures were available.

A similar consequence of the relatively high J_c in these samples is a significant self-field effect – at its peak being ~25% of B_{c2}. This skews the loops along an axis reasonably well predicted once again by the calculated b_{app}^{peak} self field line. In this case the self field corrections and indeed Bean's model itself cannot be employed as confidently as for other samples, due to a violation of Bean's "constant J_c" assumption at low applied fields. Given this uncertainty, J_c measurements are restricted to sufficiently high fields that the self-field is insignificant. The resultant $J_c(B,T)$ data are presented in Figure 4.22b.

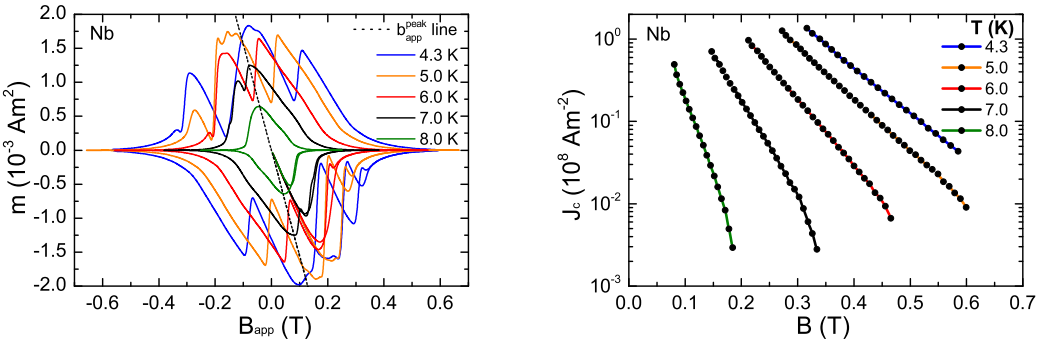

(a) (b)

Figure 4.22: (a) Magnetic hysteresis loops measured for bulk Nb at temperatures from 4.3 to 8.0 K. The b_{app}^{peak} self-field line is also plotted, showing the distortion of loops to be associated with sample shape. (b) Critical current density as a function of magnetic field, extracted from quadrant 1 of the loops in (a). The hysteresis width could not be employed on the most part due to excessive flux jumping in other quadrants.

The linearity of these curves on a semilogarithmic plot indicates an approximately exponential $J_c(B)$ dependence over a limited range of fields. The exact reason for this is not of importance and has not been investigated in detail, however such behaviour is often found for bulk, untextured, polycrystalline materials [100, 101].

4.6 Conclusions

The superconducting properties of all components of the NbTi joints produced in this project have been measured magnetically and were presented in this chapter. The chief performance parameters of all these materials, $B_{c2}(T)$ and $J_c(B,T)$, can now be compiled on single plots to draw some conclusions. These are shown in Figures 4.23a and 4.23b respectively.

This plot highlights the enormous gulf in performance between the NbTi filaments to be joined and the intermediate materials commonly employed to join them. It is clear that the only ways in which such indirect joints are able to support useful currents is by placing them in low field regions of the magnet and by creating large current transfer areas (i.e. reducing the required J) within the joint. Typical NMR joints today operate in fields of up to 1 T, and it is clear from this survey that only the leaded solders are able to facilitate current transfer under such conditions. Whilst novel Pb-free solders are under development to bridge the current performance gap,

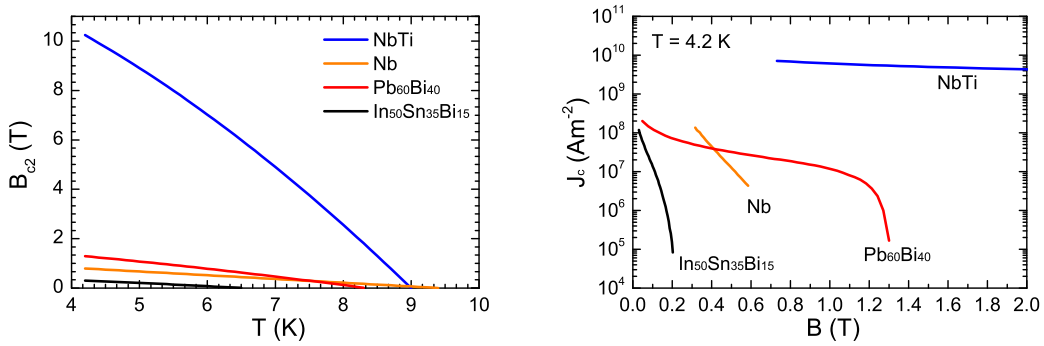

(a) (b)

Figure 4.23: A comparison of the upper critical field (a) and critical current density (b) of all joint materials used in this project.

improvements are required. In particular the B_{c2} values of such solders must be increased to beyond typical self field values for transport currents flowing into the joints.

There are clearly strong performance incentives for producing direct NbTi-NbTi joints, and one of the key research objectives of the remaining chapters of this thesis is to establish the best routes by which these may be achieved.

Finally, a recurring feature of the magnetic measurements made in this chapter has been the prevalence of flux jumping in the samples with higher J_c values. Naively, one may assume that by connecting the two wires with a large mass of high J_c material that joints with a high I_c will be produced. The measurements made here are a stark reminder of the need for thermal stability, which must not be forgotten if the joints are to operate reliably.

Chapter 5

A Novel Magnetic Joint Characterisation Technique

Fundamental studies into the Physics underpinning the performance of persistent mode joints are vital for their development. From the outset of this project a need to measure the superconducting properties of joints fabricated over a wide range of fields, temperatures and voltages was identified, which would ultimately require an inductive resistance testing (IRT) rig – the standard tool for joint testing. It was clear that to build a bespoke IRT rig incorporating a variable temperature sample space, a persistent mode magnet and a high sensitivity field sensor would require considerable cryomagnetic expertise and investment.

It was also realised that the Quantum Design MPMS already contains all three of these features, and that with some modification to the traditional IRT procedure, this may serve as versatile out-of-the-box joint testing kit. After some initial work a first-principles demonstration of the technique was made, which was published as a Fast Track Communication in *SuST* [45]. An associated short article was written by Jan Jaroszynski of the National High Magnetic Field Laboratory (NHMFL) to highlight the usefulness of the technique for fundamental studies into joints [102]. The technique was put to use in this project for characterising a range of NbTi joints, the details of which are discussed in Chapter 6. The present chapter discusses the development of this technique.

5.1 Experimental Concept

The basic concept of this technique is to characterise a small NbTi test coil whose ends are connected by the joint of interest. A schematic of the basic experimental setup is shown in Figure 5.1. The MPMS magnet serves the dual purpose of both inducing currents in the test coil and establishing a background field for the measurements. Under most conditions the joint is a weak link in the circuit and so the current flowing through the test coil is controlled by the joint's superconducting properties. The current in the test coil can be measured as a function of field, temperature and time from the coil's magnetic moment (m) by SQUID magnetometry. In principle this allows for measurement of joint I_c, B_{c2} and V-I curves over the entire superconducting B-T parameter space. Such a comprehensive characterisation would give valuable insights into the fundamental mechanisms operating in the joint.

The two main challenges faced were firstly to manufacture suitable test coils, and secondly to establish appropriate measurement sequences to obtain $m(B,T,t)$ data from which $I_{c,joint}(B,T)$, $B_{c2,joint}(T)$ and V-I curves could be extracted. Unfortunately, measurement of $I_{c,joint}(B,T)$ was not fully achieved due to factors that will be discussed. Sequences producing m-B hysteresis loops, m-T curves and m-t decay curves have all been demonstrated, and are discussed in this chapter.

The chapter begins with measurements of the magnetic field profile in the MPMS, which was a key input to the test coil design which is discussed in the following section. A simple Bean model analysis is then presented, which was constructed in order to qualitatively understand current distribution in the test coil during the various measurement sequences. The m-B, m-T and m-t measurement sequences themselves are then discussed along with the information that can be extracted. Finally, field drift measurements are performed and their influence on m-t measurements is discussed.

5.2 MPMS Field Profile, $B(z)$

The test coils used in this study were required to be several cm in length, and so an important design consideration was the homogeneity of the applied field over this non-standard sample length.

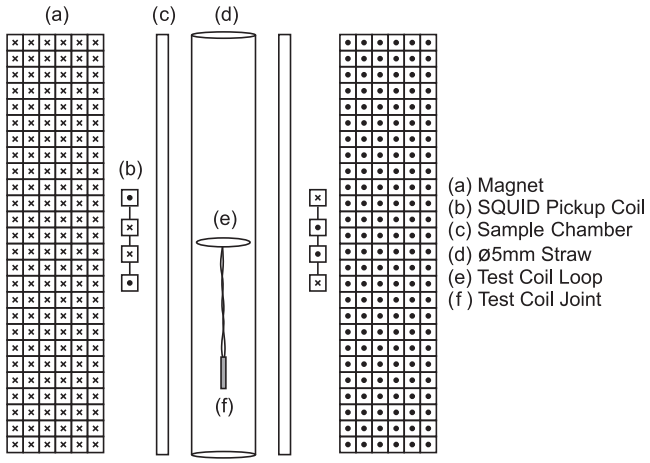

Figure 5.1: Schematic showing the basic experimental setup in which a small test coil, closed by the joint of interest, is loaded into the MPMS for magnetic testing.

Variation in the axial magnetic field (B) along the axis of the MPMS magnet (z) was measured using a Magsys HGM09 Gaussmeter, kindly supplied by Quantum Design LOT, Darmstadt. The device contains a Hall sensor on the end of a 1.2 m long probe that can be inserted into the magnet bore. The field sensitivity ($\delta B/B$) is 0.01 % in fields ranging from 10 mT up to a maximum of 4.5 T.

In order to measure $B(z)$, a simple connector was made to attach the probe to the sample transport head of the MPMS, as shown in Figure 5.2a. The probe could then be moved by as much as 12 cm along z using the stepper motor. The central position in the magnet bore (z=0) was established from the symmetry of the measured field profiles. $B(z)$ profiles were measured at various fields from 0 to 4.00 T.

5.2.1 High Field Profile

For fields larger than ∼0.01 T the profile did not change and is plotted in Figure 5.2b. It was also noted that for each measurement the central field value agreed with the target field value within ∼1.5 %, giving an indication of the uncertainty in field values for this system. Fine scale field inhomogeneity near the centre of the magnet is plotted on a logarithmic scale in the inset. Below $z = 2$ cm any field variation is below the 0.01 % sensitivity limit of the Hall probe. The manufacturer specifies <0.01 % for $|z| < 2$ cm and <0.005 % for $|z| < 1$ cm, which are noted for future reference.

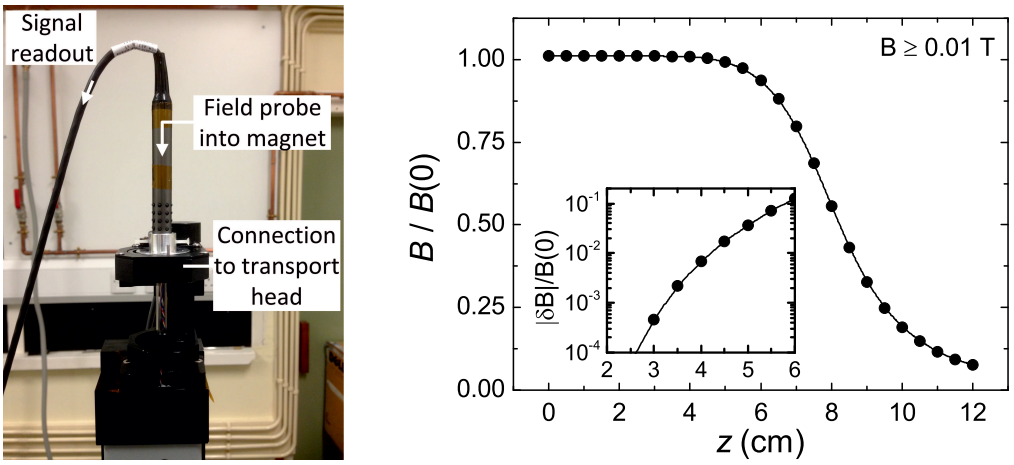

(a) (b)

Figure 5.2: (a) Photograph showing the Magsys HGM09 field probe attached to the transport head of the MPMS. (b) Plot of the magnetic field as a function of axial position (z) in the MPMS. Values are normalised to the central field value and error bars are smaller than symbol size. This profile is applicable for fields greater than $\sim$0.01 T. The inset shows the fine scale inhomogeneity near the centre.

5.2.2 Remanent Field Profile

At fields below $\sim$0.01 T, the profile is distorted by the additional contribution from trapped flux in the magnet windings. The remanent field saturates at $\sim$1 mT when the field is reduced to zero from values in excess of $\sim\pm$1 T, and the profile in this regime is provided in Figure 5.3a. The central field variation is fractionally larger in this regime as can be seen in the inset.

Performing a degaussing operation reduces the remanent field considerably to $\sim$0.065 mT, for which any spatial variations were below the sensitivity limit of the Hall probe. Performing a full magnet reset (partially quenching the magnet) had little extra benefit.

The time dependence of the remanent field in the centre of the magnet was also measured after several minutes of relaxation, as shown in Figure 5.3b. The 1 mT field was found to drift at a rate of -124 ± 1 nT/s. This result is later discussed alongside more comprehensive field drift measurements in Section 5.7.

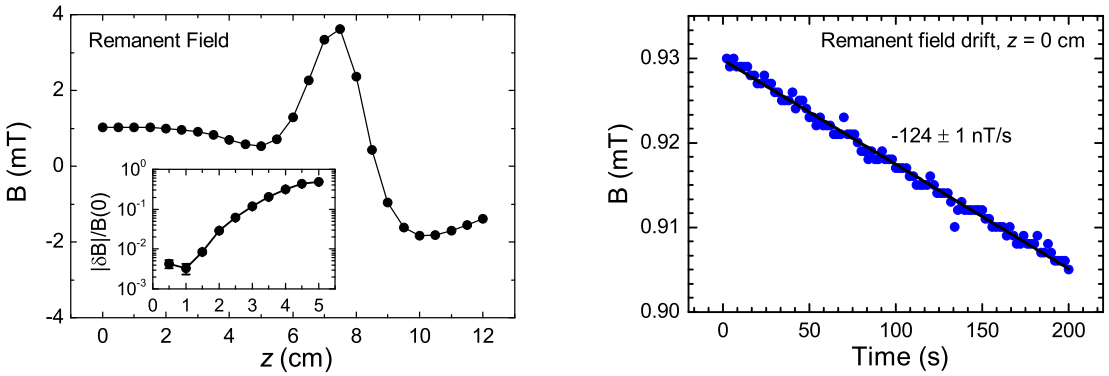

(a) (b)

Figure 5.3: (a) The profile of the remanent magnetic field along the axis of the MPMS after sweeping the field from −1 T to 0 T in *no-overshoot* mode. The inset shows the degree of inhomogeneity near the centre. (b) The time dependence of the remanent field at the centre of the magnet bore after several minutes of relaxation.

5.3 Test Coils

A number of basic test coil designs were investigated, among which the simplest and most reproducible one is pictured in Figure 5.4a. This design was used to test all of the joints discussed in this thesis. The coil incorporates a single turn loop whose axis is parallel to the applied field direction and is shown in greater detail in Figure 5.4b. The wire is wound into a groove in a specially-designed former to give a loop of diameter $D = 4.30 \pm 0.01$ mm between wire centres. The ends of the loop are brought together in a region referred to as the "neck", where the wire is bent through 90^o inside a longitudinal groove as shown. The trailing leads are then twisted to minimise their inductance, and the joint to be studied is made at their ends, closing the coil. This section discusses the key considerations that factored into the final test coil design.

5.3.1 Wire

Importantly for testing in the MPMS, the coil was required to fit inside a standard $\phi 5$ mm sample straw, demanding the use of relatively fine, flexible wire. Monofilamentary wire was chosen in order to simplify the coil and joint geometry, permitting a more detailed analysis of the measured data. Agilent Technologies kindly supplied a suitable spool of 0.4 mm OD wire, whose properties were presented in Section 4.1.

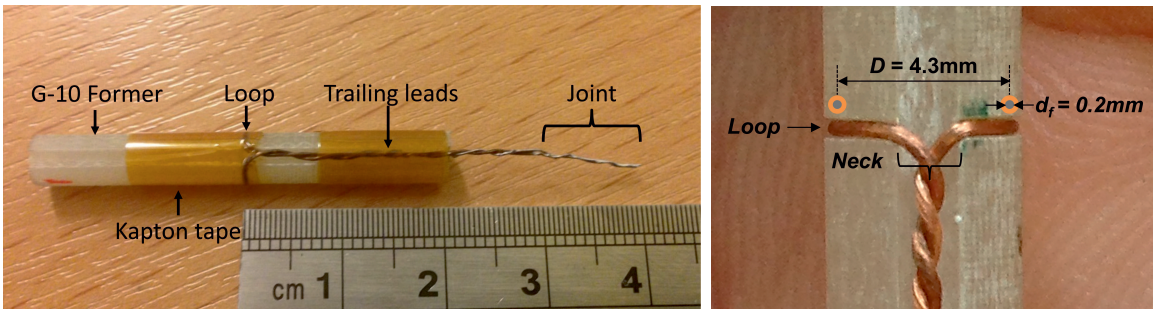

(a) (b)

Figure 5.4: (a) Photograph of a standard test coil wound for magnetic testing of joints in the MPMS. In this case the joint is soldered. (b) A closer view of the loop on a similar test coil, showing its geometry in more detail.

The manufacture of soldered joints required removal of insulation from the entire coil to avoid charring under the intense heat of the solder bath. Therefore, for consistency, all coils were uninsulated.

5.3.2 Formers

The coils were wound onto formers in order to control their geometry and limit wire movement. The chosen material was G-10 owing to its low magnetic susceptibility and ease of machining. The former was made to a length of 4 cm (longer than the 2 cm voltage scan length employed), and thus did not produce a measurable magnetic signal. The coils were bound to the former with Kapton tape.

5.3.3 Loop Geometry

The test coil was required to produce a signal that could be measured by the magnetometer and, in principle, allow the current in the coil to be calculated. As was discussed in Section 3.5.3 the magnetometer acquires voltage scans by extracting the sample through a gradiometer coil, to which an "ideal dipole" function is fitted and a magnetic moment value is calculated. Measurement of accurate current values from these moment measurements requires a host of detailed considerations. Many of these concern the nature of current flow within the wire. Calculation of current values is discussed fully in Section 5.5.1.

Nevertheless, the starting point was to incorporate a loop into the coil which produces a magnetic field approximating that of a magnetic dipole. The simplest way to achieve this was with a single-turn loop as pictured in Figure 5.4b. This was made with as large a diameter as possible to negate the non-dipole field that would inevitably be produced in the neck.

An example voltage scan measured for a typical test coil is shown in Figure 5.5. After standard detrending of the raw voltage, an ideal dipole fit is made automatically by the MPMS. The standard deviation on residuals of the fit is ∼1–2 %. The magnetic moment values generated are expected to have a similar degree of accuracy. However, not all coils are identical and this leads to a spread in measured coil properties, discussed later in Section 5.5.2.2.

It is important to note that an ideal dipole field is produced only for so-called "circuital currents", i.e. currents flowing monodirectionally around a closed coil. Unjointed or "open" coils also produce a magnetic field as a result of so-called "magnetising currents" flowing within the wire itself. As exemplified in Figure 5.5b, open coils do not produce a magnetic dipole field and their voltage scans are highly asymmetric. The MPMS software will record an erroneous magnetic moment value in this case. Nevertheless, this value is proportional to the magnetisation of the wire and remains a useful figure.

5.3.4 Coil Length

Finally, the length of the trailing leads and joints were chosen as an engineering compromise between two factors. As was discussed in Section 5.2 the magnetic field in the MPMS falls with distance along the magnet axis, and therefore it was desirable to minimise the overall coil length. However, since some joints produced a considerable magnetic field of their own it was important to maintain a sufficient loop-joint separation so that this was not detected when scanning the loop.

The final test coils had a 4 cm distance from the loop to the bottom of the joint. Joints containing bulk material were limited to a length of 5 mm. A short voltage scan length of 2 cm was also employed to minimise induction effects from movement of the coil through the inhomogeneous field of the MPMS magnet.

Under these conditions the joints did not influence the measured voltage scans and the average field on the joints was ≤0.5 % below the central field value. The field at

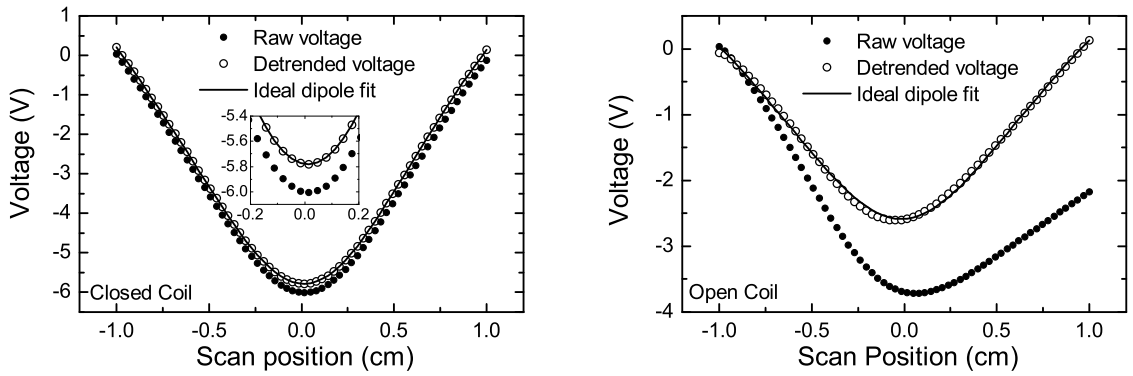

(a) (b)

Figure 5.5: (a) An example of a 2 cm voltage scan measured for a test coil closed by a superconducting joint (spot welded). The filled circles show the raw measured voltages, the open circles show the data after automated linear detrending, and the line is a best fit of the ideal dipole form to the detrended data. (b) Shows the same measurements made on an open coil (no joint), for which the detrending and fitting routine performed by the MPMS is invalid.

the bottom edge of the joint was $\leq$1.7 % below the central field value. This was an acceptable error margin and a large improvement over the long preliminary coils first tested [45], for which the field at the bottom of the joint varied by 55 % of the central field value.

In the following sections, measurements are presented exemplifying the characteristic magnetic response of the test coils to changes in applied field. A simple Bean model evaluation is also presented, which appears to provide a good qualitative explanation for the hysteretic behaviour observed, on the recommendation of Damian Hampshire.

5.4 Hysteresis Loops

5.4.1 A Simple Bean Model

The hysteretic nature of current induction in superconducting magnet windings is well known, influencing both the field produced by a magnet as well as its inductance [103]. Critical state models are a natural choice in modelling current distributions in magnet wires, and have been used widely to calculate field errors, inductance and ac-loss. A comprehensive review of this field can be found in the Ph.D. thesis of C.

Völlinger [104].

In the present work, Bean's model is employed to pictorially describe how magnetic flux is expected to penetrate the wire and joint during field ramping, and how the current distribution in the coil is expected to change as the I_c value of the joint changes with respect to that of the wire. It would be surprising if such a scenario has not been considered previously by others, however no examples could be found in the literature. This may be because in real magnets the joints are not usually the current limiting components and so the present scenario is not relevant.

The coil's geometry has been greatly simplified to a joined split-ring, as sketched in Figure 5.6a. In adherence to Bean's "semi-infinite geometry assumption" the coil is treated as though it extends infinitely along the z-axis (out of the page), such that flux penetration can be treated in a single plane.

This simplified geometry is permissible since only basic qualitative conclusions are drawn from the model. A detailed model for which quantitative calculations may be performed would need to account for the round wire cross section, wire curvature in the neck, and the twisting of the trailing leads. This would be a significant modelling task and was not attempted. Some features of the hysteresis loops measured in this project are suggestive of mechanisms beyond the scope of the simple model presented, and are discussed in Section 5.4.7.

We will firstly consider the simple case of an open coil.

5.4.2 Open Coil

In the case of an open coil (sketched in Figure 5.7a) the magnetic field is able to pass unimpeded to the centre of the loop, and so the fields on the inner and outer surfaces of the wire are equal. Therefore changes in field magnetise the wire in the same manner as for the wire sample magnetically tested in Section 4.1. A sketch showing the pattern of current flow at the open ends of the wire and also the field profile across the wires in the fully penetrated state is shown in Figure 5.7b.

The fully penetrated branches of hysteresis loops measured for an open test coil ($m_{oc}(B)$) are provided in Figure 5.7. Data at low fields and temperatures in which flux jumping was common were removed. It is reiterated that these measurements are *not* true magnetic moment values since the voltage scans are not of the ideal dipole form. Nevertheless these are proportional to the magnetisation of the wire and

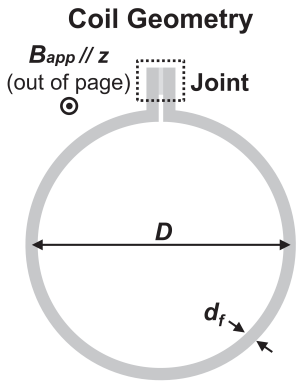

Figure 5.6: The cross section of a simplified coil geometry for which Bean's model is being applied. The applied field (B_{app}) is aligned along z (out of the page), and flux penetration is considered in this cross section only.

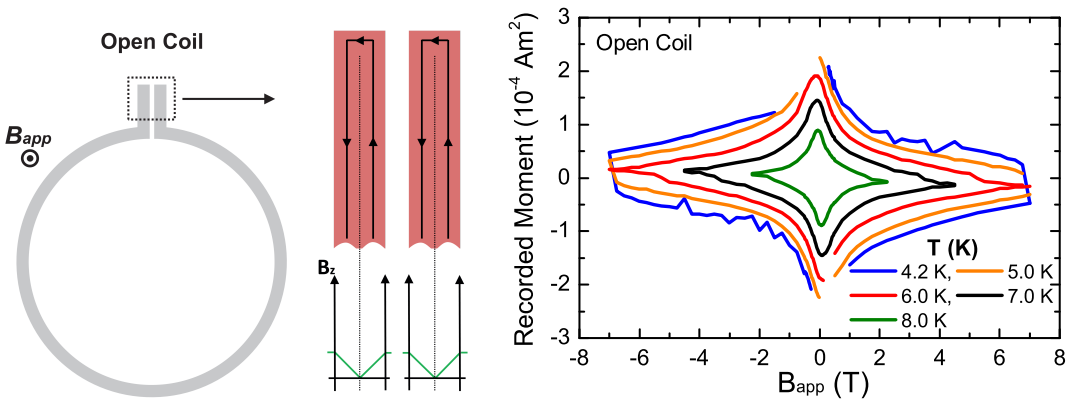

(a) (b) (c)

Figure 5.7: (a) Schematic of the open coil configuration in which the ends of the test coil are not joined. (b) Sketch of the current distribution and magnetic field profile inside the wires at the field of first penetration. (c) Magnetic moment values recorded by the MPMS during hysteresis measurements on an open test coil. These are not true magnetic moment values due to asymmetery in the voltage scans.

form the "zero current" baseline for joint measurements. This varies by ∼10 % for different test coils due to slight variations in geometry. Ideally, one would measure this baseline accurately for each test coil, however this would be very time consuming. We therefore employ the single $m_{oc}(B)$ data set in Figure 5.7 for all test coils, and accept the slight uncertainty in these values.

5.4.3 Perfect Closed Coil

The second scenario to consider is that of an hypothetical "perfect closed coil" formed from a continuous wire loop (as sketched in Figure 5.8a). In this case, flux only enters the inside of the loop by penetrating through the wire, thereby inducing the full wire I_c as shown in Figure 5.8b.

In this case we would expect the coil's performance to be wire-limited, and in the fully penetrated state (approximating the loop to be a complete ring of diameter D), the magnetic moment (m_{pcc}) of the coil would be given by:

$$m_{pcc} = \frac{\pi D^2}{4} I_{c,wire}. \tag{5.1}$$

This has been calculated for the NbTi wire used in this study and the results are plotted in Figure 5.8. $m_{pcc}(B,T)$ defines the maximum moment expected to be produced by the test coil and is a useful reference in joint measurements. However, under most conditions, flux jumping prevents the full induction of $I_{c,\mathrm{wire}}$ in jointed test coils.

5.4.4 Jointed Coil

We now consider the case in which the test coil is closed by a joint whose critical current is smaller than that of the wire. In the context of the simple Bean model presented here, the coil's state is determined only by the respective values of I_c in the joint and wire. Qualitatively similar results are obtained whether the low joint I_c is caused by filament damage or intermediate materials with low J_c.

For demonstration purposes we consider an indirect joint in which the wires are connected over a joint length l_j by a type-II superconducting filler with a critical current density $J_{c,\mathrm{joint}}$ which is smaller than $J_{c,\mathrm{wire}}$, as sketched in Figure 5.9a.

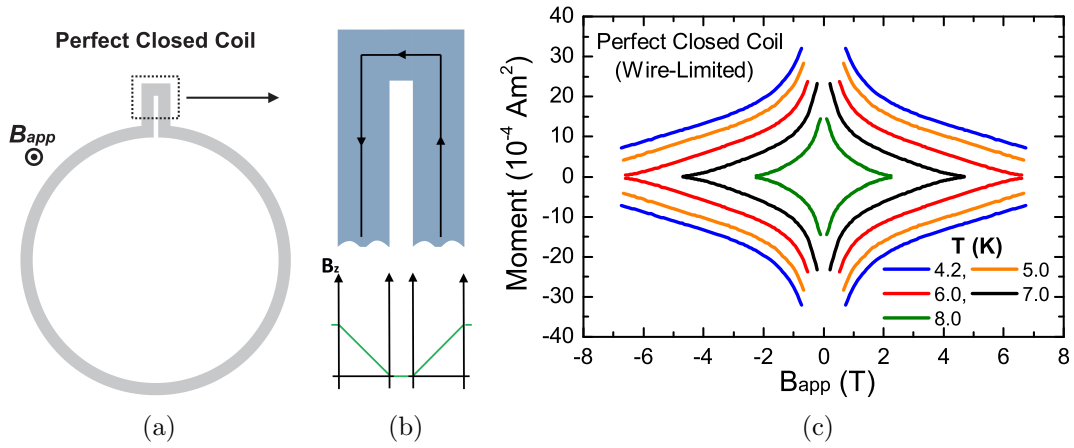

Figure 5.8: (a) Schematic of a perfect closed coil formed of a continuous wire loop. (b) The current distribution and magnetic field profile inside the wires at the field of first penetration. (c) Magnetic moment values expected for a fully-penetrated perfect closed coil, calculated using Equation 5.1 and the $I_c(B,T)$ data measured for the NbTi wire.

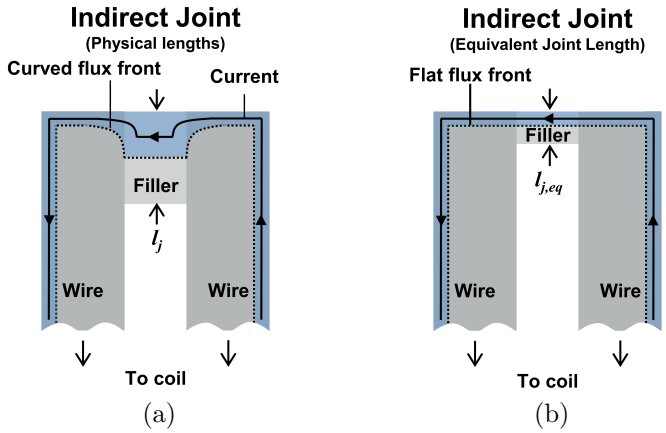

Figure 5.9: A schematic showing flux penetration into an indirect joint in which the wires are joined by an intermediate superconducting filler material over a physical joint length l_j. The flux front is curved at the wire/filler interface owing to unequal J_c values resulting in different penetration rates in the two materials. (b) An equivalent diagram in which both the filler and wires are assumed to have identical J_c values so that the flux front is flat. An equivalent joint length $l_{j,eq}$ is employed to maintain the I_c ratio of the filler to the wire.

Given their different J_c values, Bean's model dictates that for a given change in applied field, flux will penetrate further into the filler than the wire, leading to a curved flux front across the wire/filler interfaces. In order to simplify the diagrams, the wire and filler are instead assumed to have equal J_c values at all fields such that the flux front is flat. To compensate for this, the physical joint length l_j is replaced by an equivalent joint length $l_{j,eq}$, which changes with field. $l_{j,eq}$ is scaled with the wire's diameter (d_f) to maintain the ratio of $I_{c,\mathrm{joint}}/I_{c,\mathrm{wire}}$:

$$l_{j,eq} = d_f \frac{I_{c,\mathrm{joint}}}{I_{c,\mathrm{wire}}}. \tag{5.2}$$

The equivalent joint diagram is provided in Figure 5.9b.

5.4.5 Hysteresis Measurements

With the aid of simple Bean model diagrams, real hysteresis loops measured for jointed test coils can be analysed. Figure 5.10a shows a full five-quadrant hysteresis loop measured at 7.0 K for a test coil closed by a PbBi soldered joint. The open coil and perfect closed coil hysteresis loops ($m_{oc}(B)$ and $m_{pcc}(B)$) are also plotted for reference. At key points in the loop (a–f), further information on the state of the coil is provided in subfigures 5.10(a–f). These include the expected current distribution in the wires and joint, sketched profiles of the magnetic field across the wires, and also the form of the 2 cm voltage scans actually measured, from which the moment values were generated.

As the field is first raised from zero, flux begins to penetrate the wire and joint, exciting a circuital current (I) as shown in Figure 5.10a. Accordingly the voltage scan is symmetric, with just a slight asymmetry due to the coil being off-centre. The induction gradient (dm/dB) during initial charging can be calculated in principle from the loop's geometry, as will be discussed fully in Section 5.5. For closed coils, dm/dB is $\sim$20 times larger than for open coils. The high gradient, as well as the symmetry in the voltage scans, are signatures of circuital current flow and thus a functioning joint.

As applied field is increased further, $I_{c,joint}$ falls whilst I increases. At point (b) the field fully penetrates the joint and $I = I_{c,joint}$ as shown in Figure 5.10b. A local maximum in the magnitude of the coil's moment is measured. The form of the voltage scan remains unchanged.

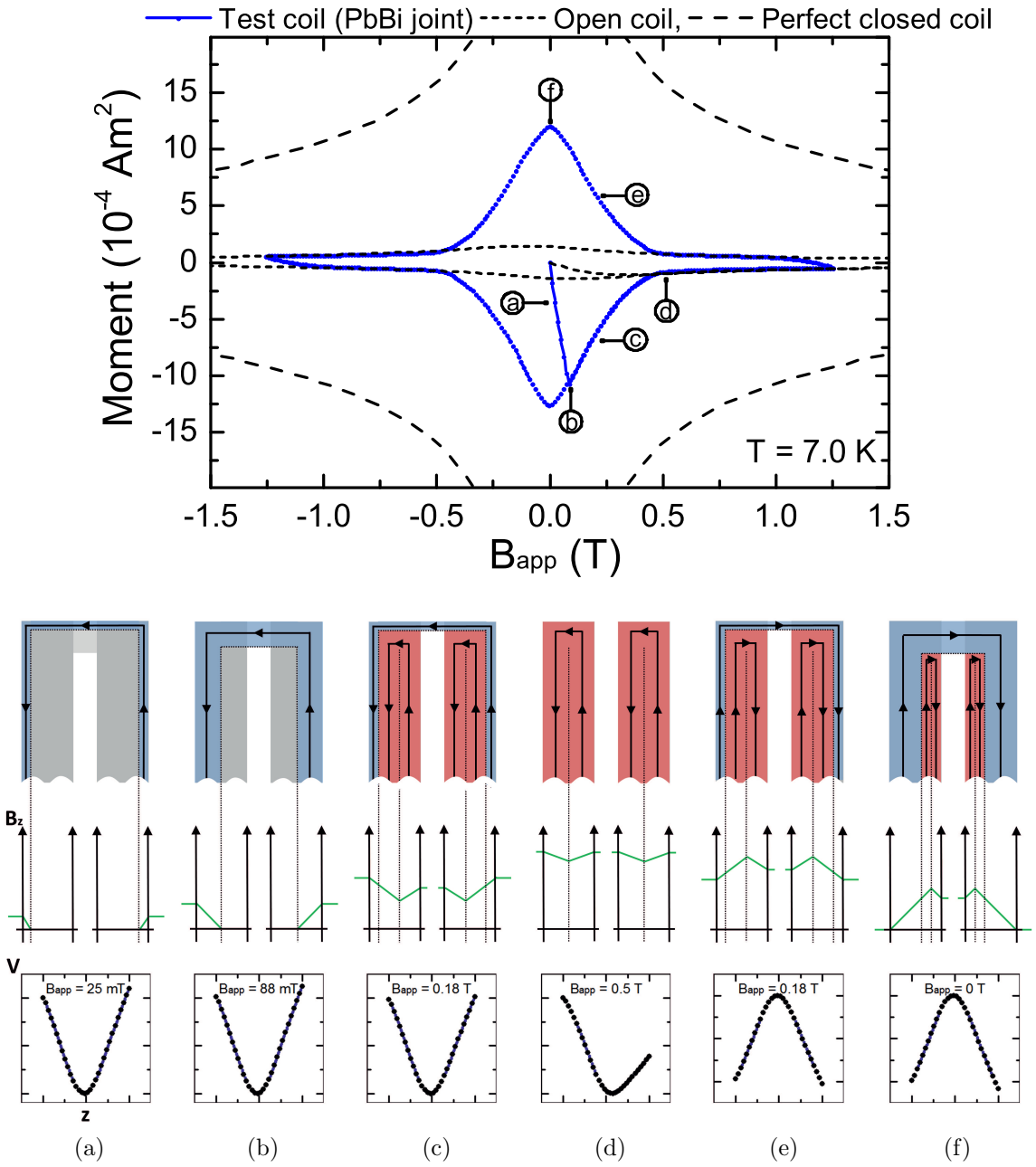

Figure 5.10: A hysteresis loop measured at 7.0 K on a test coil closed by a PbBi soldered joint. Subfigures (a)–(f) provide further information at key points. Top: Bean model sketches showing current flow in the wires and through the joint at various key fields. Middle: sketched magnetic field profiles across the wires. Bottom: 2 cm voltage scans measured by DC extraction of the test coil at corresponding fields (arbitrary voltage scale).

Further increases in field cause I to fall as $I_{c,joint}$ decreases with field, and a fraction of the applied field enters the loop. A magnetising current grows within the wire as shown in Figure 5.10c. The measured moment is now the sum of a circuital component (m_{cir}) due to circuital current flow at $I = I_{c,joint}$ (the quantity of interest), and a magnetising component (m_{mag}) due to magnetising currents. The voltage scan begins to change in form.

At point (d) the field reaches the joint's upper critical field ($B_{c2,joint}$) where $I_{c,joint} = 0$. The wire is now purely magnetised as shown in Figure 5.10d. The measured moment falls to the open coil value and the voltage scan has the asymmetric form of the open coil.

Upon reversing the field ramping direction the magnetising currents in the wire first reverse, and once the field is below $B_{c2,joint}$ a reversed circuital current begins to flow through the joint once more, as shown in Figure 5.10e.

At zero applied field (point (f)), an overall peak moment is measured. Owing to the very small quantity of solder coating the wires in the PbBi joint tested here, there is no measurable peak shift from zero associated with self fields in the joint.

The remaining portions of the loop are measured by ramping into the negative fields and back up to positive fields, obtaining a symmetric loop.

5.4.6 Flux Jumps

Whilst in general at relatively high temperatures of 7 or 8 K the coils were stable, at lower temperatures it was common for flux jumping (quenching) events to occur. A typical example of the observed behaviour is provided in Figure 5.11, which shows a hysteresis loop measured at 4.3 K for the same PbBi soldered test coil. The coil charges up to a current of approximately $I_{c,joint}$, at which point a quench occurs and the coil then recharges again. The same behaviour was found in every coil tested, including soldered, spot welded and crimped joints. Flux jumping near $I_{c,joint}$ suggests that the root cause of the quenching is heat generation in the joint as it reaches its critical current, rather than in the wire elsewhere in the coil.

Further evidence of heat generation in joints is provided in Figure 5.11b, which shows hysteresis measurements made at 6.0 K for a test coil closed by a spot welded joint. The manufacture of this joint will be discussed in full in Section 6.2.1, but in summary, the Cu matrix is etched away and the bare NbTi filaments are spot welded together.

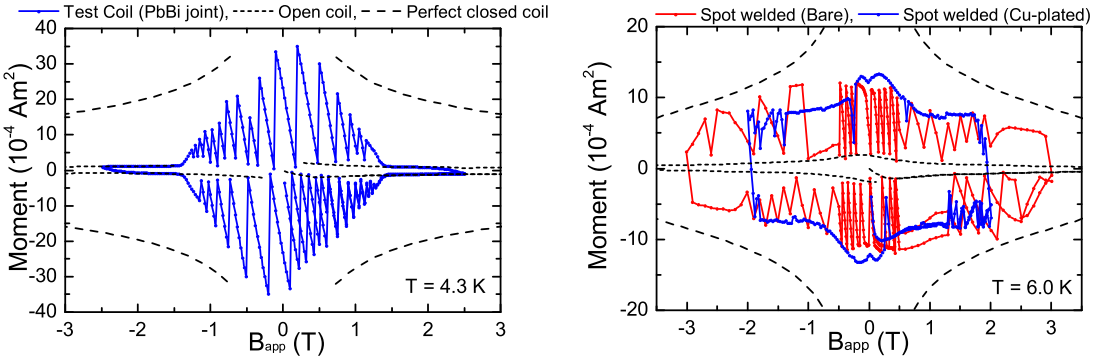

Figure 5.11: (a) An hysteresis loop measured at 4.3 K for a PbBi soldered test coil, showing regular flux jump events. (b) Hysteresis loops measured at 6.0 K for a spot welded test coil before (red) and after (blue) electroplating a Cu layer on the bare NbTi material in the joint.

Flux jumping occurs regularly for the as-made unstabilised joint. A thick Cu layer was later electroplated onto the joint to cover any exposed NbTi material, which greatly improved the stability of the coil. Although Cu stabilisation did not eliminate flux jumping altogether, it is inferred from the improvement that the Cu layer enhanced heat flow away from the joint. Whilst these observations suggest that heat is generated in the joint, we must also bear in mind that heat may flow into the NbTi filaments, and so the wires may still be the location in which the quench begins.

In further work, for the purposes of producing coils that operate stably at low temperatures, it would be advisable to coat all joints in Cu as a standard practice. The use of finer NbTi filaments ($\lesssim 50\,\mu$m) may also enhance the overall stability of the coils.

5.4.7 Anomalous Hysteretic Behaviour

For several joints, such as those given in Figure 5.12, the measured hysteresis loops contained anomalous features, indicating that some additional effects were in play beyond those discussed in Section 5.4.5.

Figure 5.12a shows two hysteresis loops measured at 8.0 K for the spot welded joint before and after applying a Cu plating. Both are asymmetric about the $m = 0$ and $B_{app} = 0$ axes, with the moment measured in the Cu plated loop even becoming negative in quadrant 2 at large negative fields. Both also have peaks in each quadrant,

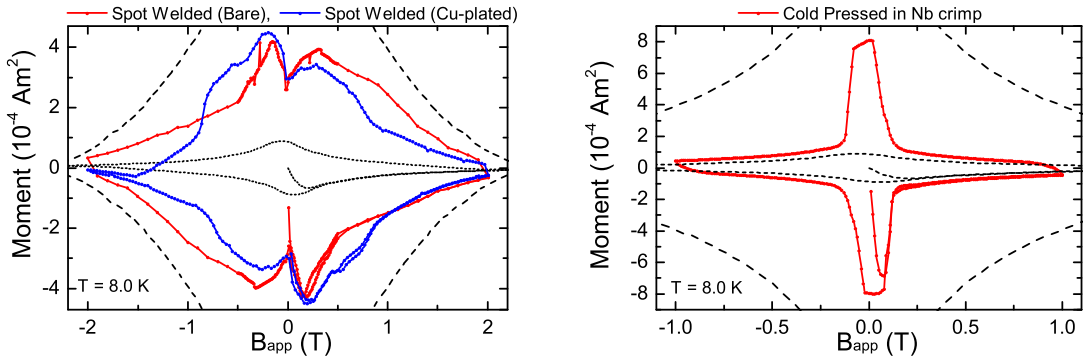

Figure 5.12: Hysteresis loops exhibiting anomalous features. (a) Spot welded test coil at 8.0 K before and after electroplating the joint with Cu. (b) Nb crimped test coil at 8.0 K. The usual perfect closed coil and open coil curves are also plotted for reference.

with the peak in quadrants 1 and 3 being smaller than in quadrants 0, 2 and 4. Furthermore, whilst the basic shapes of the loops are similar before and after Cu plating, the absolute size and shape has certainly been changed by the Cu electroplating process. We should also bear in mind that the joint was physically removed from the measurement system for electroplating, and the change in field angle on the joint when it was replaced may have produced a larger effect than the Cu coating itself.

Figure 5.12b shows a five-quadrant hysteresis loop measured at 8.0 K for a joint in which the filaments were cold pressed inside a Nb crimp. This loop also shows an anomalous plateau near zero field.

Whilst these effects are not fully understood, they do bare some resemblance to the hysteresis loops presented previously in Figure 4.7 in which a NbTi wire was held almost longitudinally in the applied field. These measurements also exhibited similar asymmetries and off-centre peaks in each quadrant. The basic cause in this case was identified to be incomplete flux penetration, resulting from longitudinal shielding currents flowing in the sample. It is plausible that in the case of these joints (both of which contain superconducting bulk material) there is some competition between magnetising currents induced in the joint and circuital currents induced in the loop, and that this results in abnormal hysteretic features. More could be understood of these effects by investigating the dependence of joint geometry and field orientation on the hysteresis loop shape.

5.4.8 $B_{c2,joint}(T)$ Measurement

One important parameter that can be acquired from hysteresis loops at various temperatures is $B_{c2,joint}(T)$ – the field at which $m(B)$ falls to $m_{oc}(B)$. Towards the end of the project a demonstration was made of the ability to measure $B_{c2,joint}(T)$ from m-T sweeps at various background fields (in an analogous fashion to the bulk measurement technique). This was performed only for the PbBi joint discussed in Section 6.1.3 and the full results are presented there. An example measurement demonstrating the technique is provided in Figure 5.13

The coil was cooled to 4.2 K in a field denoted as B_{FC}, before sweeping the field up to the desired background value (B_{BG}) for the m-T measurement. This simultaneously induces a small test current in the coil. For the present example $B_{FC} = 0.95$ T and $B_{BG} = 1.00$ T, generating a moment $m = 7 \times 10^{-4}$ Am^{-2}, which corresponds to a current value $I \approx 48$ A. The temperature is then raised whilst measuring $m(T)$.

Initially the moment falls only slightly as the temperature is raised since $I < I_{c,joint}$. At a certain temperature ($\sim$5 K in this example) $I = I_{c,joint}$ and further temperature rises cause the circuital current to fall with $I_{c,joint}(T)$. Accordingly, as discussed in Section 5.4.5, magnetising currents in the wire grow as the circuital current falls. The critical temperature of the joint ($T_{c,joint}$) is measured where $I_{c,joint}$ falls to zero and $m(T) = m_{oc}(T)$. As temperature is raised further, another transition is seen at $T_{c,wire}$. Repeating the measurement of $T_{c,joint}$ in various background fields allows $B_{c2,joint}(T)$ to be acquired. As will be discussed in Section 6.1.3, the $B_{c2,joint}$ values obtained for the PbBi joint were found to agree well with those measured for the PbBi solder itself, giving some credence to this technique.

5.5 Current Measurement and Uncertainty

The qualitatively similar form of the hysteresis loops to those of bulk samples suggested the prospect of extracting $I_{c,joint}(B,T)$ values from the loops. This information would have enabled a very thorough analysis of joint performance. In this section initially the various problems associated with extracting accurate current values from magnetic moment measurements will be discussed, and several ways proposed in which the measurements could be improved. Secondly, employing a number of simple assumptions and restrictions, basic formulas are presented for calculating current and inductance. Finally, in order to assess the accuracy of these formulas, we use them

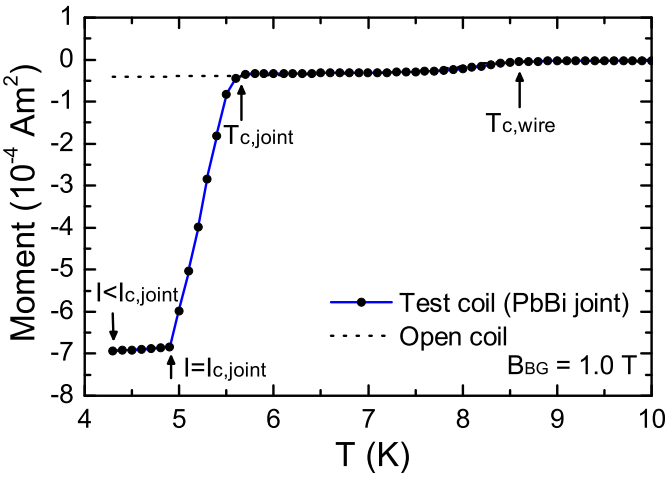

Figure 5.13: Example measurement showing test coil moment as a function of increasing temperature. The coil was cooled in a field value of B_{FC}=0.95 T before raising the field to a background value of B_{BG}=1.00 T. The moment was then measured whilst increasing the temperature. The key features of the data are explained in the main text.

to calculate the expected induction gradient for the coils (dm/dB_{app}), and compare this to measured values observed for real test coils.

5.5.1 Problems with Measurement of Current

5.5.1.1 Moment Measurement

The SQUID magnetometer was originally calibrated by Quantum Design with a Pd cylinder of 3 mm diameter and 3 mm height. Since the test coil diameter is larger than 3 mm, the voltage-to-moment calibration factor will be slightly wrong, introducing an error expected to be of the order of a few percent [105]. Furthermore, the loop is not a complete circle and thus the missing portion of the loop and the field produced by the neck will both distort the voltage scan from the ideal dipole form. Similarly typical errors of a few percent are found for fits of the ideal dipole form to the measured voltage scans.

5.5.1.2 Magnetising and Circuital Currents

As was shown in Section 5.4.5, when the joint is superconducting, the moment values measured for the fully penetrated branches of the hysteresis loop contain both circuital

and magnetising contributions. To measure $I_{c,\text{joint}}$, one must subtract the magnetising contribution, which cannot be done with a measurement of the moment alone. However it may be possible to distinguish open and closed coil contributions at the level of the voltage scan, since the two have characteristically different forms. Whilst this was not attempted here, it may be possible to address in further work.

5.5.1.3 Inhomogeneous Circuital Currents

Even for the simple case of a purely circuital current during charging of the coil, the inhomogeneous "filling up" of current from the outside of wire to the inside of the wire means that the moment-to-current calibration factor is expected to change as a function of $I/I_{c,\text{wire}}$. The same is true of the coil's inductance, which is a well documented phenomenon [48, 49, 103] with implications for IRT measurements. The scale over which the currents can spread is $\sim d_f$, and so the expected error in the moment-to-current calibration factor is $\sim d_f/D$, which is $\sim 5\,\%$ for this coil.

5.5.1.4 Proposed Improvements

Each of these problems would be alleviated by the use of finer wires, which would allow for coils to be made to a much higher precision and a reduced uncertainty due to inhomogeneous current distributions. Monofilaments are commercially available with filament diameters as small as $15\,\mu m$, and so a ten-fold reduction in d_f/D could easily be achieved (providing the filaments can still be handled).

Secondly, it would also be valuable to perform an independent magnetometer calibration for these test coils. This could be performed by using a wired probe to pass known currents around the coil and measure the current-to-SQUID voltage calibration factor during charging. The current capacity of such a probe would likely be limited, and so this would have to be performed at a relatively high fraction of T_c.

Finally, if an independent magnetometer calibration were performed, one may be able to employ an alternative coil geometry that does not require an ideal dipole field. This would be beneficial if such a coil could be made to a higher precision than the present test coil geometry.

5.5.2 A Simple Current and Inductance Calculation

Whilst the above problems must be addressed in order to permit accurate current measurements, we can proceed with some first order analysis by making some simple assumptions. We firstly restrict current calculations to cases in which the current is purely circuital. Secondly we assume that the current flows homogeneously through the wire's cross section. Finally we assume that the coil is a closed circular loop of diameter D between wire centres and filament diameter d_f.

Under these assumptions the current-to-moment relation is simply the product of the circuital current (I) and loop area (A_{loop}):

$$m = I A_{loop} = I \frac{\pi D^2}{4}. \tag{5.3}$$

We can also calculate the coil's self inductance L, assuming this is dominated by the loop. L is defined as the ratio of a change in current flowing in a circuit (ΔI) to the subsequent change in flux enclosed by the circuit ($\Delta\Phi$) [106]:

$$L = \frac{\Delta\Phi}{\Delta I}. \tag{5.4}$$

This is a standard result for a circular loop of round wire carrying a homogeneous current and is given by [107]:

$$L = \mu_o \frac{D}{2} \left[\ln\left(\frac{8D}{d_f}\right) - 1.75 \right]. \tag{5.5}$$

For the present test coil geometry the calculated self inductance is 9.18 nH. This about $1/10^{th}$ that of typical joint testing coils.

5.5.2.1 Calculation of dm/dB

Under the assumed coil geometry, the induction gradient (dm/dB_{app}) of the test coil during charging is a constant that can be calculated. This will be compared with measured values in the following section.

We begin by considering the change in flux enclosed by the loop ($d\Phi$) caused by a change in the uniform background field of the MPMS magnet (dB_{app}):

$$d\Phi = A_{enc}\, dB_{app}, \tag{5.6}$$

where $A_{enc} = (\pi/4)(D - d_f)^2$ is the area enclosed by the loop. Substituting Equation 5.6 into Equation 5.4 we obtain:

$$\frac{dI}{dB_{app}} = -\frac{A_{enc}}{L}, \tag{5.7}$$

where the minus sign is employed because the change in current opposes the change in flux (Lenz's law). We also have that:

$$\frac{dm}{dB_{app}} = \frac{dm}{dI} \cdot \frac{dI}{dB_{app}}. \tag{5.8}$$

Inserting Equations 5.3 and 5.7 into 5.8 yields the desired relation:

$$\frac{dm}{dB_{app}} = -A_{loop}\frac{A_{enc}}{L} = -\frac{\pi^2 D(D - d_f)^2}{8\mu_o\left(\ln\left(\frac{8D}{d_f}\right) - 1.75\right)}. \tag{5.9}$$

Inserting $D = 4.3\,\text{mm}$ and $d_f = 0.2\,\text{mm}$ gives an expected induction gradient of $-2.09\,\text{x}\,10^{-2}\,\text{Am}^2\text{T}^{-1}$. Thermal contraction of the wire and former upon cooling from 300 to 4.2 K is less than 0.7 % and is thus negligible [33]. This value can now be compared with values measured for real coils.

5.5.2.2 Validity Check – Measured dm/dB_{app} Values

We now assess the error in the assumed geometry, which incorporates all of the factors discussed in Section 5.5.1, by comparing the calculated value of dm/dB_{app} with measured values for real test coils.

We begin by considering changes in dm/dB_{app} for a single coil during charging. Whilst the calculated value is a geometric constant, we know that the true value will change during charging due to inhomogeneous current induction [49, 103]. In this regard, flux jumping in the low temperature hysteresis loops was useful, since the induction gradient could be measured over a range of fields, temperatures and currents each time the coil recharged. Figure 5.14a shows dm/dB_{app} as a function of $I/I_{c,\text{wire}}$ for the PbBi soldered test coil at 4.3 K and 5.0 K. Some low field $I_{c,\text{wire}}$ values were extrapolated from the limited available data, and the error of ∼10 % in these extrapolated values is responsible for the spreading of the dm/dB_{app} values with increasing current.

dm/dB_{app} is seen to fall considerably as the wire charges up. The data at both temperatures form a single (approximately linear) curve against $I/I_{c,\text{wire}}$, supporting the idea of current filling up from the outside to the inside of the wire as $I_{c,\text{wire}}$ is

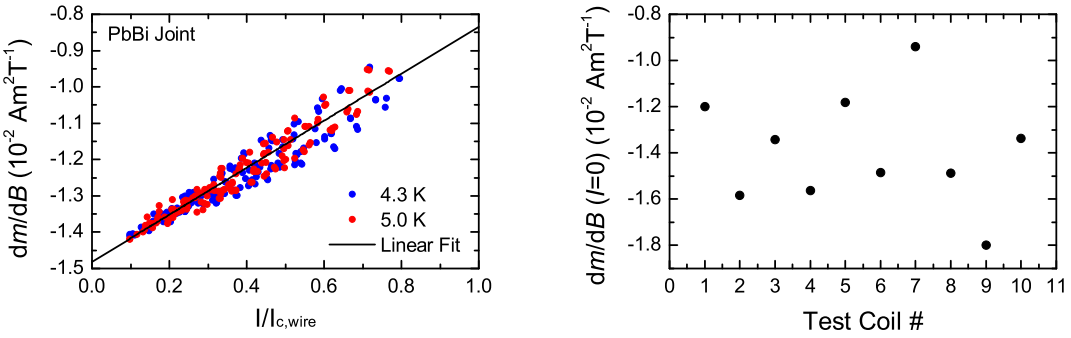

Figure 5.14: (a) The induction gradient as a function of the critical current fraction at 4.3 and 5.0 K for the PbBi jointed test coil. (b) Comparison of the zero-current induction gradients of every coil tested in this project.

approached. Overall, for this coil dm/dB_{app} falls by ∼30 % as the wire charges from 10 % to 80 % of $I_{c,\mathrm{wire}}$. Qualitatively similar behaviour is seen in the other coils.

Secondly we assess the spread in measured values for different test coils, all of which ought to be nominally identical. Figure 5.14b shows the value of dm/dB_{app} at $I = 0$ for all ten of the coils tested in the project. The set has a mean value of $1.4 \times 10^{-2}\,\mathrm{Am^2T^{-1}}$, which is ∼33 % below the calculated value. The standard deviation of the measured values is ∼14 %, showing that there is considerable variation in the geometry of the various test coils.

These measurements suggest that the combined uncertainty in the various aspects of coil geometry are appreciable. Until a full calibration, and perhaps even coil modelling, can be performed, we must accept that we do not have a full understanding of the test coil's geometry and behaviour in response to a uniform applied field and therefore must consider any current values calculated as approximate values. Nevertheless, the hysteresis loops measured are certainly sufficient to provide a first-order measure of joint current carrying ability as a function of field and temperature, and the ability to measure $B_{c2,\mathrm{joint}}(T)$ remains. Hysteresis loop measurement was an extremely convenient and useful analytic tool in characterising a range of joints, as will be shown in Chapter 6.

5.6 IRT Measurements

In this section the IRT technique developed with the aim of measuring joint *V-I* properties in the MPMS will be discussed. In order to obtain a measurement of $V(I,B,T)$, a current must be induced in the coil at a desired background field and temperature, and subsequently monitored over time to obtain an $I(t)$ decay curve. The inductive voltage is measured from the current decay rate using
$V = -L\,\mathrm{d}I/\mathrm{d}t$.

5.6.1 Current Induction

Conventional IRT rigs employ two electromagnets, a small coil for inducing currents in the test loop, and a large magnet for applying a background field to the joint. Current and field can therefore be varied independently. However, in the present case the MPMS has just one magnet and so a field-cooling protocol was devised in order to vary the test current and background field independently. Figure 5.16 demonstrates the sequence employed to perform a set of decay measurements at various currents at a single field and temperature.

The coil is firstly cooled to the measurement temperature in a certain applied field value B_{FC}. The field is then raised to the desired background field value (B_{BG}) in *no-overshoot* mode, inducing the desired moment (m) in the coil, given by:

$$m = \frac{dm}{dB_{app}}(B_{BG} - B_{FC}). \tag{5.10}$$

The induction gradient is measured from hysteresis loops in advance of performing IRT measurements, allowing the required B_{FC} value for a desired m value to be calculated.

The background field is held in the persistent mode whilst the coil's moment is measured over time. Once the $m(t)$ decay curve has been obtained the coil is warmed above T_c (usually to 10 K) to eliminate persistent currents, before proceeding with the next measurement.

As is demonstrated in Figure 5.16, it was standard practice to obtain a decay curve at many currents from zero to the maximum inducible value (i.e. the hysteresis loop value). The intention was to measure the *V-I* characteristics over a wide range of currents without having to wait for very long times for the current to decay into these

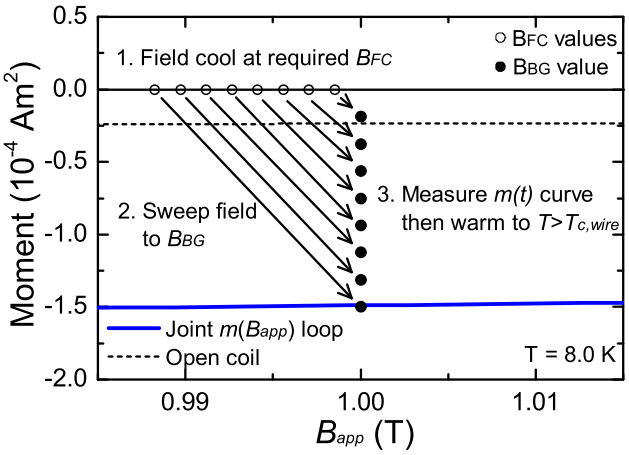

Figure 5.15: Demonstrates the field cooling sequence used to obtain decay curves at various currents at a common background field B_{BG}. This example relates to a spot welded test coil at $T = 8.0\,\mathrm{K}$ and $B_{BG} = 1.0\,\mathrm{T}$. The blue line is the fourth quadrant of the test coil hysteresis loop, which is the maximum inducible moment. The dotted line is the fourth quadrant of the fully-penetrated open coil hysteresis loop.

regimes naturally. Conventionally this approach is often unsuccessful because at low induced currents the voltage due to current settling in the wire tends to dominate the joint voltage for a long time. It was hoped that settling would occur much more quickly in this tiny test coil than in larger conventional IRT coils. In the end, background field drift compromised the low current measurements, as will be discussed in Section 5.6.5.

5.6.2 Decay Curve Measurement – $m(t)$

An example decay curve is provided in Figure 5.16a which was measured for the largest current induced in Figure 5.15. The moment is first measured ∼10 s after the magnet enters the persistent mode, and subsequently measured every 60 s by the standard dc extraction method. Each extraction takes ∼10 s to perform. Although measurements can be made successively, a 60 s gap was maintained so as not to overwork and potentially damage the sample transport head of the MPMS.

The decay measurement is carried out for a relatively short period of 20 mins before moving on to the next current measurement (which takes ∼10 mins to initiate) in order to obtain a reasonable volume of $V(I,B,T)$ data in the available time on the equipment.

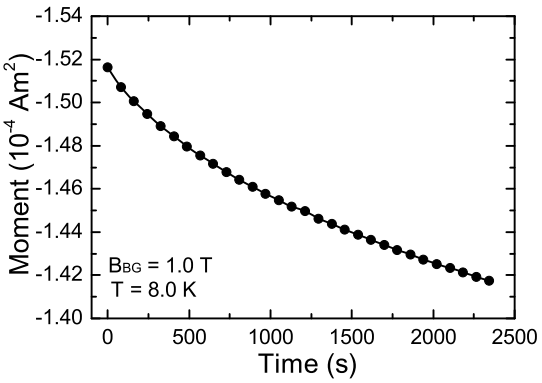

(a)

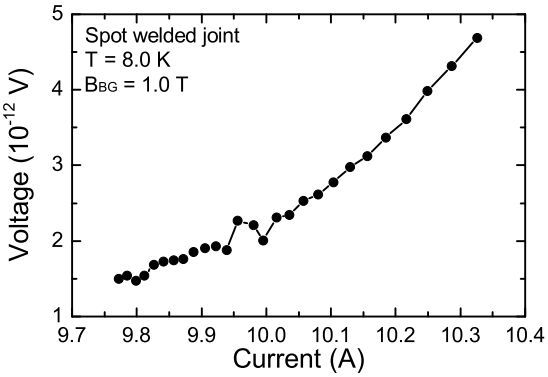

(b)

Figure 5.16: (a) An example $m(t)$ decay curve measured for the largest induced moment in Figure 5.15. (b) Voltage-current curve calculated from the $m(t)$ curve in (a).

The $m(t)$ curve was converted to an $I(t)$ curve by a method that will be described in Section 5.6.3, from which the $V(I)$ curve shown in Figure 5.16b was then obtained using $V = -LdI/dt$. As can be seen, due to the small test coil inductance (fast intrinsic decay rate) the decay measurements permit rapid access to the V-I characteristics at the picovolt level and below, which is the operational regime of persistent mode joints. Despite uncertainty in the absolute values of current and voltage extracted from these curves, such extremely low-level decay rates are sufficient to prove that these joints are truly superconducting.

5.6.3 Converting $m(t)$ to $I(t)$

In IRT measurements the initially induced current is entirely circuital and can therefore be estimated from the moment by Equation 5.3. However, as sketched in Figure 5.17, any drop in circuital current ($-dI$) through the joint will recirculate within the wire as a magnetising loop. An equivalent statement is that the field inside the loop must approach the external value as the circuital current falls towards zero, which generates magnetising currents at the wire's inner surface. The measured drop in moment ($-dm$) is therefore the sum of a drop in the circuital component ($-dm_{cir}$) and a rise in the magnetising component (dm_{mag}).

The magnetising component must be subtracted in order to calculate $I(t)$ from the measured $m(t)$. This is not accounted for in any of the IRT experiments in the literature, which may be because magnetising currents produce a negligible signal

in conventional experiments. However, for the small coils required for testing in the MPMS here, and which also permit extremely low voltage measurements, the magnetising contribution is appreciable and must be considered.

Once again the accuracy of the current conversion relies on being able to distinguish magnetising and circuital components of the measured moment, which must be accomplished in further work. Here, a simple calculation is employed to make a first-order correction for the magnetising component, which is assumed to be fully persistent.

We firstly consider the influence of a fall in circuital current ($-dI$) on the fraction of the wire carrying circuital and magnetising currents (f_{cir} and f_{mag} respectively). The change in the wire fraction carrying the circuital current ($-df_{cir}$) is simply:

$$-df_{cir} = -\frac{dI}{I_{c,\mathrm{wire}}}. \tag{5.11}$$

The change in the wire fraction carrying the magnetising current (df_{mag}) is twice as large as this, since dI must travel both up *and* down the wire:

$$df_{mag} = 2\frac{dI}{I_{c,\mathrm{wire}}}. \tag{5.12}$$

This is only true for $\mathrm{d}I/I_{c,\mathrm{wire}} \leq 1/2$, which is certainly satisfied for all measurements made here. We now calculate the change in the circuital and magnetising components of the measured moment ($-dm_{cir}$ and dm_{mag} respectively). We recall from Sections 5.4.3 and 5.4.2 that the measured moment associated with a fully penetrated circuital current is that of the perfect closed coil (m_{pcc}) and similarly for a fully penetrated magnetising current we have the open coil moment (m_{oc}). Therefore we have that:

$$-dm_{cir} = -df_{cir}|m_{pcc}| = -\frac{dI}{I_{c,\mathrm{wire}}}|m_{pcc}|, \tag{5.13}$$

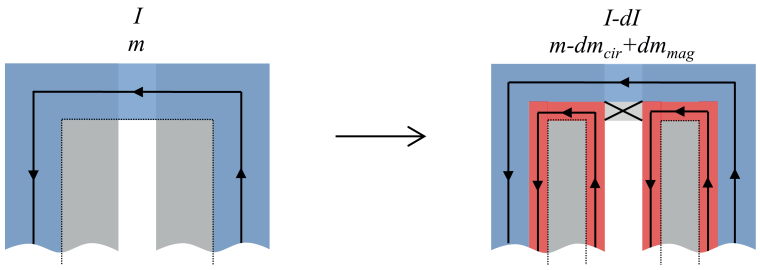

Figure 5.17: A Bean model diagram demonstrating the changing state of the test coil during IRT measurements. A fall in current through the joint ($-dI$) recirculates within the wire to form a magnetising current loop.

and

$$dm_{mag} = df_{mag}|m_{oc}| = 2\frac{dI}{I_{c,\text{wire}}}|m_{oc}|. \tag{5.14}$$

The change in the measured moment is:

$$dm = dm_{cir} - dm_{mag} = (|m_{pcc}| - 2|m_{oc}|)\frac{dI}{I_{c,\text{wire}}} \tag{5.15}$$

Substituting in Equation 5.1 and rearranging for dI yields:

$$dI = \left(\frac{1}{1 - 2|m_{oc}/m_{pcc}|}\right)\frac{dm}{\pi D^2/4}. \tag{5.16}$$

We note that this equation is identical to the simple current loop formula (Equation 5.3) with a correction factor of $1/(1 - 2|m_{oc}/m_{pcc}|)$, which accounts for the growth of magnetising currents as the circuital current decays. The ratio $|m_{oc}/m_{pcc}|$ is a constant with a value of 5.2 % for the test coils used here, which is understandably similar to the ratio of coil dimensions d_f/D which is 4.7 %. The correction factor is therefore ∼12 %.

The $m(t)$ decay curve can therefore be converted to $I(t)$ using Equation 5.16, assuming that at $t = 0$ the coil carries a purely circuital current. The inductive voltage at any current value ($V(I)$) can then be obtained from the slope of the $I(t)$ curve.

5.6.4 Noise Limit on Resistance Sensitivity

As was discussed in Section 2.2.2.4, the voltage sensitivity limit is met when the total decay over the measurement period is less than the noise level in the current measurements.

Figure 5.18 shows an example of a very slowly decaying current in which the fluctuation of the measured signal about the overall trend can be seen clearly. A linear fit is plotted which corresponds to a voltage of $2.0\,\text{x}\,10^{-14}$ V, (equivalently a resistance $R = V/I$ =$1.7\,\text{x}\,10^{-15}\,\Omega$). The normalised standard deviation of the current values from the fitted curve (σ_I/I) is ∼$4\,\text{x}\,10^{-5}$ in this case. This value was found to vary from ∼$(1-10)\,\text{x}\,10^{-5}$ over the numerous decay curves measured in this project. If we take σ_I/I as a representative metric for the current sensitivity, then the minimum measurable resistance over a standard 20 minute measurement period is in the range of ∼$(8\text{–}80)\,\text{x}\,10^{-17}\,\Omega$. This is a very high sensitivity level indeed, ∼10–100 times lower than for conventional Hall probe IRT rigs [34, 42–44, 47], and reflects the successful

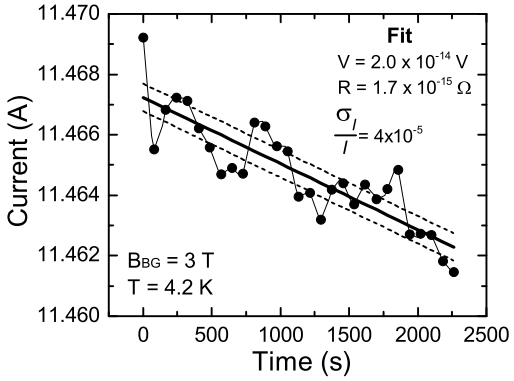

Figure 5.18: A very slowly decaying current measurement taken for the spot welded joint, which is near the noise limit of the system. A linear fit corresponding to a voltage of $2.0\,\mathrm{x}\,10^{-14}\,\mathrm{V}$ is plotted (solid line), along with dashed lines representing one standard deviation of the data from the linear fit.

application of a low inductance coil to a very sensitive SQUID magnetometry system. Joint persistence tests that might conventionally have consumed several hours of measurement can be accomplished in minutes with the present technique.

5.6.5 V-I Curves

Presented in Figure 5.19 are a set of V-I curves derived from the decay measurements described previously in Figure 5.16. Each of the coloured data sets in the plot derive from decay curves measured at different starting currents up to the maximum inducible current (I_{max}) estimated from the hysteresis loop using Equation 5.3.

The measured V-I data span three decades of voltage from $10^{-14} - 10^{-12}\,\mathrm{V}$. The two curves measured at the highest currents (red and blue), which cover the high voltage range (from $10^{-12} - 10^{-11}\,\mathrm{V}$) show two promising indications that they are related to real decay processes in the joint rather than any anomalous effects. The first is that the *V-I* characteristic here is clearly different to those at lower currents, and rises by an order of magnitude in the viscinity of I_{max}. The second positive indication is that both the red and blue curves form a common curve despite starting at different initial currents. Indeed this is the standard validity check that the intrinsic *V-I* characteristics of the wire or joint are being measured rather than any transient and history-dependent settling behaviour for example [48].

However, the *V-I* data measured at lower induced currents are not believed to be associated with real voltages in the coil. The *V-I* curves from each starting current do

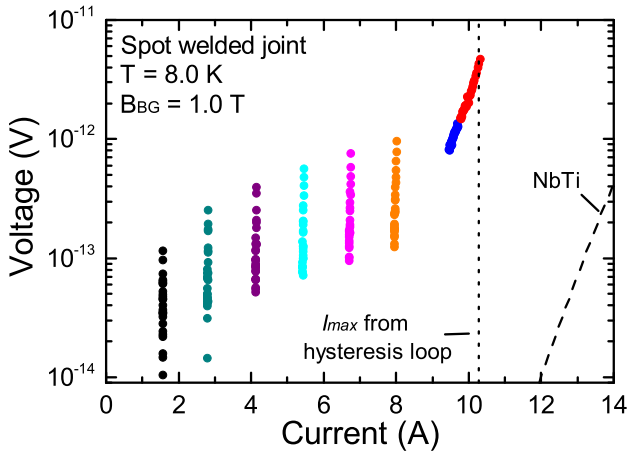

Figure 5.19: V-I measurements made on a test coil closed by a spot welded joint at 8.0 K and a background field of 1.0 T, plotted on semi-logarithmic scales. The data were extracted from decays measured from various starting currents from 0 to I_{max} by the procedure outlined in Figure 5.16. The calculated V-I characteristics of the wire under these conditions are also plotted for reference.

not meet, nor do they follow the trend seen at high currents. In each case the voltage falls by approximately one order of magnitude over the 20 minute decay period, with a general reduction in voltage towards lower currents. This behaviour was found in the vast majority of decays measured on various joints in this project, and further examples are provided in Figure 5.20.

Here the average voltage of the last few points in each decay curve (termed the "settled voltage") is plotted against current for decays taken at various fields and temperatures for the spot welded joint (Figure 5.20a) and a preliminary PbBi joint (5.20b). It is clear from these plots that there is a general increase in voltage with current, which increases from $\sim 10^{-14}$ V at 0 A to $\sim 10^{-12}$–$\sim 10^{-11}$ V at 100–200 A. The fact that the voltage tends towards a finite value of $\sim 10^{-14}$ V at zero current is a good indication that the decay is not associated with the superconductors in the test coil, and is likely an extrinsic effect.

Recalling that currents are induced in the test coil by changes in the MPMS field, drift in the background field on the coil was considered a potential source of the observed behaviour. These suspicions were made stronger after discovering decay even in measurements made on the open coil.

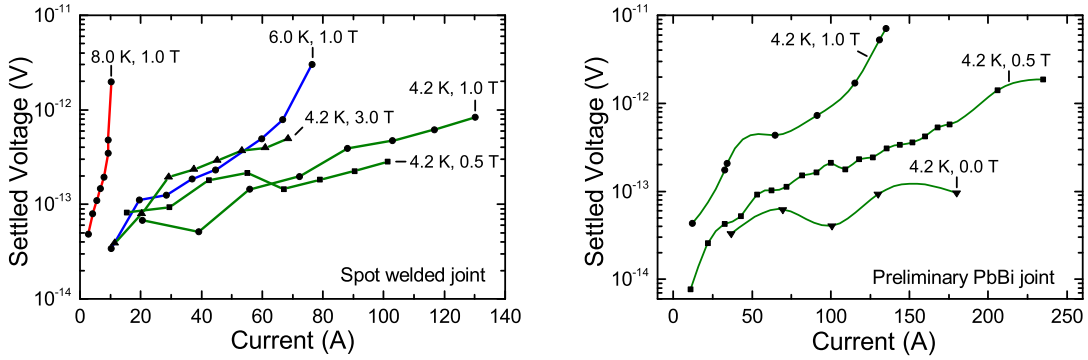

(a) (b)

Figure 5.20: Settled voltage plotted against current at various fields and temperatures for (a) spot welded joint and (b) a preliminary PbBi soldered joint.

5.6.6 Drift Voltages, V_{drift}

It was known from the inception of this technique that temporal variations in the MPMS field would provide a background drift rate in the decay curves. This so-called drift voltage (V_{drift}) is given by:

$$V_{\mathrm{drift}} = -L\frac{dI}{dt} = -L\frac{dI}{dm}\cdot\frac{dm}{dB_{app}}\cdot\frac{dB_{app}}{dt}. \tag{5.17}$$

In the conventional IRT technique, the test loop axis is held perpendicular to the background field in order to minimise this inductive coupling [44]. This is not possible here since inductive coupling of the test coil loop to the MPMS field is required in order to induce the test currents.

Nevertheless, the MPMS magnet has a nominal persistence rating of $\lesssim 1\,\mathrm{ppm/hr}$ in the persistent mode. Inserting the relevant values for the present test coil geometry into Equation 5.17 at a typical background field of 1 T, the expected drift voltage would be $\lesssim 2\,\mathrm{x}\,10^{-15}\,\mathrm{V}$ – an order of magnitude below even the lowest observed voltages.

However, the oversight made was in assuming that this drift rate comes into effect immediately once the magnet enters the persistent mode. In fact, the field settles over time following a field change, by the same processes as those relevant in IRT measurements (predominantly flux redistribution). Settling effects are particularly large when the magnet is operated in *no overshoot* mode, whilst in the *oscillate* mode the flux distribution in the wires is more uniform and thus settling effects are reduced [108].

Direct measurements of the drift rate of the MPMS field became the top priority for understanding how to proceed with IRT measurements, and these were performed as described in Section 5.7. These were sufficient to confirm that field drift was indeed the cause of the anomalous decay behaviour observed.

5.6.6.1 Movement-Induced Drift

Before discussing drift in the MPMS background field, a final comment can also be made regarding movement of the coil through the inhomogeneous field of the magnet during measurements.

As was discussed in Section 5.2, the field on the loop varies by $\lesssim 0.005\,\%$ during a 2 cm extraction measurement, whilst the bottom of the joint sees a much larger 1.7 % field excursion. During each extraction measurement, the test coil will therefore be subjected to a small hysteresis loop, with the total effect on the test coil being determined by the distributed inductance of the test coil along its length and the detailed applied field profile $B_{app}(z)$.

Due to the cyclic nature of the movements, providing the test current is not very close to $I_{c,\mathrm{joint}}$, the round-trip induced current is expected be zero. However, there would be a finite degree of ac-loss in the cycle that would cause an overall reduction in current and hence a movement-induced drift voltage V_{mov}. This would be influenced by the frequency of extraction measurements, making V_{mov} an independently measurable quantity. No such frequency dependence was found in the measurements made to-date, however one should bear this in mind in further work should the drift voltage floor be lowered. A method is also proposed in Section 5.8.2 to eliminate sample movement altogether.

5.7 MPMS Field Drift

Absolute field values in the MPMS can be measured by several methods. One way is to measure the magnetic moment of a palladium standard of known susceptibility and shape. Some measurements were tried in this way, however the noise level was restrictively high and the ability to measure extremely small field changes (of order 1 ppm/hr) demands an infeasibly high magnetometry precision. Hall probes are also unable to measure such small fractional changes in field.

In light of these shortcomings a "SQUID drift" method was developed to perform the task. This utilises the SQUID magnetometry system of the MPMS to measure extremely small changes in background field. [109] is acknowledged for demonstrating the ability to qualitatively monitor field fluctuations by this method. This basic idea was extended here by calibrating the pickup coil and electronics to permit quantitative field drift measurements. These measurements were performed on the SQUID VSM at DLS, and the results appear to be broadly compatible with the MPMS at the Clarendon lab where the IRT measurements were made, as will be discussed.

5.7.1 The SQUID Drift Method

The superconducting pickup coil of the magnetometer is wound in a second order gradiometer configuration in order to desensitise it from uniform external fields. However, due to an unavoidable imbalance between the positive and negative turns, there exists a small degree of coupling to the external field. Changes in the MPMS field induce a current in the gradiometer, which is then passed through a highly linear amplification system and SQUID, and an associated voltage is measured. This system can therefore be used in principle as a field measurement device. The gradiometer coil itself is 17 mm in diameter and 16 mm in length, and so the fields measured by this technique are average values over this cylindrical volume.

A crucial aspect of this technique is the ability to nullify a large static background field and detect only *changes* in magnetic field. The entire superconducting detection circuit can be quenched (and the SQUID reset to zero) at any time in order to eliminate any voltages generated upon ramping to an initial background field. After setting the detection circuit to zero, voltages are induced solely by further changes in field (i.e. field drift). Extremely small changes in field can be monitored due to the high sensitivity of the SQUID voltmeter and high degree of signal amplification. As will be shown, the field measurement sensitivity of this technique is around $\sim 45 - 100\,\mathrm{nT}$ in background fields of up to 1 T, allowing very low drift rates to be measured.

5.7.2 Calibrating the Gradiometer Coil

The relationship between a change in SQUID voltage and a change in uniform background field (dV/dB) can be established with an appropriate calibration measurement for each amplification setting or "range". This was done by ramping up the

MPMS field while recording the output of the SQUID voltmeter in a "log" file. In advance of each calibration measurement the magnet was degaussed, the superconducting pickup system was quenched and the SQUID voltmeter was reset to zero.

The resultant voltage-field calibration data are plotted in Figure 5.21. The relationship is highly linear, allowing dV/dB values associated with each range setting to be measured with a standard error of $\sim$0.1 % as noted in each plot. Having calibrated the gradiometer and SQUID electronics, field drift measurements (dB/dt) could then be made from changes in the voltage output of the SQUID ($V(t)$) by employing the following expression:

$$\frac{dB}{dt} = \frac{dV}{dt}\left[\frac{dV}{dB}\right]^{-1}. \tag{5.18}$$

5.7.3 Field Drift Measurements

5.7.3.1 Remanent Field Drift at 0 T

The first measurement made was to establish what is expected to be the lowest drift rate achievable during operation of the magnet. A full degaussing operation was performed at 0 T and drift in the remanent field was monitored for an hour. At the highest sensitivity setting (range 1) the SQUID drift is just distinguishable from the noise, as shown in Figure 5.22a. The voltage noise is $\sim\pm$1 mT, corresponding to a field resolution of $\sim$45 nT. The field drift rate as a function of time is plotted in Figure 5.22b, which is of the order of $\sim\pm$20 pT/s. The equivalent drift voltage for a test coil placed in this field would be $\sim 2 \times 10^{-16}$ V.

5.7.3.2 Drift Following Typical IRT Field Changes

A set of drift measurements were then performed as shown in Figure 5.23 to gauge the typical drift rates expected for IRT measurements. Measurements were performed at 1 T and 0 T as typical background fields. The following sequence of field changes were firstly performed in *no-overshoot* mode, and then repeated in *oscillate* mode for comparison.

The field was first raised to 1 T and allowed to relax after this large change for an hour. The field was then reduced by 0.1 T to 0.9 T then raised back to 1 T, simulating the induction of a relatively large current in the test coil. The subsequent field drift was measured for an hour. This cycle was then repeated, this time reducing the field

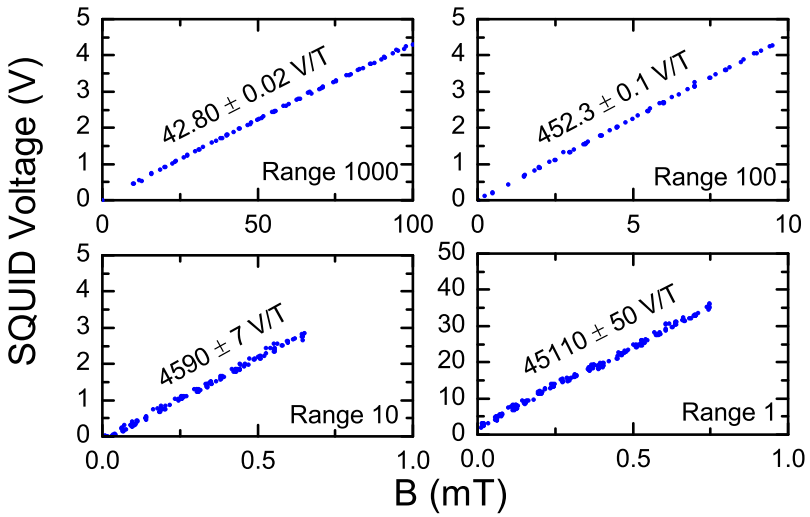

Figure 5.21: (a) The voltage response of the SQUID pickup coil at each range setting to changes in the MPMS field, which in each case was swept up from zero after a magnet reset. The measured voltage-field gradient for each range setting is provided in each plot.

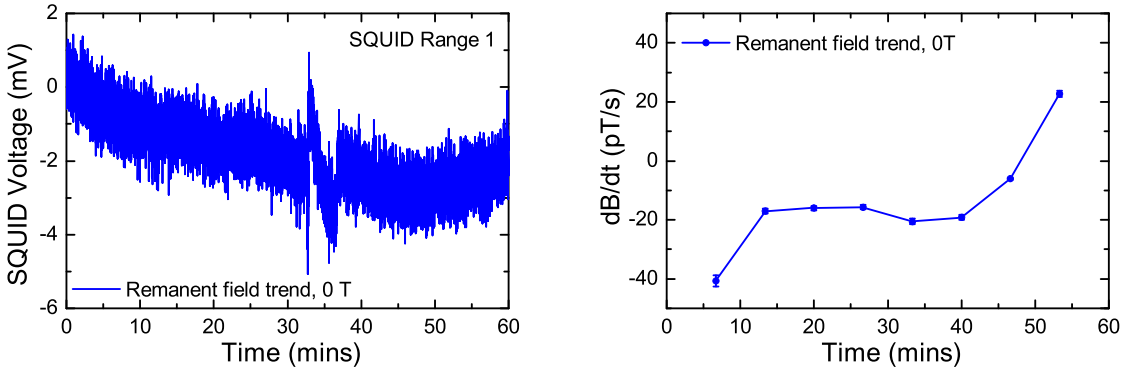

(a) (b)

Figure 5.22: (a) SQUID drift at a nominal field value of 0 T following a magnet degaussing operation. (b) The magnetic field drift rate calculated from the SQUID drift rate.

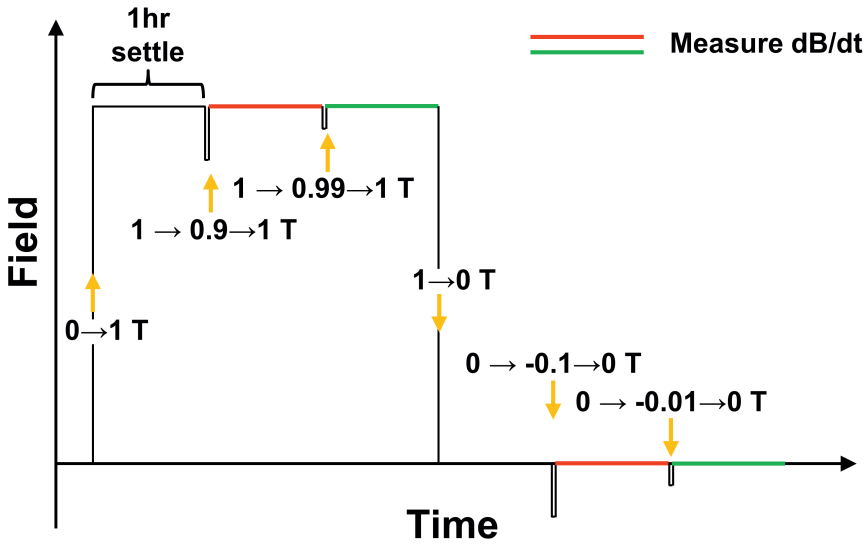

Figure 5.23: A sketch of the field vs time schedule employed for field drift measurements. Drift was monitored for a period of 1 hr following field cycles of magnitude 0.1 T (red) and 0.01 T (green) at background fields of 1 T and 0 T. The entire measurement set was performed once while sweeping the field in *no-overshoot* mode and repeated in *oscillate* mode.

by only 0.01 T to simulate inducing a relatively small current in the test coil. The field was then reduced to 0 T, performing the same 0.1 T and 0.01 T field cycles.

The resultant dB/dt measurements are presented in Figures 5.24(a–d). For brevity, the raw voltages from which the drift rates were extracted are not presented.

5.7.3.3 No Overshoot Mode

In *no-overshoot* mode the field drift behaviour is very similar at both 1 T and 0 T background fields. The drift rate is negative in all cases, indicating a decreasing field with time. This is understandable since the most recent field change in each case is positive, and so the resultant drift opposes this change. The drift rates are slightly larger in magnitude following the (red) 0.1 T field cycles (i.e. for large test coil currents) than the (green) 0.01 T field cycles (i.e. for small test coil currents). This is consistent with the test coil V-I data which shows a general increase in voltage with current. The magnitude of the drift rate falls with time at a decreasing rate, spanning approximately three decades from $\sim 10^2 - 10^0$ nT/s. The corresponding range of drift voltages for these field drift rates are 10^{-12}–10^{-14} V, which is precisely the range observed in test coils decay curves. The measured drift rates are also in

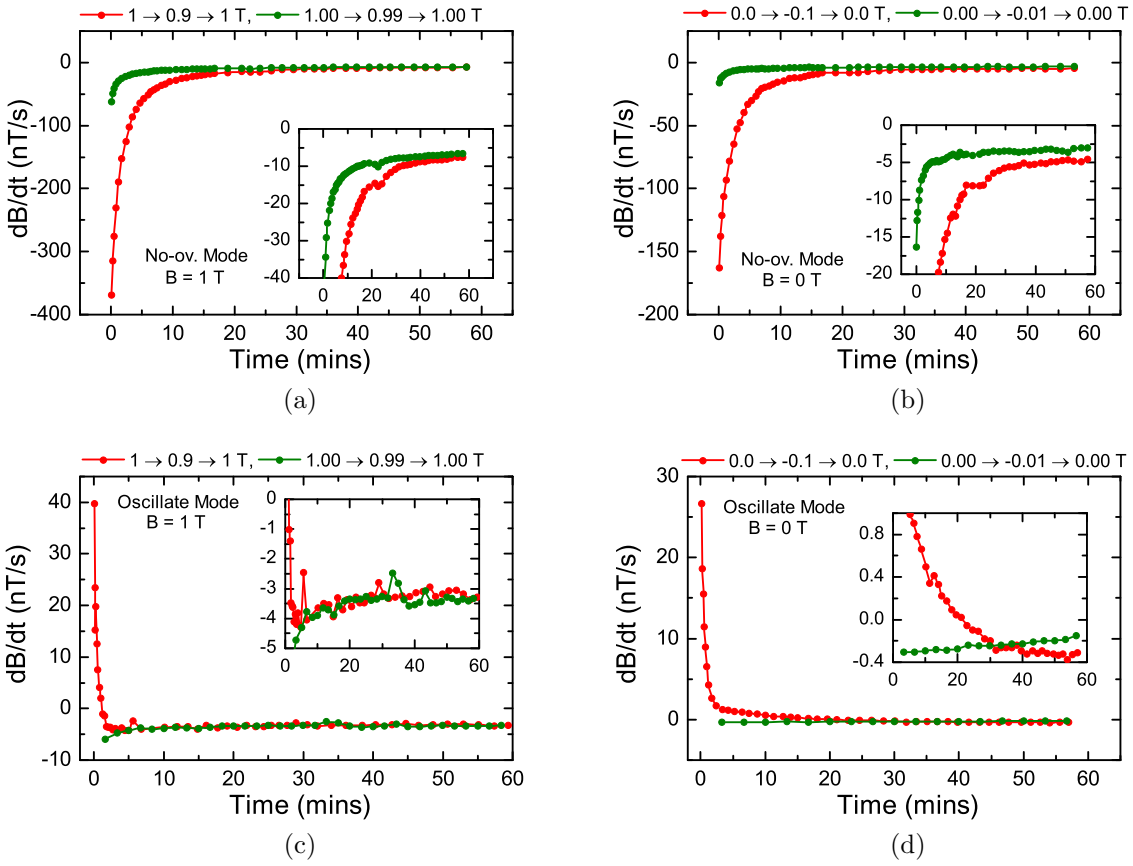

Figure 5.24: Field drift rate as a function of time following various changes in field for both *no-overshoot* and *oscillate* field sweep modes. (a) Sweeping to 1 T in *no-overshoot* mode. (b) Sweeping to 0 T in *no-overshoot* mode. (c) Sweeping to 1 T in *oscillate* mode. (d) Sweeping to 0 T in *oscillate* mode. The insets show the low level drift in more detail.

good agreement with the $-124\,\mathrm{nT/s}$ drift rate in the remanent field measured directly with a Hall probe on the Clarendon MPMS.

These observations provide some validation of the SQUID drift method employed, demonstrate a basic comparability between the magnets of the SQUID VSM at DLS and the Clarendon MPMS, and provide direct evidence that field drift is the cause of the anomalous *V-I* characteristics measured for the test coils.

5.7.3.4 Oscillate Mode

In *oscillate* mode the drift rates are reduced by around an order of magnitude, spanning from $\sim 10 - 0.1\,\mathrm{nT/s}$. The drift also appears to settle more quickly, falling by an order of magnitude within just a few minutes. Furthermore both positive and negative drift rates are found, which reflects the existence of both positive and negative currents flowing in the magnet wires, both of which settle over time with the net effect being either a decreasing or increasing total field.

5.8 Further Work on the IRT Method

It is clear that if oscillatory field sweeping could be employed to induce the test currents, drift voltages could be reduced considerably, potentially to as low as $10^{-15}\,\mathrm{V}$. The problem with this is that currents near $I_{c,joint}(B_{BG})$ cannot then be induced since, in this mode fields higher than the target field by an amount (dB) are experienced on approach and the maximum inducible current is therefore $I_{c,joint}(B_{BG} + dB)$.

5.8.1 Undercooled Induction Method

A possible way to overcome this problem would be to induce the current while the test coil is undercooled by an amount dT below the test temperature. At the undercooled temperature $(T - dT)$, $I_{c,joint}(T - dT)$ is much larger than the test current and so oscillatory field sweeping can be employed. The current is stored in the sample at this temperature until the drift in the background field has settled to a low level. The sample can then be warmed to the test temperature to begin the decay measurement. Providing rapid temperature changes can be made, only a small fraction of the decay curve would be invalid due to unstable sample temperature.

5.8.2 SQUID Drift IRT

Providing field drift could be sufficiently reduced, it may also be possible to place the test coil at a single position inside the gradiometer and measure the decaying test current from the measured drift in the SQUID voltage, i.e. to use the magnetometry system as a flux transformer. An initial extraction would be required to measure the total moment of the sample, but thereafter a higher sensitivity may be achievable by eliminating any effects associated with sample movement. It would then be possible to measure dm/dt every 0.25 s from the voltmeter output, which would also considerably increase the sampling rate.

5.9 Conclusions

In this chapter it was demonstrated that a standard commercial magnetometer can be employed to characterise superconducting joints with considerable convenience over a wide range of operating conditions, potentially enabling unprecedented fundamental studies into joint behaviour.

It was shown that the measurement of hysteresis loops (and m-T sweeps) offers a very quick and simple means of measuring $B_{c2,joint}(T)$ and joint current carrying ability at any field and temperature. These measurements have provided extremely useful information for the development of a range of NbTi joints that will be discussed in Chapter 6. Improvements have been suggested that may permit the extraction of precise $I_{c,joint}(B,T)$ values from hysteresis loops in further work, which are not presently possible due to uncertainty in coil geometry and current distributions.

An IRT method was also devised to measure the V-I characteristics of test coils. By employing a very low inductance test coil and an highly sensitive SQUID magnetometer, voltages below the pico-volt level can be measured from decay curves within just a few minutes. These have provided a very rapid means of showing that the joints made in this project are truly superconducting. However, decay of the background field in the MPMS was larger than first expected, dominating most of the decay curves measured in the project and preventing access to the intrinsic V-I behaviour of the joints vital for fundamental studies. Field drift measurements suggest that by employing oscillatory field sweeping voltage drift could reduced considerably, and a method of incorporating this into the IRT technique was proposed.

Chapter 6

The Microstructure and Superconducting Properties of NbTi Joints

As was discussed in Chapter 2, there have been three main techniques presented in the literature for producing superconducting joints between NbTi filaments – soldering, spot welding and cold pressing. The objective of the present study was to correlate joint manufacture, microstructure and superconducting properties for each of these techniques.

Monofilamentary wire was employed in order to simplify joint manufacture, measurement and analysis, and in most cases the metallurgical findings are expected to apply to the multifilamentary wires used in real magnets. A small number of multifilamentary spot welded and cold pressed joints were also analysed to provide a more complete picture.

Discussion begins with soldering, followed by spot welding and cold pressing. The cold pressed and spot welded joints discussed in this section were manufactured in collaboration with the Cryogenics and Magnetics group of the Science and Technology Facilities Council (STFC), who are located at the Rutherford Appleton Laboratory (RAL), Didcot. Joint development was under way at STFC as part of a project to build a superconducting undulator magnet for DLS.

6.1 Soldered Joints

Soldering is the industry standard jointing method for NbTi wires, and these joints are made in high volume on magnet production lines. With the need for development of Pb-free solders in mind, a key relationship to be established is the link between joint performance and solder superconducting properties. Does joint performance reach the fundamental limitations imposed by the solder, or do extrinsic factors such as reactions between the filaments and the solder provide the ultimate limitation?

In this section, joints are formed with both $Pb_{60}Bi_{40}$ (a typical industrial solder) and $In_{50}Sn_{35}Bi_{15}$ (a new Pb-free solder developed by our group). Their superconducting and microstructural properties are compared with those of the solders themselves, which were presented earlier in Chapter 4.

6.1.1 Joint Manufacture

Thornton's matrix replacement method [35] was employed to form the joints. As was discussed in Section 2.3.2, this involves submerging the wires in a Sn bath to dissolve the Cu matrix and coat the filaments in Sn, followed by dissolving the Sn coating in a solder bath. Some useful technical aspects will be mentioned before discussing the soldering process itself.

6.1.1.1 Heating the Liquid Metal Baths

Alumina crucibles of diameter 30 mm and height 40 mm, containing a typical volume of ∼10–15 ml of liquid metal, were used in the soldering process. The baths were heated to 350^{o}C on a 550 W hot plate. Bath temperature was controlled to within ∼5^{o}C, and was measured periodically by submerging a K-type thermocouple into the bath. The process was carried out inside a fume cupboard, and gloves and eye protection are essential.

6.1.1.2 Dealing with Dross

At such high temperatures an oxide skin (dross) forms on the top surface of the metal baths. Although protective atmospheres can be used to minimise dross formation [35], an open air process relevant to magnet manufacture was employed here. Care must

therefore be taken to scrape away this layer with a spatula in order to insert or remove the filaments through a clean opening in the surface of the liquid metal, to avoid coating the filaments in oxide.

6.1.1.3 Reuse of the Sn Bath

A 10 – 15 ml Sn bath can be reused to produce many joints. However, eventually the Cu content saturates and the Sn(Cu) no longer etches the submerged wires. Although there is no obvious change in the colour of the bath when it is nearing saturation, dross formation tends to increase considerably, which is a useful indication that the Sn should be replaced.

6.1.1.4 Use of G-10 Formers

The test coils are wound on G-10 formers for testing in the MPMS. However, G-10 decomposes at $\sim$150 ^{o}C and so cannot tolerate the soldering temperatures in the vicinity of the hot plate. For this reason, most of the soldering process was performed on the wire alone, before coiling the wire (with solder-coated tips) onto the former and performing a brief final soldering step to form the joint.

6.1.1.5 Matrix Replacement Soldering

The following procedure was followed to form the joints. A 10 cm length of wire was cut from the spool, the insulation was removed with SiC grinding paper, and the wire was cleaned with acetone. The wire was gently bent into a "U" shape and the tips were soldered over a length of $\sim$1 cm. The basic soldering process is the same as outlined in the patent by Thornton [35], and is sketched in Figures 6.1(a–f):

(a) Insert the filament tips into a bath of molten Sn at 350^{o}C. Agitate occasionally until the Cu matrix has dissolved, which usually takes $\sim$10 mins.

(b) Remove the filaments from the bath. They are now coated with a protective Sn layer of typical thickness $\sim$10 μm.

(c) Insert the Sn-coated filaments into a bath of molten solder at 350^{o}C. Joints were made with $Pb_{60}Bi_{40}$ and $In_{50}Sn_{35}Bi_{15}$ solders in this study. The solder dissolves the Sn layer and interacts with the underlying filament surface.

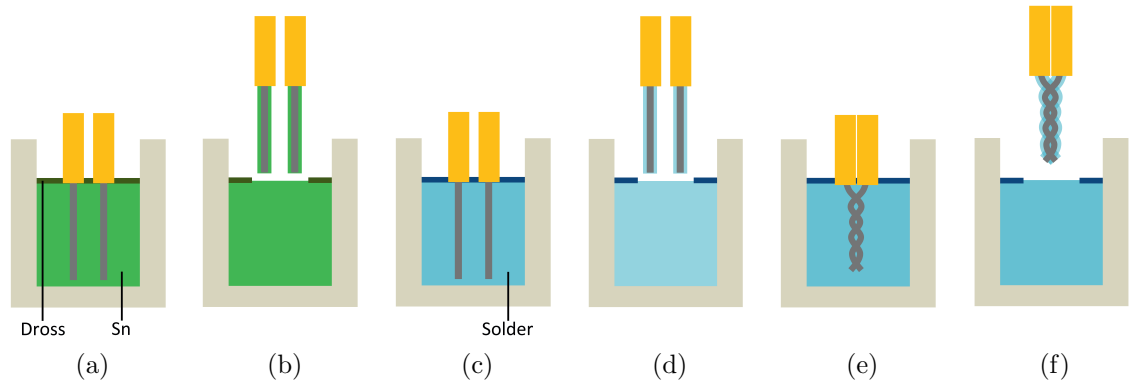

(a) (b) (c) (d) (e) (f)

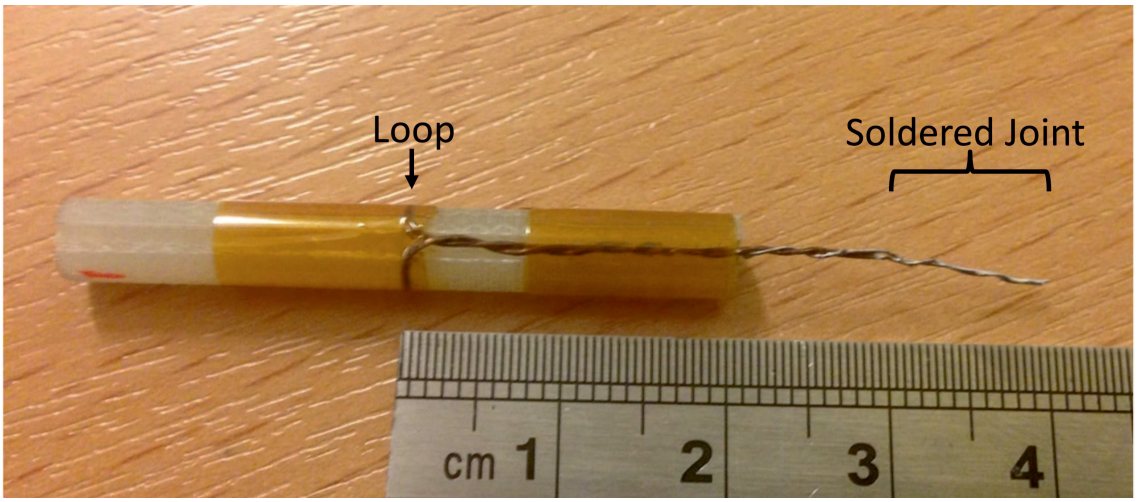

(g)

Figure 6.1: (a–f) Sketches showing the solder matrix replacement method used to produce joints between NbTi monofilaments (the steps are discussed in the main text). (g) Photograph of a test coil terminated with an 8 mm long soldered joint.

(d) Remove the filaments from the solder bath, allowing the solder coating on each filament to solidify.

(e) Wind the wire (with solder-coated tips) into a test coil. Twist together the trailing leads and filament tips and submerge the tips once more into the solder bath to a depth equal to the desired joint length (typically ∼10 mm). Allow the solder coating on the filaments to melt, which takes a few seconds.

(f) Remove the twisted filament tips slowly from the solder bath, which are now joined together with a layer of solder that encapsulates the pair.

A photograph of a typical test coil, terminated with a PbBi soldered joint, is provided in Figure 6.1g.

6.1.1.6 Joints Investigated

The first joint, PbBi_Joint_1, was made by tinning and soldering at 350^{o}C for 30 mins each, and the joint length was rather long at ∼2 cm. The superconducting properties of the joint were measured at an early stage in the development of the measurement technique. The results were published in *SuST* [45]. The joint was later inspected in the SEM, and the joint's microstructure is presented in Section 6.1.2.

In later work, the joint characterisation technique had progressed and so a new joint (PbBi_Joint_2) was made to meet the final test coil specification. The tinning and soldering times were also reduced to 10 mins each, since this was sufficient to form the joint. This joint was tested in much more detail than PbBi_Joint_1, and the MPMS results are presented in Section 6.1.3.

Finally, towards the end of the project a third joint was made with InSnBi solder in the same manner as PbBi_Joint_2. A replica joint was inspected in the microscope, and the microstructural analysis is presented in Section 6.1.4. The MPMS measurements are presented in Section 6.1.5.

6.1.2 Microscopy of PbBi_Joint_1

An optical micrograph of a transverse cross section through the joint is provided in Figure 6.2. This shows the typical structure of the joint, in which the two NbTi filaments are encased in PbBi solder. The cross section is relatively constant along the

length of the joint, as observed under the optical microscope while grinding through the joint.

Figure 6.3 shows EDX phase maps and chemical analysis of the PbBi/NbTi interface in PbBi_Joint_1, which was performed using the Zeiss-Merlin SEM.

The microstructure of the PbBi solder is consistent with that of the bulk PbBi sample discussed previously in Section 4.2.2. The average composition of the solder is 41 wt.% Bi, containing a superconducting ϵ-phase matrix with $\sim$34 wt.% Bi and micron-scale Bi particles consuming $\sim$18 vol.% of the solder.

Two reaction layers are discovered at the NbTi/PbBi interface. The first (reaction layer 1) is a few hundred nanometres in thickness and penetrates the filament in finger like structures. This layer is predominantly Nb-Ti but relatively rich in Bi, also containing some Pb and Sn. Between this and the PbBi is a second reaction layer (reaction layer 2) whose thickness varies from a few hundred nanometres to several microns. This is composed mostly of Pb and Nb, but with small amounts of Bi, Sn and Ti.

The precise mechanisms by which these reaction layers form during the soldering process was not investigated here, but their growth is expected to depend upon temperature and time spent in the tinning and soldering stages. Other group members (C. Aksoy and S. Speller) found that tinning and soldering times of 10 mins at 350^{o}C were more than sufficient to dissolve the Cu and Sn coatings respectively, and that this reduced the thickness of the reaction layers by about a factor of 2. Nevertheless, these seem to be characteristic of the matrix replacement process.

The superconducting properties of PbBi_Joint_2, which was made with 10 minute tinning and soldering times, will now be discussed. Similar results were found for

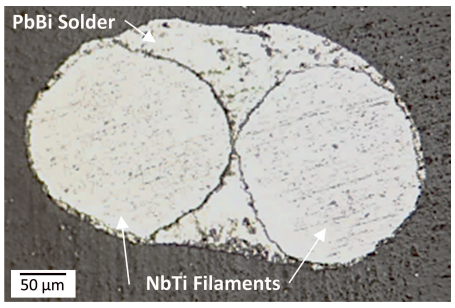

Figure 6.2: An optical micrograph of a transverse cross section through PbBi_Joint_1, showing two NbTi filaments encased in PbBi.

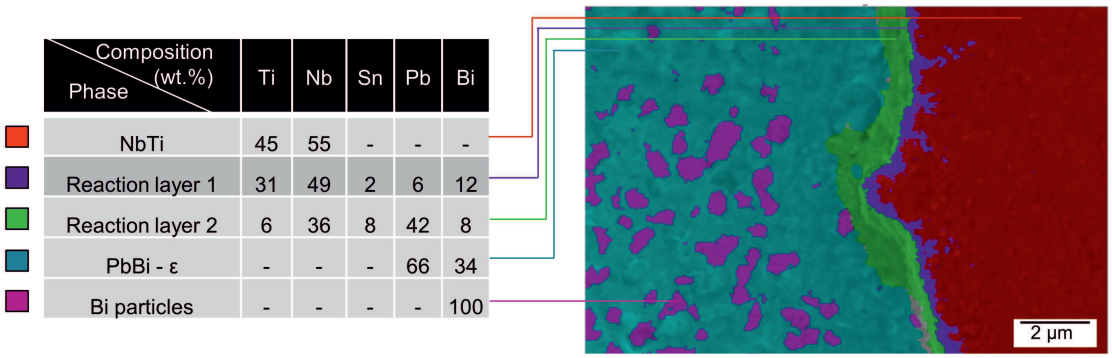

Figure 6.3: An EDX phase map showing the NbTi/PbBi interface with chemical analysis of each phase and reaction layer.

PbBi_Joint_1, albeit with larger current values owing to the longer joint length. These measurements were made around a month after the joint was first made, over which time the PbBi ϵ phase is expected to have reached its equilibrium composition, as was found in the microstructure of PbBi_Joint_1.

6.1.3 Superconducting Properties of PbBi_Joint_2

Figure 6.4a shows hysteresis loops measured for the test coil PbBi_Joint_2 at various temperatures. Much of the data was dominated by flux jumps at low fields and temperatures, so these regions were omitted for clarity. In each curve there is a bulge at low field associated with current flow through the joint, and a background extending to higher field from the open coil. As expected, the hysteresis width and the field range over which the joint is superconducting both reduce with increasing temperature.

Figure 6.4b shows $m-T$ sweeps measured at various background field values. The superconducting to normal transitions in the joint (and also the wire) are shown in greater detail in the inset. These are suppressed to lower temperatures at higher background fields.

$B_{c2,\mathrm{joint}}(T)$ values were extracted from the transition points at which the moment falls to the open coil background in the m-B and m-T plots. The results are plotted in Figure 6.4c and error bars are smaller than the symbol size. The values extracted from both m-B and m-T measurements form a single curve. A fit was made to the data with the standard WHH expression with parameters $\nu = 1.5$, $T_{c0} = 8.4\,\mathrm{K}$ and

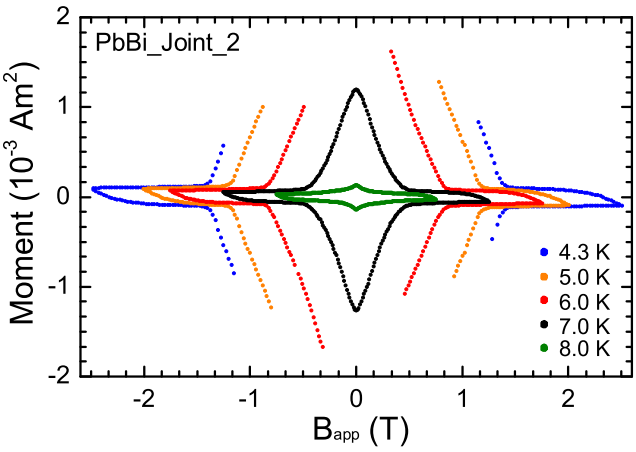

(a)

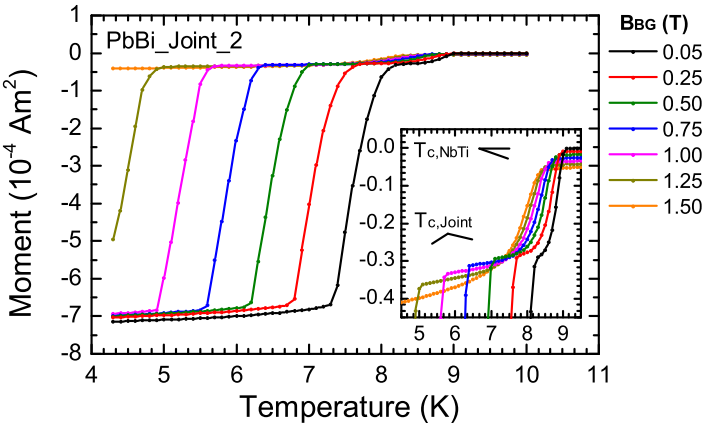

(b)

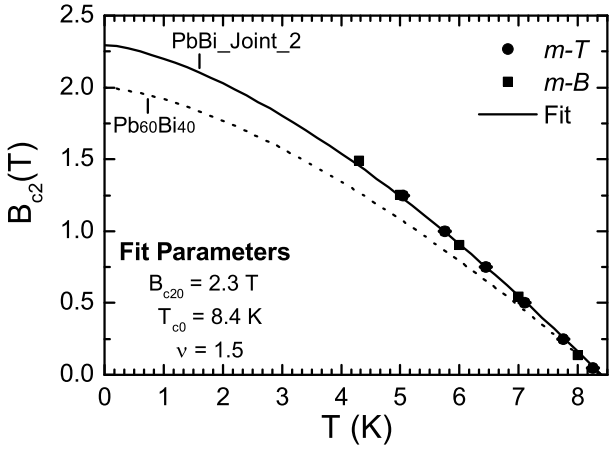

(c)

Figure 6.4: Magnetic measurements on PbBi_Joint_2. (a) $m-B$ hysteresis loops measured at various temperatures (flux jump data removed). (b) $m-T$ sweeps at various background fields. The inset shows the transitions in greater detail. (c) $B_{c2,\mathrm{joint}}(T)$ values extracted from $m-B$ and $m-T$ data in (a) and (b). A fit to Equation 3.22 is made. $B_{c2}(T)$ of $Pb_{60}Bi_{40}$ is also plotted.

$B_{c20} = 2.3\,\mathrm{T}$. The fitted B_{c20} value for the joint is 15 % larger than for thermally equilibrated $Pb_{60}Bi_{40}$ solder (also plotted), for which $B_{c20} = 2.0\,\mathrm{T}$. A number of possible explanations for this were considered.

The first is that the PbBi ϵ-phase in the joint may not have reached its room temperature equilibrium composition over the 1 month period between manufacture and testing. This is thought to be unlikely, since the measurements on PbBi bulks (Section 4.2.3) suggest this happens within a few days, and the measured composition of the ϵ-phase in PbBi_Joint_1 was the equilibrium room temperature value.

The second possibility considered was a measurement error. A temperature error on the joint can be ruled out since the T_{c0} value for the joint matches that of the solder. Similarly, since care was taken to measure the field profile in the MPMS (as discussed in Section 5.2) the applied field on the joint is at most 1.7 % smaller than the applied field value at all times, so this cannot provide an explanation. Furthermore, the criterion applied to measure the $B_{c2,\mathrm{joint}}$ values from the measured data, which was that $B_{app} = B_{c2,\mathrm{joint}}$ when $m = m_{oc}$ might lead to an *underestimation* of the true value, but not an *overestimation*. The difference might result from the different measurement techniques used to test the PbBi bulk and the jointed test coil. Different measurement techniques have been known to yield B_{c2} values which vary by such a large amount [79].

Whilst the cause of this slightly elevated B_{c20} value remains unexplained, the overall similarity between the $B_{c2}(T)$ values of the joint and the PbBi solder is a strong suggestion that the solder is the performance-limiting component.

We can test this suggestion further by comparing an estimated $I_{c,\mathrm{joint}}$ value with an independently measured J_c value for the PbBi solder. Unfortunately we cannot yet extract accurate $I_{c,\mathrm{joint}}(B,T)$ curves from the hysteresis loops, for reasons discussed in Section 5.5. Taking the test coil moment $m(0\,\mathrm{T}, 7\,\mathrm{K}) = 1.2\,\mathrm{x}\,10^{-3}\,\mathrm{Am}^{-2}$, where the magnetising current background is small (<10 %), and converting to a current value using Equation 5.3 yields $I_{c,\mathrm{joint}}(0\,\mathrm{T}, 7\,\mathrm{K}) \approx 83\,\mathrm{A}$. The peak current density in the solder at any current value I is $J_{\mathrm{solder}} = I/A_{\mathrm{solder}}$, where A_{solder} is the minimum solder area through which the current must flow in passing between the filaments (as was sketched earlier in Figure 2.2a). The minimum solder width is of the order of 200 μm and the joint length is ~8 mm, giving $A_{\mathrm{solder}} \approx 1.6\,\mathrm{mm}^2$. J_{solder} at $I = I_{c,\mathrm{joint}}(0\,\mathrm{T}, 7\,\mathrm{K})$ is therefore $\approx 5.3\,\mathrm{x}\,10^7\,\mathrm{Am}^{-2}$. This can be compared with $J_{c,\mathrm{PbBi}}(0\,\mathrm{T}, 7\,\mathrm{K}) = 9.8\,\mathrm{x}\,10^7\,\mathrm{Am}^{-2}$, which is a reasonable agreement given the level of approximation in the calculation

and supports the suggestion that the joint's performance is limited by the bulk properties of the solder. A more convincing demonstration would compare the field and temperature dependence of $I_{c,\mathrm{joint}}$ with $J_{c,\mathrm{PbBi}}$.

The important question to be answered is therefore how a persistent current is able to pass through the reaction layers. These are of micron-scale thickness and seemingly continuous across the NbTi/PbBi interface. Were these normal metals, current transport would presumably rely on either proximity or tunnelling effects [110, 111], which seem unlikely since the coherence lengths in the NbTi and PbBi materials are just 6 nm and 16 nm at 4.2 K (calculated using the GL expression in Equation 1.1). On the other hand it is conceivable that the reaction layers are both reasonably good type-II superconductors. Reaction layer 1 is mostly Nb and Ti, and reaction layer 2 is rich in Nb and Pb, for which several superconducting compounds exist [112]. It would be interesting to investigate the reaction layers more closely by transmission electron microscopy, to say with greater confidence which alloys and compounds are present at the interface.

6.1.4 InSnBi Joint Microscopy

A transverse cross section of the InSnBi joint was inspected in the Zeiss-Merlin SEM, and the results are shown in Figure 6.5. A BSE image is provided in Figure 6.5a, which shows an overview of the joint. This joint has a similar overall structure to the PbBi joint, however in this case the solder coating does not wet the filaments uniformly and approximately one third of the filament surfaces are uncoated. In the centre of the joint (shown in Figure6.5b) the filaments are in close proximity with no intermediate solder, but are separated by a reaction layer which surrounds the entire filament. The layer has a thickness which varies from $\sim 0.1 - 1\,\mu$m and is present around the entire filament surface, including regions not coated with solder in the final joint. The layer has a well defined composition of $In_{25}Sn_{56}Nb_{16}Ti_3$ (wt.%), which is $In_{23}Sn_{51}Nb_{19}Ti_7$ in at.%. As will now be discussed, the solder wets the filament surface well in some regions, and so the non-uniform coating may simply be due to the dipping method employed.

Figure 6.5b shows a phase map from a solder coated region of one filament. The solder coating has an overall composition of $In_{54}Sn_{33}Bi_{13}$ (wt.%), which is similar to the measured composition of the solder bath used to produce the joint ($In_{51}Sn_{34}Bi_{15}$). The chemical composition of all phases detected at the joint are provided in the table

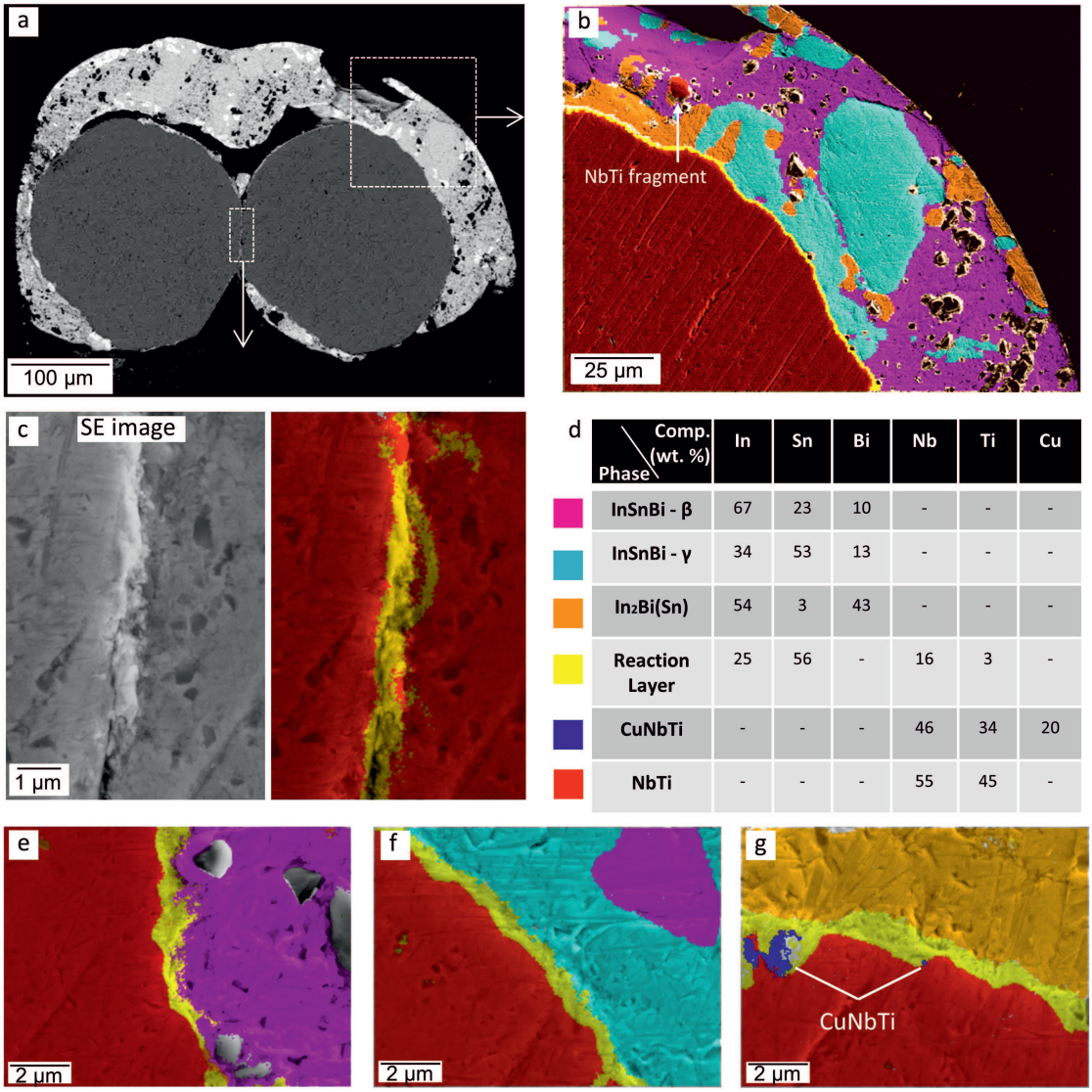

Phase \ Comp. (wt. %)	In	Sn	Bi	Nb	Ti	Cu
InSnBi - β	67	23	10	-	-	-
InSnBi - γ	34	53	13	-	-	-
$In_2Bi(Sn)$	54	3	43	-	-	-
Reaction Layer	25	56	-	16	3	-
CuNbTi	-	-	-	46	34	20
NbTi	-	-	-	55	45	-

Figure 6.5: (a) BSE image showing a transverse cross section through the NbTi/InSnBi soldered joint. (b) EDX phase map providing an overview of the solder coating on the filament. (c) SE image and phase map showing the filament-filament interface from the centre of the joint, with an intermediate reaction layer on the surface of each filament but no solder. (d) Table showing the measured composition of each phase in the joint. (e,f,g) High magnification phase maps showing the interfaces between the NbTi and β, γ and In_2Bi solder phases respectively.

in Figure 6.5d. The solder coating has the same three-phase microstructure as the bulk solder sample discussed previously in Section 4.4.2, with the chemistry of the β, γ and In_2Bi phases matching those of the bulk sample to within 2 wt.%.

Figures 6.5(e–g) show the interfaces between the NbTi and β, γ and In_2Bi solder phases respectively, at higher magnification. As can be seen, each of the solder phases wets the filament surface, which is expected to allow current to flow out of the filament over reasonably large areas. However, the poor coating of the pair of filaments is expected to severely limit the current able to pass through the joint.

A final interesting feature seen in Figure 6.5g is a number of partially dissolved CuNbTi particles at the filament surface. The origin and significance of these features will be discussed fully in Section 6.3. However, this image appears to directly show them being dissolved from the NbTi surface in the soldering process, leaving behind a serrated filament surface. None were found in any other of the soldered or tinned wire samples inspected throughout the project, suggesting that the tinning process is effective at dissolving them.

6.1.5 InSnBi Joint Superconducting Properties

Figure 6.6 shows three low-field hysteresis loops measured at 4.2 K, 5.0 K and 6.0 K for the InSnBi joint. The measured loops are dominated by magnetising currents in the wire, and have an elliptical shape because the wire is not fully penetrated over the ± 0.5 T field range. Nevertheless, at 4.2 K a small peak (labelled δm) can be distinguished at $B_{app} = 0$ T, indicating a small degree of current flow through the joint. The peak is less pronounced at 5.0 K and disappears altogether at 6.0 K.

The background is too large to obtain a confident measure of $B_{c2,\mathrm{joint}}$ from the loops, however the peak at 4.2 K certainly falls within the 0.18 T B_{c2} value measured for the solder sample extracted from the same solder bath. The measurements are sufficient to show that a very small persistent current is able to pass through the joint (likely constricted by the poor solder coating), but the overwhelming background signal prevents further analysis. Similarly to the PbBi joint, the current must pass through the reaction layer at the NbTi/InSnBi interface. Again, it is conceivable that the layer is itself superconducting (as are many phases in the In-Nb-Sn-Ti system [112]), although no reference data was found in the literature to support this claim.

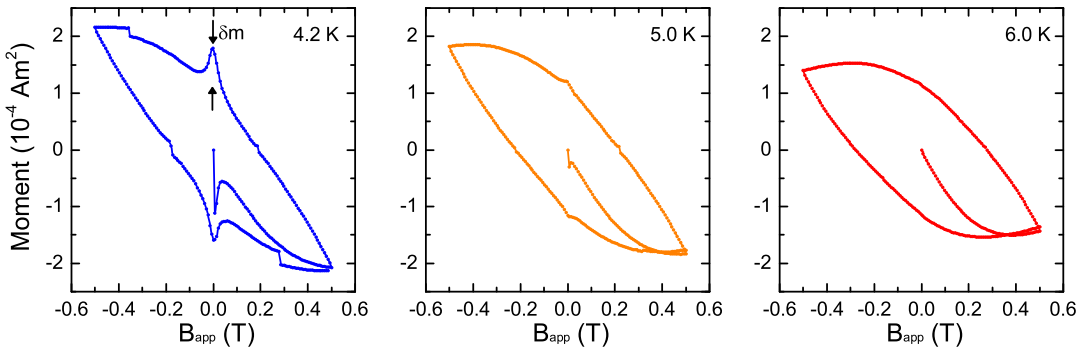

Figure 6.6: Low field hysteresis loops measured for the InSnBi test coil. The peak labelled "δm" at $B_{app} = 0$ and 4.2 K is associated with current flow through the joint, and decreases with increasing temperature.

6.1.6 Conclusions – Soldering

The microstructural and superconducting properties of PbBi soldered joints produced by the industry-standard matrix replacement method have been investigated, in an attempt to identify their performance-limiting features. The study has shown that despite the production of micron-scale reaction layers at the NbTi/PbBi interface, a superconducting current path is established from the filament to the solder. A first order agreement has been found between the upper critical field and critical current of currents flowing through the joint, and the independently-measured superconducting properties of the solder, suggesting the joint's performance is limited by the solder rather than the reaction layers. This conclusion supports the approach of searching for Pb-free solders with high B_{c2} and J_c values, however filament-solder interactions should not be neglected in this search. A preliminary joint made with our group's present-best Pb-free solder was shown to pass a small but nonetheless persistent current, which would likely be much higher if the coating was more uniform (which may have been a one-off problem for the joint tested).

6.2 Spot Welded Joints

Spot welding is a means of establishing direct bonds between NbTi filaments, thereby offering the potential for performance levels approaching that of the wires themselves. The major concern regarding this technique, however, is the influence of such intense heat on the carefully tailored nanostructure of the NbTi material and thus J_c and B_{c2} in the joint region.

Two types of spot welded joint are discussed in this section. The first is a set of multifilamentary joints produced by STFC for the superconducting undulator project, which will be discussed in Section 6.2.2. The second is a joint between bare NbTi monofilaments, discussed in Section 6.2.3. Parts of this work have been published in the *IEEE Transactions on Applied Superconductivity* journal [113].

6.2.1 Spot Welding Method

Joints were produced with a spot welder made by Portable Welders (UK), which is shown in Figure 6.7a. The system did not provide current pulse readouts, however, but was rated at 20 A and 240 V which gives some indication of the maximum power. The power control unit had three arbitrary dials for control of the pressure, time and "heat" of the welding process. Pressure and time were fixed at mid-range values commonly used by STFC, and the heat setting was used to vary the overall weld intensity. Cu electrodes were used with a tip diameter of 4 mm.

Joints were made by charging the capacitors in the control unit, selecting the desired settings, placing the pieces to-be-joined between the electrodes and finally pressing down the lever arm to bring the electrodes together under pressure and deliver the current pulse. This was usually accompanied by a brief puff of smoke as the filaments fused together. There was sufficient range in the heat setting to vary the welding intensity from the level of forming no bond at all to completely melting and fragmenting the filaments. The joint would normally stick slightly to the electrodes after welding and could be gently released without damage. The maximum welding intensity was limited by the filaments becoming inseparable from the electrodes. In this case there was commonly arcing and fusing together of the electrodes themselves, which was somewhat hazardous. Spot welding is likely to be a fire hazard for very fine NbTi filaments (known to be flammable).

Prior to each welding operation, the electrode surfaces were lightly abraded with SiC paper and swabbed with acetone to return the surface to a consistent condition. A photograph showing a twisted pair of NbTi/Cu wires being welded between the electrodes is provided in Figure 6.7b.

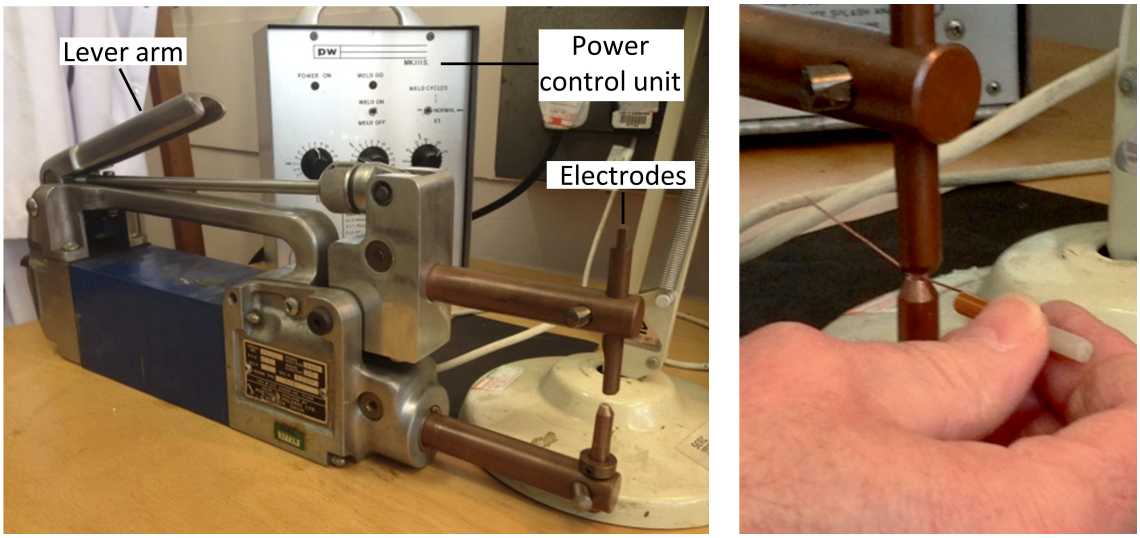

(a) (b)

Figure 6.7: (a) Photograph of the spot welding equipment used to produce all joints in this study. (b) Magnified image of twisted wires being spot welded between the electrodes

6.2.2 Multifilamentary Joints

The first joints investigated were between multifilamentary NbTi wires containing 24 filaments of 110 μm diameter. Section 6.2.2.2 discusses the microstructural characteristics of these joints. Some conventional magnetic measurements were also made on fused NbTi material from the spot welds, which are discussed in Section 6.2.2.3.

6.2.2.1 Joint Manufacture

STFC's standard process was as follows. The Cu matrix was dissolved from the wire in 50 % aqueous nitric acid solution over a 5 cm length and the filaments were rinsed in water and then ethanol. The filaments from each wire were split into three bundles and braided with those from the other wire. Twelve spot welds were made in series over the length of the joint, as shown in Figure 6.8. The welding "heat" setting was increased from the first weld to the last (as shown), from the minimum required to form a joint to the maximum at which the filaments were fragmented. In each weld the filaments are fused over a diameter of 2–3 mm, which increases slightly with heat setting.

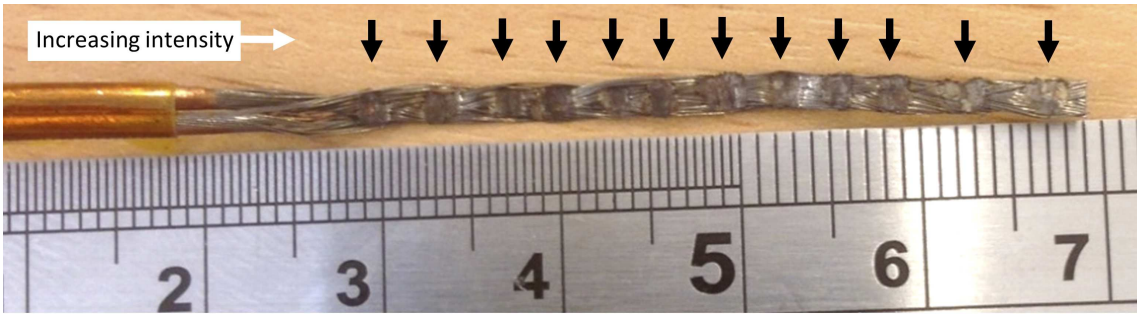

Figure 6.8: Photograph showing the spot welded joint produced between multifilamentary NbTi wires by C. Lockett (STFC). Individual welds are indicated by the black arrows and welding intensity was increased from left to right.

6.2.2.2 Microscopy

The microstructure of the welded NbTi material in various spot welds made over the full range of heat settings were investigated in the SEM. Similar characteristic features were discovered in all joints and at various locations inside each weld. A thorough analysis was performed with the Zeiss-Merlin SEM for one such weld (made with a high heat setting). Only this microscope had the necessary spatial resolution for sub-micron EDX analysis. The results are shown in Figure 6.9.

Figure 6.9a shows a transverse cross sectional SE image through the welded NbTi material. The electrode pressing directions are vertical as shown. It is clear that spot welding overcomes any surface oxides to form direct metal-metal contacts over large areas. The result is a consolidated bulk with just a few stray filaments at the edge.

Figure 6.9b shows a BSE image from the top surface of the joint. Here a small capping of Cu from the electrodes was found, along with a thin Cu-Nb-Ti reaction layer of thickness $\sim 5\,\mu$m. This contaminated layer is relatively small and thus not likely to greatly degrade the joint's performance. Cu is also found to infiltrate the weld in some regions, but does not react widely with the NbTi material.

Figure 6.9c is a BSE image of the fused NbTi material with a high gain setting on the BSE detector. Under these conditions a significant degree of compositional inhomogeneity in the NbTi material becomes apparent. The cross section contains a distinct central band and two outer bands, which in analogy with standard spot welding terminology [114] will be referred to as the fusion zone (FZ) and heat affected

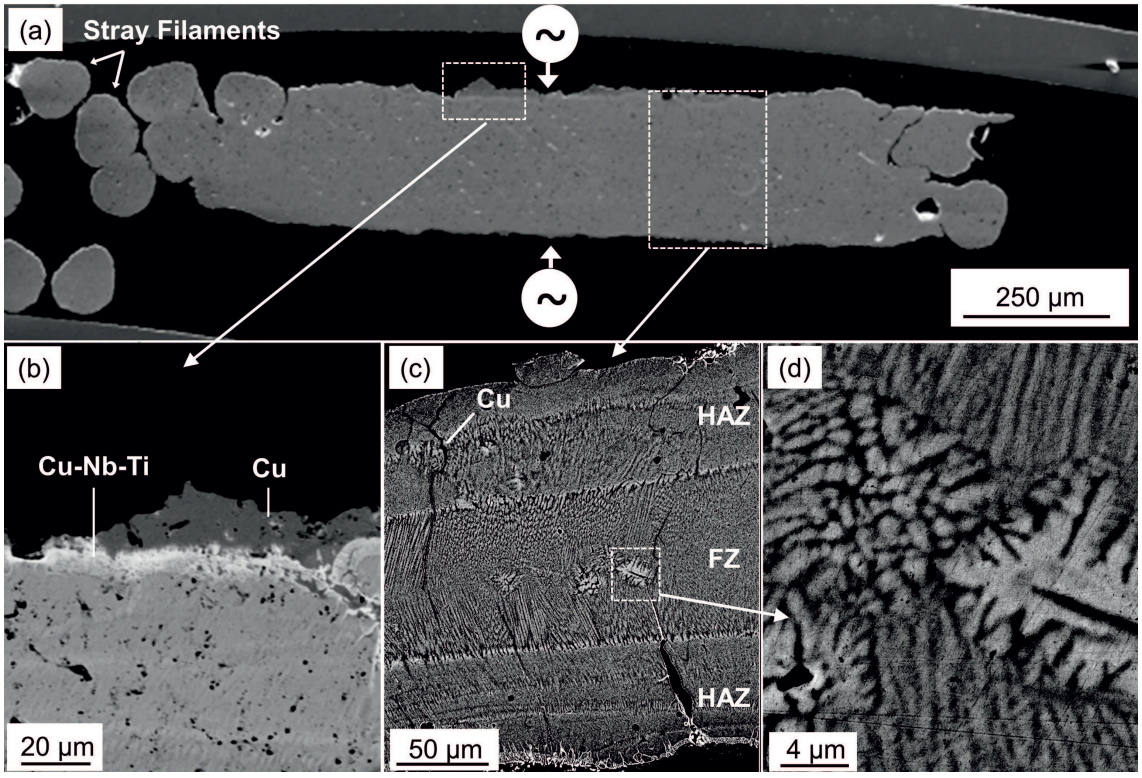

Figure 6.9: (a) SE image of spot welded NbTi filaments in transverse cross section, with the electrode pressing directions indicated. (b) BSE image showing Cu electrode contamination and a Cu-Nb-Ti reaction layer on the top side of the joint. The black spots are diamond contamination from polishing. (c) BSE image demonstrating Nb-Ti compositional inhomogeneity (and Cu inflitration) resulting from high temperatures and melting during spot welding. The fusion zone (FZ) and heat affected zones (HAZs) are discussed in the main text. (d) Shows an expanded region from the FZ in which dendritic growth is apparent.

.

zones (HAZs) respectively. These can be explained with reference to the Nb-Ti phase diagram in Figure 1.6b, which was presented in Section 1.6.1.

The FZ has a cast microstructure, indicating that it becomes completely molten during the welding process and that local temperatures must exceed ∼2000^{o}C. Coarse cored dendrites are nucleated at the edge of the HAZ (which appears to remain solid on the whole), and grow in the direction of the vertical cooling gradient established by the electrodes. Figure 6.9d shows an example of dendritic growth in greater detail.

Ti content varies from ∼42 wt.% in bright regions to ∼50 wt.% in dark regions. Such large variations are consistent with the phase diagram, which has a wide composition gap between the liquidus and solidus lines. Although the flux-pinning α-Ti nanostructure of the wire could not be observed directly in the SEM, it is expected to have been severely damaged by the high temperatures implied by the observed microstructure.

6.2.2.3 Superconducting Properties

Although these joints could not be characterised by the newly devised joint testing method (since the wire is too large), the fused NbTi material itself was tested in the MPMS by standard bulk magnetometry. Fused material from a spot weld made with a mid-range heat setting was sliced from the joint and oriented in the MPMS with the field perpendicular to its flat face. The sample had a width $w = 2.1\,\mathrm{mm}$, a length $l = 1.5\,\mathrm{mm}$ and a thickness $t = 0.30\,\mathrm{mm}$. Hysteresis loops were measured at 4.2 K and 5.0 K, field cooling at $-1.5\,\mathrm{T}$ and completing a loop out to 3.5 T, as shown in Figure 6.10a. These measurements were repeated on another mid-range spot weld, yielding similar results.

J_c values were calculated from the hysteresis width by Bean's model for the present slab geometry, assuming a homogeneous current density flows throughout the sample [99]:

$$J_c = \frac{16\Delta m}{w^2 l t(1 - w/3l)}. \tag{6.1}$$

The resultant J_c data are presented in Figure 6.10b. No self field corrections were applied. Equivalent data for the monofilamentary wire used in this thesis are also plotted as typical values for undamaged technological NbTi material.

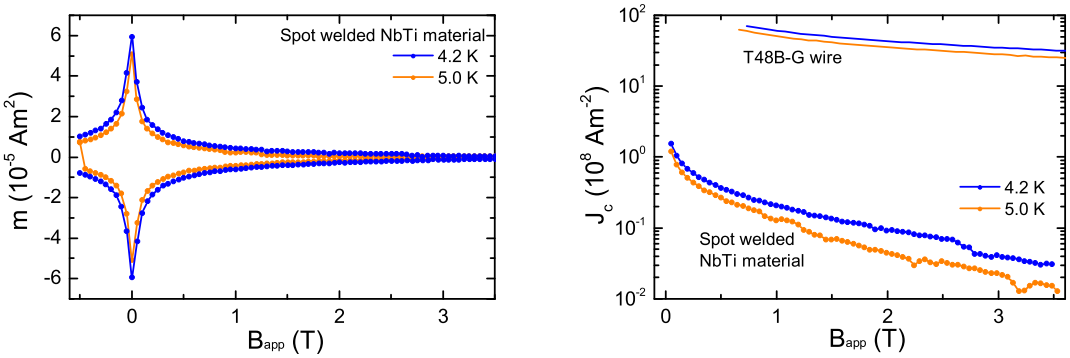

(a) (b)

Figure 6.10: Magnetic measurements made on fused NbTi material from a multifilamentary spot weleded joint. (a) Hysteresis loops measured at 4.2 K and 5.0 K. (b) $J_c(B,T)$ values calculated from the hysteresis loops by Bean's model.

The heat damage has caused a devastating reduction in J_c, which is more than two orders of magnitude smaller than in technological wires. The damage is most likely dominated by a destruction of the flux pinning nanostructure at high temperatures, however since $J_c(B)$ also falls more sharply with field than for pristine material, a possible B_{c2} reduction may also be responsible. As can be seen from Figure 1.6a shown previously in Section 1.6.1, we would not have expected B_{c2} to vary greatly in the sample as a result of the compositional inhomogeneity of 42 – 50 wt.% Ti seen in microscopic analysis, which suggests the measured inhomogeneity may be an underestimate.

Better performance can no doubt be achieved by optimising the spot welding parameters, but nevertheless these measurements highlight the potential for very high degrees of heat damage caused by spot welding, which may well impact on the reliability of the technique as a commercial process.

6.2.3 Monofilamentary Joint

6.2.3.1 Joint Manufacture

Efforts were next turned to producing a joint between monofilamentary wires which could tested in a closed circuit by the MPMS joint testing method. A standard test coil was wound, the Cu matrix was dissolved as before and the exposed filaments were twisted together. Three spot welds were then made over the bottom 6 mm of the leads with a mid-range heat setting.

As was discussed previously in Section 5.4.6, to improve the thermal stability of the joint, a Cu layer of thickness $\sim$100 μm was electroplated on the exposed filaments and spot welds with a simple $CuSO_4$ solution, Cu anode and small power supply. After re-testing the joint, the welds were cut from the coil and studied in the SEM.

6.2.3.2 Microscopy

A BSE image of a transverse cross section through one of the spot welds is provided in Figure 6.11a. The two filaments have been completely metallurgically bonded into a single bulk. It is noted that the cross sectional area of the fused filaments is $\sim$20 % smaller than the sum of the two original filaments, indicating that under the heat and pressure of the spot welding process the welded material was stretched longitudinally. This area reduction is another potential source of damage in spot welding.

Unlike the multifilamentary joint, very little Nb-Ti compositional inhomogeneity was discovered in any of the joints, suggesting a lesser degree of heating in this case. Since heat is generated by resistance at interfaces in spot welding, it is possible that these large monofilaments can be joined without generating as much heat as the multifilamentary case, owing to the greatly reduced density of interfaces.

The largest damage features in this joint are Nb-Cu-Ti phases shown in Figure 6.11b, presumably formed due to Cu infiltration from the electrodes. As is shown by the Nb and Cu EDX maps, in these regions there is a two-phase Nb/Cu/Ti microstructure. Contained in these are Nb-rich dendrites of composition 55/20/25 wt.% in a Cu-rich matrix of composition 13/60/27 wt.%. Nevertheless, these phases appear to consume only a minor fraction of the cross section and do not appear to have severely degraded the joint I_c, as will now be discussed.

6.2.3.3 Superconducting Properties

Figure 6.12 shows hysteresis loops measured at 4.2 K, 6.0 K and 8.0 K for the test coil closed by the spot welded (Cu-plated) joint. Flux jumps still occur at 4.2 K, and the loops exhibit various anomalous asymmetries discussed previously in Section 5.4.7.

Nevertheless, it is clear that the joint superconducts over the entire field range in each loop. Whilst the intrinsic properties of the joint are obscured by the anomalous hysteretic features (particularly at higher temperatures), it is evident that the joint

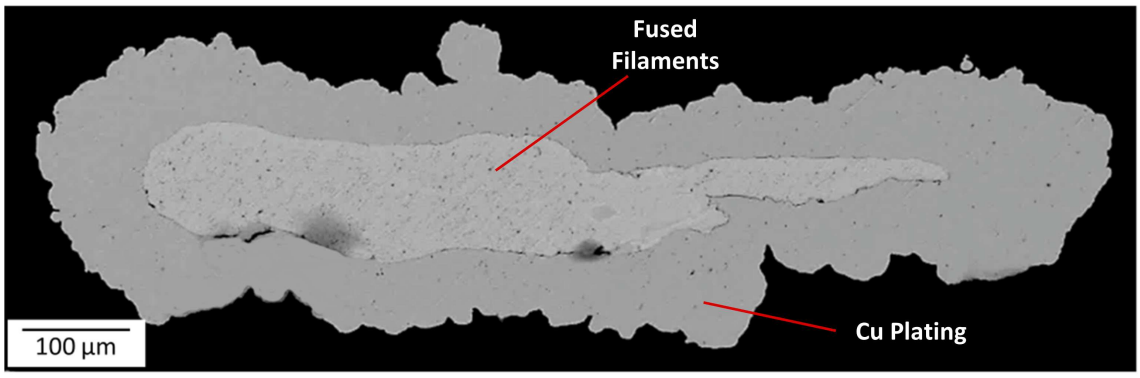

(a)

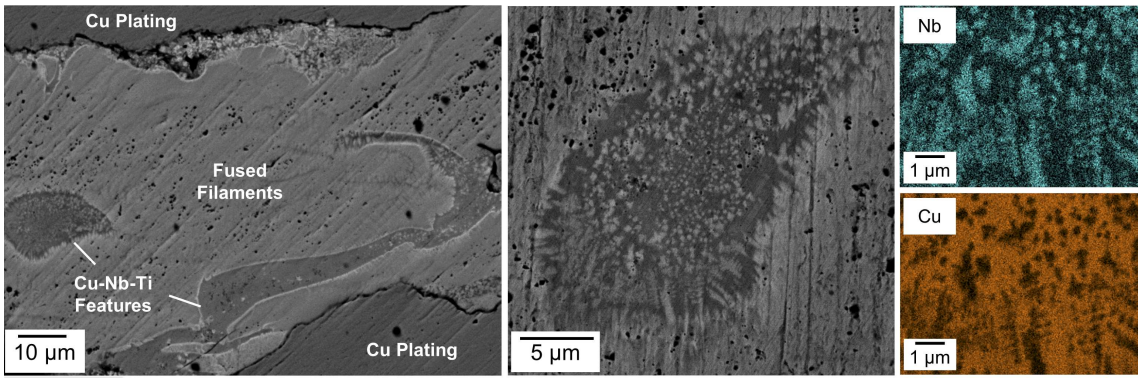

(b)

Figure 6.11: (a) BSE image of a transverse cross section through the centre of the monofilamentary NbTi joint. The joint was made between bare filaments and the Cu was electroplated on afterwards. (b) BSE image of a region showing Cu-Nb-Ti features (left), one of which is shown at higher magnification (middle), along with Nb and Cu EDX maps from inside this feature (right), showing Nb-rich dendrites in a Cu-rich matrix.

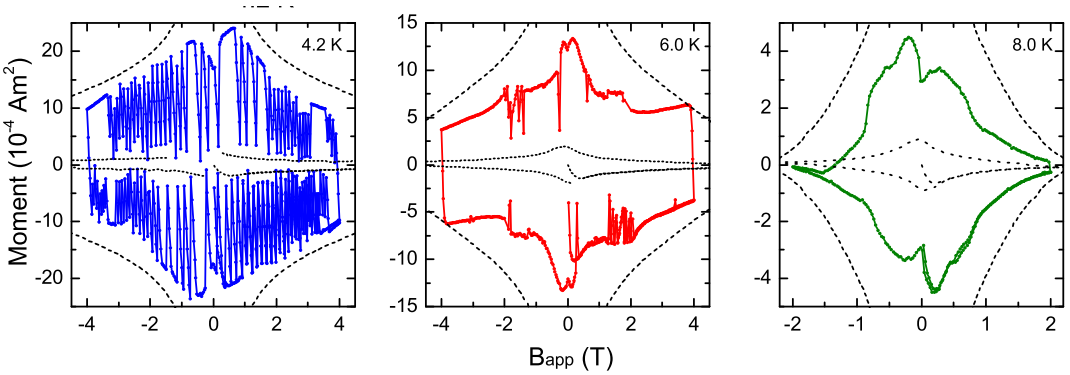

Figure 6.12: Hysteresis loops measured for the test coil closed by the spot welded joint, after Cu plating. The dashed and dotted curves are the standard perfect closed coil and open coil curves.

is able to pass a current that is a high fraction of the wire's I_c. Indeed at 4.2 K the outer boundary of the loop appears to have a similar field dependence to the perfect closed coil, suggesting the current-limiting component in the circuit is pristine NbTi material. Given the uncertainties in current measurement discussed in Section 5.5, it is possible that the performance of this test coil is limited by the wire rather than the joint.

6.2.4 Conclusions – Spot welding

This study has shown that spot welding is capable of producing complete metallurgical bonds between NbTi filaments. For the monofilamentary joints analysed, microstructural analysis showed little sign of heat damage, and the MPMS measurements suggested that critical currents approaching the wire's I_c can be achieved. This is a promising indication of the potential of this technique as a Pb-free, HF-free jointing technique.

By contrast, the multifilamentary joints made by STFC had dramatic cast microstructures in the fused material, indicating that large-scale melting had occurred. Magnetic measurements on bulk material from the joints indicated the material had a very low J_c compared with typical pristine NbTi.

Whilst this suggests spot welding may be better suited to monofilamentary joints due to the lower density of interfaces, one would need to conduct a much wider survey before any fundamental conclusions could be drawn. It is likely that damage in multifilamentary joints could be reduced by optimising the welding conditions. Nevertheless, the potential for heat damage by this jointing method is a concern for repeatability on the production line.

6.3 Cold Pressed Joints

The final jointing method investigated was cold pressing, in which the bare NbTi filaments are crimped together in metal tubes at room temperature. Since the joints are made directly between NbTi filaments without heating, this method has the potential to yield joints with performance comparable to the NbTi filaments themselves. The drawback is that bonding must rely on the surface condition of the filaments, and many researchers clean the filaments in HF-based solutions prior to jointing [44,63,64],

which is highly undesirable for magnet manufacturers. However, the exact role played by HF cleansing has not been discussed in the literature, and its requirement for the production of functioning joints is not clear.

This section presents a basic study into the metallurgical and superconducting properties of joints made by simply pressing together bare NbTi filaments in metallic crimps at room temperature. Microscopy was first performed on multifilamentary joints produced by STFC, highlighting some metallurgical factors. A batch of monofilamentary joints were then made with both Cu and Nb crimps, their performance was tested in the MPMS, and the joints were inspected under the microscope.

6.3.1 Joint Manufacture

A common basic technique was employed to produce all of the joints discussed in this study. The wires were prepared by abrading away the insulation with SiC papers over the desired length, dissolving the Cu matrix in nitric acid and rinsing in water and ethanol.

Metal tubes (crimps) of the desired size were turned on the lathe and cleaned in ethanol. The NbTi filaments to be joined were twisted (in the case of monofilamentary wire) or placed on top of one another (in the case of multifilamentary wire) and inserted in the crimp, ready for pressing.

Uniaxial pressing was performed between steel anvils with a Testometric 50 kN press, as shown in Figure 6.13a. A load cell provides a force-displacement (F-z) readout to allow for controlled pressing. As standard practice, prior to jointing the anvils were pressed together to embed them and measure the baseline F-z curve. The crimp was then loaded, pressed to the desired force, and then removed.

6.3.2 Multifilamentary Joint

Preliminary joints were produced by STFC between multifilamentary wires with 50 μm filaments. The filaments from each wire were placed on top of one another, inserted into a Nb crimp of 1 mm ID, 3 mm OD and 6 mm length, then pressed between flat anvils up to a force of 50 kN. The flattened crimp had a thickness of $\sim$0.8 mm, expanding to a final length of $\sim$8 mm and a width of $\sim$7.25 mm. The final pressure on the crimp at 50 kN was therefore $\sim$0.86 GPa (similar to that employed by Phillip et al [64]). Three such joints were made in series as shown in Figure 6.14.

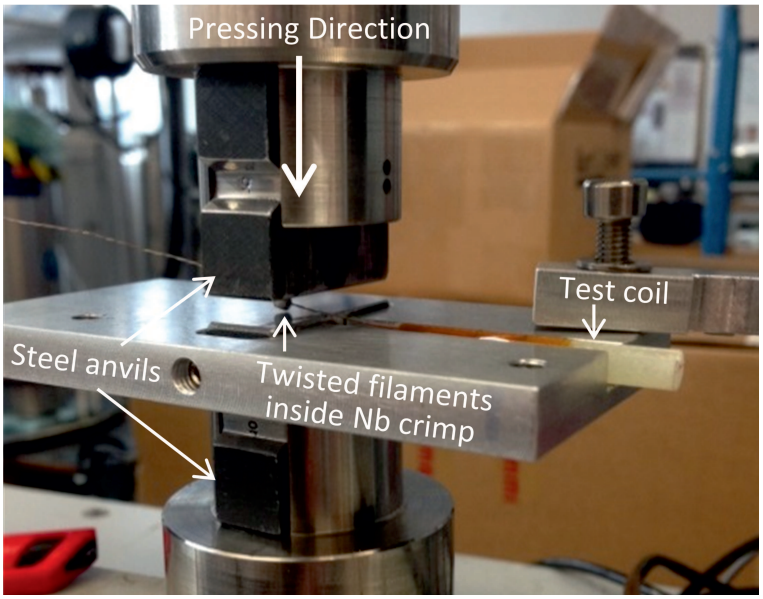

Figure 6.13: A photograph of the experimental setup employed to produce cold pressed joints in the Testometric press. In this case a Nb crimp was slid over twisted monofilaments and pressed between steel anvils to terminate a test coil.

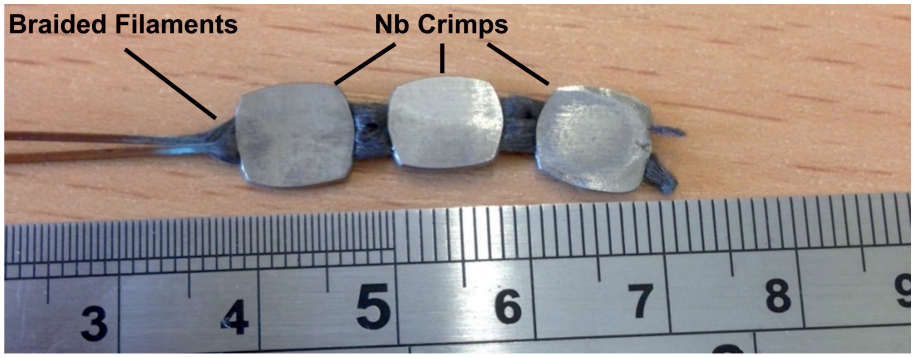

Figure 6.14: Photograph of braided NbTi filaments cold pressed in Nb crimps

6.3.2.1 Microscopy

The joints were mounted and prepared for microscopy in different orientations, however the filaments tended to fray away and detach from the joint when preparing longitudinal cross sections. A transverse cross section through the centre of one joint is shown in Figure 6.15.

The overall structure of the joint is shown in an optical image in Figure 6.15a. The filaments are compressed tightly in the centre of the crimp. A BSE image in Figure 6.15b shows that although the filaments are held in close contact inside the crimp, interfaces are visible and in most regions the filaments are not metallurgically bonded.

EDX analysis was performed using the Ziess Merlin SEM on a typical filament interface, as shown in Figure 6.15c. Oxygen was found at the interfaces, which was expected since the nitric acid etch used to dissolve the Cu matrix is oxidising. Cu-containing particles were also discovered.

The origin of these Cu-containing particles was investigated further by inspecting the surface of a bare NbTi monofilament laid flat in the SEM. As is shown in Figure 6.16, the filament's surface is littered with these micron-scale particles. The surrounding material is heavily striated along the drawing direction of the filament and appears to flow around the particles, suggesting them to be harder than the NbTi material. These appear to be intermetallic "nodules" which are well known to form at the NbTi/Cu interface during wire manufacturing [26]. Studies show these are composed predominantly of $TiCu_4$, but $(Ti_xNb_{1-x})Cu$, with $x \sim 0.5$ is also known to form [115]. EDX analysis performed here on polished particles suggests a composition of $Cu_{19}Nb_{33}Ti_{48}$ (at. %), however given their small size the EDX analysis may be inaccurate.

Clearly these nodules are not dissolved by nitric acid and present a barrier to current transfer out of the filaments in the cold pressed joints studied here. It is possible that commonly used HF-based etchants may dissolve these particles, and this may be a benefit of their use, however the presence of these nodules is not discussed in the literature. Interestingly, the nodules are not found commonly in soldered joints and are seemingly dissolved by the molten Sn used to remove the Cu matrix. The prospect of producing cold pressed joints between solder coated filaments (with no nodules) is explored later in Section 6.3.4.

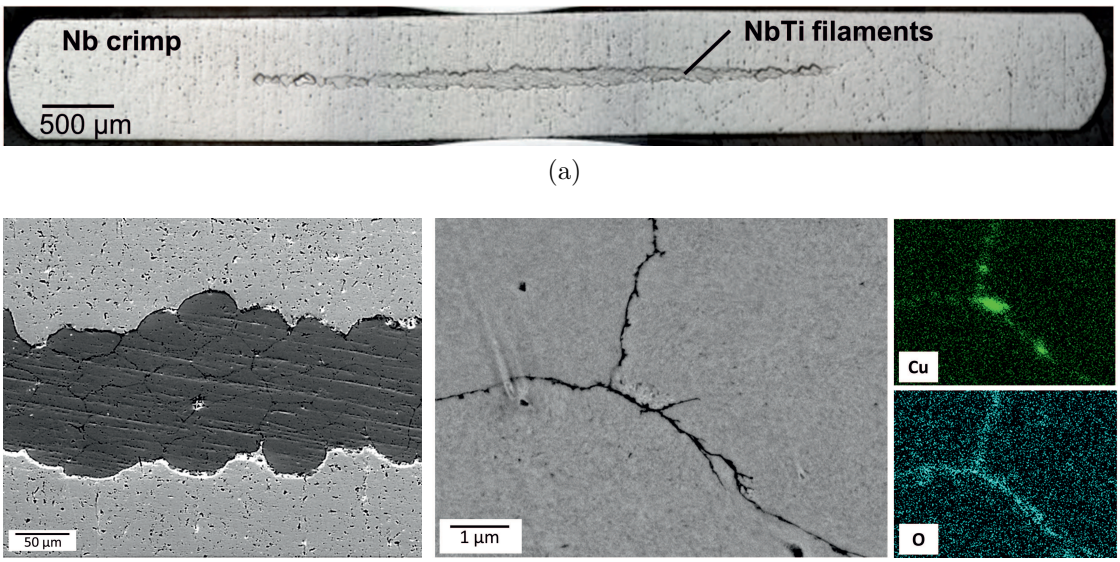

Figure 6.15: (a) Optical micrograph of a transverse cross section through the centre of one of the joints. (b) BSE image from the centre of the filament bundle, in which interfaces between the filaments are clearly visible. (c) BSE image at the interface between three filaments at high magnification. EDX maps (right) indicate O and Cu at the interfaces.

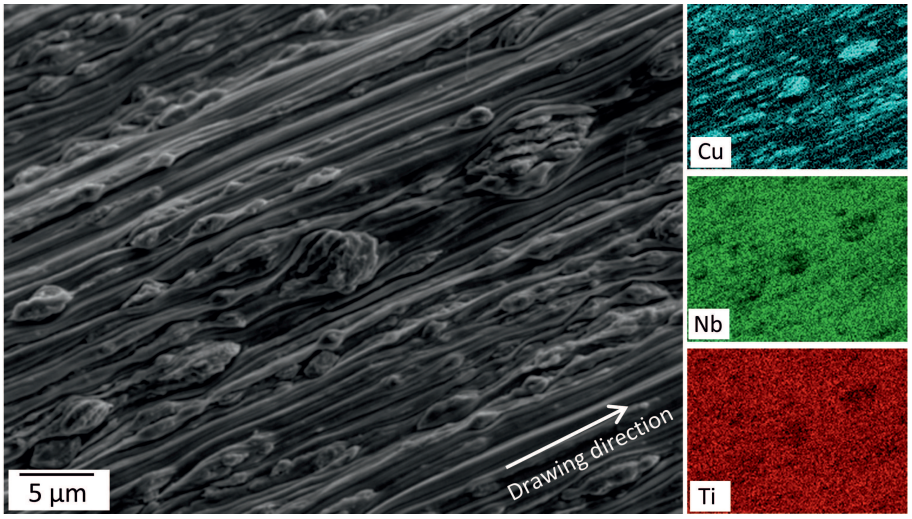

Figure 6.16: SE image showing intermetallic nodules on the surface of a bare NbTi filament from which the Cu matrix has been dissolved in nitric acid.

The microstructural and superconducting properties of a batch of monofilamentary joints made in the same way as this multifilamentary joint are first investigated, in order to measure the typical current densities that can be passed through nitric acid-etched filament surfaces.

6.3.3 Monofilamentary Joints

A batch of test coils was made with cold pressed joints for which both the superconducting and microstructural properties could be tested. Joints were made with both Cu and Nb crimps. Cu crimps were used to test for direct filament-filament current flow alone, whilst Nb crimps provided an additional filament-Nb-filament superconducting current path. The crimp dimensions were 0.5 mm ID, 2.0 mm OD and 3 mm in length, which were small enough to fit in a standard MPMS straw after pressing. The filaments were twisted inside the crimp, crossing over three times over the 3 mm crimp length.

The values of total linear contraction on cooling from 293 K to ∼4.2 K ($L_{293K}-L_{4.2K}/L_{4.2K}$) for Cu, Nb and NbTi are 0.324 %, 0.143 % and 0.188 % respectively [116]. Since the crimp volume is ∼7 times larger than the NbTi filament volume, the crimps will contract slightly more than the filaments upon cooling to the measurement temperatures, maintaining the filament contact achieved in pressing at room temperature.

The degree of flattening (i.e. the maximum pressing force) was also varied by grinding a depression (of width W) in the anvils, as shown in Figure 6.17. The crimp is compressed inside the depression until its thickness is equal to W, beyond which the load is taken by the system. Three anvils were produced with $W = 0.9$ mm, 0.35 mm and 0 mm, for which the maximum forces seen by the crimps (as recorded by the load cell) were approximately 2.5 kN, 10 kN and 50 kN respectively. One joint was made for each crimp material and pressure. A table and photograph of the jointed test coils are provided in Figure 6.17. Each test coil was characterised in the MPMS and then inspected by SEM.

6.3.3.1 Filament Breakages

As shown in Figure 6.18, near the centre of each cold pressed joint a breakage in the filaments was discovered. As is sketched in the figure, the cause of this is believed

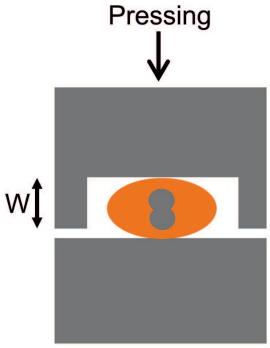

Coil #	Crimp	W (mm)
1	Nb	0.00
2	Cu	0.00
3	Nb	0.90
4	Cu	0.90
5	Nb	0.35
6	Cu	0.35

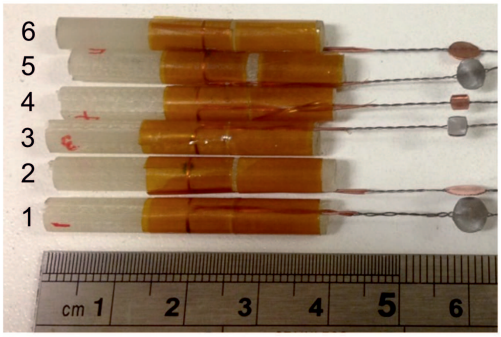

Figure 6.17: Production of cold pressed joints between NbTi monofilaments. Left: Schematic of pressing anvils with a depression (W) ground to control the degree of pressing applied to the crimp. Middle: Matrix of jointed coils produced for MPMS measurements. Right: Photograph of the jointed coils.

to be longitudinal expansion of the crimp as it was flattened. This is hardly surprising, since the tensile strength of NbTi is typically ∼1.3 GPa [117], giving a breaking force for these 200 μm filaments of just ∼40 N. Clearly only a very small fraction of the total pressing force must be transmitted longitudinally by expansion of the crimp in order to snap the filaments. The same problem was encountered by Nuding when joining NbZr filaments by this technique [63]. In later work the pressing anvils were redesigned to prevent longitudinal crimp expansion, as will be discussed later in Section 6.3.4.1.

The consequence of these breakages for the current batch of joints was that their length was effectively halved, and so their critical current is expected to have been reduced by a similar factor. Such filament breakages were not discovered in the multifilamentary joints, suggesting the filament bundles together had a sufficiently high tensile strength to withstand the 50 kN force.

The measured superconducting properties of the joints will now be discussed alongside microstructural analysis.

6.3.3.2 Cu-Crimped Joints

Figure 6.19 shows the measured m-B behaviour of Coils 2, 4 and 6, which were closed by Cu crimped joints. The joints had a relatively low current carrying capacity and so measurements were focussed on low fields at 4.2 K, and only the zeroth quadrant of the hysteresis loop was measured.

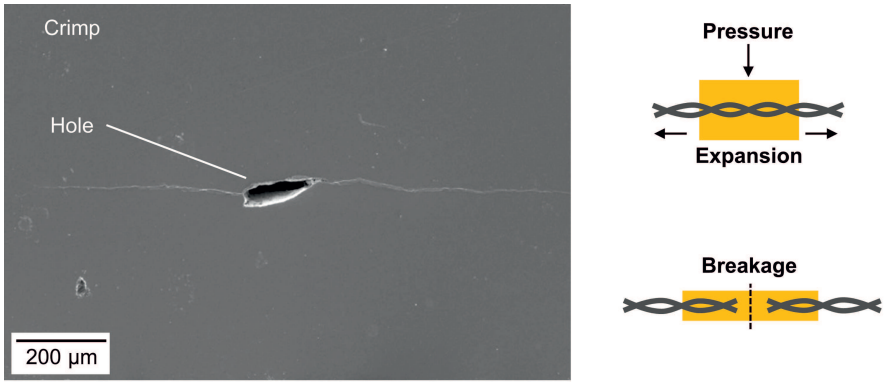

Figure 6.18: SEI of a transverse cross section through the centre of a typical cold pressed joint. The filaments have been snapped in two by the longitudinal expansion of the crimp during pressing (as illustrated), leaving behind a central hole.

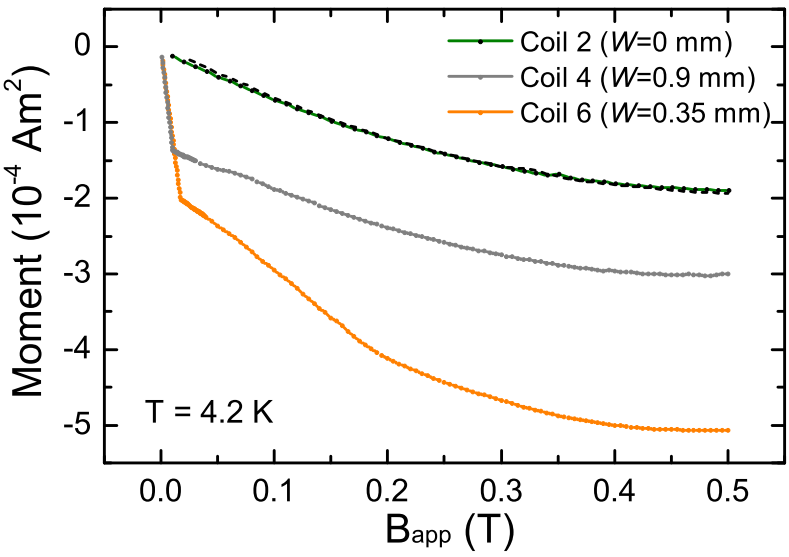

Figure 6.19: Magnetic moment of the Cu-crimped test coils as a function of applied field, raised from zero at 4.2 K. The open coil signal is shown by the dotted line.

The curve measured for Coil 2 ($W = 0$) is identical to that of the open coil, indicating that essentially zero current was able pass through the joint. Figure 6.20 shows SE images for this joint. Whilst the filaments have clearly been pressed together, there is a micron-scale void at both the filament-filament interface and filament-crimp interface, suggesting that the filaments may be slightly loose inside the crimp. The equivalent Nb-crimped joint (Coil 1) also exhibited a relatively low filament-filament current (as will be discussed). It is possible that the crimps are unable to maintain the pressure on the filaments when flattened to such an extent.

Coils 4 and 6 both exhibited closed-coil charging behaviour at low fields, indicating current flow through their joints. The open coil background signal is seemingly superimposed on the circuital current signal as field is further increased. Coil 6 passes the highest filament-filament current of the three joints, estimated to be $\sim$14 A from the peak of the closed-coil charging trend at 0.017 T. This is $\sim$5 % of the wire I_c.

Microstructural analysis of the joint for Coil 6 is shown in Figure 6.21. As can be seen from the BSE image in Figure 6.21a, the Cu has flowed around the filaments, completely encapsulating them and pushing the two into intimate contact. An SE image showing the crimp-filament interface in greater detail is provided in Figure 6.21b. An EDX linescan was performed across the interface, showing a small peak in oxygen (as expected) but no measurable void, suggesting the filaments are held tightly by the crimp. Figure 6.21c shows the filament-filament interface at high magnification, which is very similar to those found in the multifilamentary joint. There is no measurable void, however on the most part the filaments are not metallurgically bonded – the interface containing Cu and O from nodules and surface oxides, which are evident in EDX Linescan 1. However, there were some minor regions of seemingly clean metal-metal bonding, as shown in EDX linescan 2.

The filament-filament current transfer area of the overlapping filaments is difficult to measure accurately, but is certainly larger than the cross sectional area of a single filament. The average current density able to pass through the filament-filament interface is therefore estimated to be just a few percent of the wire's J_c. It cannot be said whether the current passes at low density through the "dirty" interfacial regions or at high density through the narrow metal to metal bonds but, regardless of this, the measurements show that the poor surface condition of the filaments inhibits current transfer.

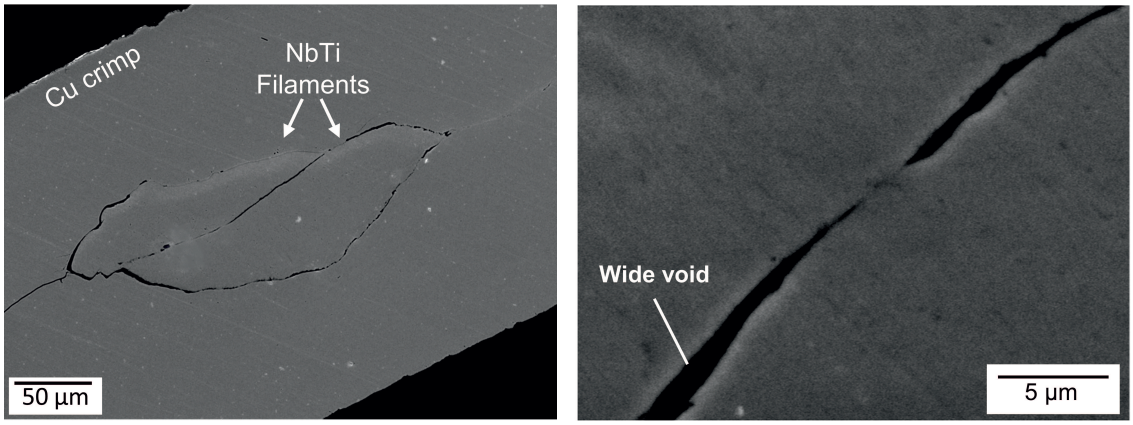

(a) (b)

Figure 6.20: (a) SE image of filaments pressed into contact in the joint of Coil 2 (Cu crimp, pressed at 50 kN), which passed no measurable current. (b) An image of the filament-filament interface at higher magnification, which has a micron-scale void across the entire interface.

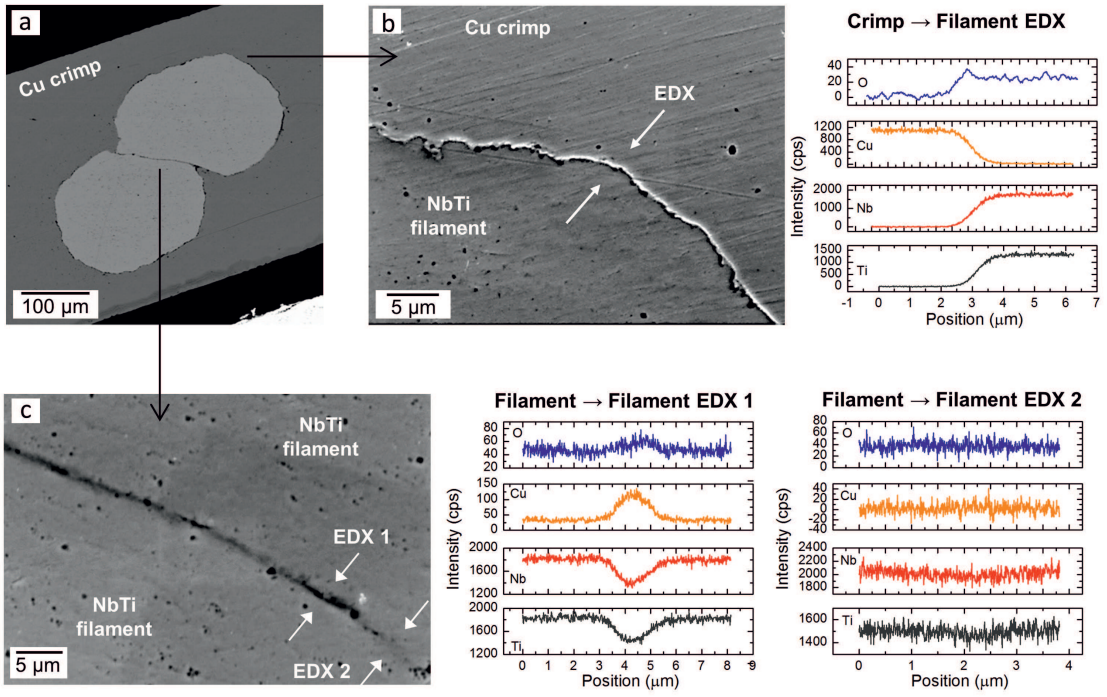

Figure 6.21: (a) BSE image of filaments pressed into contact in the joint of Coil 6 (Cu crimp, $W = 0.35$ mm) (b) SE image of the crimp-filament interface with an EDX linescan showing intimate contact but with intermediate oxides. (c) BSE image of the filament-filament interface with EDX linescans. Linescan 1 shows the typical interfacial condition, which contains O and Cu. Linescan 2 shows that in some small regions there appears to be clean metal-metal bonding.

6.3.3.3 Nb-Crimped Joints

The Nb crimped joints all exhibited similar performance characteristics, as shown in the hysteresis loops provided in Figure 6.22. Figure 6.22a shows hysteresis loops measured for each coil at 8.0 K, at which temperature there is no flux jumping. Quadrant 0 is omitted for clarity. The independently measured B_{c2} of the Nb material used for the crimps is also indicated for reference. Further loops measured for Coil 1 at various temperatures are also provided in Figure 6.22b.

At higher fields the moment is only slightly larger than the open coil background, indicating a small degree of direct filament-filament current flow, as was seen for the Cu-crimped joints. However, the loops each have an additional peak below the B_{c2} value of Nb, indicating current flow through the Nb crimp. These peaks are asymmetric about $B_{app} = 0$, being diamagnetically skewed towards quadrants 1 and 4. This is believed to be a self-field effect due to significant screening currents flowing in the Nb crimp at low fields, as was seen in the hysteresis loops of the bulk Nb sample tested in Section 4.5.2. The peaks also exhibit an anomalous plateau at low field, which is not well understood and has already been discussed in Section 5.4.7.

Figure 6.23 shows an SE image from the joint in Coil 5 (which passed the highest current through the Nb). The chemical make-up of the interfaces found in the Nb crimped joints were not notably different to those found in the Cu-crimped and multifilamentary joints, and needn't be repeated. Figure 6.23 highlights the main reason as to why much larger currents can flow via the Nb rather than directly between the filaments in these monofilamentary joints, which is that the filament-crimp contact area is much larger than the filament-filament contact area. There is at least an order of magnitude difference over the millimetre-scale joint length. This is simply because the filaments are twisted rather than laid on top of one another, such that over most of the joint length they are side by side and not pressed together. This geometrical bias towards current flow through the crimp may not be so large in multifilamentary joints (for which the filaments may easily be laid on top of one another), and thus in this case the Nb may make a smaller contribution to the joint's current carrying ability.

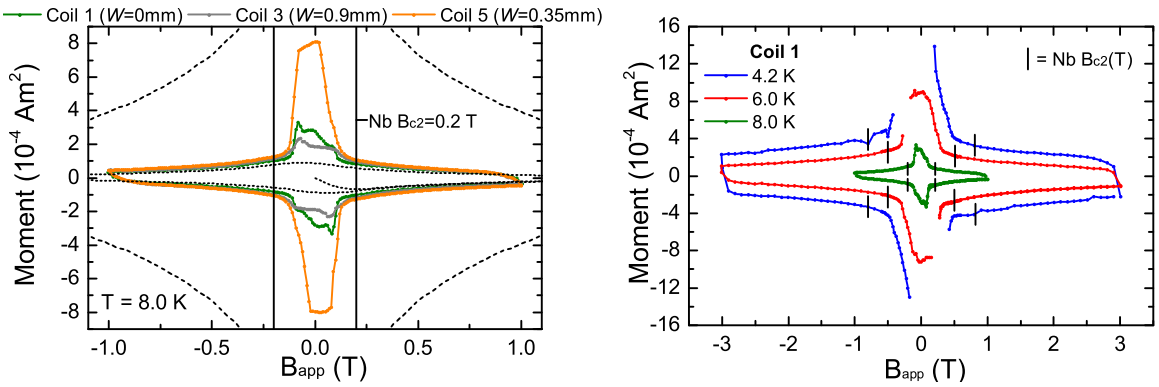

Figure 6.22: (a) Hysteresis loops measured at 8.0 K for each of the Nb-crimped coils, showing a low field peak associated with current flow through the Nb. (b) Further loops measured for Coil 1 at temperatures of 4.2, 6.0 and 8.0 K, with B_{c2} values for Nb indicated at each temperature.

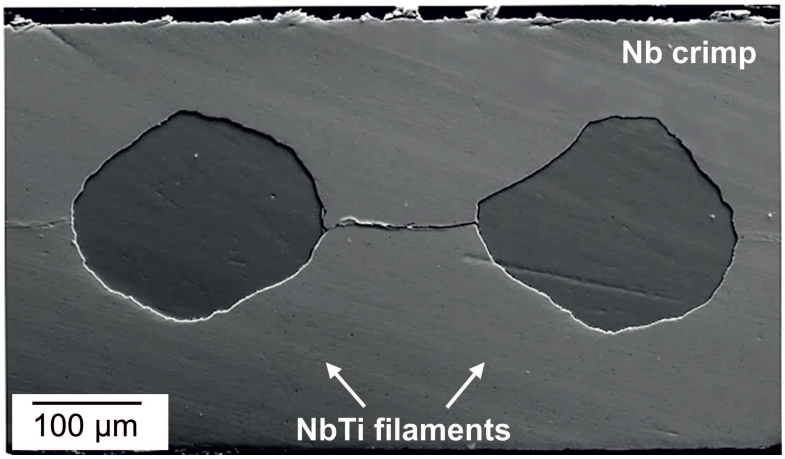

Figure 6.23: SE image of the Nb-crimped joint in Coil 5 (which passed the highest current through the Nb) at a location where the twisted filaments are side-by-side and encased in Nb. This cross section is typical of most of the joint length.

6.3.4 Cold Pressing of Solder-Coated Filaments

It appears that only a low current density is able to pass through the surface of filaments whose Cu matrix has been dissolved with nitric acid. This appears to be due to oxides and intermetallic nodules discovered on the filament surfaces that prevent metal-to-metal bonding over most of the interfaces. Whilst HF-based etchants may help to cleanse the bare filaments, their use is highly undesirable for commercial magnet manufacture. However, the solder matrix replacement method of dissolving the Cu matrix appears to dissolve the nodules from the NbTi surface, whilst also protecting the filaments from oxidation with a soft solder coating. Whilst some reaction layers are formed, these do not appear to limit current flow out of the filament. Some cold pressed joints were therefore made between solder-coated filaments, in the hope that as the filaments deform, the solder may be dislodged and clean bonds may be formed between the underlying filaments. This section presents some initial results from this investigation.

6.3.4.1 Joint Manufacture

As was discussed in Section 6.3.3.1, longitudinal crimp expansion during pressing causes the filaments to snap. To constrain the crimp length during pressing, a depression was ground into the lower anvil, as shown in Figure 6.24a, and a protrusion in the upper anvil. The crimp size was changed slightly to fit inside, having a 3 mm OD, 0.6 mm ID and 4 mm length. The new design completely eliminated filament breakages. Boron nitride was also sprayed onto the anvils to help release the pressed crimps. The crimps remained irremovable when pressed at loads greater than ∼5 kN, however this was a sufficient force to press the filaments into contact.

The joints were made between filaments coated in PbBi solder by the standard matrix replacement process, since this was known to produce a clean, superconducting interface. In future, if good filament-filament bonding is achieved, it is expected that PbBi could be replaced with a suitable Pb-free alternative whose superconducting properties would not be important.

The PbBi coated filaments were twisted together as normal, threaded through the crimp and pressed at the maximum force of 5 kN (a pressure of ∼400 MPa). A photograph of a crimped test coil is provided in Figure 6.24a. Multiple replica joints were made for microscopy.

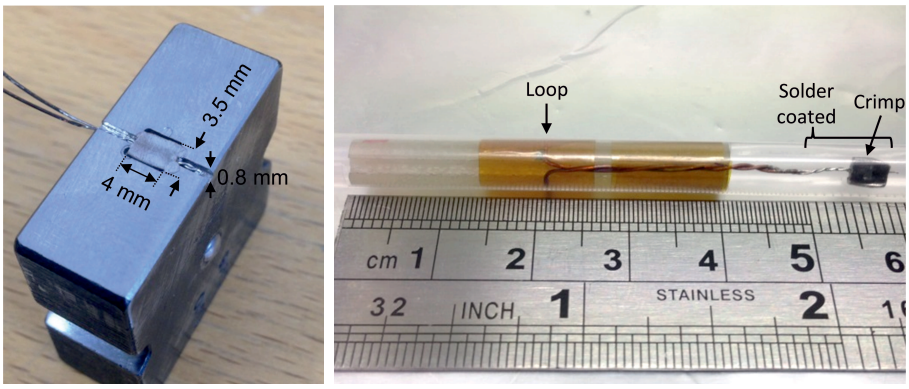

(a) (b)

Figure 6.24: (a) Photograph of the re-designed (lower) pressing anvil. The crimp is pressed into a depression which prevents longitudinal expansion. The upper anvil (not pictured), contains a protrusion which just fits inside the depression. (b) Photograph of the test coil jointed by pressing PbBi coated filaments inside a Nb crimp.

6.3.4.2 Analysis

Figure 6.25 shows BSE images and EDX data from a typical joint. It appears that the deformation of the filaments and crimp as the joint was pressed was effective in pushing aside much of the PbBi coating from around the filaments. As shown in Figure 6.25b, this has allowed the underlying NbTi material in the filaments to form seemingly clean metal-metal bonds in some areas, as was hoped. Figure 6.25c shows the well bonded region of the filament-filament interface in greater detail. The interface runs from the top left to the bottom right corner of the image, and is barely visible in most regions. Linescan 1 shows a seemingly clean NbTi-NbTi bond. Such bonds are seen over lengths of several tens of microns across the filament interface, which is promising. However, over most of the filament-filament interface, small amounts of Pb, Bi and Sn are found, which was expected from the reaction layers formed in the soldering process and any residual PbBi not displaced during pressing. No Cu was discovered, indicating the nodules had been dissolved as required.

Hysteresis loops measured for the test coil closed by this joint are shown in Figure 6.26. The joint performs well at fields below the B_{c2} of the PbBi, which is not surprising and was not the objective of the test. At 8.5 K the PbBi is in the normal state, and the low field peak observed reflects currents flowing via the Nb crimp. Whilst this was also not the objective of the test, this does demonstrate that PbBi is being removed from the filament surfaces during pressing. However, despite observing

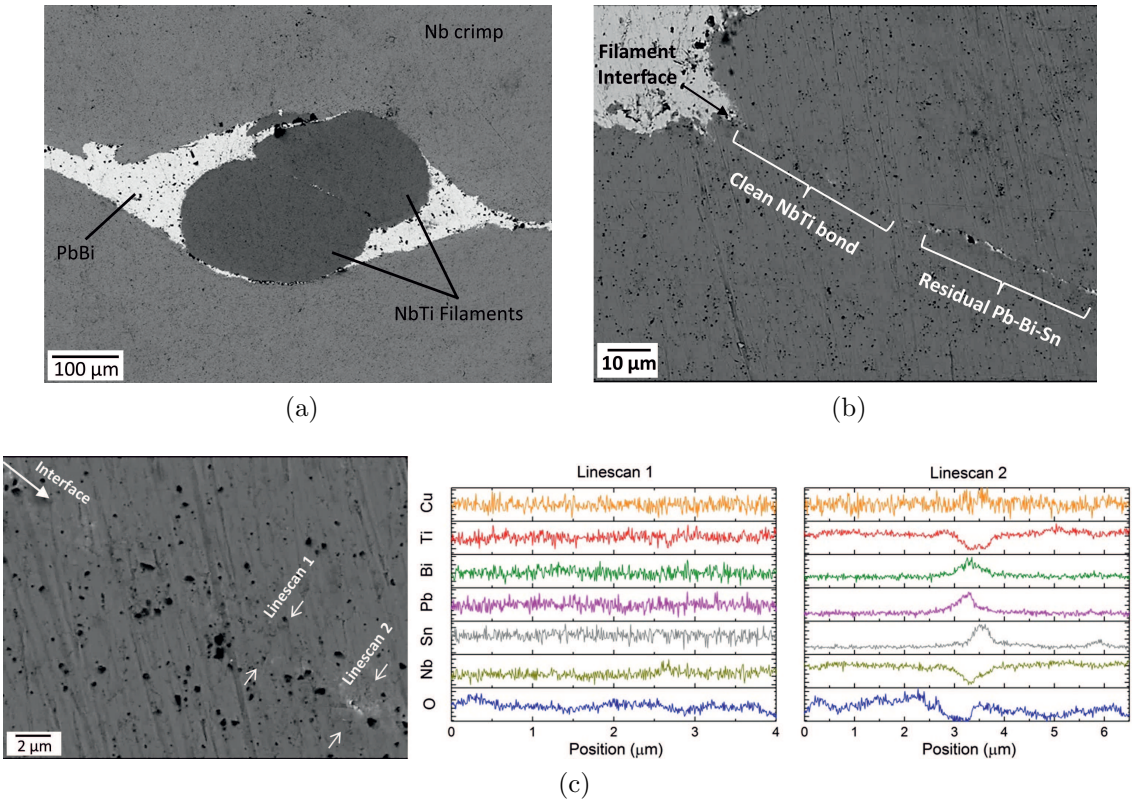

Figure 6.25: (a) BSE image of PbBi coated filaments pressed inside a Nb crimp. (b) Shows the filament-filament interface in greater detail, with some areas appearing to be cleanly bonded and others containing residual Pb, Bi and Sn from the matrix replacement process. This is evidenced in (c) by a high magnification image from the mostly cleanly bonded region, with EDX Linescan 1 showing a clean bond and Linescan 2 showing Pb, Bi and Sn at the interface.

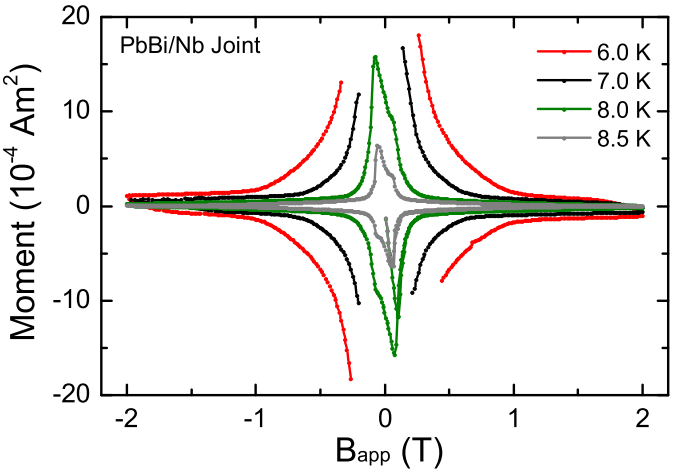

Figure 6.26: Hysteresis loops measured at various temperatures for a test coil closed by a Nb crimped joint made between PbBi coated filaments. At 8.5 K the PbBi is in the normal state.

promising filament-filament bonds in the micrographs, the current flowing directly between the filaments remains disappointingly low. From this it is concluded that either the apparent increase in cleanly-bonded filament-filament contact area is not large enough to have caused a significant improvement in performance, or the bonds are not as clean as the chemical analysis appears to suggest. The focus of further work should be to encourage displacement of the PbBi coating on the filaments by pressing at moderate temperatures.

6.3.5 Conclusions – Cold Pressing

The microstructural and superconducting properties of cold pressed joints between NbTi filaments exposed with nitric acid were investigated. It was found that oxides and intermetallic nodules on the filament surfaces inhibit metallurgical bonding. Measurements made on monofilamentary joints suggest that the current densities able to pass through such interfaces are very low – estimated to be just a few percent of the wire's J_c. Appreciable currents can pass through a superconducting Nb crimp, which is thought to be due to the large filament-crimp contact area in the particular joints made here.

In an attempt to improve metallurgical bonding between the filaments, cold pressed joints were made between solder coated filaments, for which the nodules appear to have been dissolved and oxides do not form. Preliminary results show promising signs that larger-scale metal-to-metal bonds can be produced, however as-yet the degree of filament-filament current flow has not been greatly improved. It may be possible to improve this method by crimping at moderate temperatures, in order to enhance the outflow of solder from between the filaments during pressing.

Chapter 7

Conclusions and Further Work

Studies into joints are a vital aspect of superconducting magnet development, both for novel conductors and well established materials. This thesis has presented a fundamental study into NbTi joints, which has established many key links between joint performance, their physical makeup, and the superconducting properties of their component parts. The work done here paves the way for a rigorous scientific development of new jointing methods for next generation NbTi magnets.

In Chapter 4 the superconducting properties of common jointing materials were characterised in fine detail. This facilitated an in-depth analysis of joint performance later in the thesis, but also highlighted the enormous gulf in performance between technological NbTi wires themselves and the materials typically used to join them. The development of a suitable Pb-free solder would provide a very convenient replacement for PbBi in the conventional soldering process, however at present the best Pb-free solder produced (InSnBi) falls far short of the mark in terms of performance. Future efforts in this regard should be aimed at producing low melting point solders with both high J_c and B_{c2}, not forgetting that the self field produced by the transport current flowing through the joint may reach a fraction of a Tesla. Nevertheless, the performance incentive for producing direct joints between the NbTi filaments themselves is significant.

The development of joints demands a quick and simple method of measuring their superconducting performance. In Chapter 5 a novel magnetic joint characterisation method was presented, allowing their current carrying ability to be measured in considerable detail over their entire superconducting phase space, employing a standard SQUID magnetometer. This allows highly detailed measurements to be made at the push of a button – a revolutionary technique for fundamental studies into joints. The

method highlighted the performance limiting aspects of a range of NbTi joints in this study and has now become the standard tool for joint measurements in the author's research group.

With further development, the technique could be used to extract precise $I_c(B,T)$ curves from magnetic hysteresis loops. To achieve this, wires with finer filaments must be employed to thermally stabilise the coils at low temperatures and fields, and also to reduce the size of magnetising currents which complicate the calculation of current from the measured magnetic moment. Finer wires would also allow a more precise coil to be wound, reducing uncertainties associated with coil geometry. Moreover, it will be vital to perform a proper calibration measurement by passing a known current through the coil and measuring the resultant moment.

The technique was also used to make IRT measurements, demonstrating the ability to access V-I characteristics at the pico-volt level in very short times. Whilst these served to show that the joints were truly superconducting, fundamental studies into their structure were affected by drift in the background field supplied by the magnetometer. Direct measurement of this drift highlighted that it may be reduced to a sufficiently low level by employing oscillatory field sweeping. It is believed that this will be compatible with IRT measurements providing the coil is sub-cooled whilst the background drift is settling. Development of this aspect of the technique may yield novel and much needed insights into the V-I characteristics of joints, and thus highlight the resistive mechanisms in operation.

Finally, in Chapter 6 the microstructural and superconducting properties of soldered, spot welded and cold pressed joints were investigated in detail. It was found that the performance of PbBi soldered joints appears to be limited by the bulk properties of the PbBi solder itself, which is quite remarkable given that the soldering process produces micron scale reaction layers at the NbTi/PbBi interface. This discovery suggests that the reaction layers themselves have relatively good superconducting properties, which is perhaps by virtue of the fact that many niobium-containing compounds exhibit strong superconducting properties (quite a stroke of luck). Future research into Pb-free solders ought to bear in mind that solder-filament reactions may not always be so fortuitous.

Studies into spot welding discovered dramatic cast microsructures in the weld zones of multifilamentary joints, and the fused material was found to have extremely low J_c values. Such damage was far less extensive in monofilamentary joints, which were

found to carry high fractions of the wire's I_c at all fields and temperatures. Spot welding is clearly capable of producing high quality joints, however can severely damage the NbTi material if the degree of heating is too high. Future research that might highlight a method of controlling the degree of heating in the joints sufficiently well for industrial magnet manufacture would be highly valuable.

Finally, the study of cold pressed joints between nitric acid etched filaments showed that intermetallic nodules and oxides remain on the filament surfaces and disturb the cold welding process. Current densities able to pass through such filament interfaces are well below those of pristine NbTi material itself. The materials challenge to be solved is the production of clean metal-to-metal bonds between the filaments without the use of dangerous HF acid cleansing or high temperature processes which may be difficult to control. The present study has highlighted a possible route: to press together solder-coated filaments at moderate temperatures, making use of the superconducting interface produced in Thornton's matrix replacement method.

Use of a NbTi crimp may assist in ensuring even sharing of the current between the filaments of each wire, and also provide some additional field shielding. Of course, the same matrix replacement process would have to be applied to the NbTi crimp in order to produce a clean bond to the filaments. The NbTi crimp would preferably not be too large in size either, to minimise the risk of flux jumping. It may be possible to incorporate a specially engineered composite NbTi/metal crimp such as that shown in Figure 7.1. The crimp would have a metallic outer sheath (undissolvable in molten Sn), a NbTi cylinder, and a Cu core (dissolvable in molten Sn). The core could be dissolved by the standard matrix replacement method and then pressed around solder coated filaments at moderate temperatures, allowing the NbTi filaments and NbTi

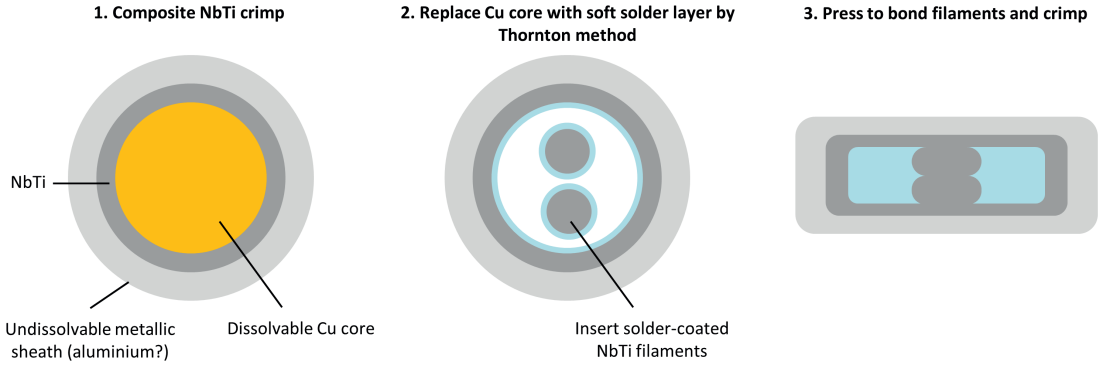

Figure 7.1: A composite NbTi crimp design that could be incorporated into the solder-coating/cold pressing technique.

crimp to be bonded. Wire manufacturers may be able to produce a large diameter wire of this architecture by the conventional wire drawing process, which could then be chopped into small lengths for use as a crimp.

References

[1] L. Rossi, "Superconductivity: its role, its success and its setbacks in the large hadron collider of CERN," *Supercond. Sci. Technol.*, vol. 23, no. 3, p. 034001, 2010.

[2] A. Devred, I. Backbier, D. Bessette, G. Bevillard, M. Gardner, M. Jewell, N. Mitchell, I. Pong, and A. Vostner, "Status of ITER conductor development and production," *IEEE Trans. Appl. Supercond.*, vol. 22, no. 3, p. 4804909, 2012.

[3] J. Liu, J. Cheng, and Q. Wang, "Evaluation of NbTi superconducting joints for 400 MHz NMR magnet," *IEEE Trans. Appl. Supercond.*, vol. 23, no. 6, pp. 34–39, 2013.

[4] M. Lakrimi, A. M. Thomas, G. Hutton, M. Kruip, R. Slade, P. Davis, A. J. Johnstone, M. J. Longfield, H. Blakes, and S. . Calvert, "The principles and evolution of magnetic resonance imaging," *J. Phys.: Conf. Ser.*, vol. 286, p. 012016, 2011.

[5] "Directive 2011/65/EU," *OJ L174*, p. 88, 2011.

[6] "Directive 2014/9/EU," *OJ L4*, p. 61, 2014.

[7] J. Bardeen, L. N. Cooper, and J. R. Schrieffer, "Theory of superconductivity," *Phys. Rev.*, vol. 108, pp. 1175–1204, 1957.

[8] S. E. Sebastian, N. Harrison, F. F. Balakirev, M. M. Altarawneh, P. A. Goddard, R. Liang, D. A. Bonn, W. N. Hardy, and G. G. Lonzarich, "Normal-state nodal electronic structure in underdoped high-Tc copper oxides," *Nature*, vol. 511, no. 7507, pp. 61–64, 2014.

[9] F. London and H. London, "The electromagnetic equations of the supraconductor," in *Proc. Roy. Soc. A*, vol. 149, pp. 71–88, The Royal Society, 1935.

[10] V. L. Ginzburg and L. D. Landau, "On the theory of superconductivity," *Zh. Eksp. Teor. Fiz.*, vol. 20, p. 1064, 1950.

[11] A. A. Abrikosov, "On the magnetic properties of superconductors of the second group," *JETP*, vol. 5, pp. 1174–1118, 1957.

[12] W. Meissner and R. Ochsenfeld, "Ein neuer effekt bei eintritt der supraleitf higkeit," *Naturwissenschaften*, vol. 21, no. 44, pp. 787–788, 1933.

[13] Y. B. Kim, C. F. Hempstead, and A. R. Strnad, "Flux-flow resistance in type-II superconductors," *Phys. Rev.*, vol. 139, pp. A1163–A1172, Aug 1965.

[14] A. M. Campbell, J. Evetts, and D. Dew-Hughes, "Pinning of flux vortices in type-II superconductors," *Phil. Mag.*, vol. 18, pp. 313–43, 1968.

[15] C. P. Bean, "Magnetization of hard superconductors," *Phys. Rev. Lett.*, vol. 8, no. 6, pp. 250–253, 1962.

[16] D. Dew-Hughes, "Flux pinning mechanisms in type-II superconductors," *Phil. Mag.*, vol. 30, no. 2, pp. 293–305, 1974.

[17] W. A. Fietz and W. W. Webb, "Hysteresis in superconducting alloys, temperature and field dependence of dislocation pinning in niobium alloys," *Phys. Rev.*, vol. 178, pp. 657–667, Feb 1969.

[18] P. Anderson, "Theory of flux creep in hard superconductors," *Phys. Rev. Lett.*, vol. 9, no. 7, pp. 309–311, 1962.

[19] J. E. Evetts, A. M. Campbell, and D. Dew-hughes, "Flux instabilities in hard superconductors," *Phil. Mag.*, vol. 10, no. 104, pp. 339–343, 1964.

[20] R. G. Mints and A. L. Rakhmanov, "Critical state stability in type-II superconductors and superconducting-normal-metal composites," *Rev. Mod. Phys.*, vol. 53, no. 3, pp. 551–592, 1981.

[21] M. N. Wilson, *Superconducting magnets*. Clarendon Press: Oxford, 1983.

[22] M. Wilson, "Stabilization of superconductors for use in magnets," *IEEE Trans. Magn.*, vol. 13, no. 1, pp. 440–446, 1977.

[23] W. Warnes and D. Larbalestier, "Critical current distributions in superconducting composites," *Cryogenics*, vol. 26, no. 12, pp. 643–653, 1986.

[24] R. Jones, E. Rhoderick, and A. Rose-Innes, "Non-linearity in the voltage-current characteristic of a type-2 superconductor," *Phys. Lett. A*, vol. 24, no. 6, pp. 318–319, 1967.

[25] W. H. Warnes, "A model for the resistive critical current transition in composite superconductors," *J. Appl. Phys.*, vol. 63, no. 5, p. 1651, 1988.

[26] P. J. Lee, *Wiley Encyclopedia of Electrical and Electronics Engineering*, ch. Superconductors, Metallurgy of Ductile Alloys. John Wiley & Sons, Inc., 2001.

[27] G. Enderlein, A. Handstein, F. Lange, and P. Verges, "Anisotropy of the critical current density in superconducting niobium-titanium wires," *Cryogenics*, vol. 13, no. 7, pp. 426–429, 1973.

[28] G. D. Brittles, T. Mousavi, C. R. M. Grovenor, C. Aksoy, and S. C. Speller, "Persistent current joints between technological superconductors," *Supercond. Sci. Technol.*, vol. 28, no. 9, p. 093001, 2015.

[29] J. H. Kim, B. K. Ji, J. Joo, C.-W. Yang, and W. Nah, "Superconducting joint between Bi-Pb-Sr-Ca-Cu-O superconductor tapes," *IEEE Trans. Appl. Supercond.*, vol. 10, no. 1, pp. 1182–1185, 2000.

[30] N. Bagrets, C. Barth, and K.-P. Weiss, "Low temperature thermal and thermomechanical properties of soft solders for superconducting applications," *IEEE Trans. Appl. Supercond.*, vol. 24, no. 3, pp. 1–3, 2014.

[31] D. Dummer, P. Andersen, and W. Weyhmann, "Superconductivity of Au-Sn eutectic solder," *Cryogenics*, vol. 31, no. 5, pp. 388–389, 1991.

[32] D. Taylor and D. Hampshire, "The scaling law for the strain dependence of the critical current density in Nb_3Sn superconducting wires," *Supercond. Sci. Technol.*, vol. 18, no. 12, pp. S241–S252, 2005.

[33] S. A. Keys and D. P. Hampshire, *Handbook of superconducting materials: Characterization of conductors*. Institute of Physics Pub.: Bristol, 2003.

[34] Y. Park, M. Lee, H. Ann, Y. H. Choi, and H. Lee, "A superconducting joint for $GdBa_2Cu_3O_{7-\delta}$-coated conductors," *NPG Asia Mater.*, vol. 6, no. 5, p. 98, 2014.

[35] R. F. Thornton, "Superconducting joint for superconducting wires and coils," Apr 1986. US Patent 4,584,547.

[36] H. Wen, L. Lin, and S. Han, "Joint resistance measurement using current-comparator for superconducting wires in high magnetic field," *IEEE Trans. Magn.*, vol. 28, no. 1, pp. 834–836, 1992.

[37] W. Yao, J. Bascunan, S. Hahn, and Y. Iwasa, "A superconducting joint technique for MgB_2 round wires," *IEEE Trans. Appl. Supercond.*, vol. 19, no. 3, pp. 2261–2264, 2009.

[38] T. Fukuzaki, H. Maeda, S. Matsumoto, S. Nimori, S. Yokoyama, and T. Kiyoshi, "Development of a superconducting joint for high field NMR," *IEEE Trans. Appl. Supercond.*, vol. 16, no. 2, pp. 1547–1549, 2006.

[39] D. Ryan, H. Jones, W. Timms, and N. Killoran, "Critical current measurements at electric fields in the pV/m regime," *IEEE Trans. Appl. Supercond.*, vol. 7, no. 2, pp. 1455–1458, 1997.

[40] R. Musenich, P. Fabbricatore, S. Farinon, and M. Greco, "Determination of the V-I characteristic of NbTi wires in a wide resistivity range," *Physica C*, vol. 401, no. 1-4, pp. 260–264, 2004.

[41] M. Leupold and Y. Iwasa, "Superconducting joint between multifilamentary wires 1. joint-making and joint results," *Cryogenics*, vol. 16, no. 4, pp. 215–216, 1976.

[42] T. Fukuzaki, H. Maeda, S. Matsumoto, S. Yokoyama, and T. Kiyoshi, "Study of joint resistance in Nb_3Al-NbTi superconducting joint for high field nmr," *IEEE Trans. Appl. Supercond.*, vol. 17, no. 2, pp. 1435–1437, 2007.

[43] J. Cheng, J. Liu, Z. Ni, C. Cui, S. Chen, S. Song, L. Li, Y. Dai, and Q. Wang, "Fabrication of NbTi superconducting joints for 400-MHz NMR application," *IEEE Trans. Appl. Supercond.*, vol. 22, no. 2, pp. 4300205–4300205, 2012.

[44] J. Liu, J. Cheng, F. Zhou, Q. Wang, K. Chang, and X. Li, "Electrical properties of cold-pressing welded NbTi persistent joints," *Cryogenics*, vol. 58, pp. 62–67, 2013.

[45] G. D. Brittles, P. Noonan, S. A. Keys, C. R. M. Grovenor, and S. Speller, "Rapid characterisation of persistent current joints by SQUID magnetometry," *Supercond. Sci. Technol.*, vol. 27, no. 12, p. 122002, 2014.

[46] D. Ni, W. Yang, S. Han, L. Zhu, X. Zhang, B. Wu, and L. Ma, "A test system for superconducting joints based on GM cryocooler," *IEEE Trans. Appl. Supercond.*, vol. 24, no. 3, pp. 1–5, 2014.

[47] S. Liu, X. Jiang, G. Chai, and J. Chen, "Superconducting joint and persistent current switch for a 7-T animal mri magnet," *IEEE Trans. Appl. Supercond.*, vol. 23, no. 3, pp. 4400504–4400504, 2013.

[48] D. Ryan, *Critical currents of commercial superconductors in the picovolt per metre electric field regime.* PhD thesis, University of Oxford, 1997.

[49] J. Duchateau, B. Turck, L. Krempasky, and M. Polak, "The self-field effect in twisted superconducting composites," *Cryogenics*, vol. 16, no. 2, pp. 97–102, 1976.

[50] S. Mizumaki and A. Yamamoto, "Experimental study of current sharing and transfer in superconductor joint," *IEEE Trans. Appl. Supercond.*, vol. 7, no. 2, pp. 805–807, 1997.

[51] J. Halbritter, "On the oxidation and on the superconductivity of niobium," *Appl. Phys. A*, vol. 43, no. 1, pp. 1–28, 1987.

[52] A. Aspart and C. Antoine, "Study of the chemical behavior of hydrofluoric, nitric and sulfuric acids mixtures applied to niobium polishing," *Appl. Surf. Sci*, vol. 227, no. 1-4, pp. 17–29, 2004.

[53] C. Swenson and W. Markiewicz, "Persistent joint development for high field NMR," *IEEE Trans. Appl. Supercond.*, vol. 9, no. 2, pp. 185–188, 1999.

[54] Priv. Comm. with P. Noonan (Agilent Technologies), 2014.

[55] A. Moorhead, J. Woodhouse, and D. Easton, "Soldering of copper-clad niobium–titanium superconductor composite," tech. rep., Oak Ridge National Lab., TN (USA), 1977.

[56] B. Seeber, *Handbook of applied superconductivity.* Institute of Physics Pub.: Bristol, 1998.

[57] A. M. Campbell, J. E. Evetts, and D. Dew-Hughes, "The behaviour of type-II superconductors," *Phil. Mag.*, vol. 10, no. 104, pp. 333–338, 1964.

[58] A. Campbell and J. Evetts, "Flux vortices and transport currents in type ii superconductors," *Adv. Phys*, vol. 21, no. 90, pp. 199–428, 1972.

[59] J. Evetts and J. Wade, "Superconducting properties and the phase diagrams of the Pb-Bi and Pb-In alloy systems," *J. Phys. Chem. Solids*, vol. 31, no. 5, pp. 973–982, 1970.

[60] R. I. Coote, J. E. Evetts, and A. M. Campbell, "Flux line pinning by large normal particles in type-II superconductors," *Can. J. Phys.*, vol. 50, no. 5, pp. 421–427, 1972.

[61] K. Seo, S. Nishijima, K. Katagiri, and T. Okada, "Evaluation of solders for superconducting magnetic shield," *IEEE Trans. Magn.*, vol. 27, no. 2, pp. 1877–1880, 1991.

[62] T. Tominaka, S. Kakugawa, N. Hara, and N. Maki, "Electrical properties of superconducting joint between composite conductors," *IEEE Trans. Magn.*, vol. 27, no. 2, pp. 1846–1849, 1991.

[63] J. M. Nuding, "Method of making a superconductive joint," Jan 1969. US Patent 3,422,529.

[64] S. Phillip, J. V. Porto, and J. M. Parpia, "Two methods of fabricating reliable superconducting joints with multifilamentary Nb-Ti superconducting wire," *J. Low. Temp. Phys.*, vol. 101, no. 3-4, pp. 581–585, 1995.

[65] M. Blumenthal and M. Lakrimi, "Method for joining superconducting wires, and superconducting joint," May 2014. US Patent 2014/0135223 A1.

[66] G. Luderer, P. Dullenkopf, and G. Laukien, "Superconducting joint between multifilamentary wires," *Cryogenics*, vol. 14, no. 9, pp. 518–519, 1974.

[67] E. Karvonen and J.-M. Rayroux, "Electrical connection between superconductors," Sept 1970. US Patent 3,527,876.

[68] J. Williams, S. Pourrahimi, Y. Iwasa, L. Neuringer, and L. Motowidlo, "600 MHz spectrometer magnet," *IEEE Trans. Magn.*, vol. 25, no. 2, pp. 1767–1770, 1989.

[69] D. Zhang, S. Lin, C. G. Cui, and Z. Chen, "Upper critical field of Nb and Nb+1 at percent Ta determined by calorimetric and magnetic methods," *J. Low. Temp. Phys.*, vol. 55, no. 3-4, pp. 303–308, 1984.

[70] T. Mousavi, C. Aksoy, C. R. M. Grovenor, and S. Speller, "Microstructure and superconducting properties of Sn-In and Sn-In-Bi alloys as Pb-free superconducting solders," *Supercond. Sci. Technol.*, vol. In Press, 2015.

[71] C. P. Bean, "Magnetization of high-field superconductors," *Reviews of Modern Physics*, vol. 36, no. 1, pp. 31–39, 1964.

[72] M. D. Ainslie and H. Fujishiro, "Modelling of bulk superconductor magnetization," *Superconductor Science and Technology*, vol. 28, no. 5, p. 053002, 2015.

[73] Y. B. Kim, C. F. Hempstead, and A. R. Strnad, "Critical persistent currents in hard superconductors," *Phys. Rev. Lett.*, vol. 9, no. 7, pp. 306–309, 1962.

[74] Y. B. Kim, C. F. Hempstead, and A. R. Strnad, "Magnetization and critical supercurrents," *Phys. Rev.*, vol. 129, no. 2, pp. 528–535, 1963.

[75] A. Morandi and M. Fabbri, "A unified approach to the power law and the critical state modeling of superconductors in 2D," *Superconductor Science and Technology*, vol. 28, no. 2, p. 024004, 2014.

[76] J. A. Osborn, "Demagnetizing factors of the general ellipsoid," *Phys. Rev.*, vol. 67, no. 11-12, pp. 351–357, 1945.

[77] H. Wiesinger, F. Sauerzopf, and H. Weber, "On the calculation of j_c from magnetization measurements on superconductors," *Physica C: Superconductivity*, vol. 203, no. 1-2, pp. 121–128, 1992.

[78] G. Woan, *The Cambridge handbook of physics formulas*. Cambridge University Press: Cambridge, 2000.

[79] F. Fickett, "Standards for measurement of the critical fields of superconductors," *J. Res. Natl. Bur. Stan.*, vol. 90, no. 2, p. 95, 1985.

[80] D. Zheng, P. Lang, J. Xiang, and Z. Zhao, "Determination of irreversibility fields in low temperature superconductors," *Physica C: Superconductivity*, vol. 386, pp. 14–17, 2003.

[81] M. Lubell, "Empirical scaling formulas for critical current and critical field for commercial NbTi," *IEEE Trans. Magn.*, vol. 19, no. 3, pp. 754–757, 1983.

[82] A. Godeke, M. C. Jewell, A. A. Golubov, B. T. Haken, and D. C. Larbalestier, "Inconsistencies between extrapolated and actual critical fields in Nb_3Sn wires as demonstrated by direct measurements of H_{c2} , H* and T_c," *Supercond. Sci. Technol.*, vol. 16, no. 9, pp. 1019–1025, 2003.

[83] N. Cheggour and D. P. Hampshire, "The unified strain and temperature scaling law for the pinning force density of bronze-route Nb_3Sn wires in high magnetic fields," *Cryogenics*, vol. 42, no. 5, pp. 299–309, 2002.

[84] N. R. Werthamer, E. Helfand, and P. C. Hohenberg, "Temperature and purity dependence of the superconducting critical field, h_{c2} . III. electron spin and spin-orbit effects," *Phys. Rev.*, vol. 147, no. 1, pp. 295–302, 1966.

[85] L. Bottura, "A practical fit for the critical surface of NbTi," *IEEE Trans. Appl. Supercond.*, vol. 10, no. 1, pp. 1054–1057, 2000.

[86] L. Affinito, S. Chiarelli, V. Corato, A. d. Corte, G. D. Marzi, A. D. Zenobio, C. F. Zignani, G. Messina, L. Muzzi, and M. Napolitano, "Variable-temperature characterization of NbTi strands in the low critical-current density range," *J. Phys.: Conf. Ser.*, vol. 97, p. 012306, 2008.

[87] L. Zani, E. Mossang, M. Tena, J.-P. Serries, and H. Cloez, "$j_c(b,t)$ characterization of NbTi strands used in ITER PF-relevant insert and full-scale sample," *IEEE Trans. Appl. Supercond.*, vol. 15, no. 2, pp. 3506–3509, 2005.

[88] A. Martinelli and B. Turck, "Some effects of field orientation on the magnetization of superconducting wires," *Cryogenics*, vol. 18, no. 3, pp. 155–161, 1978.

[89] K. Jungst, "Orientation effects on the magnetization of NbTi superconductors," *IEEE Trans. Magn.*, vol. 13, no. 1, pp. 209–212, 1977.

[90] K. Best, D. Genevey, H. Hillmann, L. Krempasky, M. Polak, and B. Turck, "Anisotropy of the critical current in solid solution superconductor NbTi," *IEEE Trans. Magn.*, vol. 15, no. 1, pp. 395–397, 1979.

[91] S. Takacs and I. Hlasnik, "Pinning in superconductors with anisotropic defects," *Journal of Low Temperature Physics*, vol. 54, no. 3-4, pp. 397–410, 1984.

[92] S. Yoon and H. Lee, "A thermodynamic study of phase equilibria in the Sn-Bi-Pb solder system," *Calphad*, vol. 22, no. 2, pp. 167 – 178, 1998.

[93] I. Ohnuma, Y. Cui, X. J. Liu, Y. Inohana, S. Ishihara, H. Ohtani, R. Kainuma, and K. Ishida, "Phase equilibria of Sn-In based micro-soldering alloys," *J. Electron. Mater.*, vol. 29, no. 10, pp. 1113–1121, 2000.

[94] S. A. Levy, "Effect of structure on the superconducting properties of eutectic alloys," *J. Appl. Phys.*, vol. 37, no. 10, p. 3659, 1966.

[95] W. H. Warren, "Superconductivity measurements in solders commonly used for low temperature research," *Rev. Sci. Instrum.*, vol. 40, no. 1, p. 180, 1969.

[96] M. Merriam and M. Von Herzen, "Superconductivity in the indium-tin system," *Phys. Rev*, vol. 131, no. 2, pp. 637–643, 1963.

[97] D. Saint-James and P. Gennes, "Onset of superconductivity in decreasing fields," *Physics Letters*, vol. 7, no. 5, pp. 306–308, 1963.

[98] Z.-H. Sung, A. Dzyuba, P. J. Lee, D. C. Larbalestier, and L. D. Cooley, "Evidence of incomplete annealing at 800^{o}C and the effects of 120^{o}C baking on the crystal orientation and the surface superconducting properties of cold-worked and chemically polished Nb," *Superconductor Science and Technology*, vol. 28, no. 7, p. 075003, 2015.

[99] C. P. Poole, *Superconductivity.* Academic Press: New York, 2007.

[100] W. A. Fietz, M. R. Beasley, J. Silcox, and W. W. Webb, "Magnetization of superconducting Nb-25%Zr wire," *Phys. Rev.*, vol. 136, no. 2A, pp. 335–345, 1964.

[101] D. Hampshire, "A barrier to increasing the critical current density of bulk untextured polycrystalline superconductors in high magnetic fields," *Physica C: Superconductivity*, vol. 296, no. 1-2, pp. 153–166, 1998.

[102] J. Jaroszynski, "Race against time: resistance of superconducting joints measurements," *Supercond. Sci. Technol.*, vol. 28, no. 1, p. 010501, 2014.

[103] V. Sytchev, V. Zenkevitch, V. Andrianov, and F. Ternovskiy, "Flux linkage and self-inductance of superconducting solenoids," *Cryogenics*, vol. 7, no. 6, pp. 344–350, 1967.

[104] C. Völlinger, *Superconductor Magnetization Modeling for the Numerical Calculation of Field Errors in Accelerator Magnets.* PhD thesis, Dept. of Electrical Engineering and Computer Science, Berlin Institute of Technology, 2003.

[105] M. Sawicki, W. Stefanowicz, and A. Ney, "Sensitive SQUID magnetometry for studying nanomagnetism," *Semicond. Sci. Technol.*, vol. 26, no. 6, p. 064006, 2011.

[106] I. S. Grant and W. R. Phillips, *Electromagnetism - 2nd ed.* Wiley: Chichester, 1990.

[107] F. W. Grover, *Inductance calculations*. Dover: New York, 2009.

[108] Quantum Design Application Note 1070-207 - "*Using PPMS superconducting magnets at low fields*", 2009.

[109] Web Address: http://squid-cmmp.blogspot.co.uk/2013/08/magnet-field-relaxation.html [Accessed online March 2016].

[110] N. R. Werthamer, "Theory of the superconducting transition temperature and energy gap function of superposed metal films," *Phys. Rev.*, vol. 132, no. 6, pp. 2440–2445, 1963.

[111] P. G. deGennes, "Boundary effects in superconductors," *Rev. Mod. Phys.*, vol. 36, no. 1, pp. 225–237, 1964.

[112] B. W. Roberts, "Survey of superconductive materials and critical evaluation of selected properties," *Journal of Physical and Chemical Reference Data*, vol. 5, no. 3, p. 581, 1976.

[113] G. Brittles, C. Aksoy, C. Grovenor, T. Bradshaw, S. Milward, and S. Speller, "Microstructural properties and magnetic testing of spot welded joints between Nb-Ti filaments," *IEEE Trans. Appl. Supercond.*, p. in press, 2016.

[114] N. Charde, "Effects of electrode deformation of resistance spot welding on 304 austenitic stainless steel weld geometry," *J. Mech. Eng. Sci*, vol. 3, pp. 261–270, 2012.

[115] D. Larbalestier, P. Lee, and R. Samuel, "The growth of intermetallic compounds at a copper-niobium-titanium interface," *Adv. Cryo. Eng. (Materials)*, vol. 32, pp. 715–722, 1986.

[116] J. W. Ekin, *Experimental techniques for low-temperature measurements*. Oxford University Press: Oxford, 2006.

[117] J. Seuntjens, F. Clark, M. Erdmann, E. Coleman, and B. Jones, "Comparisons of processes and performance of SSC-VQP material," in *Supercollider 5*, pp. 151–154, Springer, 1994.